Cloud cycling, scavenging and aerosol vertical profiles: Process sensitivity and observational constraints

Zak Kipling, Linacre College

Trinity Term 2013

Thesis for the degree of Doctor of Philosophy in
Atmospheric, Oceanic and Planetary Physics

Cloud cycling, scavenging and aerosol vertical profiles: Process sensitivity and observational constraints

Zak Kipling, Linacre College, University of Oxford

Trinity Term 2013

Thesis for the degree of Doctor of Philosphy in
Atmospheric, Oceanic and Planetary Physics

Abstract

The effects of aerosol in the atmosphere account for some of the largest uncertainties in estimates of the human impact on climate. These effects depend not only on the total mass of aerosol, but also its size distribution, mixing state and vertical profile.

Previous studies have suggested that both the size distribution and mixing state of aerosol may be strongly influenced by repeated cycling through non-precipitating cloud. The extent of this process is assessed in the HadGEM3–UKCA model; although fewer cycles are seen for all aerosol than in previous studies, the figure varies considerably between aerosol types.

The role of scavenging by precipitating cloud is also considered, and several approaches to increasing the physical realism of its representation are considered. In particular, coupling convective scavenging into the convective transport scheme is shown to provide significant benefits over an operator-split approach (which underestimates removal and allows excess aerosol to reach the upper troposphere and be transported to remote regions).

To evaluate the alternative convective scavenging schemes, a method is developed for carrying out a pointwise evaluation against vertically-resolved in-situ observations from large-scale aircraft campaigns, based on nudging and flight-track sampling in the model. It is demonstrated that this approach can help to constrain the choice between different model configurations with a degree of statistical confidence.

Finally, the processes controlling the vertical profile of aerosol are investigated using a series of model-based sensitivity tests, along with the extent to which these processes can account for the large diversity in vertical profiles seen amongst current models. For mass profiles and number profiles of large particles (greater than about 100 nm dry diameter), removal and secondary production processes are shown to be most important; for number profiles of smaller particles, microphysical processes are shown to become increasingly dominant.

In Memoriam

Caroline Mason, 1953–2011

Acknowledgements

I would like to take this opportunity to thank the many people who have helped to make this work possible.

Firstly I would like to thank my supervisors for their support and guidance throughout my work on this thesis. Philip Stier has been a source of support and inspiration throughout, helping me to develop and clarify the direction this work has taken whenever necessary but never over-managing the project. Colin Johnson, at the Met. Office, has also been an invaluable source of ideas and advice throughout. In addition to my formal supervisors, both Till Wagner and Nick Schutgens have served as post-doctoral advisers over the course of the project, and provided much valuable input and advice.

This work was supported by the Natural Environment Research Council and the Met. Office through a CASE studentship. I would therefore like to thank both organisations, without whose financial support I would not have been able to undertake this project.

The link with the Met. Office has both been of great practical help in connecting with the right people whenever I've had questions regarding more or less arcane aspects of HadGEM and the Unified Model, and provided a valuable insight into the working of such an institution.

I would like to thank the great many people involved in developing the HadGEM3–UKCA and ECHAM5–HAM2 models, without which this work would obviously not have been possible. I am also grateful to both the Met. Office/NERC Joint Weather & Climate Research Programme (JWCRP) and Deutsche Klimarechenzentrum (DKRZ) for providing the high-performance computing resources necessary for running HadGEM3–UKCA and ECHAM5–HAM2 respectively; and to the National Centre for Atmospheric Science (NCAS) Computational Modelling Support (CMS) group for facilitating access to the Unified Model through the PUMA system, and their timely response to many support queries.

Thanks are also due to all those involved in the UKCA project – in addition to Colin, Graham Mann, Mohit Dalvi and Paul Telford (who provided much of the code for flight-track sampling used in Chapter 4) deserve a particular mention. Beyond UKCA, discussions with Cyril Morcrette, Rachel Stratton and Paul Field at the Met. Office have been of great help at various points.

Working with the HIPPO observations in Chapter 4, and with the AeroCom model data in Chapter 5, has provided opportunities for international collaboration, for which I am very grateful. In particular, Shuka Schwarz at NOAA and the University of Colorado has been ever patient and ready to provide help in working with the Single-Particle Soot Photometer (SP2) data from HIPPO, and I am most grateful to Shuka and his colleagues for providing access to the detailed dataset from this instrument. Tommi Bergman was also very helpful in re-processing some of the output from the ECHAM5–SALSA model for the AeroCom vertical profile analysis.

I am also grateful to those who have provided the many software tools I have used for data analysis in the course of this work, in particular Python, NumPy, SciPy, Matplotlib, NCO, CDO and xconv/convsh.

I would like to thank the other members of the Climate Processes group in Atmospheric, Oceanic and Planetary Physics: Philip, Till and Nick as mentioned above, and also Rosalind West, Benjamin Grandey, Ed Gryspeerdt, Natalie Weigum, Steffen Lohrey, Mirek Andrejczuk, Daniel Partridge, Sarah Taylor and Bethan White. All have been a pleasure to work with, and have contributed in one way or another to my time here. In addition to my academic colleagues, I am indebted to the administrative staff who have helped steer me through the maze of bureaucracy that a university can be – in particular Sarah Harrington, AOPP Graduate Studies Administrator, who has done a fantastic job of making sure everything goes smoothly. I would also like to thank AOPP's outgoing Director of Graduate Studies, Don Grainger, for his help and support at various stages.

Last, but very far from least, I would like to thank my wonderful wife, Marianne, without whose support, encouragement, and unconditional love I could never have completed this work.

This thesis is dedicated to the memory of my late mother, Caroline Mason, who (along with my father, Stuart Kipling) never failed to encourage and nurture my curiosity and interest in learning about and understanding the world around us throughout my childhood, for the majority of which I was taught informally at home.

Additional data sources

The HIPPO flight data used in Chapter 4 were provided by NCAR/EOL under sponsorship of the National Science Foundation (`http://data.eol.ucar.edu/`). The ERA-Interim data used for nudging were provided by Paul Berrisford and the European Centre for Medium-Range Weather Forecasts (ECMWF). The GFED3.1 biomass-burning emissions data used in Chapters 4 and 5 were provided by Guido van der Werf. The AeroCom median model data used in Chapter 4, and the individual model data used in Chapter 5, were supplied by the AeroCom project, from data provided by the contributing modellers.

Contents

List of Tables

List of Figures

Chapter 1

Introduction

1.1 Aerosols in the climate system

Aerosol particles (small solid or liquid particles suspended in the atmosphere) play an important role in both global and regional climate, both through absorption and scattering of radiation (Section 1.1.2) and interaction with clouds and precipitation (Section 1.1.3). Aerosol particles come from a variety of natural and anthropogenic sources, vary substantially in size and chemical composition, and have a very non-uniform geographical distribution (Section 1.1.1).

The direct radiative effect of any change in composition on the climate is often quantified in terms of its radiative forcing, defined as the resulting change in net downward radiative flux at the tropopause after stratospheric temperatures have re-adjusted to equilibrium, but with the tropospheric state unchanged (Forster et al., 2007).

Aerosol effects represent some of the largest uncertainties in estimates of total anthropogenic radiative forcing (Forster et al., 2007); they are thought to be a negative forcing, but the extent to which they presently cancel the positive forcing from greenhouse gases is poorly quantified. There are also many complex interactions and feedbacks between aerosol processes and other elements of the climate system, which have only recently begun to be represented in climate modelling studies (Carslaw et al., 2010). It is thus important to develop a better understanding of aerosol processes, and their effects on climate, if these uncertainties are to be reduced.

In addition to their effects on climate, it is important to note that many anthropogenic trace gases and aerosols are known or suspected to be harmful to human health, and therefore emission controls are likely to be desirable irrespective of their effects on climate.

1.1.1 Nature, sources and geographical distribution

Aerosol particles are described as either primary (emitted in particulate form at source – see Section 1.2.1) or secondary (produced from atmospheric trace gases by nucleation/condensation and/or chemical reactions – see Section 1.2.4). Although fresh primary aerosol may have a very specific composition determined by its source, particles are typically of mixed composition due to coagulation between particles and condensation of one substance onto the surface of another (Andreae et al., 2008).

The size spectrum of atmospheric aerosol ranges from freshly-nucleated (mostly sulphate) particles a few nm in diameter up to coarse mechanically-produced particles many µm in diameter. In between lie what are termed Aitken particles (10 nm–100 nm), and accumulation-mode particles (100 nm–1 µm). The accumulation and coarse modes account for most of the aerosol mass in the atmosphere; however the smaller nucleation-mode and Aitken particles are much more numerous.

Atmospheric aerosol consists of many different chemical components; the major ones are described below.

Sulphates

While some sulphate (SO_4^{2-}) aerosol may be emitted directly in particulate form, the majority is formed from atmospheric sulphur dioxide (SO_2) either by oxidation by the hydroxyl radical (OH) to form sulphuric acid (H_2SO_4) vapour followed by nucleation/condensation, or by oxidation in the aqueous phase (within cloud droplets) by ozone (O_3) or hydrogen peroxide (H_2O_2) to produce dissolved aerosol (Seinfeld and Pandis, 2006, §22.1). SO_2 is itself produced by oxidation of a variety of precursor gases – in particular hydrogen sulphide (H_2S), dimethyl sulphide (DMS, CH_3SCH_3), carbon disulphide (CS_2) and carbonyl sulphide (OCS) – as well as by direct emission (Seinfeld and Pandis, 2006, §2.2). DMS (produced in the oceans by phytoplankton) accounts for much of the natural sulphate precursor emissions, while the (currently larger) anthropogenic contribution comes from the burning of fossil fuel (especially coal) in the form of SO_2.

The SO_4^{2-} ions may occur in a variety of ionic compounds. Although they generally originate in H_2SO_4, chemical reactions with ammonia-based compounds convert much of this to ammonium sulphate, $(NH4)_2SO_4$.

Sea-salt

Over the ocean, salt particles released by the evaporation of sea spray are a significant source of aerosol particles, composed largely of sodium chloride (NaCl); the rate at which such particles are produced is strongly dependent on surface wind speed.

Carbonaceous aerosol and soot

A wide variety of carbon compounds are found in aerosol particles; however, these are usually divided into two broad classes:

black carbon (or elemental carbon), strongly light-absorbing graphite-like material produced during combustion as a principal component of soot; and

particulate organic matter (or organic aerosol), consisting of biological debris and secondary aerosol from chemical processing and condensation of organic gases of both natural and anthropogenic origin.

Soot particles produced during combustion are typically a mixture of both black carbon (BC) and particulate organic matter (POM), along with other chemical components.

The light-absorbing properties of black carbon set it apart from the other commonly-occurring types of aerosol, which are predominantly scattering. This leads to localised heating of the atmosphere and the so-called "semi-direct" aerosol effects, as will be discussed in Section 1.1.4.

Black carbon is also insoluble in water and other common solvents, and able to withstand very high temperatures. In addition to its absorption, this latter property is commonly used in measurements to separate black carbon from other aerosol – in which context the term "elemental carbon" (EC) is often used.

A recent and thorough review of the role of black carbon in the climate system is given in Bond et al. (2013).

Particulate organic matter contains a wide range of carbon-based compounds, and vary considerably in their complexity, volatility and solubility; although all such material is commonly treated as a single category in climate models. The term "organic carbon" (OC) is used to refer to the carbon content within POM.

Although soot particles are generally insoluble and hydrophobic at source, over time they can accumulate a coating of soluble material (e.g. sulphate or soluble organic compounds) by condensation or coagulation, allowing such particles to become hygroscopic and thus act as cloud condensation nuclei (CCN).

Mineral dust

Mineral dust is carried into the air by wind blowing over soil or sand; over and downwind of arid regions in particular, this contributes a large proportion of the aerosol population.

Nitrogen compounds

Both ammonia (NH_3) and nitric acid (HNO_3) vapour may condense onto aerosol particles, dissociating to form ammonium (NH_4^+) and nitrate (NO_3^-) ions (Andreae et al., 2008, §3.2.6); as mentioned above, the former are often found bound to sulphate ions in ammonium sulphate aerosol. Although nitrogen compounds can form a significant fraction of total aerosol mass in some regions (Jimenez et al., 2009, Fig. 1, reproduced as Figure 1.1), and both their potential effect on the nitrogen cycle and their contribution to aerosol direct and indirect effects has been recognised (Denman et al., 2007, §7.4.2), these aerosol components have received relatively little attention in climate modelling studies.

1.1.2 Direct radiative effect

Aerosol particles can directly alter the radiative balance of the atmosphere by absorbing or scattering incoming solar radiation. Scattering aerosols effectively increase the planetary albedo, leading to a cooling effect. Absorbing aerosols (e.g. black carbon, as the name implies) may have a cooling or warming effect, depending on the albedo of the underlying surface. The net direct radiative effect of anthropogenic aerosol is estimated to be a cooling one, although its magnitude is rather uncertain (Schulz et al., 2006; Forster et al., 2007).

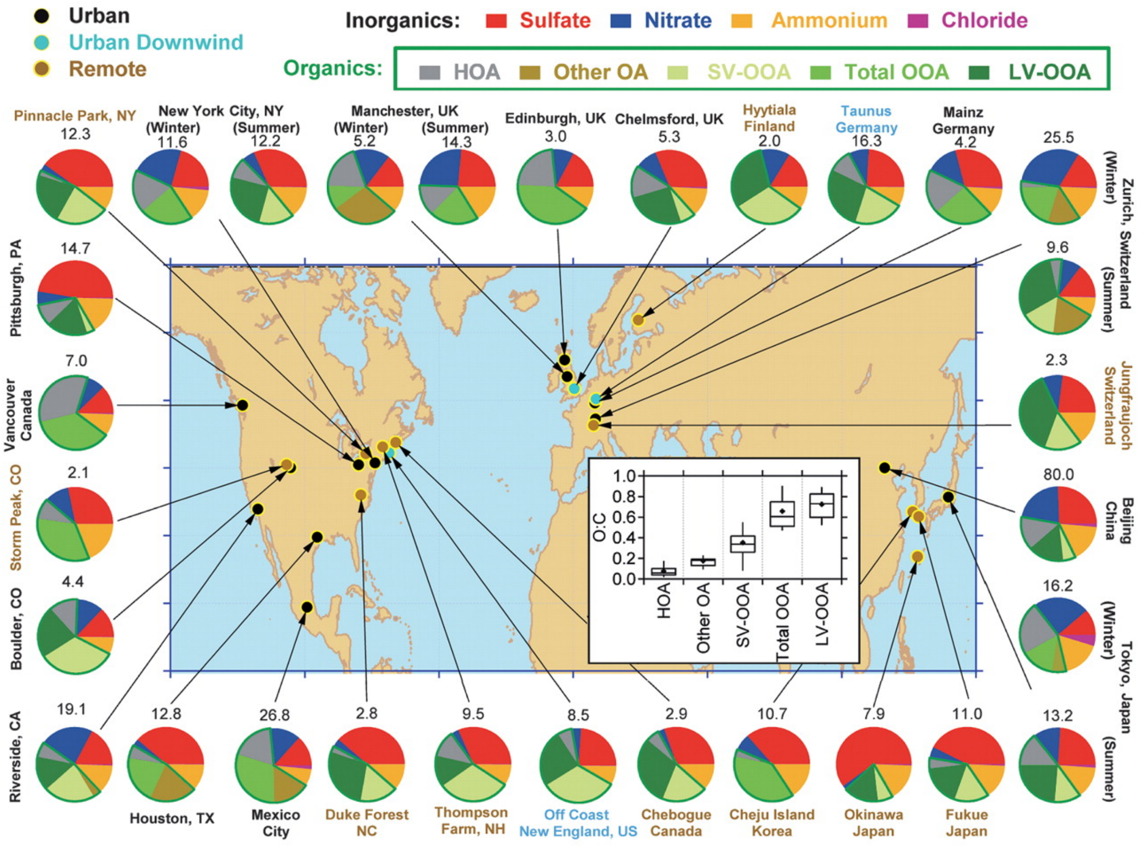

Figure 1.1: Total mass concentration (in µg m^{-3}) and mass fractions of non-refractory inorganic species and organic components in sub-µm aerosols measured at multiple surface locations in the Northern Hemisphere. From Jimenez et al. (2009, Fig. 1). Reprinted with permission from AAAS.

1.1.3 Indirect effects via cloud and precipitation

Aerosol particles can also alter the climate through their roles in cloud and precipitation microphysics:

- cloud condensation nuclei (CCN) are required for new liquid cloud droplets to form from water vapour (Rogers and Yau, 1989, ch. 6);
- ice nuclei (IN) are required for new ice particles to form directly from water vapour, or by the freezing of supercooled liquid cloud droplets at temperatures above about −40°C (Rogers and Yau, 1989, ch. 9).

Changes in these processes can alter both the radiative properties and precipitation efficiency of clouds; together these are termed *indirect effects* and are reviewed in Lohmann and Feichter (2005) and Denman et al. (2007, §7.5.2).

Two main mechanisms for such an indirect effect have been identified and studied: the *cloud albedo effect* and the *cloud lifetime effect* (also known as the first and second indirect effects respectively). A number of other mechanisms, mostly involving mixed-phase cloud, have also been proposed but have not been studied in such detail.

Cloud albedo effect

The size distribution of cloud droplets is heavily dependent on the number of CCN available; an increase in the number of suitable aerosol particles will lead to a greater number of smaller droplets for a given liquid water content. In most cases this leads to an increase in cloud albedo (Twomey, 1977), thus having an overall cooling effect.

Cloud lifetime effect

As well as increasing the cloud albedo, the reduction in droplet size may delay the onset of precipitation in shallow low-level cloud, which requires the development of much larger drops (Albrecht, 1989). This has been hypothesised to increase the lifetime of such clouds; assuming that the availability of water vapour is not a limiting factor (which is unlikely at least in maritime environments), this in turn increases the mean coverage of low-level cloud. Such cloud has little effect on outgoing long-wave radiation, but has a high short-wave albedo, thus exerting a further cooling effect.

Other indirect effects

There are a number of other proposed mechanisms for indirect effects, including:

- The “glaciation indirect effect” (Lohmann, 2002), where an increase in the number of aerosol particles acting as ice nuclei enhances glaciation in mixed-phase clouds, thus increasing precipitation and reducing their lifetime.
- The “de-activation effect”, where increased sulphate forms a coating on particles that would otherwise act as ice nuclei, preventing them from doing so (Pruppacher and Klett, 1996, §9.2).
- The “riming indirect effect”, where smaller cloud droplets lead to less riming of ice in mixed-phase clouds (Borys et al., 2003).
- Thermodynamic effects: smaller cloud droplets freeze at lower temperatures, delaying the onset of glaciation and precipitation in mixed-phase clouds (Rosenfeld and Woodley, 2000; Khain et al., 2001); consequent changes in latent heat release may invigorate or reduce further convection (Khain et al., 2005).

These additional effects involving mixed-phase clouds are somewhat less well understood than the cloud albedo and cloud lifetime effects on liquid cloud, although at least one recent study (Lohmann and Hoose, 2009) suggests that these may contribute significantly to the total anthropogenic aerosol indirect effect. However, all these effects which potentially affect cloud lifetime are subject to considerable uncertainty, as their interactions with cloud dynamics are poorly understood. It has been suggested (e.g. Stevens and Feingold, 2009) that dynamical feedbacks may lead to cloud fields adjusting to compensate for these aerosol effects, and damping any overall impact on the radiative balance.

1.1.4 Semi-direct effects via localised heating

There are also so-called “semi-direct” effects, where cloud properties and atmospheric stability are influenced by the local atmospheric heating caused by absorbing aerosol particles. The first such effect to be described was the evaporation of cloud caused by local heating (Hansen et al., 1997). This reduction of cloud cover has been demonstrated in cloud-resolving models (e.g. Ackerman et al., 2000; Hill and Dobbie, 2008). Absorbing aerosol below cloud level can increase cloud cover, however, by destabilising the boundary layer and promoting convection (e.g. Feingold et al., 2005).

The effects of absorbing aerosol above cloud are more complex. The resulting warming will tend to stabilise the lower troposphere, strengthening the cloud-top inversion in regions of stratocumulus and increasing cloud cover (e.g. Johnson et al., 2004). In regions of convective cloud, however, this stabilisation is likely to suppress convection and decrease cloud cover (e.g. Fan et al., 2008).

A recent review of these effects is given in Koch and Del Genio (2010).

1.1.5 Quantifying aerosol effects on climate

With the exception of the cloud albedo effect, none of the indirect or semi-direct effects can be properly considered radiative forcings as defined in e.g. Forster et al. (2007, §2.2), as they do not directly alter the radiation budget if the tropospheric state is fixed; instead they cause changes in the hydrological cycle and these in turn modify the radiation budget. This, along with the high level of uncertainty in these effects, is why they do not appear in the IPCC Fourth Assessment Report’s summary of radiative forcings, although they are discussed elsewhere in the report

(Denman et al., 2007, §7.5.2). In order to quantify the full range of aerosol indirect effects, an alternative methodology must be used, such as *radiative flux perturbation* (Haywood et al., 2009; Lohmann et al., 2010) which can take into account feedback processes which are fast compared to the timescale of changes to global mean surface temperature (Bala et al., 2010) – thus separating "fast" aerosol/cloud/precipitation effects (which typically occur over a few cloud lifetimes) from the "slow" climate feedbacks induced by global warming over a period of decades or longer.

1.2 Processes influencing atmospheric aerosol

1.2.1 Primary emissions

Aerosol particles are emitted directly from a number of sources, both natural and anthropogenic, e.g. combustion of fossil fuels and biofuels across a wide range of human activity, biomass burning in wildfires, volcanic eruptions, sea spray and dust lifted by wind. Detailed inventories of global emissions have been constructed, as in e.g. Lamarque et al. (2010) and Diehl et al. (2012).

These emissions may be injected into the atmosphere at or near the surface (as for sea spray, dust and road traffic) or at a higher altitude (as for volcanic eruptions, air traffic and smoke plumes from major wildfires). In addition, for particulate emissions, it is not sufficient to know the total mass of aerosol material that is emitted: the post-emission behaviour of particles may depend on their size distribution; the height at which emissions are injected may also be important for both particulate and gaseous emissions.

1.2.2 Transport: advection, diffusion and convection

Aerosol is transported through the atmosphere along with its containing air mass, through advection by large-scale winds, turbulent diffusion and convection. While

Table 1.1: Categorisation of scavenging processes

	Nucleation	**Impaction**
In-cloud	Activation as cloud condensation or ice nuclei	Collision with cloud droplets or ice crystals
Below-cloud	—	Collision with falling precipitation

large-scale advection is responsible for the long-range horizontal transport of aerosol, the weak nature of large-scale vertical motion in the troposphere means that convective updraughts are expected to have a large role in controlling vertical transport (see e.g. Hoyle et al., 2011), along with turbulent diffusion in the boundary layer.

1.2.3 Removal: scavenging and deposition

There are two main routes by which aerosol particles are removed from the atmosphere, referred to as dry and wet deposition. In dry deposition, aerosol particles settle out due to gravity, diffusion and other processes and eventually attach to the surface. This process is not a major focus of this work, but is described in more detail in e.g. Ruijgrok et al. (1995). In wet deposition, aerosol particles are taken up ("scavenged") by hydrometeors (cloud droplets, ice particles and precipitation) and carried to the surface in precipitation.

There are a variety of scavenging processes, which are usually divided either into in-cloud scavenging (by cloud droplets or ice crystals) and below-cloud scavenging (by falling precipitation), or into nucleation scavenging (where aerosol particles act as cloud condensation or ice nuclei) and impaction scavenging (where aerosol particles collide with existing hydrometeors). Nucleation scavenging only occurs in-cloud, while impaction scavenging occurs both in- and below-cloud (see Table 1.1).

Note that scavenged aerosol is not necessarily removed from the atmosphere by wet deposition at the surface: if cloud droplets evaporate (or ice crystals sublime) without forming precipitation, or if precipitation evaporates/sublimes before reaching the surface, then the aerosol is released back to the atmosphere. This cloud/precipitation processing of aerosols is discussed in more detail in Section 1.3.

Nucleation scavenging

Nucleation scavenging occurs when aerosol particles form cloud condensation or ice nuclei, and thus become dissolved or embedded in the resulting hydrometeor.

For liquid cloud this process, described by Köhler theory, depends on the aerosol composition and size distribution and local supersaturation (Rogers and Yau, 1989, ch. 6; Pruppacher and Klett, 1996, §9.1). The theory is well established, and detailed parameterisations have been developed to represent the activation process in models with size-resolved aerosol (e.g. Nenes and Seinfeld, 2003; Fountoukis and Nenes, 2005), as well as more parameterised schemes (e.g. Abdul-Razzak and Ghan, 2000).

Heterogeneous nucleation of ice is somewhat more complex, with the crystal structure of the aerosol particles (which may depend on both the composition and history of the particle) also playing an important role (Pruppacher and Klett, 1996, §9.2; Cantrell and Heymsfield, 2005). A theoretical parameterisation thus requires knowledge of details of the aerosol microphysical state which are not usually available in current models; thus current modelling generally relies on empirical relationships such as those of DeMott et al. (2010).

Impaction scavenging

Impaction scavenging occurs when aerosol particles collide and coalesce with hydrometeors, thus becoming dissolved, attached or embedded. This can be driven by a number of processes, which dominate in different regions of the joint aerosol-hydrometeor size spectrum, including Brownian diffusion, interception, inertial impaction, electrostatic and phoretic effects (Pruppacher and Klett, 1996, §17.4.2).

An assessment of the uncertainties in current parameterisations of impaction scavenging by raindrops by these processes is given by Wang (2010); they conclude that estimates of the collision efficiency between droplets and aerosol particles in the 0.01 µm to 3 µm range are the major contributor, with theoretical parameterisations an order of magnitude or more below that required to match observed scavenging rates. Increased scavenging due to turbulent flow (Grover and Pruppacher, 1985; Pinsky and Khain, 1997; Khain and Pinsky, 1997) is suggested as a possible cause of this mismatch between theoretical parameterisations (usually assuming non-turbulent flow) and observations (usually subject to boundary-layer turbulence).

Parameterisations of impaction scavenging by ice and snow are less well developed, and tend to be heavily dependent on the shape of the ice particles. A detailed discussion of the theory and available observations can be found in Wang (2002, ch. 5), and Feng (2009) presents a physically-based parameterisation using up-to-date estimates of the relevant parameters.

Previous experiments with detailed scavenging schemes

Croft et al. (2009, 2010) consider the effect of introducing a detailed size-resolved scheme for impaction scavenging by rain and cloud droplets in the ECHAM5–HAM model (Stier et al., 2005, described in more detail in Section 1.6.2), along with a highly parameterised activation scheme for nucleation scavenging, and show modest but noticeable improvements in simulated aerosol distribution compared to a simple scheme using prescribed scavenging ratios for in-cloud scavenging and a first-order loss rate for impaction scavenging.

1.2.4 Microphysics and chemistry

In addition to the emission, transport and removal processes described above, there are a number of microphysical and chemical processes which can affect aerosol particles in the atmosphere: nucleation of new particles, and condensation onto existing particles, from the gas phase; coagulation of particles; and the in-cloud production of aerosol material by aqueous chemistry.

Nucleation

Secondary sulphate aerosol particles can be formed directly from H_2SO_4 vapour in the atmosphere. The principal mechanism is generally thought to be binary homogeneous nucleation of H_2SO_4 and H_2O to produce sulphuric acid droplets. This process can occur even when the vapour pressures of both H_2SO_4 and H_2O are well below saturation (Seinfeld and Pandis, 2006, §11.6–11.7).

Although binary homogeneous nucleation of H_2SO_4 and H_2O is the nucleation process which is best understood, there are a number of other processes which have been proposed, such as ion-induced nucleation (Yu and Turco, 2000), nucleation from organic vapours (Hoffmann et al., 1997) and ternary processes involving a third component such as ammonia (Korhonen et al., 1999).

Condensation

Existing aerosol particles may grow by the condensation of vapours (in particular H_2SO_4 and various organic compounds) onto their surface (Seinfeld and Pandis, 2006, §13.2). This process competes with nucleation for the available vapour: a large surface area of existing particles will deplete the vapour phase as it condenses onto these particles, reducing the rate at which new particles are nucleated. Note that the condensing vapour need not be of the same composition as the existing aerosol; in particular, the condensation of material such as sulphate onto insoluble primary particles to form a water-soluble coating can enable these particles to act as cloud condensation nuclei. This is often referred to as “ageing” of the particles.

Coagulation

Aerosol particles which come into contact with one another may coagulate to form a single larger particle (Seinfeld and Pandis, 2006, §13.3). These particles may have different composition, and so (like condensation) this process can lead to particles of mixed composition and thereby contribute to the ageing of insoluble aerosol.

Aqueous chemistry

Aqueous reactions between dissolved gases within cloud droplets can lead to the formation of secondary aerosol material, which will then be combined with that in the original CCN in the particle left behind if the droplet evaporates. In particular, the oxidation of dissolved SO_2 by O_3 and H_2O_2 leads to the in-cloud production of sulphate aerosol (Seinfeld and Pandis, 2006, §7.5).

1.3 Cloud cycling

A significant proportion of cloud water is not removed by precipitation, but returned to the atmosphere as water vapour by evaporation: Pruppacher and Jaenicke (1995) estimate (based on a simple global budget argument) that cloud water goes through 10 condensation–evaporation cycles on average before falling to the ground as precipitation. Since the formation of cloud droplets (or ice crystals) involves the take-up of aerosol particles as CCN or IN (and further particles may be taken up by impaction scavenging), it follows that some of this material will be released from evaporating clouds and precipitation. However, the physical and chemical characteristics of these released particles may be different to those of the scavenged particles: cloud droplets typically undergo many collision/coalescence events during their lifetime, thus each evaporating droplet will in general release an aerosol particle containing the material from several CCN and/or IN, plus that taken up from impaction scavenging or

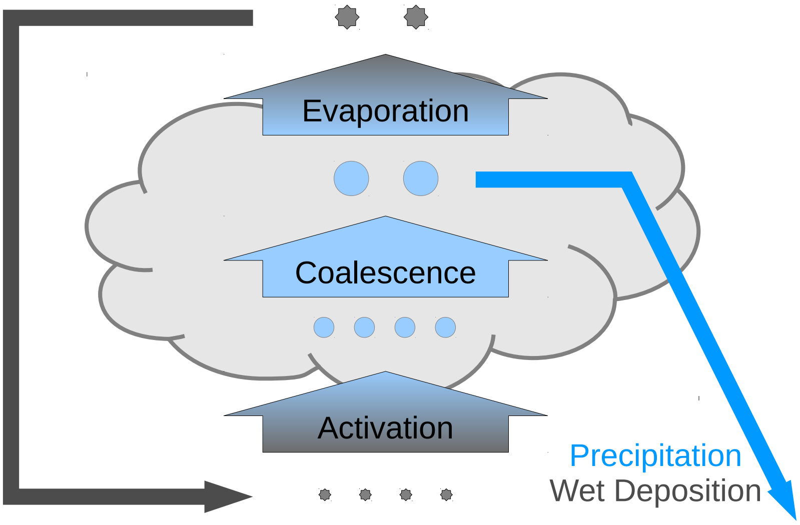

Figure 1.2: Schematic showing how cloud cycling may cause a shift towards larger and well-mixed aerosol particles

produced by aqueous chemistry. Thus cloud processing can be expected to cause a shift from small aerosols with diverse composition towards larger aerosols with a well-mixed composition, as illustrated in Figure 1.2.

Pruppacher and Jaenicke (1995) estimate that a typical aerosol particle in the atmosphere has been cycled through cloud three times, thus suggesting that cloud processing is likely to play a significant role in the aerosol life cycle.

Hoose et al. (2008a) diagnose the cloud cycling rate for stratiform clouds only (i.e. excluding parameterised convective cloud) using the ECHAM5–HAM model. Despite significant differences in aerosol emissions and liquid water path from the values used by Pruppacher and Jaenicke (1995), the stratiform cloud-cycling rates are in fair agreement.

It is worth noting, however, that the approach of Pruppacher and Jaenicke (1995) suggests that most of the cloud cycling occurs in convective cloud – the rates are reduced from 10 to 2.6 times for water and from 3 to 0.4 times for aerosol particles when only stratiform cloud is considered. Croft (2011, ch. 4) has extended the work of Hoose et al. (2008a) to include cycling through convective cloud; her results suggest a more equal split between cycling in stratiform and convective clouds.

1.4 The importance of the vertical distribution

The direct, indirect and semi-direct effects of atmospheric aerosol all depend upon its vertical distribution, and especially its position in relation to cloud layers. In the case of the indirect effect, aerosol will have most impact at the levels where cloud is formed. The strength of the direct effect for a given amount of black carbon (absorbing and non-hygroscopic unless aged) increases significantly with height, while that for sulphate (scattering and hygroscopic) remains fairly constant with height (Samset and Myhre, 2011). However, these results depend strongly on the interaction with clouds, without which Samset and Myhre find that the vertical sensitivity for BC is much weaker – consistent with the results of Zarzycki and Bond (2010) showing an increased effect for BC above reflective clouds. The semi-direct effect is also sensitive to the vertical position of aerosol, as touched upon in Section 1.1.4: Johnson et al. (2004) show in a large-eddy model that absorbing aerosol below an area of marine stratocumulus causes a decrease in liquid water and a positive semi-direct forcing, while placing such aerosol above the cloud increases liquid water and produces a negative semi-direct forcing.

Because of the importance of the vertical distribution for the aerosol effects, a number of recent studies have focused on observational constraints on this distribution on a global scale. While limited analysis of the relative height of cloud and aerosol layers is possible from traditional passive satellite observations (Peters et al., 2011; Wilcox, 2012), the use of satellite-based LIDAR instruments (such as CALIOP, on the CALIPSO satellite) and large-scale aircraft campaigns (such as HIPPO, discussed in more detail in Chapter 4) can provide more detailed observations of aerosol vertical profiles over large regions (Koffi et al., 2012; Schwarz et al., 2010).

1.5 Parameterisation of cloud, precipitation and aerosol in General Circulation Models

1.5.1 Cloud and precipitation schemes

Cloud and precipitation in global climate models exist on both resolved and unresolved scales. Large-scale stratiform clouds, such as marine stratocumulus and frontal clouds, may cover multiple grid boxes and persist over many timesteps. These are thus typically treated as resolved-scale processes, based on grid-box values of cloud water and cloud fraction and an assumed shape for the distribution of water over the grid box (e.g. Smith, 1990). Cloud and precipitation microphysics can then operate at the resolved scale, although only over the cloudy fraction of each grid box (e.g. Wilson and Ballard, 1999). Although early schemes diagnosed both cloud water and cloud fraction at each timestep based on prognostic variables such as relative humidity, in modern schemes these are either prognostic quantities in their own right (e.g. Wilson et al., 2008) or derived from prognostic moments of the sub-grid-scale moisture distribution (e.g. Tompkins, 2002). There are also hybrid schemes such as Sundqvist et al. (1989) where cloud water is prognostic but cloud fraction is diagnosed at each timestep.

Convective cloud and precipitation, on the other hand, occurs on scales much smaller than the typical resolution of a global climate model, although the susceptibility of a given region to convection can be diagnosed from the resolved-scale tropospheric stability. They are commonly parameterised using a “mass-flux” approach (e.g. Tiedtke, 1989; Gregory and Rowntree, 1990), in which it is assumed that the effects of a heterogeneous ensemble of convective clouds in a grid box can be approximated by the action of a single updraught and downdraught, with suitably parameterised entrainment and detrainment rates. Neither the cloud fraction nor the vertical velocities of the updraught and downdraught are explicitly known in such a scheme, only the grid-box mean upward and downward mass fluxes. In models where large-scale cloud water and ice are prognostic (e.g Wilson et al., 2008), liquid water and ice may be detrained into the large-scale scheme; it is this detrained cloud which represents the anvils of deep convective cloud and interacts with radiation.

In reality, however, there is no clear scale separation between large-scale and convective cloud, with a whole range of mesoscale systems in between. Although total precipitation is energetically constrained, the division between cloud represented by the two schemes in a model is therefore somewhat arbitrary and likely to depend on the model resolution.

1.5.2 Size distributions of hydrometeors and aerosols

Many microphysical processes involving aerosol particles and/or hydrometeors are heavily dependent on their size distribution, and not just on their total mass mixing ratio in the atmosphere. For example:

- surface processes (e.g. growth by condensation or deposition) depend more on total surface area (which is greater for smaller droplets or particles at a given total mass);
- there is a critical size at which aerosol particles can activate to form cloud droplets, dependent on their composition and the local supersaturation of water vapour according to Köhler theory;
- larger cloud droplets are more likely to grow to form raindrops;
- smaller raindrops are more likely to evaporate before reaching the surface.

In simple “bulk” schemes, only the total mass of each type of aerosol particle or hydrometeor is transported, and either a fixed or diagnosed size distribution is assumed when parameterising the microphysical processes; this assumed distribution may be tuned individually for each process to match observations without necessarily having a physical justification. While rain may be distinguished from cloud, or coarse aerosol from fine, there is no way to capture changes of particle size within these broad categories.

Increasing computing power has made it possible to represent the size distribution prognostically, allowing it to evolve according to the microphysical and transport processes rather than assuming a distribution at each timestep based on diagnostic relationships. There are two main approaches to this: bin-resolved (or sectional) schemes and multi-moment modal schemes.

In bin-resolved schemes (e.g. Spracklen et al., 2005), the size spectrum for each particle type is divided into a large number of discrete "bins" each covering a relatively narrow size range; the number or mass of particles in each bin is then transported separately, with explicit representation of the microphysical processes that grow or shrink particles from one bin to another. While such schemes are able to represent the evolution of size distributions very well, the large number of prognostic variables required makes them very expensive in terms of computing time and storage when used in global models.

Multi-moment modal schemes attempt to capture the evolving size distribution with a much smaller number of variables than required for a bin scheme. The size distribution of each type of particle is assumed to be a superposition of a small number of "modes" with prescribed (usually gamma or log-normal) distributions. The moments of the distribution for each mode are then carried as prognostic variables:

- with one moment, the distribution is fixed, and only the strength of each mode can change – this is essentially the same as the bulk schemes mentioned above;
- with two moments, typically number (zeroth moment) and mass (proportional to the third moment), the mean particle size in each mode can vary, but the distribution shape still remains fixed;
- with additional moments, the width and shape of each mode can also vary.

In a fully modal scheme, the physical processes would be represented in terms of integrals over the size distribution of each mode. Many aerosol schemes, however, use a simplified “pseudo-modal” approach where some or all of the physical processes are parameterised using an average or “effective” radius for each mode rather than an integral (e.g. Vignati, 2004). In addition to the explicit microphysical processes that grow or shrink the particles within a mode, an additional parameterisation is needed to move particles from one mode to another (so that e.g. the largest cloud droplets can become raindrops, or the largest nucleation-mode aerosol particles can move to the Aitken mode).

In cloud schemes, a variety of “autoconversion” parameterisations are used for this purpose (e.g. Tripoli and Cotton, 1980; Khairoutdinov and Kogan, 2000), which may be empirically tuned to adjust the distribution of precipitation in the model. In multi-moment aerosol schemes, a more numerically-based approach is often used, referred to variously as reallocation (Vignati, 2004), repartitioning (Stier et al., 2005) or mode-merging (Mann et al., 2010). This transfers the number and mass of particles in the upper tail of one mode (larger than a pre-determined threshold) into the next largest mode, subject to certain restrictions.

1.5.3 Mixing state

As mentioned in Section 1.1.1, aerosol particles are generally of mixed composition. This has important implications for both their radiative and microphysical properties (Seinfeld and Pandis, 2006, §24.6; Levin and Brenguier, 2008, §6.2.1); parameterisations which assume separate populations of sulphate and black carbon aerosol (“externally-mixed”), for example, may behave quite differently to those which assume they are well mixed in the same particles (“internally-mixed”).

There is also the matter of aerosol/water mixing: not only do hydrometeors generally contain some dissolved or embedded aerosol material, but hygroscopic aerosol particles (e.g. sulphate) usually contain some condensed water even if they are too small to activate as cloud droplets. Some recent studies (e.g. Ovchinnikov and Easter, 2010) have used a two-dimensional joint distribution to capture the evolution of the aerosol/water mixing state; while such an approach can be useful in a limited-area model, the increased computational cost makes it unsuitable for use in a global model.

There is also a distinction to be made between models which transport in-droplet and in-ice aerosol as separate prognostics (and thus remember the activation history) and those which diagnose the in-cloud fraction afresh at each timestep. Hoose et al. (2008a,b) show that introducing a prognostic treatment to ECHAM5–HAM has a significant impact on simulated aerosol distributions. Ghan and Easter (2006) examine a range of approaches from fully prognostic to fully diagnostic in-cloud aerosol, using an otherwise identical model setup. They show little difference between the fully-prognostic and the non-advected configurations, but significant local error and global bias when using diagnostic in-cloud aerosol.

1.6 Models used in this study

Most of the work described here is based on HadGEM3–UKCA simulations, although for Chapter 4 some simulations were also carried out with ECHAM5–HAM2 for comparison. These two models are described in the following sections.

1.6.1 HadGEM3–UKCA

HadGEM3 (Hewitt et al., 2011) is the latest version of the Hadley Centre Global Environmental Model developed at the UK Met. Office. Although the full model contains many components (atmosphere, land surface, ocean, sea ice etc.), this work is concerned only with the uncoupled atmosphere component, using prescribed sea-surface temperature (SST) and sea ice fields. The dynamical core (Davies, 2005) is non-hydrostatic and fully compressible, with semi-Lagrangian advection and a hybrid-height vertical coordinate.

The version of the model described here will be referred to as HadGEM3–UKCA-2010, and is the version used in Chapter 2 and the first part of Chapter 3. A later version, which includes an updated parameterisation of large-scale scavenging similar to that described in Section 3.3, is the basis for the rest of the work in this thesis: this will be referred to as HadGEM3–UKCA-2011.[1]

Cloud and precipitation

HadGEM3 implements a prognostic cloud scheme (PC2; Wilson et al., 2008) for large-scale (as opposed to sub-grid-scale convective) cloud. This treats liquid water content, ice content and (liquid/ice/mixed) cloud fraction as prognostic variables allowing clouds to evolve and be transported between timesteps. As a one-moment bulk scheme, there is no tracking of the cloud droplet size distribution; the detailed microphysics of the large-scale precipitation scheme (Wilson and Ballard, 1999) uses assumed size distributions based on diagnostic relationships.

Convection, which takes places on sub-grid scales not explicitly resolved by the model, is parameterised by a mass-flux scheme (Gregory and Rowntree, 1990) which diagnoses both convective precipitation and vertical transport of tracers and momentum. In PC2-based configurations, convective cloud cover (e.g. for radiation) is treated by detraining cloud water into the large-scale cloud scheme, rather than using a separate convective cloud fraction.

Atmospheric chemistry and aerosols: UKCA

The standard tropospheric chemistry scheme in UKCA (O'Connor et al., 2013) is used. This includes oxidants (O_x, HO_x and NO_x) and hydrocarbons (CO, ethane and

---

[1] These are based on the standard jobs `xeunb` and `xfxld`, using the UKCA code from the `VN7.3_UKCA_MODE_RADAER` and `VN7.3_MODEBLN_Rad_Indir` branches respectively.

propane) with eight emitted species, 102 gas-phase reactions, 27 photolytic reactions and interactive wet and dry deposition. An additional aerosol-precursor chemistry scheme treats the oxidation of sulphur compounds (SO_2 and dimethyl sulphide) and monoterpene to form the sulphuric acid and organic compounds which may condense to form secondary aerosol material.

The aerosol scheme in UKCA (Mann et al., 2013) is the two-moment modal version of the Global Model of Aerosol Processes (GLOMAP-mode; Mann et al., 2010), which follows the M7 framework (Vignati, 2004) in transporting five components (sulphate, sea-salt, black carbon, particulate organic matter and mineral dust) in seven internally-mixed log-normal modes (four soluble and three insoluble; not all components are found in all modes). Because mineral dust is transported by a separate scheme (Woodward, 2001) in current versions of HadGEM3, only four components and five modes are enabled in the UKCA configuration of GLOMAP-mode used here (omitting the two larger insoluble modes which contain only mineral dust). The representation of aerosol microphysical processes is based on the sectional GLOMAP-bin scheme (Spracklen et al., 2005), with each process acting sequentially in an operator-split manner (except nucleation, coagulation and condensation which are solved iteratively). Transport of aerosol by large-scale dynamics, convection and boundary-layer mixing is handled by the generic tracer transport scheme in HadGEM3.

New particle formation by nucleation from gas-phase H_2SO_4 is calculated following Kulmala et al. (1998). The resulting change in nucleation-mode aerosol is calculated simultaneously with that due to coagulation between particles, as in Vignati (2004), with coagulation kernels calculated following Seinfeld and Pandis (1998). Condensation rates are calculated following Fuchs and Sutugin (1971). Soluble material which coagulates with, or condenses onto, insoluble particles “ages” a fraction of these particles, transferring them to the corresponding soluble mode at a rate consistent with a 10-monolayer coating being required for such a particle to become soluble. Soluble particles in clouds larger than a critical size of 37.5 nm can also grow by aqueous oxidation of dissolved SO_2 by O_3 and H_2O_2, whose concentrations are calculated interactively by the UKCA tropospheric chemistry scheme following Henry's law.

All sizes of soluble and insoluble aerosol particles may be removed by dry deposition and below-cloud impaction scavenging; soluble accumulation- and coarse-mode particles may also be removed by in-cloud nucleation scavenging. Dry deposition and gravitational sedimentation are calculated following Slinn (1982) and Zhang et al. (2001). Below-cloud scavenging follows Slinn (1984), using Beard and Grover (1974) scavenging coefficients and terminal velocities from Easter and Hales (1983), assuming a modified Marshall-Palmer raindrop size distribution (Sekhon and Srivastava, 1971).

In-cloud scavenging by large-scale precipitation assumes that 100% of the aerosol in the soluble accumulation and coarse modes is taken up by cloud water in any 3D grid box containing cloud, and is then removed at a rate of 50% over 6 hours.[2] (Nucleation, Aitken and insoluble modes are not subject to in-cloud scavenging.) Aerosol is removed immediately, and is not returned to the atmosphere when rain evaporates (something which will be investigated further in Section 3.5).

Convective rainfall is treated similarly, but assumes a cloud fraction of 30% and a conversion rate of 99% over 6 hours in all grid boxes where convective rain is produced. (This is different to the TOMCAT-based version of GLOMAP-mode, in which convective scavenging is dependent on the rain rate, while large-scale scavenging uses a fixed removal timescale of 99.9% over 6 hours.) The scavenged aerosol is removed from the grid-box mean tracers after the convection scheme has run – i.e. from the post-convection environmental air at the level where the

---

[2] This is the parameterisation used in HadGEM3–UKCA-2010. HadGEM3–UKCA-2011 uses a revised scheme similar to that described in Section 3.3: aerosol in the soluble accumulation and coarse modes is only taken up by cloud water in the cloudy fraction of the grid box, from where it is then removed at the same rate as the large-scale cloud water is converted to rain.

precipitation formed, rather than the convective updraught itself. This allows a greater separation of the convection and aerosol schemes, but may limit the ability of convective scavenging to control vertical transport (as will be discussed further in Sections 3.4 and 4.5.1).

Configuration and emissions

The model configuration used here is based on a development version of HadGEM3 (atmosphere-only, climatological SST, Met. Office Unified Model version 7.3) at N96L38 resolution (1.25° latitude × 1.875° longitude × 38 vertical levels up to $\sim 40\,\mathrm{km}$) with UKCA in a standard tropospheric chemistry and aerosol configuration as described above, with aerosol feedbacks disabled.

Sulphur-cycle emissions from a number of sources are included in the model. Ocean DMS emissions are calculated interactively following Jones and Roberts (2004) using prescribed concentrations in sea water from Kettle et al. (1999), while DMS emissions from land are prescribed following Spiro et al. (1992). Volcanic SO_2 emissions are prescribed following Andres and Kasgnoc (1998), while anthropogenic SO_2 emissions are prescribed following Lamarque et al. (2010). 2.5% of the SO_2 from all sources is assumed to be emitted directly as sulphate aerosol (and thus already oxidised to SO_4^{2-}) rather than into the gas phase. Particulate emissions from anthropogenic sources are split equally by mass between the soluble accumulation and coarse modes, where they are emitted with geometric mean diameters of 150 nm and 1.5 µm respectively; those from volcanic sources are split equally by mass between the soluble Aitken and accumulation modes with geometric mean diameters of 60 and 150 nm respectively.

Carbonaceous aerosol emissions are taken from the AeroCom hindcast inventory (Diehl et al., 2012), including black and organic carbon emissions from fossil fuel, biofuel and biomass burning through to the end of 2006. Primary particles use the AeroCom recommended size distributions (Dentener et al., 2006), as modified by Stier et al. (2005), but with biofuel emissions using the same distribution as fossil fuel rather than biomass burning. Fossil-fuel and biofuel emissions are added to the lowest model level with a geometric mean diameter of 60 nm, while biomass-burning emissions have a geometric mean diameter of 150 nm and are distributed uniformly in height over levels 2 to 12 ($\sim$ 50 m to 3 km, compressed over orography). Emissions from all these sources are added to the insoluble Aitken mode. Although the simulations for much of this work begin in 2008, the fossil fuel and biofuel emissions have little interannual variability and so those for 2006 are simply repeated. Biomass burning, however, has significant interannual variability; since the emissions inventory does not cover the required period, the simulations use a monthly climatology derived from the “modern” portion of the AeroCom hindcast inventory (1997 to 2006), which is based on monthly-mean emission fields of the Global Fire Emissions Database (GFED) version 2 (van der Werf et al., 2006).

Bin-resolved sea-salt and mineral dust emissions are calculated interactively, based on Gong (2003) and Marticorena and Bergametti (1995) respectively. In the case of sea-salt, bins with dry diameters smaller than 1 µm are emitted into the soluble accumulation mode, while larger bins are emitted into the soluble coarse mode.

Additional gas-phase emissions not included in Diehl et al. (2012) but required by the UKCA chemistry scheme are taken from year 2006 of Representative Concentration Pathway (RCP) 8.5 (Riahi et al., 2011).

1.6.2 ECHAM5–HAM2

ECHAM5 (Roeckner et al., 2003) is the fifth-generation climate model developed at the Max Planck Institute for Meteorology. It has a spectral dynamical core, solving prognostic equations for vorticity, divergence, surface pressure and temperature in spherical harmonics with a triangular truncation. A hybrid sigma/pressure vertical coordinate is used. Physical parameterisations are solved on a corresponding Gaussian grid. Tracer transport is semi-Lagrangian in grid-point space (Lin and Rood, 1996).

Large-scale cloud follows the two-moment scheme of Lohmann et al. (2007) with modifications by Lohmann and Hoose (2009) and Abdul-Razzak and Ghan (2000) aerosol activation, with Sundqvist et al. (1989) cloud cover. Convection follows the mass-flux scheme of Tiedtke (1989), with modifications by Nordeng (1994).

HAM 2.0 (Stier et al., 2005; Zhang et al., 2012) is also a two-moment modal aerosol scheme based on the M7 framework (Vignati, 2004), transporting five components (sulphate, sea-salt, black carbon, particulate organic matter and mineral dust) in seven internally-mixed log-normal modes (four soluble and three insoluble). Unlike in UKCA, mineral dust in ECHAM5–HAM2 is incorporated into the M7 framework.

Primary BC emissions use a modified version of the AeroCom recommended size distributions, accounting for the width of the M7 modes. Fossil-fuel and biofuel emissions are added as a surface flux to the boundary-layer vertical diffusion equations, while biomass-burning emissions use a biome-dependent vertical profile, as specified for AeroCom Phase I (Dentener et al., 2006). BC aerosol is initially insoluble, but can be “aged” by sulphate through condensation and coagulation to become soluble; in contrast to UKCA only a single monolayer is required.

Dry deposition of soluble and insoluble particles follows Ganzeveld et al. (1998), modified to use the explicit size distribution from the model, and is applied as a surface flux to the boundary-layer vertical diffusion along with the emissions. Below-cloud scavenging is calculated according to the rain and snow fluxes, using size-dependent collection efficiencies from Seinfeld and Pandis (1998). In-cloud scavenging assumes that a prescribed fraction of the number and mass of aerosol in each mode from the cloudy part of each grid box is susceptible to removal, at the rate at which large-scale cloud water/ice is converted to rain/snow. Scavenging in convective clouds is coupled with the tracer transport in the mass-flux convection scheme, and proceeds similarly but removing aerosol from the convective tracer flux according to the rate at which water and ice are removed in convective precipitation. Where (a fraction of) the precipitation in a column evaporates before reaching the ground, the same fraction of the aerosol removed from the column is returned to the atmosphere.

The model configuration used here is based on ECHAM 5.5 (atmosphere-only, AMIP2 prescribed SST) at T63L31 resolution ($\sim 1.875° \times 31$ vertical levels up to $\sim 10\,\mathrm{hPa}$) with HAM 2.0. Aerosol and precursor emissions are taken from the AeroCom hindcast inventory (Diehl et al., 2012) for 2006, with biomass-burning emissions using a 1997 to 2006 climatology as described for HadGEM3–UKCA.

1.7 Aims of this thesis

The effects of atmospheric aerosol on Earth's climate depend not only on the total mass of aerosol, but also on its size distribution, mixing state and vertical profile, as discussed in the previous sections.

With a view to reducing the uncertainty in estimates of the direct and indirect radiative effects of aerosol, the work presented in this thesis aims to address several aspects of this dependence. This is approached primarily from a model perspective, but use is also made of satellite and in-situ aircraft observations to provide constraints and evaluation.

Chapter 2 aims to quantify the extent to which aerosol is cycled through non-precipitating cloud (as described in Section 1.3), in order to assess its potential role in controlling the size distribution and mixing state of aerosol. This is investigated by analysing simulations with a specially-instrumented configuration of a sophisticated current-generation global aerosol–climate model (HadGEM3–UKCA), and the results are compared with previous work to establish whether different models (both simple and complex) can provide consistent estimates of this process.

Chapter 3 moves on to look at the influence of precipitating cloud via scavenging processes, asking to what extent the representation of scavenging by both large-scale and convective cloud and precipitation can be improved through greater physical realism, as opposed to tuning parameters. A detailed microphysical scheme is proposed, and three specific approaches to increased realism within the existing framework are described and evaluated.

Chapter 4 investigates the use of vertically-resolved in-situ measurements from a large-scale aircraft campaign to constrain the simulated vertical profile, and thereby the processes controlling it. The chapter asks to what extent the use of nudging, flight-track sampling and a pointwise comparison approach can offer robust constraints on processes in the model. In particular, this approach is applied to evaluate more thoroughly the largest changes in simulated aerosol from the work on scavenging in Chapter 3, and also the impact of different inventories for biomass-burning emissions.

Chapter 5 extends the focus on vertical distribution effects, and aims to identify the principal processes controlling the vertical profile of aerosol through a series of model-based sensitivity tests. The resulting impact of these processes on the direct radiative forcing due to anthropogenic aerosol is also assessed. The process sensitivity tests are also used to ask to what extent the range of explicit physical processes in a single model can account for the large inter-model diversity in aerosol vertical profiles.

Finally, Chapter 6 provides a summary of the work in the above chapters and the main conclusions, along with recommendations for further work.

Chapter 2

A model assessment of cloud cycling

As discussed in Section 1.3, the cycling of aerosol through cloud may have a significant impact on the size distribution, composition and mixing state of atmospheric aerosol. In turn, this may have implications for both the direct radiative effect of aerosol and its indirect effects via the hydrological cycle. However, the extent of this cycling process is not well constrained by direct observations.

The work presented in this chapter aims to quantify the extent of this cloud cycling process, and is inspired by the approach of Pruppacher and Jaenicke (1995): first calculating the number of times water is cycled through (large-scale) cloud before precipitating, and then considering the cycling of aerosol through the cloud. However, while Pruppacher and Jaenicke base their estimate on a simple global budget analysis, the work presented here aims to quantify the water and aerosol cycling rates based on simulations using a sophisticated current-generation global aerosol–climate model (HadGEM3–UKCA). These results are also compared with those of Hoose et al. (2008a), which were obtained using a different model (ECHAM5–HAM), to assess the extent to which estimates of cloud cycling are consistent between models.

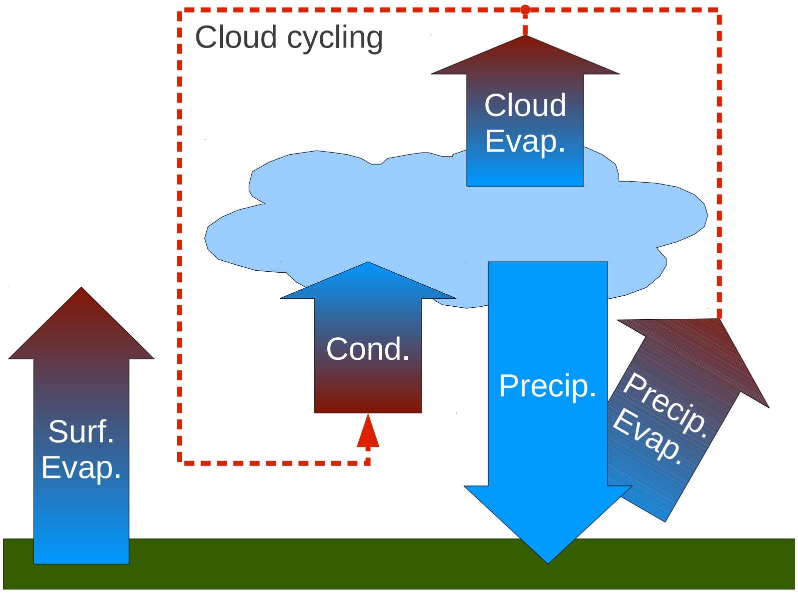

Figure 2.1: Diagram of the atmospheric water budget, showing evaporation from the surface, condensation and evaporation of cloud water, precipitation and evaporation of falling precipitation. (Red represents water vapour; blue represents condensed water.)

2.1 Method

The experiment described here was carried out using a free-running (non-nudged) configuration of HadGEM3–UKCA-2010, as described in Section 1.6.1. The model was spun up for three months from 1 September 1999, with results taken over the following 12 months (December 1999–November 2000 inclusive).

To diagnose both the water and aerosol cycling rates, additional diagnostics had to be implemented into the model, as described in the following sections.

2.1.1 Diagnosing the cloud water cycle

Following Pruppacher and Jaenicke (1995), the number of re-evaporation cycles is given by the ratio of evaporation of cloud water to precipitation reaching the surface (see the diagram of the atmospheric water budget in Figure 2.1). The latter is easily obtained from standard model output; for large-scale cloud the former can be

Table 2.1: Processes from which increments to water vapour and cloud variables are obtained in the PC2 cloud scheme (Wilson et al., 2008)

Pure transport	
adv	advection by large-scale dynamics
Pure phase change	
rad	radiation
exp	adiabatic expansion due to large-scale ascent
init	cloud initiation
chk	bounds checking
Complex processes	
conv	convection
lsp	large-scale precipitation
bl	boundary layer

calculated by separating out the water vapour increments due to phase changes in the atmosphere (as opposed to transport or surface fluxes). Because convective cloud only exists transiently within the model, there are no readily-available diagnostics for the evaporation of sub-grid-scale convective cloud (although those for convective *precipitation* will be introduced in Section 3.5); thus only cycling through large-scale cloud is considered in this analysis.

In the PC2 cloud scheme, prognostic variables for (grid-box mean) water vapour (q), liquid (q_{cl}) and ice (q_{cf}) evolve through increments from each of the dynamical and physical processes in the model (Wilson et al., 2008):

$$\frac{\partial q_x}{\partial t} = \underbrace{\left.\frac{\partial q_x}{\partial t}\right|_{\mathrm{adv}}}_{\text{pure transport}} + \underbrace{\left.\frac{\partial q_x}{\partial t}\right|_{\mathrm{rad}} + \left.\frac{\partial q_x}{\partial t}\right|_{\mathrm{exp}} + \left.\frac{\partial q_x}{\partial t}\right|_{\mathrm{init}} + \left.\frac{\partial q_x}{\partial t}\right|_{\mathrm{chk}}}_{\text{pure phase change}} + \underbrace{\left.\frac{\partial q_x}{\partial t}\right|_{\mathrm{conv}} + \left.\frac{\partial q_x}{\partial t}\right|_{\mathrm{lsp}} + \left.\frac{\partial q_x}{\partial t}\right|_{\mathrm{bl}}}_{\text{complex processes}}, \tag{2.1}$$

for $q_x \in \{q, q_{\mathrm{cl}}, q_{\mathrm{cf}}\}$, where the labels on the terms are defined in Table 2.1. A detailed analysis of the increments from the various processes is presented in Morcrette and Petch (2010); here they are simply used to obtain condensation and evaporation rates for cloud water.

The first term (advection by the large-scale model dynamics) is a pure transport process which does not correspond to any evaporation or condensation of cloud, only its transport from one grid box to another (and thus conserves globally integrated q_x). This can be ignored when calculating the condensation/evaporation rate.

The next four terms (radiation, adiabatic expansion due to large scale ascent, cloud initiation[1] and bounds checking[2]) represent pure phase change processes (and thus conserve total grid-box water $q + q_{\mathrm{cl}} + q_{\mathrm{cf}}$). Thus each process P contributes

$$(E - C)|_P = \left.\frac{\partial q}{\partial t}\right|_P = -\left.\frac{\partial q_{\mathrm{cl}}}{\partial t}\right|_P - \left.\frac{\partial q_{\mathrm{cf}}}{\partial t}\right|_P \tag{2.2}$$

to the net (evaporation − condensation) rate. (Sublimation and deposition of ice cloud are thus included, as if they occurred via the liquid phase.)

The final three terms (convection, large-scale precipitation and the boundary layer) represent more complex schemes which include both phase change and transport or surface exchange processes:

- Convective cloud water and ice are considered transient in the model, as described in Section 1.5.1; they do not appear in q_{cl} or q_{cf}, except for that which is detrained from the convective plumes as large-scale cloud (though detrainment to the large scale scheme followed by evaporation may well represent the main evaporation pathway for convective cloud water in the model). From a large-scale perspective, there is a vertical transport of water vapour (and possibly cloud water or ice if they are entrained) in the convective plumes, a sink of this water to the surface in convective precipitation, a downward transport due to subsidence to balance the upward mass flux in the plumes,

---

[1] This is a closure term which increases the cloud fraction from 0 when the relative humidity exceeds a threshold value so that cloud can start to form. Similarly, cloud fraction is decreased from 1 when the relative humidity drops below the threshold value.

[2] Small adjustments may be made to the q_x and C_x prognostics to ensure physical consistency, for example by evaporating any liquid water where $C_{\mathrm{l}} = 0$.

and condensation where water or ice is detrained:

$$\left.\frac{\partial q_x}{\partial t}\right|_{\text{conv}} = \underbrace{\left.\frac{\partial q_x}{\partial t}\right|_{\substack{\text{conv}\\\text{plume}}} + \left.\frac{\partial q_x}{\partial t}\right|_{\substack{\text{conv}\\\text{precip}}} + \left.\frac{\partial q_x}{\partial t}\right|_{\substack{\text{conv}\\\text{subsidence}}}}_{\text{transport}} + \underbrace{\left.\frac{\partial q_x}{\partial t}\right|_{\substack{\text{conv}\\\text{detrain}}}}_{\text{phase change}} . \tag{2.3}$$

Because the individual contributions of these processes are not easily separable in the model diagnostics, it is assumed that the contributions from entrainment and subsidence of large-scale water and ice are small, and thus

$$(E - C)|_{\text{conv}} \approx - \left.\frac{\partial q_{\text{cl}}}{\partial t}\right|_{\text{conv}} - \left.\frac{\partial q_{\text{cf}}}{\partial t}\right|_{\text{conv}} . \tag{2.4}$$

This approximation is not ideal, and could certainly be improved on in the context of a more detailed approach to convective diagnostics which would also allow analysis of condensation–evaporation cycling in convective cloud.

- The large-scale precipitation scheme includes increments to q_x due to falling or gravitational settling of water and ice (i.e. downward transport of q_{cl} and q_{cf}, but not q), in-cloud freezing and melting (exchange between q_{cl} and q_{cf}), removal of water and ice as precipitation (loss of q_{cl} and q_{cf}), ice deposition (conversion of q to q_{cf}) and evaporation/sublimation (conversion of q_{cl}, q_{cf} or rain to q). Thus, although q_{cl} and q_{cf} are subject to transport and surface exchange processes, the only increments to q are due to evaporation and deposition/sublimation of ice:

$$\left.\frac{\partial q}{\partial t}\right|_{\text{lsp}} = \underbrace{\left.\frac{\partial q}{\partial t}\right|_{\substack{\text{lsp}\\\text{evap}\\\text{cloud}}} + \left.\frac{\partial q}{\partial t}\right|_{\substack{\text{lsp}\\\text{evap}\\\text{rain}}} + \left.\frac{\partial q}{\partial t}\right|_{\substack{\text{lsp}\\\text{dep}\\\text{ice}}} + \left.\frac{\partial q}{\partial t}\right|_{\substack{\text{lsp}\\\text{sub}\\\text{ice}}}}_{\text{phase change}} , \tag{2.5}$$

and thus the contribution can be calculated as

$$(E - C)|_{\mathrm{lsp}} = \left.\frac{\partial q}{\partial t}\right|_{\mathrm{lsp}} . \tag{2.6}$$

- The boundary layer scheme includes increments from surface exchange (principally evaporation of surface water), turbulent mixing (transport of q_x) and condensation resulting from adiabatic expansion during this mixing:

$$\left.\frac{\partial q}{\partial t}\right|_{\mathrm{lsp}} = \underbrace{\left.\frac{\partial q}{\partial t}\right|_{\substack{\mathrm{bl}\\ \mathrm{surface}}} + \left.\frac{\partial q}{\partial t}\right|_{\substack{\mathrm{bl}\\ \mathrm{mixing}}}}_{\text{transport}} + \underbrace{\left.\frac{\partial q}{\partial t}\right|_{\substack{\mathrm{bl}\\ \mathrm{cond}}}}_{\text{phase change}} . \tag{2.7}$$

Additional diagnostics have been added to isolate this third term, so that the boundary layer contribution can be calculated as

$$(E - C)|_{\mathrm{bl}} = \left.\frac{\partial q}{\partial t}\right|_{\substack{\mathrm{bl}\\ \mathrm{cond}}} = - \left.\frac{\partial q_{\mathrm{cl}}}{\partial t}\right|_{\substack{\mathrm{bl}\\ \mathrm{cond}}} - \left.\frac{\partial q_{\mathrm{cf}}}{\partial t}\right|_{\substack{\mathrm{bl}\\ \mathrm{cond}}} . \tag{2.8}$$

Thus the net (evaporation − condensation) rate of large-scale cloud in each grid box can be calculated as:[3]

$$\begin{aligned}(E - C) \approx &- \left.\frac{\partial q_{\mathrm{cl}}}{\partial t}\right|_{\mathrm{rad}} - \left.\frac{\partial q_{\mathrm{cf}}}{\partial t}\right|_{\mathrm{rad}} + \left.\frac{\partial q}{\partial t}\right|_{\mathrm{exp}} + \left.\frac{\partial q}{\partial t}\right|_{\mathrm{init}} + \left.\frac{\partial q}{\partial t}\right|_{\mathrm{chk}} \\ &- \left.\frac{\partial q_{\mathrm{cl}}}{\partial t}\right|_{\mathrm{conv}} - \left.\frac{\partial q_{\mathrm{cf}}}{\partial t}\right|_{\mathrm{conv}} + \left.\frac{\partial q}{\partial t}\right|_{\mathrm{lsp}} + \left.\frac{\partial q}{\partial t}\right|_{\substack{\mathrm{bl}\\ \mathrm{cond}}} .\end{aligned} \tag{2.9}$$

In grid boxes where this is positive, evaporation is diagnosed; where it is negative, condensation. It is tempting to split the contribution from each process separately into positive (evaporation) and negative (condensation) components in an attempt to capture at least some cases where both occur in the same grid box. However, doing so appears misguided since a warming process (e.g. absorption of solar radiation) might

---

[3] $-\frac{\partial q_{\mathrm{cl}}}{\partial t}|_{\mathrm{rad}} - \frac{\partial q_{\mathrm{cf}}}{\partial t}|_{\mathrm{rad}}$ is used instead of $\frac{\partial q}{\partial t}|_{\mathrm{rad}}$ due to technical issues with model diagnostics; theoretically they should be equivalent.

actually inhibit the condensation due to a cooling process (e.g. adiabatic expansion), rather than evaporating the water after it condenses.

2.1.2 Diagnosing cycling of aerosol through clouds

It is somewhat harder to diagnose the rate at which aerosol particles in HadGEM3–UKCA are cycled through cloud, since there is no prognostic treatment of the split between in-cloud and interstitial aerosol; thus there are no increments which can be analysed as for the water cycle. Instead, this split is defined diagnostically, following the approach of the in-cloud nucleation scavenging parameterisation: a fixed scavenging ratio α_M is defined for each mode M, so that the in-cloud fraction of both number and mass in that mode is given by $C\alpha_M$ where C is the grid-box cloud fraction; the in-cloud mass of aerosol species i is then

$$m_{\mathrm{c}}^{(i)} = \sum_{M \in \mathcal{M}} C \alpha_M m_M^{(i)}, \tag{2.10}$$

where $\mathcal{M}$ is the set of aerosol modes and $m_M^{(i)}$ is the mass of aerosol species i in mode M. In standard configurations,

$$\alpha_M = \begin{cases} 1 & \text{for the soluble accumulation and coarse modes} \\ 0 & \text{for all other modes,} \end{cases} \tag{2.11}$$

i.e. in the presence of cloud all aerosol in these two modes is considered to be taken up into the cloud water, while all aerosol in other modes is considered to be interstitial. (Most of the budget analysis which follows is focused on aerosol mass; however a number budget can be constructed similarly.)

Differentiating, the change of this diagnosed in-cloud aerosol mass is

$$\frac{\partial m_{\mathrm{c}}^{(i)}}{\partial t} = \sum_{M \in \mathcal{M}} \alpha_M \left(m_M^{(i)} \frac{\partial C}{\partial t} + C \frac{\partial m_M^{(i)}}{\partial t} \right), \tag{2.12}$$

splitting it into changes due to changing cloud cover and aerosol microphysics. (Because the diagnosed in-cloud aerosol fraction depends on cloud fraction but not cloud water content, there is no change due to condensation or evaporation unless the cloud fraction changes; this would not be the case for a fully prognostic treatment of in-cloud aerosol.)

The change in cloud cover can be diagnosed similarly to the evaporation and condensation rates, by taking the non-transport increments to C from PC2:

$$\begin{aligned}\left.\frac{\partial C}{\partial t}\right|_{\text{non-transport}} \approx {} & \left.\frac{\partial C}{\partial t}\right|_{\text{rad}} + \left.\frac{\partial C}{\partial t}\right|_{\text{exp}} + \left.\frac{\partial C}{\partial t}\right|_{\text{init}} + \left.\frac{\partial C}{\partial t}\right|_{\text{chk}} \\ & + \left.\frac{\partial C}{\partial t}\right|_{\text{conv}} + \left.\frac{\partial C}{\partial t}\right|_{\text{lsp}} + \left.\frac{\partial C}{\partial t}\right|_{\substack{\text{bl}\\ \text{cond}}} \end{aligned} \tag{2.13}$$

(again assuming the transport component of the convective increment is small). Increasing cloud cover implies take-up of aerosol in the newly-cloudy fraction of the grid-box, while decreasing cloud cover implies release in the newly-clear fraction. (This makes two implicit assumptions: that the cloud fraction changes are due to evaporation of cloud regions or condensation in clear air, rather than the bodily expansion or contraction of existing cloud; and that the aerosol population is uniformly distributed the over grid box. The latter of these is already assumed by many parts of the GLOMAP-mode aerosol scheme, although the former is not.)

Table 2.2: Processes in UKCA affecting the mass of each aerosol component in each mode.

Source processes	
prim	primary particle emissions
nucl	nucleation of new sulphate particles from the gas phase
cond	condensation of sulphate and organics onto existing particles
wetox	aqueous oxidation of SO_2 to form sulphate aerosol in cloud droplets
Removal processes	
dry dep	dry deposition and sedimentation
nuc scav	in-cloud nucleation scavenging (rainout)
imp scav	below-cloud impaction scavenging (washout)
Inter-modal processes	
coag	coagulation of aerosol particles
age	ageing of insoluble particles to become soluble
merge	redistribution of large particles to the next mode

The changes due to aerosol microphysics can be split according to the individual processes (described in the paragraphs which follow):

$$\begin{aligned}\left.\frac{\partial m_M^{(i)}}{\partial t}\right|_{\text{non-transport}} &= \underbrace{\left.\frac{\partial m_M^{(i)}}{\partial t}\right|_{\text{prim}} + \left.\frac{\partial m_M^{(i)}}{\partial t}\right|_{\text{nucl}} + \left.\frac{\partial m_M^{(i)}}{\partial t}\right|_{\text{cond}} + \left.\frac{\partial m_M^{(i)}}{\partial t}\right|_{\text{wetox}}}_{\text{source processes}} \\ &\quad \underbrace{+ \left.\frac{\partial m_M^{(i)}}{\partial t}\right|_{\substack{\text{dry}\\\text{dep}}} + \left.\frac{\partial m_M^{(i)}}{\partial t}\right|_{\substack{\text{nuc}\\\text{scav}}} + \left.\frac{\partial m_M^{(i)}}{\partial t}\right|_{\substack{\text{imp}\\\text{scav}}}}_{\text{removal processes}} \\ &\quad \underbrace{+ \left.\frac{\partial m_M^{(i)}}{\partial t}\right|_{\text{coag}} + \left.\frac{\partial m_M^{(i)}}{\partial t}\right|_{\text{age}} + \left.\frac{\partial m_M^{(i)}}{\partial t}\right|_{\text{merge}}}_{\text{inter-modal processes}}, \end{aligned} \tag{2.14}$$

where the labels on the terms are defined in Table 2.2. However, the contribution of these processes to aerosol take-up or release needs considering carefully.

With the exception of aqueous (in-cloud) oxidation, the source processes (primary emissions, nucleation and condensation) are straightforward: a fraction $C\alpha_M$ of the aerosol produced in each mode M is assumed to be taken up into the cloud. Wet oxidation, however, can only take place in-cloud; thus the full amount produced is assumed to be taken up, but a fraction $(1 - C\alpha_M)$ immediately released to preserve the model's assumption that aerosol is distributed uniformly throughout the grid box and thus close the budget.

Aerosol removed by dry deposition is assumed to be interstitial; thus the fraction $C\alpha_M$ implicitly removed from the diagnostic in-cloud aerosol mass is assumed to be released immediately prior to removal. (In fact, the dry deposition term also includes a vertical transport component due to gravitational settling; this is not currently diagnosed separately and, like the transport component of the convective q_x and C increments, assumed to be small. It should, however, be treated by considering the change in scavenged fraction across the grid-box boundary.)

Nucleation scavenging, like wet oxidation, can only take place in-cloud; thus the fraction $(1 - C\alpha_M)$ implicitly removed from the diagnostic interstitial aerosol is assumed to be taken up immediately prior to removal. (This is particularly important where convective scavenging occurs but there is little large-scale cloud.) Impaction scavenging may remove either interstitial or in-cloud aerosol; no take-up or release is inferred, but separate diagnostics are introduced to identify the contribution to the in-cloud aerosol budget.

The inter-modal processes (coagulation, ageing and mode-merging) are assumed to take up or release aerosol if the scavenging ratios for the source and destination modes differ: for a transfer from M' to M,

$$\left.\frac{\partial m_{\mathrm{c}}^{(i)}}{\partial t}\right|_{M' \to M} = (\alpha_M - \alpha_{M'}) \left.\frac{\partial m_M^{(i)}}{\partial t}\right|_{M' \to M} . \tag{2.15}$$

(This implicitly assumes that the aerosol undergoing these processes is uniformly distributed between the clear and cloudy parts of the grid box – in general this may not be realistic, but it is consistent with the formulation of other elements of the aerosol scheme.) It should be noted that, in practice, these processes can never release aerosol from cloud, as they always move particles to a larger or more-soluble mode (which thus has a greater or equal scavenging ratio).

Putting all these terms together, the total rates of aerosol take-up into, and release from, cloud water are given by:

$$
\begin{aligned}
T^{(i)} = \sum_{M\in\mathcal{M}} \Bigg\{ & \underbrace{\alpha_M m_M^{(i)} \left[\left.\frac{\partial C}{\partial t}\right|_{\text{non-transport}} \right]^{+}}_{\text{take-up due to increasing cloud fraction}} \\
& + \underbrace{C\alpha_M \left(\left.\frac{\partial m_M^{(i)}}{\partial t}\right|_{\text{prim}} + \left.\frac{\partial m_M^{(i)}}{\partial t}\right|_{\text{nucl}} + \left.\frac{\partial m_M^{(i)}}{\partial t}\right|_{\text{cond}} \right)}_{\text{take-up due to interstitial sources}} \\
& + \underbrace{\left.\frac{\partial m_M^{(i)}}{\partial t}\right|_{\text{wetox}}}_{\substack{\text{take-up due to}\\ \text{in-cloud sources}}} + \underbrace{(1-C\alpha_M)\left.\frac{\partial m_M^{(i)}}{\partial t}\right|_{\text{nuc scav}}}_{\substack{\text{take-up due to}\\ \text{in-cloud removal}}} \\
& + \underbrace{\sum_{\substack{M'\in\mathcal{M}\\ \alpha_{M'}<\alpha_M}} (\alpha_M-\alpha_{M'}) \left(\left.\frac{\partial m_M^{(i)}}{\partial t}\right|_{\substack{\text{coag}\\ M'\to M}} + \left.\frac{\partial m_M^{(i)}}{\partial t}\right|_{\substack{\text{age}\\ M'\to M}} + \left.\frac{\partial m_M^{(i)}}{\partial t}\right|_{\substack{\text{merge}\\ M'\to M}} \right)}_{\text{take-up due to inter-modal processes}} \Bigg\}
\end{aligned}
\tag{2.16}
$$

and

$$
\begin{aligned}
R^{(i)} = \sum_{M\in\mathcal{M}} \Bigg\{ & \underbrace{- \alpha_M m_M^{(i)} \left[\left.\frac{\partial C}{\partial t}\right|_{\text{non-transport}} \right]^{-}}_{\text{release due to decreasing cloud fraction}} \\
& + \underbrace{(1-C\alpha_M)\left.\frac{\partial m_M^{(i)}}{\partial t}\right|_{\text{wetox}}}_{\substack{\text{release due to}\\ \text{in-cloud sources}}} + \underbrace{C\alpha_M \left.\frac{\partial m_M^{(i)}}{\partial t}\right|_{\text{dry dep}}}_{\substack{\text{release due to}\\ \text{interstitial removal}}} \\
& + \underbrace{\cancel{\sum_{\substack{M'\in\mathcal{M}\\ \alpha_{M'}>\alpha_M}} (\alpha_{M'}-\alpha_M) \left(\left.\frac{\partial m_M^{(i)}}{\partial t}\right|_{\substack{\text{coag}\\ M'\to M}} + \left.\frac{\partial m_M^{(i)}}{\partial t}\right|_{\substack{\text{age}\\ M'\to M}} + \left.\frac{\partial m_M^{(i)}}{\partial t}\right|_{\substack{\text{merge}\\ M'\to M}} \right)}}_{\text{release due to inter-modal processes, =0 as explained in text}} \Bigg\},
\end{aligned}
\tag{2.17}
$$

where $[\ldots]^{\pm}$ are positive/negative clipping operators:

$$[X]^{+} = \begin{cases} X & X \geq 0 \\ 0 & X \leq 0 \end{cases} \qquad \text{and} \qquad [X]^{-} = \begin{cases} X & X \leq 0 \\ 0 & X \geq 0, \end{cases} \tag{2.18}$$

such that the in-cloud aerosol budget is

$$\left.\frac{\partial m_{\mathrm{c}}^{(i)}}{\partial t}\right|_{\text{non-transport}} = T^{(i)} - R^{(i)} + \left.\frac{\partial m_{\mathrm{c}}^{(i)}}{\partial t}\right|_{\substack{\text{nuc}\\\text{scav}}} + \left.\frac{\partial m_{\mathrm{c}}^{(i)}}{\partial t}\right|_{\substack{\text{imp}\\\text{scav}}}. \tag{2.19}$$

2.2 Results

Figure 2.2 and Table 2.3 show the global-mean large-scale cloud water budget over the year, calculated as described above from HadGEM3–UKCA and compared with the results of Hoose et al. (2008a), obtained using the ECHAM5–HAM model, as well as the simple global budget estimates of Pruppacher and Jaenicke (1995), from where the notation used originates. From this, it appears that approximately as much large-scale cloud water is lost to evaporation as to precipitation in HadGEM3–UKCA. Although all three precipitation rates are very similar, the condensation and evaporation rates are not: Hoose et al. find twice as much evaporation as precipitation, and Pruppacher and Jaenicke estimate three times as much. While the estimate of cloud water lifetime with respect to precipitation from HadGEM3–UKCA ($\tau_{\mathrm{c,p}} = \mathrm{TWP}/P = 2.0\,\mathrm{h}$) is in the same range as the other estimates, the cloud water cycling rate ($E_{\mathrm{v,c}}/P = 0.91$ times) is about half (and the lifetime with respect to evaporation about four times) that of Hoose et al.; the cycling rate is even further from that of Pruppacher and Jaenicke.

Figure 2.3 shows the budgets for in-cloud and total mass of each aerosol component. From the total-aerosol budgets, it appears that large-scale in-cloud nucleation scavenging dominates the removal of sulphate (SU) and organic carbon (OC) mass,

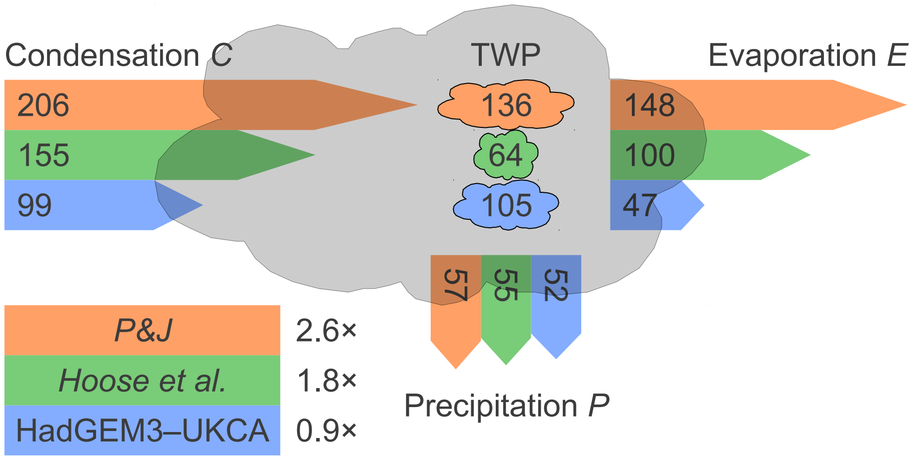

Figure 2.2: Comparison of global annual large-scale cloud water budget and cycling rate as simulated by HadGEM3–UKCA-2010 with estimates derived from ECHAM5–HAM (Hoose et al., 2008a) and global budget arguments (Pruppacher and Jaenicke, 1995, P&J). (TWP = total water path, i.e. liquid plus ice, in $\mathrm{g\,m^{-2}}$. Fluxes are in $\mathrm{g\,m^{-2}\,h^{-1}}$.)

Table 2.3: Comparison of global annual cloud water budget, timescales and cycling rate as simulated by HadGEM3–UKCA-2010 with previous estimates derived from ECHAM5–HAM (Hoose et al., 2008a) and global budget arguments (Pruppacher and Jaenicke, 1995)

	P&J[a]	Hoose[b]	HadGEM3–UKCA[c]
TWP / $\mathrm{g\,m^{-2}}$	136	64	105
P / $\mathrm{g\,m^{-2}\,h^{-1}}$	57	55	52
$C_{\mathrm{v,c}}$ / $\mathrm{g\,m^{-2}\,h^{-1}}$	206	155	99
$E_{\mathrm{v,c}}$ / $\mathrm{g\,m^{-2}\,h^{-1}}$	148	100	47
$E_{\mathrm{v,c}}$ / $C_{\mathrm{v,c}}$	0.72	0.64	0.48
$E_{\mathrm{v,c}}$ / P	2.6	1.8	0.91
$\tau_{\mathrm{c,p}}$ / h	2.4	1.2	2.0
$\tau_{\mathrm{c,e}}$ / min	55	38	133

TWP	total water path (liquid + ice)
P	large-scale precipitation rate at surface
$C_{\mathrm{v,c}}$	condensation rate of cloud water
$E_{\mathrm{v,c}}$	evaporation rate of cloud water and precipitation
$\tau_{\mathrm{c,p}}$	lifetime of cloud water with respect to precipitation, = TWP/P
$\tau_{\mathrm{c,e}}$	lifetime of cloud water with respect to evaporation, = TWP/$E_{\mathrm{v,c}}$

---

[a] Pruppacher and Jaenicke (1995), recalculated for stratiform clouds only following Hoose et al. (2008a).

[b] Hoose et al. (2008a), using ECHAM5–HAM with a prognostic in-cloud aerosol scheme, for all stratiform clouds.

[c] Diagnosed from HadGEM3–UKCA as described in the text, for all stratiform clouds.

and to a lesser extent black carbon (BC), while dry deposition is the dominant removal process for sea-salt (SS). This is broadly consistent with the analysis of removal rates for the AeroCom Phase I models in Textor et al. (2006, §7 and Fig. 5). In terms of sources, primary emissions are the only source of sea-salt and black carbon, while condensation of organic vapours provides a secondary but significant source of organic carbon; for sulphate, however, primary emissions play only a small role and in-cloud oxidation of SO_2 is the dominant source, followed by condensation of H_2SO_4 vapour. The in-cloud budgets show that more in-cloud aerosol is released by evaporating cloud than is removed by scavenging processes, with the possible exception of sea-salt where the split is almost even. This suggests a strong role for cloud processing in determining the nature and distribution of atmospheric aerosol.

There are small residuals in both the diagnosed cloud water and aerosol budgets, which do not always match the net change over the year; these may in part be due to the approximate treatment of some processes, as discussed in the preceding sections. However they are in general small compared to the dominant processes in the water and aerosol cycles, so any impact on the results presented here should be minor.

Figure 2.4 and Table 2.4 compare these results for aerosol to those of Hoose et al. (2008a) and Pruppacher and Jaenicke (1995), as was done above for cloud water. The aerosol cloud cycling rate ($E_{\mathrm{AP,c}}/S_{\mathrm{AP}} = 0.17$) is also much lower – less than half that of Pruppacher and Jaenicke (1995), and just over a quarter that of Hoose et al. (2008a). The total aerosol mass source ($12040\ \mathrm{Tg\,yr^{-1}}$) is more than 50% larger than that used by Hoose et al. (2008a), while the mass released by evaporation ($E_{\mathrm{AP,c}} = 2006\ \mathrm{Tg\,yr^{-1}}$) is about half. The former is in spite of the fact that the HadGEM3–UKCA figure does not include mineral dust, which is handled by a separate scheme from other aerosol; the latter may be partially explained by the lack of release due to evaporation of rain (which probably explains the lower $E_{\mathrm{AP,c}}/C_{\mathrm{AP,c}}$) and a much larger below-cloud scavenging rate, as well as reduced take-up into the cloud water.

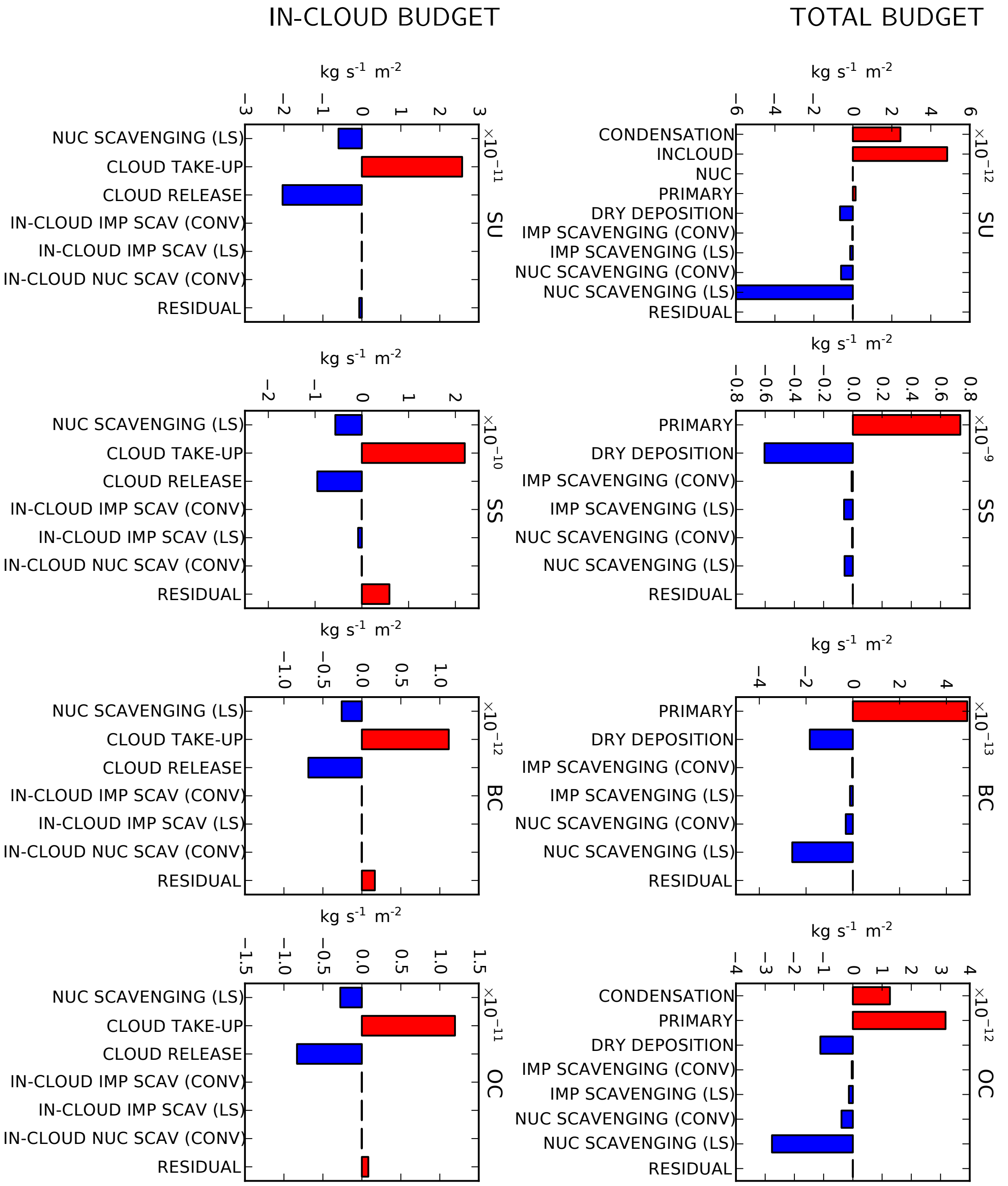

Figure 2.3: Global-mean budgets for in-cloud (left) and total (right) mass of each aerosol component for one year, as simulated by HadGEM3–UKCA-2010. (SU=sulphate; SS=sea-salt; BC=black carbon; OC=organic carbon. Mineral dust is not included, as it never interacts with cloud in the model.)

Table 2.4: Comparison of global annual total and in-cloud aerosol budget, timescales and cycling rate as simulated by HadGEM3–UKCA-2010 with estimates derived from ECHAM5–HAM (Hoose et al., 2008a) and global budget arguments (Pruppacher and Jaenicke, 1995)

	P&J[a]	Hoose[b]	HadGEM3–UKCA[c]
m_{AP} / Tg	3	34.9[d]	8.02
$m_{\mathrm{AP,ic}}$ / Tg	–	–	0.964
$C_{\mathrm{AP,c}}$ / $\mathrm{Tg\,yr^{-1}}$	1072	5596	4167
$E_{\mathrm{AP,c}}$ / $\mathrm{Tg\,yr^{-1}}$	775	4027	2006
$W_{\mathrm{dep,ic}}$ / $\mathrm{Tg\,yr^{-1}}$	297	1570	1059
$W_{\mathrm{dep,bc}}$ / $\mathrm{Tg\,yr^{-1}}$	74	237	970
W_{dep} / $\mathrm{Tg\,yr^{-1}}$	371	1826	2030
D_{dep} / $\mathrm{Tg\,yr^{-1}}$	1639.[e]	5750.[e]	9760
S_{AP} / $\mathrm{Tg\,yr^{-1}}$	2000	7576	12040
$E_{\mathrm{AP,c}}$ / $C_{\mathrm{AP,c}}$	0.72	0.72	0.48
$E_{\mathrm{AP,c}}$ / S_{AP}	0.4	0.53	0.17
$\tau_{\mathrm{AP,p}}$ / h	71	167	34.7
$\tau_{\mathrm{AP,e}}$ / h	34	75.9	35.1
$\tau_{\mathrm{AP,d}}$ / h	16	53.1	7.2
$\tau_{\mathrm{AP,ic,p}}$ / h	–	–	7.98
$\tau_{\mathrm{AP,ic,e}}$ / h	–	–	4.21

m_{AP}	total mass of aerosol
$m_{\mathrm{AP,ic}}$	total mass of in-cloud aerosol
$C_{\mathrm{AP,c}}$	take-up rate of aerosol into cloud water
$E_{\mathrm{AP,c}}$	release rate of aerosol from cloud water
$W_{\mathrm{dep,ic}}$	in-cloud scavenging rate of aerosol
$W_{\mathrm{dep,bc}}$	below cloud scavenging rate of aerosol
D_{dep}	dry deposition rate of aerosol
W_{dep}	total scavenging rate of aerosol, $= W_{\mathrm{dep,ic}} + W_{\mathrm{dep,bc}}$
S_{AP}	total aerosol source (from primary emissions and secondary production)
$\tau_{\mathrm{AP,p}}$	lifetime of aerosol with respect to precipitation, $= m_{\mathrm{AP}}/W_{\mathrm{dep}}$
$\tau_{\mathrm{AP,e}}$	lifetime of aerosol with respect to evaporation, $= m_{\mathrm{AP}}/E_{\mathrm{AP,c}}$
$\tau_{\mathrm{AP,d}}$	lifetime of aerosol with respect to dry deposition, $= m_{\mathrm{AP}}/D_{\mathrm{dep}}$
$\tau_{\mathrm{AP,ic,p}}$	lifetime of in-cloud aerosol with respect to precipitation, $= m_{\mathrm{AP,ic}}/W_{\mathrm{dep,ic}}$
$\tau_{\mathrm{AP,ic,e}}$	lifetime of in-cloud aerosol with respect to evaporation, $= m_{\mathrm{AP,ic}}/E_{\mathrm{AP,c}}$

---

[a] Pruppacher and Jaenicke (1995), recalculated for stratiform clouds only following Hoose et al. (2008a).

[b] Hoose et al. (2008a), using ECHAM5–HAM with a prognostic in-cloud aerosol scheme, for all stratiform clouds.

[c] Diagnosed from HadGEM3–UKCA as described in the text, for all stratiform clouds. Mineral dust is not included in the aerosol figures, as it is treated separately from UKCA, and does not interact with cloud.

[d] treating sulphate aerosol as H_2SO_4, as in UKCA

[e] These figures are not given, but assuming a closed budget in equilibrium $S_{\mathrm{AP}} = W_{\mathrm{dep}} + D_{\mathrm{dep}}$.

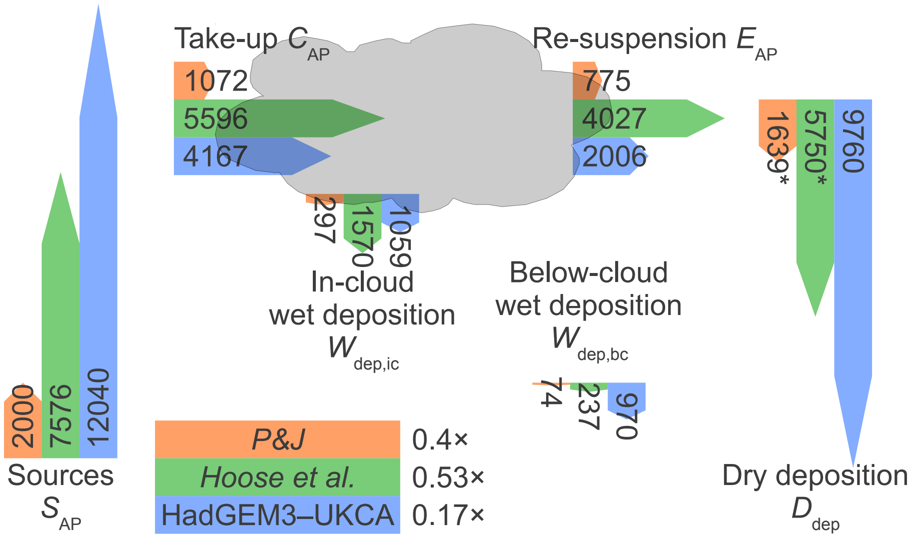

Figure 2.4: Comparison of global annual total and in-cloud aerosol budget and cycling rate as simulated by HadGEM3–UKCA-2010 with estimates derived from ECHAM5–HAM (Hoose et al., 2008a) and global budget arguments (Pruppacher and Jaenicke, 1995, P&J). Fluxes are given in Tg yr^{-1} over the globe.

It is worth noting that these figures vary significantly for different aerosol species, as shown in Figure 2.5 and Table 2.5. In particular, it appears that the low cycling rate obtained from HadGEM3–UKCA is dominated by the behaviour of sea-salt, which comprises over 97% of the total aerosol mass source but is mostly removed quickly by dry deposition so that it accounts for less than half the total mass burden. The other species show much larger cycling rates, with the non-speciated estimate of Pruppacher and Jaenicke (1995) well within the range spanned by the cycling rates of the different species in HadGEM3–UKCA.

This dominance of sea-salt in the total aerosol emissions may be exacerbated in HadGEM3–UKCA by the operator-splitting of emissions and dry deposition, compared to a model such as ECHAM5–HAM where both processes act together as a net surface flux in the boundary-layer mixing scheme. Operator-splitting (where the equations describing the two processes are discretised sequentially within each timestep, rather than being applied simultaneously) works on the assumption that the model timestep is short compared to the timescales of the processes involved;

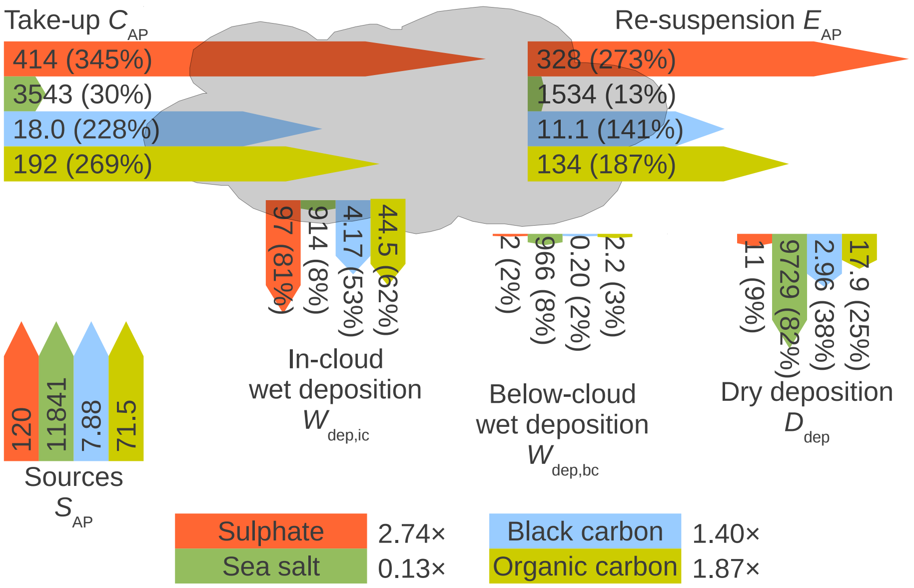

Figure 2.5: As Figure 2.4 for HadGEM3–UKCA-2010, for each aerosol component. (SU=sulphate; SS=sea-salt; BC=black carbon; OC=organic carbon. Mineral dust is not included, as it never interacts with cloud in the model. Fluxes are given in Tg yr^{-1} over the globe.)

Table 2.5: As Table 2.4 for HadGEM3–UKCA-2010, for each aerosol component. (SU=sulphate; SS=sea-salt; BC=black carbon; OC=organic carbon. Mineral dust is not included, as it never interacts with cloud in the model.)

	SU	SS	BC	OC
m_{AP} / Tg	1.89	4.72	0.114	1.30
$m_{\mathrm{AP,ic}}$ / Tg	0.153	0.755	0.00466	0.0515
$C_{\mathrm{AP,c}}$ / Tg yr^{-1}	414	3543	18.0	192
$E_{\mathrm{AP,c}}$ / Tg yr^{-1}	328	1534	11.1	134
$W_{\mathrm{dep,ic}}$ / Tg yr^{-1}	97	914	4.17	44.5
$W_{\mathrm{dep,bc}}$ / Tg yr^{-1}	2.22	966	0.196	2.19
W_{dep} / Tg yr^{-1}	99	1880	4.37	46.7
D_{dep} / Tg yr^{-1}	10.6	9729	2.96	17.9
S_{AP} / Tg yr^{-1}	120	11841	7.88	71.5
$E_{\mathrm{AP,c}}$ / $C_{\mathrm{AP,c}}$	0.79	0.43	0.62	0.70
$E_{\mathrm{AP,c}}$ / S_{AP}	2.74	0.13	1.40	1.87
$E_{\mathrm{AP,c}}$ / $W_{\mathrm{dep,ic}}$	3.39	1.68	2.65	3.01
$\tau_{\mathrm{AP,p}}$ / h	168	22.0	228	243
$\tau_{\mathrm{AP,e}}$ / h	50.7	27.0	90.2	84.9
$\tau_{\mathrm{AP,d}}$ / h	1566	4.25	336	635
$\tau_{\mathrm{AP,ic,p}}$ / h	13.9	7.24	9.79	10.1
$\tau_{\mathrm{AP,ic,e}}$ / h	4.10	4.32	3.70	3.37

however, the global-mean dry deposition timescale for sea-salt ($\tau_{\mathrm{AP,d}}$) is only 4.25 h, which is 8½ model timesteps in this configuration. In some regions the timescale may be significantly shorter, calling this assumption into question. It is thought that such an operator-splitting failure may also be responsible for anomalously high sea-salt concentrations found around certain coastlines in this version of the model (C. E. Johnson, pers. comm.)

Overall aerosol cloud cycling rates calculated in this way are thus heavily dependent on the relative emissions of the different species – a factor which is not considered in the simple analysis of Pruppacher and Jaenicke (1995) where a homogeneous aerosol population is assumed. Although Hoose et al. (2008a) use a model which treats the different aerosol species explicitly, they do not discuss their different cloud-cycling rates. In an extension of that work to convective cycling, however, Croft (2011, ch. 4) observes a similar variation, with sea-salt (and dust, which does not interact with cloud in UKCA at present) undergoing significantly fewer cloud cycles than sulphate and carbonaceous aerosol.

2.3 Summary and conclusions

This chapter aimed to quantify the extent to which aerosol is cycled through large-scale cloud, in order to assess its likely role in controlling the size distribution and mixing state of aerosol in the atmosphere, and to compare the results with previous work to establish how consistent such estimates are between different studies.

This was achieved by developing a method to diagnose the rates at which water and aerosol are cycled through large-scale cloud in the HadGEM3–UKCA model. For water, this was done using the increments to water vapour, liquid water and ice from the various evaporation and condensation processes in the prognostic cloud scheme. However, because there is no prognostic representation of aerosol taken up by cloud water, the aerosol cycling rate must be calculated differently – this was done following the diagnostic assumptions about the split between in-cloud and interstitial aerosol used by the scavenging scheme.

The results obtained here were compared with those of Hoose et al. (2008a) from the ECHAM5-HAM model, and the simple global budget argument of Pruppacher and Jaenicke (1995). While the global precipitation rates are quite consistent (being both energetically constrained and likely to have been tuned in the models), the water cycling rate (i.e. the average number of times cloud water evaporates and re-condenses in a new cloud, before falling as precipitation) is less constrained and varies considerably between the models: HadGEM3–UKCA gave 0.96, compared with 1.8 from Hoose et al. (2008a) and 2.6 from Pruppacher and Jaenicke (1995).

HadGEM3–UKCA also gave a lower total cycling rate for aerosol: 0.17, compared to 0.53 (Hoose et al., 2008a) and 0.4 (Pruppacher and Jaenicke, 1995). However, the figure for HadGEM3–UKCA varied considerably between the different aerosol components, from 0.13 for sea-salt (removal of which is dominated by dry deposition) to 2.74 for sulphate (dominated by wet deposition, and where in-cloud production is a major source). This range is considerably larger than the spread in the three estimates of all-aerosol cycling, suggesting that differences in the relative proportion of different aerosol types may account for some of this spread.

The analysis presented here only considered cycling through large-scale cloud, as opposed to parameterised sub-grid-scale convective cloud. However, from the modelling perspective, the split between these is somewhat arbitrary and resolution-dependent. The figures given in Pruppacher and Jaenicke (1995) suggest that the cycling rates are likely to be considerably higher if convective clouds are included (presumably due to the many short-lived non-precipitating shallow cumulus clouds). Unfortunately, however, diagnostics for the condensation and evaporation of convective cloud water (which only exists transiently, rather than as a prognostic variable) are not readily available in the model used here.

Chapter 3

Improving the physical representation of scavenging in HadGEM3–UKCA

Having considered the role of non-precipitating cloud in processing atmospheric aerosol via cloud cycling in Chapter 2, this chapter moves on to consider the influence of precipitating cloud via scavenging and wet deposition. Chapter 1 alluded to some shortcomings of the current scavenging scheme in HadGEM3–UKCA; these are first discussed in more detail, and then a more physically-detailed approach is derived, aiming for consistency with the large-scale precipitation scheme. This is partly motivated by a desire to investigate the extent to which such a scheme can give improved predictions of global aerosol distributions (particularly with regard to long-range transport) on a physical basis, without a heavy reliance on empirically-tuned coefficients. Such an approach requires significant complexity, however, and consideration is then given to how significant improvements can be made while retaining much of the simplicity of the existing framework.

3.1 Problems with the current scheme

The current aerosol scavenging scheme in HadGEM3–UKCA-2010 (the same model version used in Chapter 2) is quite simplistic in its representation of the interactions between aerosol, cloud and precipitation. In particular:

- Nucleation scavenging assumes a fixed proportion of each mode is taken up by the cloud water; this proportion is the same for mass and number (equivalent to scavenging uniformly across the size spectrum of the mode), and is not dependent on a detailed parameterisation of droplet activation.

- Nucleation scavenging assumes a fixed removal timescale in any 3D grid-box where rain is formed (i.e. flux out > flux in); no account is taken of the cloud fraction or precipitation rate, although these are readily available from the cloud and precipitation schemes.

- Impaction scavenging by cloud droplets is ignored, although this is understood to be an important removal mechanism for particles too small to act as CCN or IN.

- Neither nucleation nor impaction scavenging by snow is considered; the former incorrectly occurs where snow melts to form rain.

- Scavenged aerosol contained in evaporating precipitation is not returned to the atmosphere; this may lead to removal being too fast, and also ignores a mechanism for downward transport.

- Convective transport and scavenging are operator-split, such that aerosol can be transported above the level at which it should be scavenged and detrained before the scavenging scheme sees it; this may slow down removal and exaggerate upward transport.

The tropospheric chemistry component of UKCA (O'Connor et al., 2013) also implements in-cloud scavenging for trace gases; while there are intrinsic differences because the mechanism of take-up into cloud water is different from that for aerosol, and unavoidable differences due to the different numerical formulation of the chemistry and aerosol schemes, there are several apparently arbitrary differences in the treatment of precipitation microphysics in the two schemes, summarised in Table 3.1. In a coupled chemistry–aerosol scheme such as UKCA, it is clearly desirable that both should interact with precipitation in a consistent way.

3.2 An improved, microphysically-consistent scheme

The goal of the scheme presented here is to treat wet deposition of chemical and aerosol species by large-scale precipitation in a consistent way, taking account of the detailed microphysical processes diagnosed by the large-scale precipitation scheme. It should also be implemented such that it can interface with the convection scheme in the future (with the addition of the necessary hooks and additional diagnostics therein) to provide consistent convective scavenging.

The PC2 large-scale cloud scheme (Wilson et al., 2008) used in HadGEM3 partitions each grid box into clear, liquid, ice and mixed-phase volume fractions (C_0, C_l, C_i and C_mp respectively). The precipitation scheme (Wilkinson et al., 2009) adds a rain volume fraction C_R which overlaps with these (in a well-defined order of preference: $C_\mathrm{l} \rightarrow C_\mathrm{mp} \rightarrow C_\mathrm{i} \rightarrow C_0$).

The water in the grid box is split into vapour, liquid cloud, ice crystals, snow aggregates, rain and graupel (q, q_cl, q_cfc, q_cfa, q_R, and q_graup respectively). In typical climate configurations, only q, q_cl and a combined $q_\mathrm{cf} = q_\mathrm{cfc} + q_\mathrm{cfa}$ exist as prognostics, and graupel is turned off completely; however, there are options for prognostic rain, separate ice/snow prognostics and (prognostic) graupel. (This is assuming PC2 is in use; if PC2 is turned off, even q_cl is not prognostic, but is diagnosed based on

Table 3.1: Differences between the chemistry and aerosol in-cloud scavenging schemes in HadGEM3–UKCA-2010

		Chemistry **(O'Connor et al., 2013)**	**Aerosols** **(Mann et al., 2010, 2013)**
Formulation of parent scheme	**Updating**	Process rate calculated and solved in parallel with other chemical processes.	Process directly updates tracer amount in a sequential fashion.
	Grid	Working on 3D arrays.	Working on 1D arrays.
Intrinsic differences	**Aqueous fraction**	Henry's law for chemical species, using fixed cloud liquid water content.	Prescribed scavenging coefficient for aerosol mode.
Arbitrary differences	**Relation to precipitation rate P_k out of layer**	Empirical linear relation of removal rate to $$\sum_{k'=k}^{k_{max}} P_{k'}.$$ (counting precipitation from higher levels multiple times[a]).	Prescribed removal timescale applied where any rain is formed (i.e. $P_k > P_{k+1}$).
	Convection	Large-scale and convective precipitation handled independently.	Scavenging by convective precipitation only where no large-scale precipitation is formed; otherwise the latter is assumed to dominate.
	Ice	Linear minimum temperature cut-off (between 0°C and −20°C) for removal by large-scale precipitation in polar regions (beyond 65°).	Insoluble modes not scavenged unless $T < -15.15$°C (although the default scavenging ratios for these modes are zero in any case).
	Snow	Included in P_k: treated identically to rain.	Not included in P_k: treated as newly-formed rain where it melts.

[a] This appears to be a bug.

relative humidity. The new scavenging scheme is not intended to be used in non-PC2 configurations, and they will not be considered further here.)

The large-scale precipitation scheme calculates mass transfer rates for a number of separate microphysical processes which transfer mass between these phases, as shown in Table 3.2, as well as fall rates for each phase.

The new scheme is based on the idea that, once taken up by liquid water or ice, a chemical or aerosol species should "follow" that water through these processes, until one of the following occurs:

1. The water returns to the vapour phase. In this case, a proportion of each aerosol species is released corresponding to that contained within completely-evaporated droplets (or completely-sublimed ice particles), as one aerosol particle per droplet or ice particle. Chemical species are taken up or released by liquid water according to Henry's law to maintain equilibrium as the liquid water content changes. Specific notes on the different vapour-phase processes are given in Table 3.2.

2. The water falls out of the grid-box, taking any contained chemical or aerosol with it into the grid-box below, or depositing it at the surface if it falls out of the lowest level (i.e. where precipitation reaches the surface).

3. The water remains in the grid-box at the end of the timestep, in which case any contained chemical or aerosol is also retained in the grid-box. (In a prognostic treatment, such aerosol would be retained in separate tracers from interstitial aerosol, however in the present framework this distinction is lost between timesteps. Additional tracers for dissolved chemical species are unnecessary if instant re-equilibration according to Henry's law is assumed.)

At the start of the timestep, chemical species are taken up into liquid water according to Henry's law. Aerosol is taken up into liquid water and ice according to

Table 3.2: Transfer processes in the large-scale precipitation scheme in HadGEM3 (based on Wilkinson et al., 2009, Table 11, with permission from the Met. Office)

Process	From → To	Description	Note
LSETEV	$q_{\mathrm{cl}} \rightarrow q$	Evaporation of liquid cloud drops settling out of cloud	(1)
RACW	$q_{\mathrm{cl}} \rightarrow q_{\mathrm{R}}$	Collection of liquid cloud by rain	
RAUT	$q_{\mathrm{cl}} \rightarrow q_{\mathrm{R}}$	Autoconversion of liquid cloud to rain	
REVP	$q_{\mathrm{R}} \rightarrow q$	Evaporation of rain	(2)
IACW	$q_{\mathrm{cl}} \rightarrow q_{\mathrm{cfc}}$	Collection of liquid cloud by ice crystals	
IDEP1	$q_{\mathrm{cl}} \rightarrow q \rightarrow q_{\mathrm{cfc}}$	Deposition of vapour from liquid cloud onto ice crystals	(3)
IDEP2	$q \rightarrow q_{\mathrm{cfc}}$	Deposition of vapour onto ice crystals	
IPRM1	$q_{\mathrm{cl}} \rightarrow q_{\mathrm{cfc}}$	Heterogeneous nucleation of ice from liquid cloud	(4)
IPRM2	$q \rightarrow q_{\mathrm{cfc}}$	Heterogeneous nucleation of ice from vapour	(4)
IFRW	$q_{\mathrm{cl}} \rightarrow q_{\mathrm{cfc}}$	Homogeneous freezing of liquid cloud	
IMLT	$q_{\mathrm{cfc}} \rightarrow q_{\mathrm{R}}$	Melting of ice crystals	
ISUB	$q_{\mathrm{cfc}} \rightarrow q$	Sublimation of ice crystals	(5)
IMLTEV	$q_{\mathrm{cfc}} \rightarrow q$	Evaporation of melting ice crystals	(5)
IACR	$q_{\mathrm{R}} \rightarrow q_{\mathrm{cfc}}$	Collection of rain by ice crystals	
SACW	$q_{\mathrm{cl}} \rightarrow q_{\mathrm{cfa}}$	Collection of liquid cloud by ice aggregates	
SDEP1	$q_{\mathrm{cl}} \rightarrow q \rightarrow q_{\mathrm{cfa}}$	Deposition of vapour from liquid cloud onto ice aggregates	(3)
SDEP2	$q \rightarrow q_{\mathrm{cfa}}$	Deposition of vapour onto ice aggregates	
SMLT	$q_{\mathrm{cfa}} \rightarrow q_{\mathrm{R}}$	Melting of ice aggregates	
SSUB	$q_{\mathrm{cfa}} \rightarrow q$	Sublimation of ice aggregates	(5)
SMLTEV	$q_{\mathrm{cfa}} \rightarrow q$	Evaporation of melting ice aggregates	(5)
SACR	$q_{\mathrm{R}} \rightarrow q_{\mathrm{cfa}}$	Collection of rain by ice aggregates	
SAUT	$q_{\mathrm{cfc}} \rightarrow q_{\mathrm{cfa}}$	Autoconversion of ice crystals to aggregates	
SACI	$q_{\mathrm{cfc}} \rightarrow q_{\mathrm{cfa}}$	Collection of ice crystals by aggregates	
GAUT	$q_{\mathrm{cfa}} \rightarrow q_{\mathrm{graup}}$	Autoconversion of ice aggregates to graupel	
GACW	$q_{\mathrm{cl}} \rightarrow q_{\mathrm{graup}}$	Collection of liquid cloud by graupel	
GACS	$q_{\mathrm{cfa}} \rightarrow q_{\mathrm{graup}}$	Collection of ice aggregates by graupel	
GMLT	$q_{\mathrm{graup}} \rightarrow q_{\mathrm{R}}$	Melting of graupel	

Table 3.2: continued

(1) LSETEV: Liquid cloud droplets falling into the clear-sky portion of a grid box are evaporated across the whole size spectrum (however the falling droplets will be predominantly the larger ones with faster terminal velocities in the first place). Any contained chemical or aerosol species are released.

(2) REVP: Raindrops shrink by evaporation, causing chemical species to be released until Henry's law equilibrium is restored. Aerosol is only released from those raindrops which evaporate completely, each of which produces one aerosol particle.

(3) IDEP1/SDEP1: Deposition occurs preferentially from the liquid phase, to represent the Bergeron–Findeisen process. However this involves evaporation followed immediately by deposition, thus any contained chemical or aerosol species are left behind in the liquid phase and released according to Henry's law (for chemical species) or for completely-evaporated droplets (for aerosol).

(4) IPRM1/IPRM2: Heterogeneous nucleation involves the take-up of ice nuclei; however this is handled separately at the start of each timestep according to the scavenging coefficients.

(5) ISUB/IMLTEV/SSUB/SMLTEV: Ice particles shrink by sublimation or melting followed by evaporation. Aerosol is only released from those particles which sublime (or melt and evaporate) completely, each of which produces one aerosol particle.

scavenging coefficients which may be either fixed for each aerosol mode and water phase, or derived from the number of activated droplets.

Any chemical or aerosol which is thus taken up into droplets or ice particles is excluded from the "dry" processes, in particular dry deposition and sedimentation (as they will instead fall along with the water). Aerosol produced by wet oxidation is assumed to be taken up into the cloud liquid water.

The take-up of chemical species by ice particles has not been discussed here – although such take-up has been observed, and a number of approaches proposed (e.g. Neu and Prather, 2012), there is no established theoretical framework to describe them and this work is primarily focused on aerosol; such processes are thus neglected for now.

When aerosol is returned to the prognostic tracers, either due to evaporation/sublimation or at the end of the timestep, it assumes a size distribution derived from the size distribution of the droplets or ice particles in which it was contained. Because the current HadGEM3 cloud and precipitation schemes are one-moment bulk mass, rather than size-resolved, schemes, the droplet and ice particle size distributions are prescribed by those schemes rather than explicitly simulated. For evaporation/sublimation, it is assumed that each hydrometeor leaves behind one aerosol particle; however there are two complications which must be considered:

- If evaporation/sublimation is not complete, only the smallest hydrometeors will do so fully (thus releasing aerosol particles) while the larger particles will shrink (Pruppacher and Klett, 1996, §13.2.3). A theoretical calculation of the size distribution of hydrometeors which are fully evaporated/sublimed is not straightforward (see e.g. Tzivion et al., 1989); it thus seems prudent to carry out a sensitivity study with the limiting cases before doing so. Such cases could be (a) no hydrometeors shrink, and a uniform fraction across the size spectrum are removed; (b) no hydrometeors shrink, and only the smallest are removed;

and (c) all hydrometeors shrink, and none are removed until no liquid or ice remains.

- The concentration of aerosol in hydrometeors (mass of aerosol per unit mass of water/ice) may not be uniform, but rather vary across the size spectrum. This is particularly so for small droplets, where growth is dominated by condensation and size well correlated with that of the initial condensation nucleus (Pruppacher and Klett, 1996, §17.3); for larger droplets growth is dominated by coalescence which leads to a more uniform concentration by the time raindrops are formed. In addition, the production of secondary aerosol material within the droplet by aqueous chemistry may not be proportional to the droplet mass, e.g. due to different dissolved concentrations of gaseous precursors; detailed modelling by Ovchinnikov and Easter (2010) suggests this can have a significant impact on the relationship between droplet size and dissolved aerosol concentration. A further sensitivity study may be needed to assess the effect of different assumptions for this relationship.

The microphysically-detailed scheme proposed above is summarised in Table 3.3; a detailed derivation of the prognostic equations is presented in Appendix A. However, the proposed scheme is likely to be computationally expensive as well as significantly increasing code complexity. In addition, because HadGEM3 uses a one-moment bulk mass formulation for cloud and precipitation, many assumptions about hydrometeor size distributions would still be required – which may result in a model with no fewer arbitrary tuning parameters than at present. Given this, it may be possible to achieve some improvement to aerosol scavenging in a much simpler way, making better use of the HadGEM3 model fields already available to UKCA. This possibility is explored in the following sections, focusing on accounting for rain rate and cloud fraction (Section 3.3), the coupling between convective scavenging and transport (Section 3.4) and the re-evaporation of rain (Section 3.5).

Table 3.3: Overview of a microphysically-consistent in-cloud scavenging and wet deposition scheme for HadGEM3–UKCA

	Chemistry	**Aerosols**
1	Calculate mass ratio of chemical species in cloud liquid water (and prognostic rain if enabled) using Henry's law, based on actual liquid water content from cloud scheme.	Calculate number and mass ratio of aerosol species in cloud liquid water and ice (and prognostic rain/snow/graupel if enabled) using separate number/mass scavenging coefficients for each mode and phase (either fixed, or diagnosed from the activation scheme).
	Chemical species diagnosed to be in an aqueous phase should be subject to aqueous-phase chemistry only, and not to gas-phase chemistry.	Aerosol diagnosed to be in an aqueous phase should not be subject to any of the dry aerosol processes.
	Chemical species produced by aqueous-phase reactions should go directly into the diagnosed aqueous mass, rather than the gas-phase mass.	Aerosol produced by wet oxidation should go directly into the diagnosed aqueous mass, rather than the dry aerosol mass.
2	Iterating down the wet levels in a column, transfer mass between the different phases, and pass to the level below, in proportion to the water transferred, as given by the microphysics and fall-rate diagnostics from the precipitation scheme.	
	Re-equilibrate falling drops to their new environment according to Henry's law.	For liquid drops and ice particles which evaporate or sublime completely, add any contained aerosol to the dry aerosol number and mass, with a size distribution given by the assumed size distribution of the source phase.
3	Feed the net change in mass from the transfers into the main chemistry scheme solver.	Update the number and mass tracers, giving aerosol in aqueous phases a size distribution according to that of the water phase in which it is dissolved.

3.3 Initial improvements: a first-order proportional scheme for scavenging by large-scale precipitation

The existing scheme for in-cloud scavenging in HadGEM3–UKCA-2010 uses a fixed removal timescale (half the aerosol number and mass in scavenged modes is removed in 6 hours, wherever rain is produced):

$$\frac{\partial n}{\partial t} = \begin{cases} -\dfrac{\ln 2}{\tau} f \alpha n & \dfrac{\partial R}{\partial z} < 0 \\ 0 & \dfrac{\partial R}{\partial z} \geq 0, \end{cases} \tag{3.1}$$

where n is the number or mass mixing ratio of aerosol in a particular mode (the size spectrum and composition do not change), R is the downward rain flux, τ is the assumed half-life of cloud water with respect to rain (6 hours), α is the scavenging ratio (1 for soluble accumulation and coarse modes, and 0 for other modes) and f represents the assumed fraction of the grid box over which the rain falls (0.3 for convective rain and 1 for large-scale rain). These cloud fractions are likely to be over-estimates in many cases, causing too much of the aerosol in the grid box to be susceptible to removal; the fixed removal timescale is likely to remove aerosol too quickly in light drizzle and too slowly in very heavy rain.

In discrete form, for one timestep Δt on model level k (increasing upwards), the above equation becomes:

$$\Delta n_k = \begin{cases} \left(2^{-\frac{\Delta t}{\tau}} - 1\right) f \alpha n_k & R_k > R_{k+1} \\ 0 & R_k \leq R_{k+1}. \end{cases} \tag{3.2}$$

However, since for large-scale precipitation the cloud liquid water content q_{cl}, liquid cloud fraction C_{l} and downward rain flux R are readily available, it is straightforward to construct a scheme based on a first-order loss rate over the cloudy portion of the grid box, assuming that aerosol in scavenged modes is removed by precipitation at the same rate as cloud water:

$$\frac{\partial n}{\partial t} = \frac{C_\mathrm{l} \alpha n}{q_\mathrm{cl}} \left.\frac{\partial q_\mathrm{cl}}{\partial t}\right|_\mathrm{lsp} = -\frac{C_\mathrm{l} \alpha n}{\rho_\mathrm{air} q_\mathrm{cl}} \frac{\partial R}{\partial z}. \tag{3.3}$$

This at least relates the removal rate to the strength of the rainfall in a physical way, although it still has many shortcomings – in particular, evaporation of rain is ignored and melting snow is still misdiagnosed as the production of rain from cloud water. (These processes require following the precipitation down each model column, requiring larger structural changes to the model.) In discrete form, this becomes:

$$\Delta n_k = \begin{cases} \left(\exp\left(-\frac{R_k - R_{k+1}}{\rho_k \left(z_{k+1/2} - z_{k-1/2} \right) q_{\mathrm{cl},k} \Delta t} \right) - 1 \right) C_{\mathrm{l},k} \alpha n_k & R_k > R_{k+1} \\ 0 & R_k \leq R_{k+1}. \end{cases} \tag{3.4}$$

Similarly, the removal rate from the existing below-cloud scavenging scheme can be scaled by the fraction C_R of the grid box covered by rain,[1] which is currently ignored. (The rain rate is already accounted for in below-cloud scavenging.)

These changes were implemented in HadGEM3–UKCA-2010, and two one-year simulations were run for comparison – with and without the modified scavenging scheme. The change to the mean burden (column-integrated mass per unit area) of the four aerosol components is shown in Figure 3.1. Each simulation had a 3-month spin-up period, and aerosol feedbacks were not included (thus both runs had identical meteorology). Modest changes are seen to global mean burdens (a $\sim 9\%$ reduction for sulphate, less for other components), while local changes are up to ±20%. Sulphate, black carbon and organic carbon are strongly reduced over the polluted regions of the northern mid-latitudes, while there is relatively little change in the tropics where the majority of precipitation is convective, and there are areas of increased aerosol over central Africa and the maritime continent. For sea-salt, the pattern is rather

---

[1] In cloud, where rain is produced, C_R is always set equal to C_l in the precipitation scheme and so the question of which to use in (3.3) and (3.4) for in-cloud scavenging is moot.

different with alternating regions of increase and decrease over the large ocean basins, and a general decrease over high northern latitudes. Changes of a similar magnitude are seen in the per-mode number burdens, as shown in Figure 3.2, showing distinct changes in the size distribution – in particular, a shift to smaller sizes throughout most of the mid-latitudes. In theory, changes in large-scale scavenging may be partly compensated for by convective scavenging; however this is unlikely in this particular model, firstly because its convective scavenging is very weak (as will be discussed in Section 3.4), and secondly because the convective scavenging scheme only operates where there is no large-scale scavenging at all (see Table 3.1).

These results suggest that improving the physical representation of large-scale scavenging may have a significant effect on the global distribution of aerosols in the model. However, evaluating burden changes directly is difficult, as burdens are not readily retrieved from observations (although this is a point that will be returned to in Chapter 4). The model's radiation scheme can calculate the resulting change in aerosol optical depth (AOD), which is more directly comparable with satellite observations. Figure 3.3 shows the annual mean AOD at 550 nm wavelength for the year from March 2000 to February 2001 inclusive from Terra–MODIS (averaged from the level 3 collection 5 daily `Optical_Depth_Land_And_Ocean_Mean` product and bilinearly interpolated to the HadGEM3 model grid; global mean 0.159), and that simulated by each configuration of HadGEM3–UKCA-2010 nudged to ERA-40 for the same time period and sampled on those grid points and days where there is valid MODIS data (global mean 0.128 for fixed scavenging, 0.118 for proportional). Thus there is a large overall negative bias in the model AOD compared to MODIS, which gets slightly worse with the proportional scavenging scheme. However, the difference between the model versions is much smaller than that between either simulation and the MODIS retrieval, and the model bias is likely to be the result of many separate issues in the model and also uncertainties and errors in the observations (especially over land, where AOD retrievals are generally less reliable than over ocean).

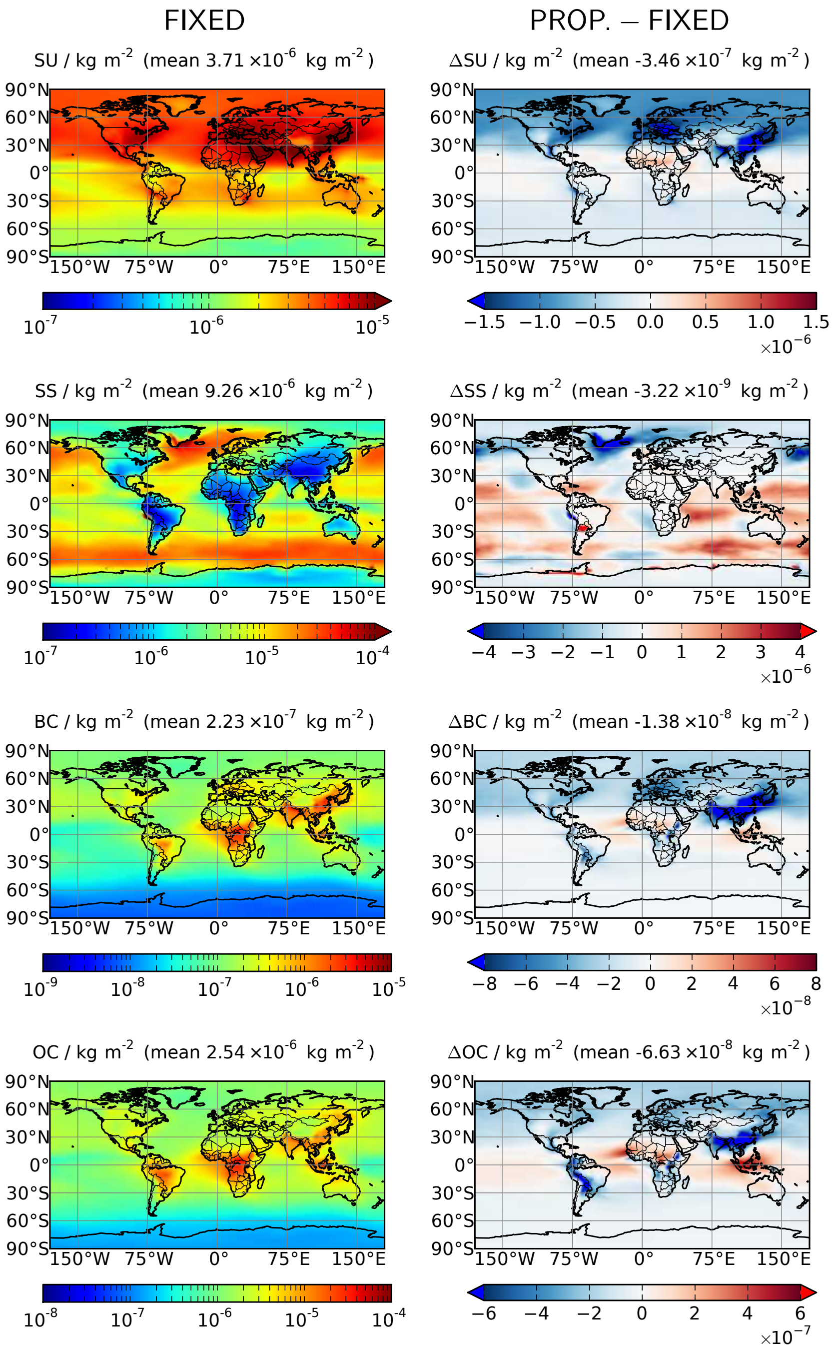

Figure 3.1: One-year mean column mass burdens for each aerosol component as simulated by HadGEM3–UKCA-2010 using the existing fixed scavenging (left), and the change when a first-order scheme based on cloud liquid water content, rain flux and cloud/rain fraction is used (right; see text). (SU=sulphate; SS=sea-salt; BC=black carbon; OC=organic carbon; mineral dust is omitted because it is unchanged.)

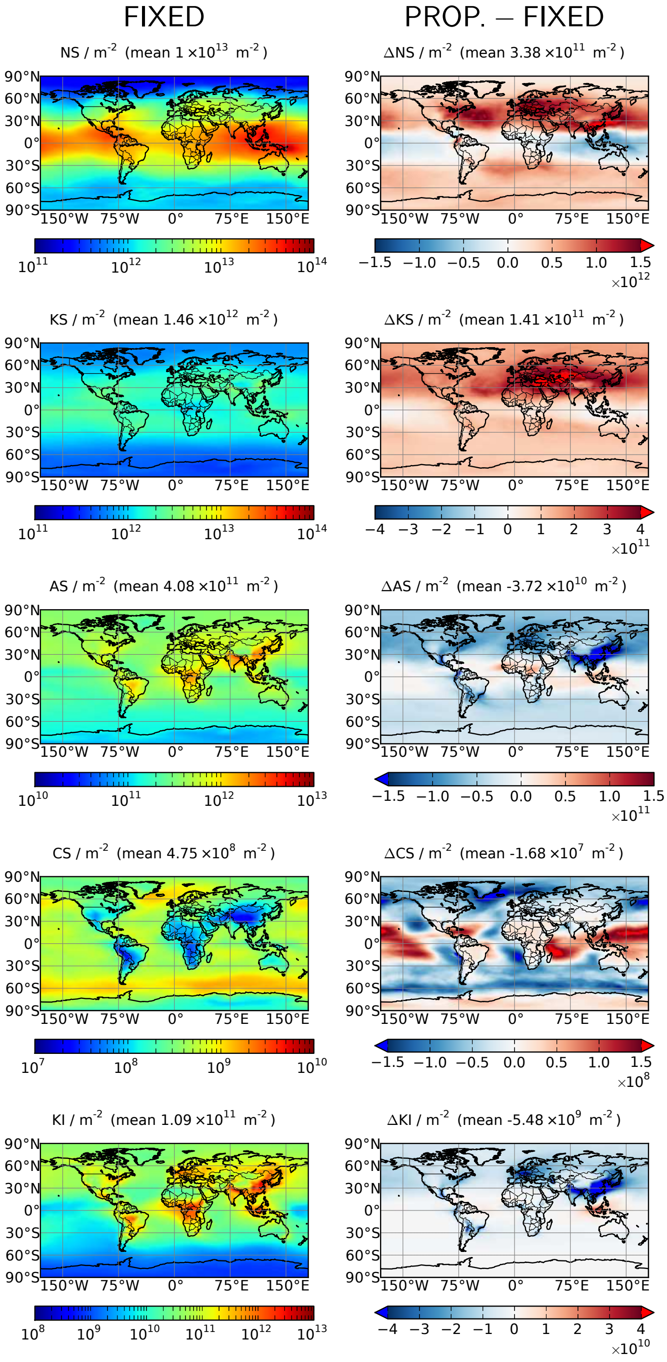

Figure 3.2: One-year mean column number burdens for each aerosol mode as simulated by HadGEM3–UKCA-2010 using the existing fixed scavenging (left), and the change when a first-order scheme based on cloud liquid water content, rain flux and cloud/rain fraction is used (right; see text).(NUC=nucleation mode, AIT =Aitken mode, ACC=accumulation mode, COR=coarse mode; SOL=soluble, INS=insoluble. Mineral dust particles are not included in these modes, and are not shown because they are unchanged.)

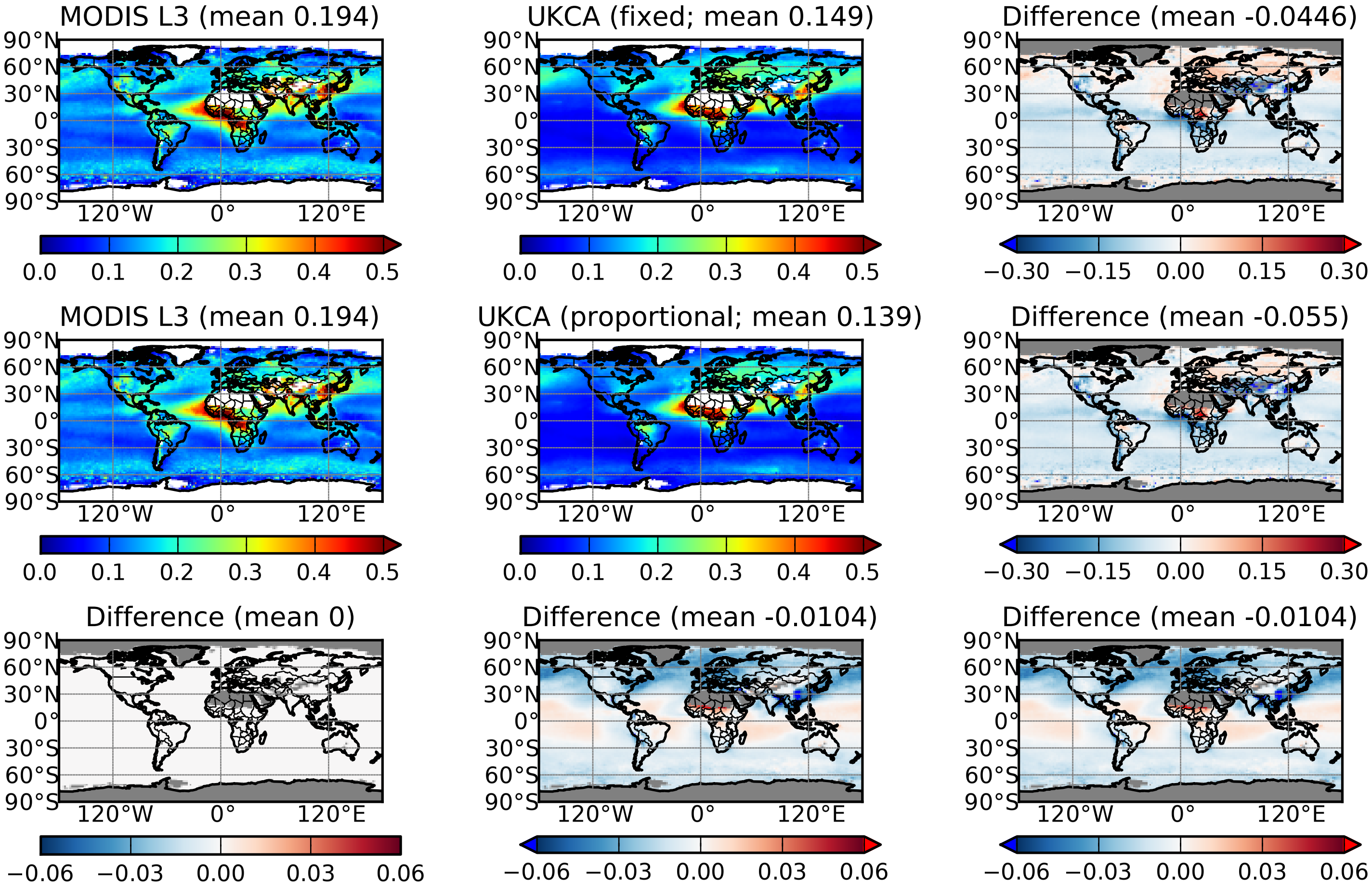

Figure 3.3: One-year mean aerosol optical depth from Terra–MODIS (left: level 3, collection 5 for March 2000–February 2001) and HadGEM3–UKCA-2010 (centre: nudged to ERA-40 for the same time period, and collocated with the daily MODIS dataset), and the difference between them (right: model minus satellite). The top row is using the existing fixed scavenging in UKCA, the middle row is using the proportional-to-rain-rate scheme described in the text, and the bottom row shows the difference between these two cases (middle row minus top).

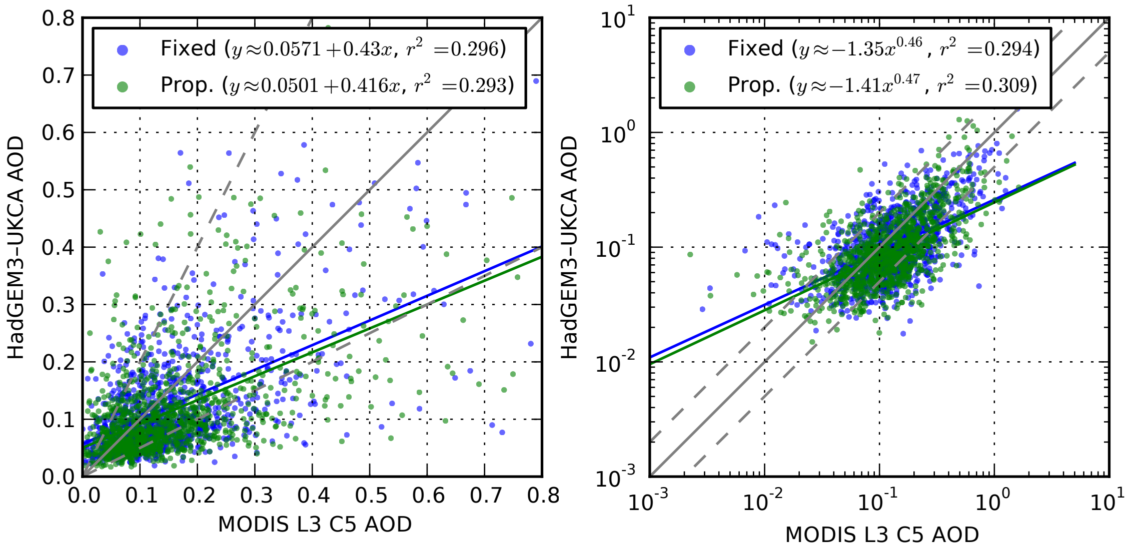

Figure 3.4: Scatter plot and linear regression of daily-mean AOD (left) and its logarithm (right) from HadGEM3–UKCA-2010, using the existing fixed scavenging in UKCA and the proportional-to-rain-rate scheme described in the text, against that from Terra–MODIS (collection 5, level 3), over the model grid points, for March 2000–February 2001. The scatter plots are sub-sampled to show only 5000 randomly-selected points for each simulation; however the regression statistics use the full data set. The dashed lines represent a factor of two either side of the solid grey 1:1 line.

Figure 3.4 shows a linear regression of the daily-mean AOD from the two simulations against that retrieved from MODIS, over the individual days and model grid points. Both the retrieved and simulated AOD distributions show a long upper tail (as can be seen in the left-hand plot), which is likely to distort the regression statistics, and thus a linear regression of log(daily mean AOD) is used instead (which appears to have a distribution closer to normal, and is shown in the right-hand plot). From this it can be seen that, although the proportional scavenging produces a larger bias than the fixed scavenging, it has a stronger correlation with MODIS ($r^2 = 0.309$ compared to 0.294). This suggests that it may be simulating the effects of scavenging more accurately, even though it unmasks compensating errors elsewhere. The impact of scavenging on the simulated AOD suggests that the direct radiative effect of aerosol is likely to be sensitive to changes in its parameterisation.

A first-order scheme for in-cloud scavenging similar to that described in this section is now included in more recent versions of UKCA, and specifically in the version used as a base for the rest of this work (which will be referred to as HadGEM3–UKCA-2011). However, the other issues identified in Section 3.1 remain – and in particular the use of $-\partial R/\rho_{\mathrm{air}}\partial z$ for the rate at which rain is produced means that melting snow is included. A brief experiment was conducted, replacing (3.3) with

$$\frac{\partial n}{\partial t} = -\frac{C_{\mathrm{l}}\alpha n}{q_{\mathrm{cl}}}\left(P_{\mathrm{RAUT}} + P_{\mathrm{RACW}} - P_{\mathrm{REVP}}\right), \tag{3.5}$$

where P_{RAUT}, P_{RACW} and P_{REVP} are the rates (in $\mathrm{kg_{water}\,kg_{air}^{-1}\,s^{-1}}$) at which cloud water is converted to rain by autoconversion and accretion, and at which rain evaporates, respectively. The results are not shown here, but although there are changes in aerosol distribution they are about an order of magnitude smaller than those between the fixed and proportional schemes.

3.4 An in-plume convective scavenging scheme

Convection plays a dominant role in the upward transport of both gaseous and particulate matter in the atmosphere, with wide variation amongst models especially for short-lived species (Hoyle et al., 2011). However, convection (especially the vigorous, deep convection that can transport air parcels from the boundary layer to the upper troposphere) is also often associated with intense precipitation, and thus a significant amount of material may be removed by wet scavenging before it is detrained from the convective updraught.

Convective transport and scavenging are treated in an operator-split manner in HadGEM3–UKCA (both -2010 and -2011 versions): scavenging removes aerosol from the grid-box mean tracer field at the end of each timestep, after the convection scheme (which includes tracer transport) has already run. The scavenging parameterisation removes aerosol from those 3D grid boxes in which convective rain is formed (i.e. the downward rain flux diagnosed by the convection scheme is greater than that from the box above), according to a fixed timescale and assuming convective rain falls over a fixed fraction (30%) of the grid box. However, the air parcel from which the rain was produced will likely have continued to, and been detrained at, a higher (and non-precipitating) level, and thus its aerosol load will not be available for scavenging. This may result in too little removal by convective scavenging, and too much aerosol being lifted to the upper troposphere; in turn this may exaggerate both the lifetime and long-range transport of aerosol in regions (e.g. the tropics) where convective precipitation is widespread. These concerns are borne out by the relative proportions of water and aerosol removed by large-scale and convective precipitation: convection is responsible for $\sim 60\%$ of precipitation at the surface in the model, but less than 10% of the aerosol mass removal by in-cloud scavenging.

In this section, an alternative scheme for convective scavenging is presented, which removes scavenged aerosol from within the convective updraught at the same time as water is removed in precipitation.

In common with the parameterisations used in many global atmospheric GCMs, the Gregory and Rowntree (1990) convection scheme in HadGEM3 uses a bulk mass flux approach. Conceptually, there is an ensemble of many convective clouds within a model grid box, having a spectrum of different properties (updraught mass flux, entrainment and detrainment rates, heat and moisture content). However, the assumption is made that this ensemble can be represented as a single updraught whose properties are defined by integrating over this conceptual ensemble.

When convection is initiated in a grid box, a convective “parcel” is defined which takes its initial properties from the environment, and is given an initial mass flux via a closure based on the diagnosed convective available potential energy (CAPE). The parcel then ascends from one model level to the next, mixing with the environment via entrainment and detrainment, until its buoyancy drops below a threshold and the entire parcel is detrained. As the parcel ascends, it cools adiabatically until it reaches saturation, at which point condensation releases latent heat as cloud forms. Precipitation is diagnosed by a fairly simple heuristic: if the cloud depth has exceeded a fixed threshold, and the cloud condensate exceeds a fixed minimum $l^{\mathrm{P}}_{\mathrm{min}}$, then condensate is converted to precipitation during the ascent to the next model level such that only $l^{\mathrm{P}}_{\mathrm{min}}$ remains. Cloud water is assumed to be frozen below -10°C, allowing for the existence of supercooled liquid cloud, while precipitation is assumed to freeze or melt at 0°C.

The in-cloud scavenging is described by a first-order loss rate as in Section 3.3, but formulated in terms of an air parcel within the convective updraught as it rises[2] from level k to $k+1$, rather than the environmental air in the grid box:

$$\Delta n^{\mathrm{P}}_{k} = \frac{\alpha g P_k n^{\mathrm{P}}_{k+1}}{M_{k+1} l^{\mathrm{P}}_{k+1}}, \tag{3.6}$$

where n^{P}_{k+1} is the number or mass mixing ratio of aerosol in a particular mode within the parcel at level $k+1$ (but before scavenging), l^{P}_{k+1} is the mass mixing ratio of liquid water and/or ice in the parcel after it has been lifted to level $k+1$ (but before precipitation has been removed), M_{k+1} is the updraught mass flux at level $k+1$ (expressed in pressure coordinates, hence the factor g), and P_k is the rate at which precipitation is produced through lifting from level k to $k+1$.

Liquid and ice cloud are not differentiated in this parameterisation, effectively assuming that most of the ice particles which form in the upper part of the convective cloud originate from the freezing of liquid drops – which will have taken up cloud condensation nuclei (CCN) by nucleation scavenging when they formed. This is a simplification, as additional ice particles will form via deposition onto ice nuclei

---

[2] Model levels are enumerated from the surface upwards in HadGEM3 – this differs from the notation in Gregory and Rowntree (1990), which is based on an earlier GCM where model levels are enumerated from the top downwards and the parcel rises from level k to $k-1$.

(IN) and rime splintering. Also, CCN may be released as droplets evaporate in the Bergeron–Findeisen process, and IN may be taken up as droplets freeze on them.

While the large-scale scavenging scheme only removes aerosol from the soluble accumulation and coarse modes, the stronger updraughts found in convective cloud will produce higher supersaturations allowing smaller particles to activate and thus be removed by in-cloud scavenging. There is also no equivalent for convective cloud of the “cloud processing” process in UKCA which moves soluble aerosol larger than 37.5 nm from the Aitken to the accumulation mode in the presence of large-scale cloud. Scavenging is therefore extended into the soluble Aitken mode, setting $\alpha = 0.5$ for convective scavenging of this mode. Ideally, the critical diameter for activation would be diagnosed via Köhler theory; however this requires knowledge of the updraught velocity, which is not known explicitly in a mass-flux convection scheme. Work is under way, however, to implement this for large-scale scavenging, based on the work of West et al. (2013).

Figure 3.5 shows the effect of the in-plume convective scavenging scheme on the annual-mean column mass burden of each aerosol component in a one-year nudged simulation for 2009. Burdens of sulphate, sea-salt, black carbon and organic carbon are all reduced over wide areas of the globe. Although the largest absolute reductions are in regions of high burden, there are also order-of-magnitude reductions in the low burdens in regions remote from sources (e.g. for sea-salt over land, and for black carbon over the mid-Pacific and Southern Ocean). There is no change in mineral dust, which is not – and does not interact with any aerosol which is – subject to in-cloud scavenging in the model.

Figure 3.6 shows the effect on the annual-mean number burden in each of the UKCA aerosol modes. While soluble accumulation and coarse mode numbers are much reduced due to their removal by convective scavenging, there are large increases in soluble nucleation and Aitken mode numbers (despite the fact that the soluble Aitken mode is subject to quite strong removal in this scheme). A likely explanation

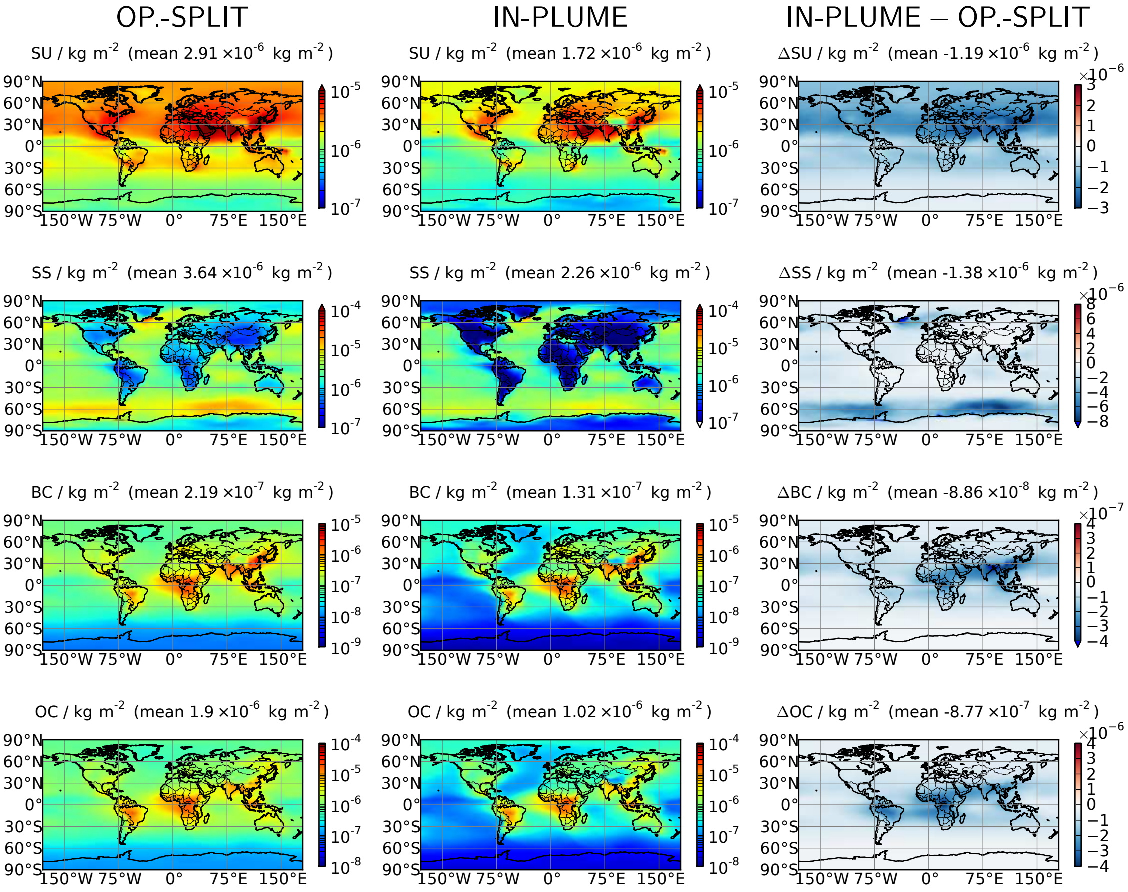

Figure 3.5: Annual mean 2009 mass burden of each aerosol component simulated by HadGEM3–UKCA-2011 with the standard operator-split convective scavenging scheme (left) and the in-plume scheme described in the text (centre), and the difference between these (right: in-plume minus operator-split). (SU=sulphate; SS=sea-salt; BC=black carbon; OC=organic carbon; mineral dust is omitted because it is unchanged.)

for this is that the removal of particles in the larger modes reduces the condensation sink for H_2SO_4 vapour, leading to increased nucleation of new sulphate particles, which subsequently grow by coagulation with one another to form Aitken-mode particles. The changes to insoluble Aitken mode numbers are rather weaker and more localised, as these particles are not directly affected by in-cloud scavenging, only indirectly by changes in the soluble modes with which they interact.

Figure 3.7 shows the effect on the annual and zonal mean vertical profile of the number concentration (i.e. the number of particles per unit volume of air) in each of the soluble UKCA aerosol modes. The reduction in soluble accumulation-mode aerosol occurs throughout most of the free troposphere, except at high latitudes where there is little convective precipitation. This is consistent with the in-plume scheme scavenging aerosol that was allowed to detrain from the convective updraught by the operator-split scheme. The increase in nucleation-mode aerosol occurs in the upper tropical troposphere, where the nucleation process is known to be most active, and which overlaps with the area of reduced accumulation-mode aerosol (and hence reduced condensation sink). The increase in Aitken-mode aerosol occurs throughout the free troposphere below the region of enhanced nucleation, consistent with this being “fed” from above by the growth of additional particles from the nucleation mode. The largest reduction in the coarse mode (which is dominated by sea-salt) is in the lower troposphere over the Southern Ocean (where coarse sea-salt is concentrated); however there is also an order-of-magnitude reduction in the much smaller number of coarse particles found in the middle and upper troposphere, as for the accumulation mode.

The effect of the in-plume scheme on year-2009 mean 550 nm AOD is shown in Figure 3.8, against that from Terra–MODIS as in Section 3.3. As before, there is a large negative bias in the model AOD, which gets worse when the in-plume scheme is introduced (simulated global-mean AOD 0.057, compared to 0.088 with the operator-split scheme, and 0.168 from MODIS). Figure 3.9 shows a linear regression

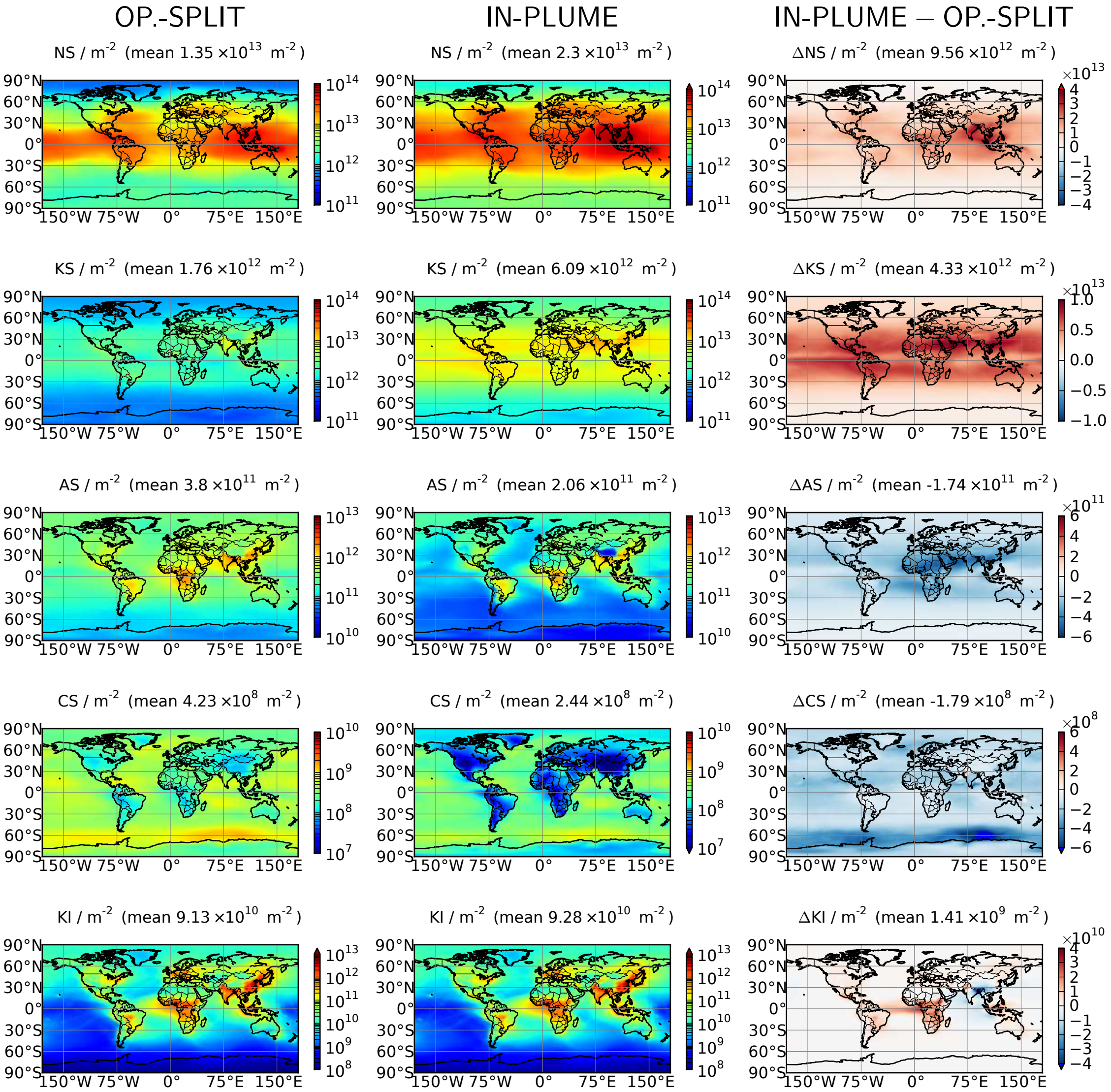

Figure 3.6: Annual mean 2009 number burden of each aerosol mode as simulated by HadGEM3–UKCA-2011 with the standard operator-split convective scavenging scheme (left) and the in-plume scheme described in the text (centre), and the difference between these (right: in-plume minus operator-split). (NS=soluble nucleation mode; KS=soluble Aitken mode; AS=soluble accumulation mode; CS=soluble coarse mode; KI=insoluble Aitken mode. Mineral dust particles are not included in these modes, and are not shown because they are unchanged.)

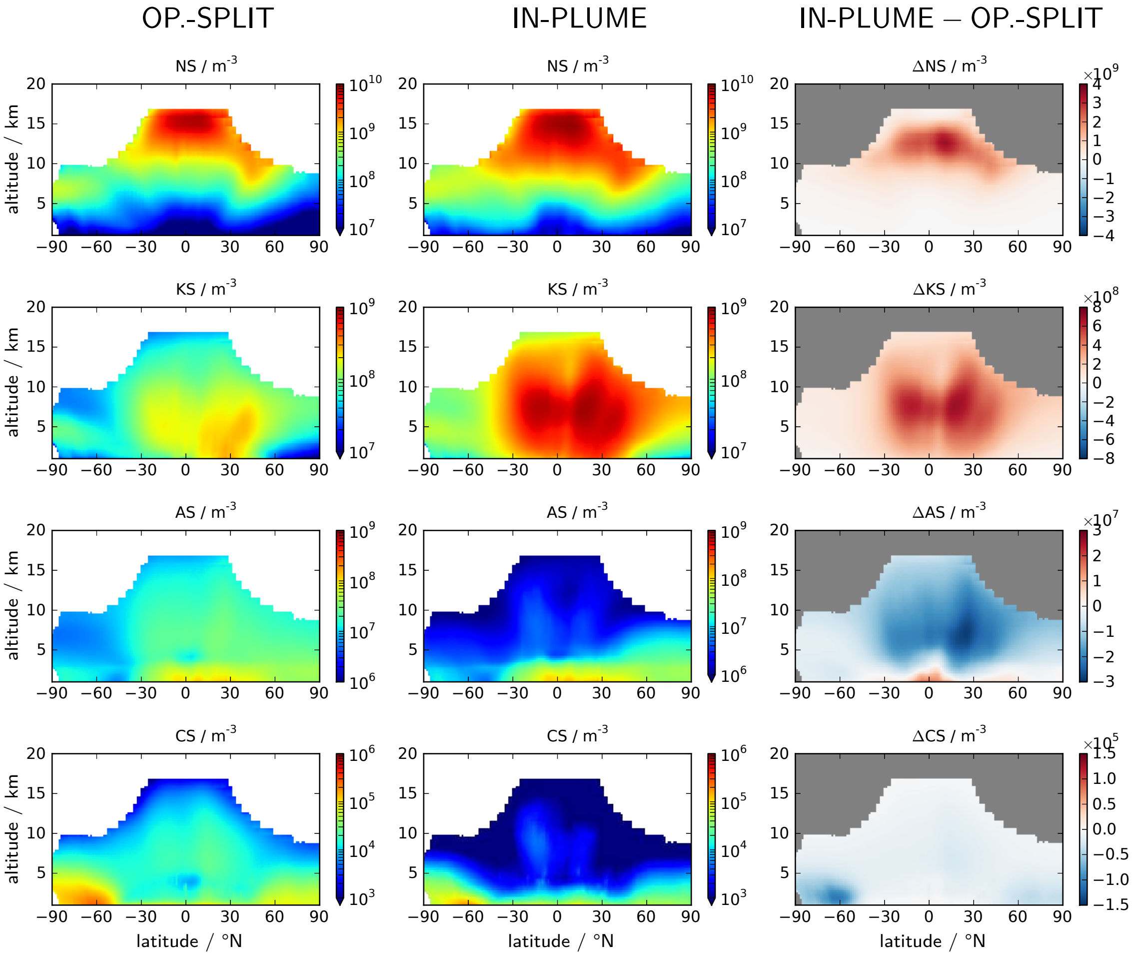

Figure 3.7: Annual and zonal mean 2009 number concentration profile of each soluble aerosol mode as simulated by HadGEM3–UKCA-2011 (up to the mean tropopause height) with the standard operator-split convective scavenging scheme (left) and the in-plume scheme described in the text (centre), and the difference between these (right: in-plume minus operator-split). (NS=soluble nucleation mode; KS=soluble Aitken mode; AS=soluble accumulation mode; CS=soluble coarse mode.)

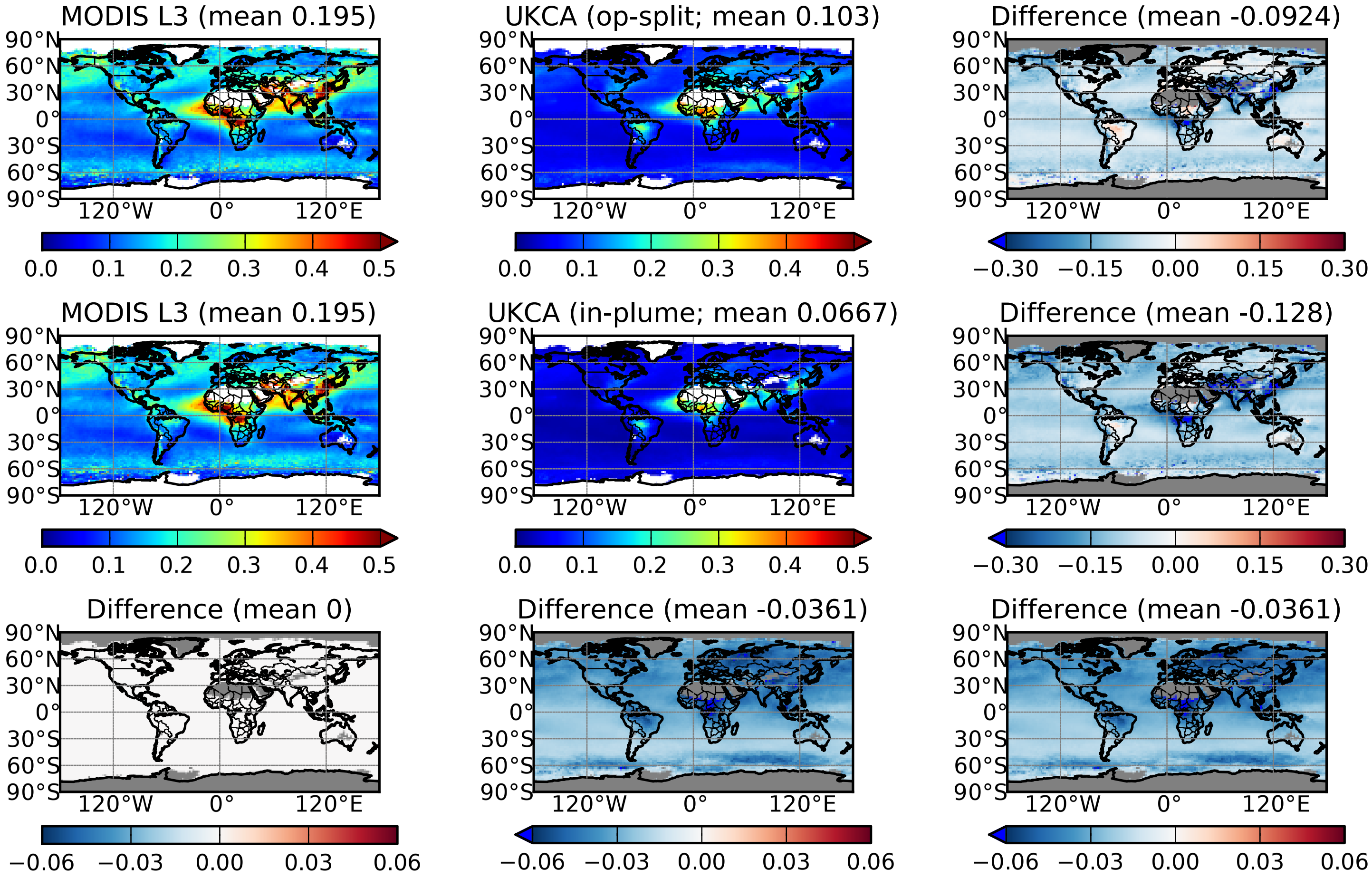

Figure 3.8: One-year mean aerosol optical depth from Terra–MODIS (left: level 3, collection 5 for the year 2009) and HadGEM3–UKCA-2011 (centre: nudged to ERA-40 for the same year, and collocated with the daily MODIS dataset), and the difference between them (right: model minus satellite). The top row is using the existing operator-split convective scavenging in UKCA, the middle row is using the in-plume scheme described in the text, and the bottom row shows the difference between these two cases (middle row minus top).

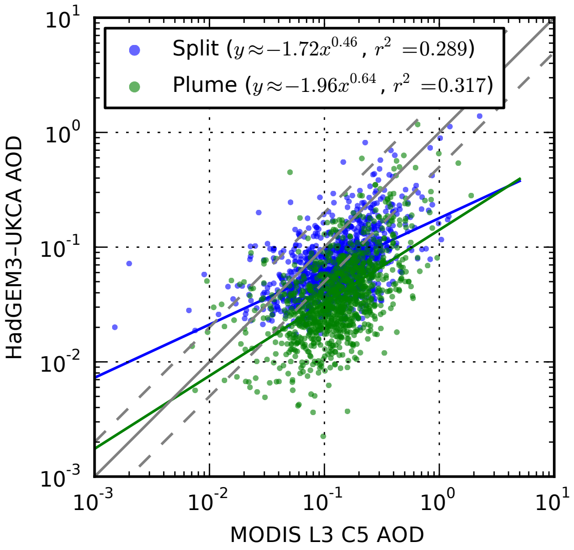

Figure 3.9: Scatter plot and linear regression of daily-mean log(daily-mean AOD) from HadGEM3–UKCA-2011, using the existing operator-split convective scavenging in UKCA and the in-plume scheme described in the text, against that from Terra–MODIS (collection 5, level 3), over the model grid points, for the year 2009. The scatter plot is sub-sampled to show only 5000 randomly-selected points for each simulation; however the regression statistics use the full data set. The dashed lines represent a factor of two either side of the solid grey 1:1 line.

of log(daily-mean AOD) from both simulations against that from MODIS. There is an increase in correlation when the in-plume scheme is used ($r^2 = 0.317$ compared to 0.289 for the operator-split scheme).

A more detailed evaluation of this scheme is presented in Chapter 4, after introducing the methodology for assessing its impact on the vertical distribution of aerosol using in-situ observations from aircraft campaigns.

Development of HadGEM3–UKCA has continued beyond the versions used in this work, and an effort is currently under way to incorporate the convective scavenging scheme described in this section into version 8.6 of the Met. Office Unified Model (MetUM). Initial experiments using earlier 8.x versions in a General Atmosphere (GA) 4.0 configuration (Walters et al., 2013) suggest that the impact is even greater than in HadGEM3–UKCA-2011 (based on MetUM 7.3): unrealistic constant drizzle over ocean has been reduced by the introduction of a prognostic rain scheme, and the proportion of total precipitation produced by the convection scheme has increased. The in-plume scavenging scheme substantially reduces the large *positive* AOD biases seen in these versions (C. E. Johnson, pers. comm.)

3.5 Treatment of aerosol contained in evaporating precipitation

Some of the precipitation which is produced never reaches the surface, but evaporates (or sublimes) below the cloud. From an aerosol scavenging perspective, there are two scenarios to consider:

- droplets evaporate (or ice particles sublime) completely, releasing and re-suspending any dissolved or embedded aerosol; or
- droplets (or ice particles) shrink due to evaporation (or sublimation), but remain in existence and retain any dissolved or embedded aerosol.

Where the precipitation evaporates completely, then only the first scenario is possible. However, where only some of the precipitation evaporates, a mixture of the two should be expected: some droplets will shrink and retain their aerosol, while others will evaporate completely and release it. In a bulk cloud scheme such as that used in HadGEM3, it is not known explicitly how many droplets evaporate completely in this case.

Figure 3.10 shows the annual mean amount of both large-scale and convective precipitation which is produced and which evaporates in HadGEM3–UKCA-2011 (based on a one-year nudged simulation for 2009). While the proportion of convective precipitation which evaporates never exceeds 30% except in very dry regions where there is little to evaporate anyway, there are several areas where the majority of large-scale precipitation evaporates before reaching the surface. In particular, in the ocean regions to the west of the major continents where persistent stratocumulus decks are found, 60–70% of the large-scale precipitation in the model evaporates; in parts of the maritime continent, the figure is even higher, reaching 80%. As a result, it seems likely that the model will overestimate the removal of aerosol by large-scale wet deposition in these regions. This may provide at least a partial explanation for the unrealistically low CCN numbers found by West et al. (2013) in HadGEM3–UKCA-2010 over the south-eastern Pacific, compounded by the too-rapid scavenging of aerosol in light drizzle due to the use of a fixed scavenging timescale in that version as discussed in Section 3.3.

To investigate the impact of this, a parameterisation of aerosol release by the evaporation of large-scale precipitation has been introduced into HadGEM3–UKCA-2011, based on the approach of Bellouin et al. (2007). Rather than operating independently in each 3D model grid box, as in the existing scheme, in-cloud scavenging operates from the top down in each column. When rain is produced and aerosol is scavenged, its number and mass are passed on to the grid box below. When all the rain falling from the grid box above evaporates, the accumulated aerosol number and mass scavenged in the grid box(es) above is returned to the atmosphere; if only a fraction β of the rain evaporates, then a fraction $\frac{\beta}{2}$ of the scavenged aerosol is returned (i.e. it assumed that the loss of rain mass due to evaporation is split evenly between droplets which evaporate completely and those which shrink but remain). There is no change in the size distribution between scavenging and re-suspension, although in reality there would be a shift to larger sizes due to the coagulation of many cloud droplets to form a raindrop. The melting and sublimation of snow are not considered here, because the model does not currently include in-cloud scavenging by ice and snow.

Figure 3.11 shows the effect on the annual-mean column mass burden of each aerosol component in a one-year nudged simulation for 2009 (including the in-plume convective scavenging scheme from Section 3.4). Although globally the change is rather small (the colour scale on the absolute differences in the middle column

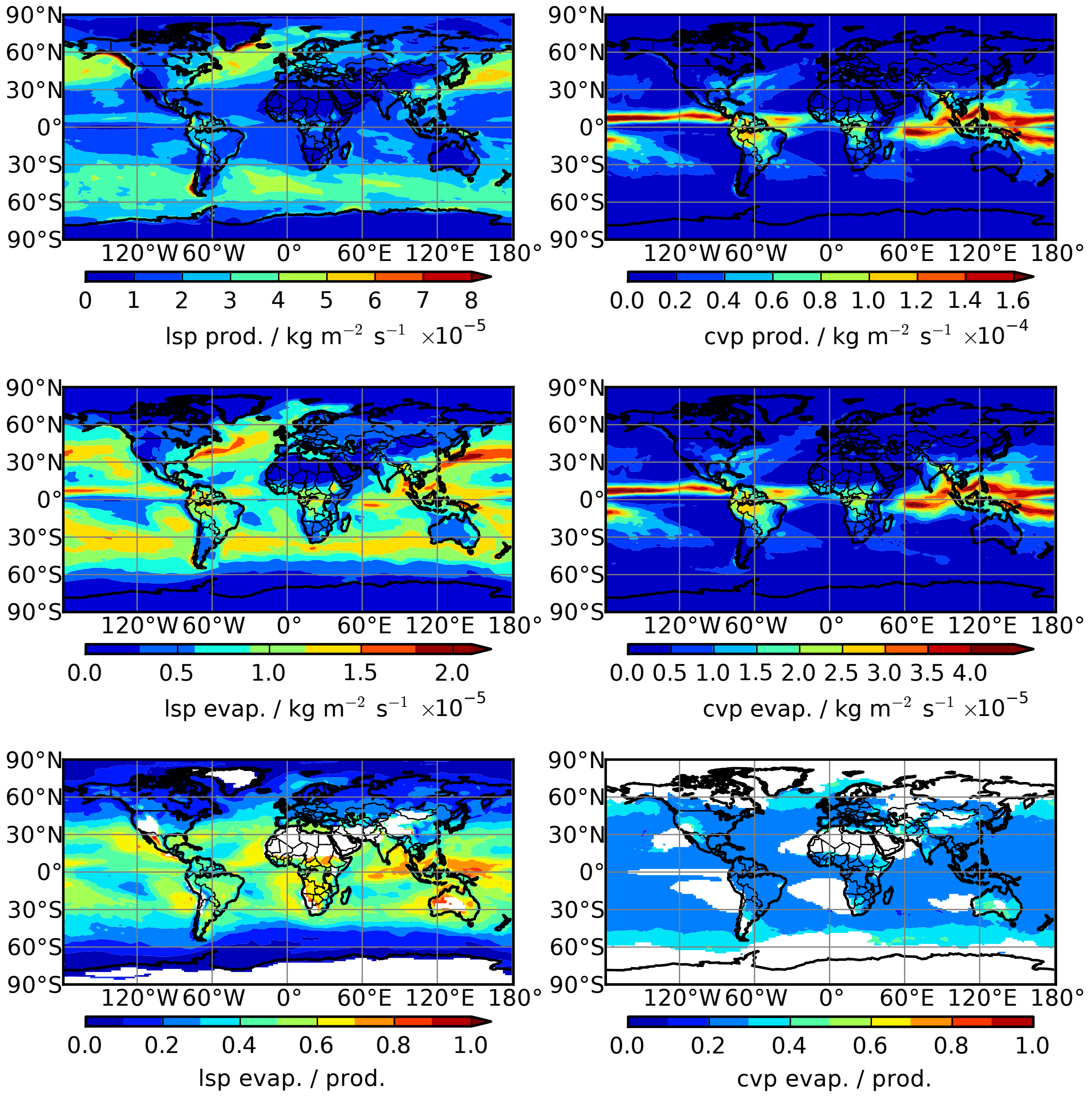

Figure 3.10: One-year mean production (top) and evaporation (middle) rates of large-scale (left) and convective (right) precipitation in HadGEM3–UKCA-2011. The bottom row shows the fraction of each type of precipitation which evaporates (excluding very dry regions with annual mean precipitation less than 5×10^{-6} kg m^{-2} s^{-1}).

extends to only ±1% of the maximum value of the scale for the burdens in the left column), there are substantial relative increases in some regions (shown in the right column). In particular, the sea-salt burden is almost doubled over the eastern edge of many of the ocean basins where persistent stratocumulus is found. There are similar, but smaller, increases for sulphate and carbonaceous aerosol; but there is no change in mineral dust, which is not subject to in-cloud scavenging in the model.

Figure 3.12 shows the effect on the number burden in each of the UKCA aerosol modes. It is clear that particle numbers are increased due to re-evaporation (and not just the mass per particle), and that the increase is concentrated in the soluble accumulation and coarse modes. This is as expected, since these are the modes which are depleted by the in-cloud scavenging scheme, and hence replenished by subsequent re-evaporation; effects on other modes must be caused indirectly by interactions between modes.

Figure 3.13 shows the zonal-mean vertical profile of the changes due to re-evaporation. For all components, most of the increase occurs in the lowest 2 km of the atmosphere, from where the particles are likely to find their way back into cloud-forming updraughts to be re-activated as CCN – which means they are likely to be of importance for aerosol indirect effects.

The effect of re-evaporation on year-2009 mean 550 nm AOD is shown in Figure 3.14, against that from Terra–MODIS as in Section 3.3. This time the negative bias is slightly reduced, as re-evaporation increases the amount of aerosol in the model (simulated global-mean AOD 0.069, compared to 0.057 without re-evaporation, and 0.168 from MODIS). Figure 3.15 shows a linear regression of log(daily-mean AOD) from both simulations against that from MODIS. There is a slight decrease in correlation when re-evaporation is included ($r^2 = 0.307$ compared to 0.317). It is thus not possible to conclude that re-evaporation improves the simulated AOD on the global scale. However, the most significant effects are likely to be localised at low

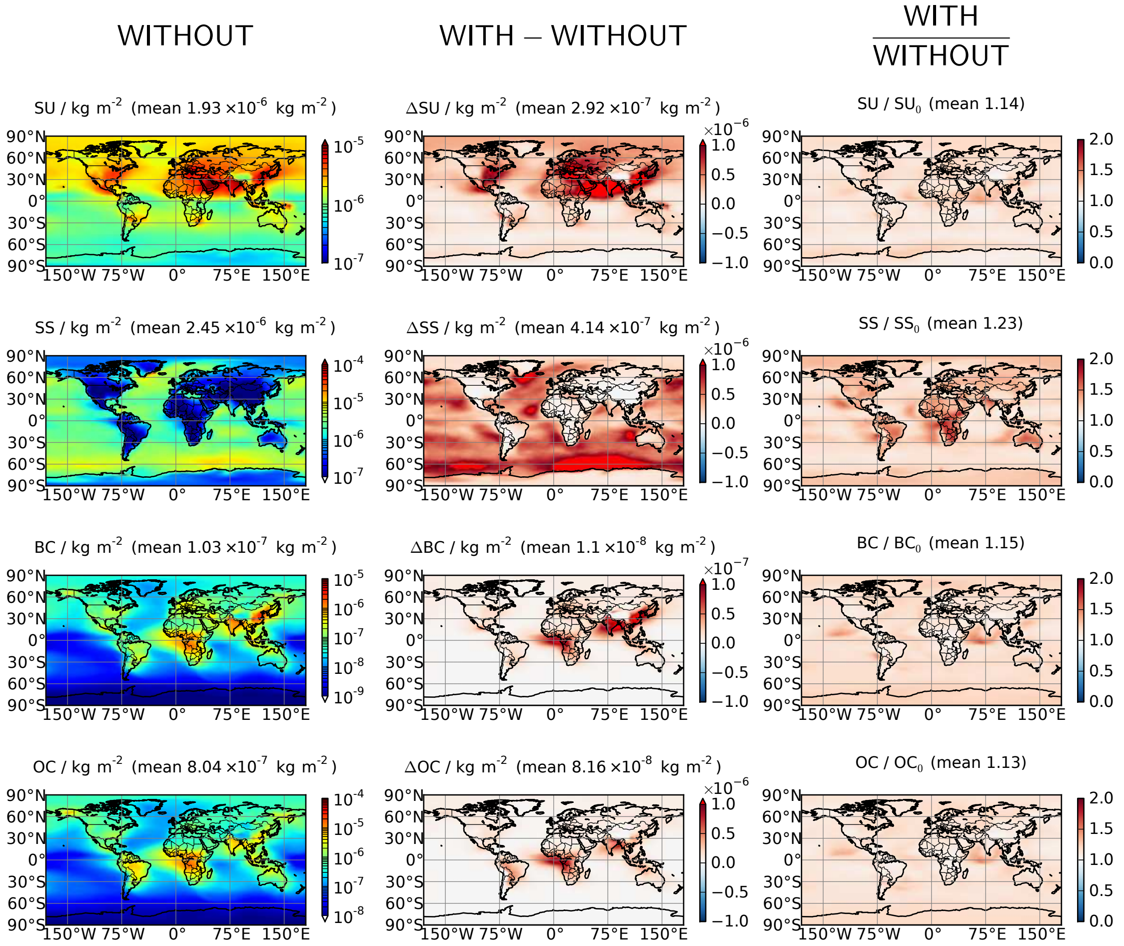

Figure 3.11: Annual mean 2009 mass burden of each aerosol component simulated by HadGEM3–UKCA-2011 (including the in-plume convective scavenging of Section 3.4) without aerosol release by re-evaporation of precipitation (left), and the change when this is included for in-cloud nucleation scavenging by large-scale precipitation – expressed as an absolute difference (middle), and in relative form as (burden with)/(burden without) such that 1.0 means no difference (right). (SU=sulphate; SS=sea-salt; BC=black carbon; OC=organic carbon; mineral dust is omitted because it is unchanged.)

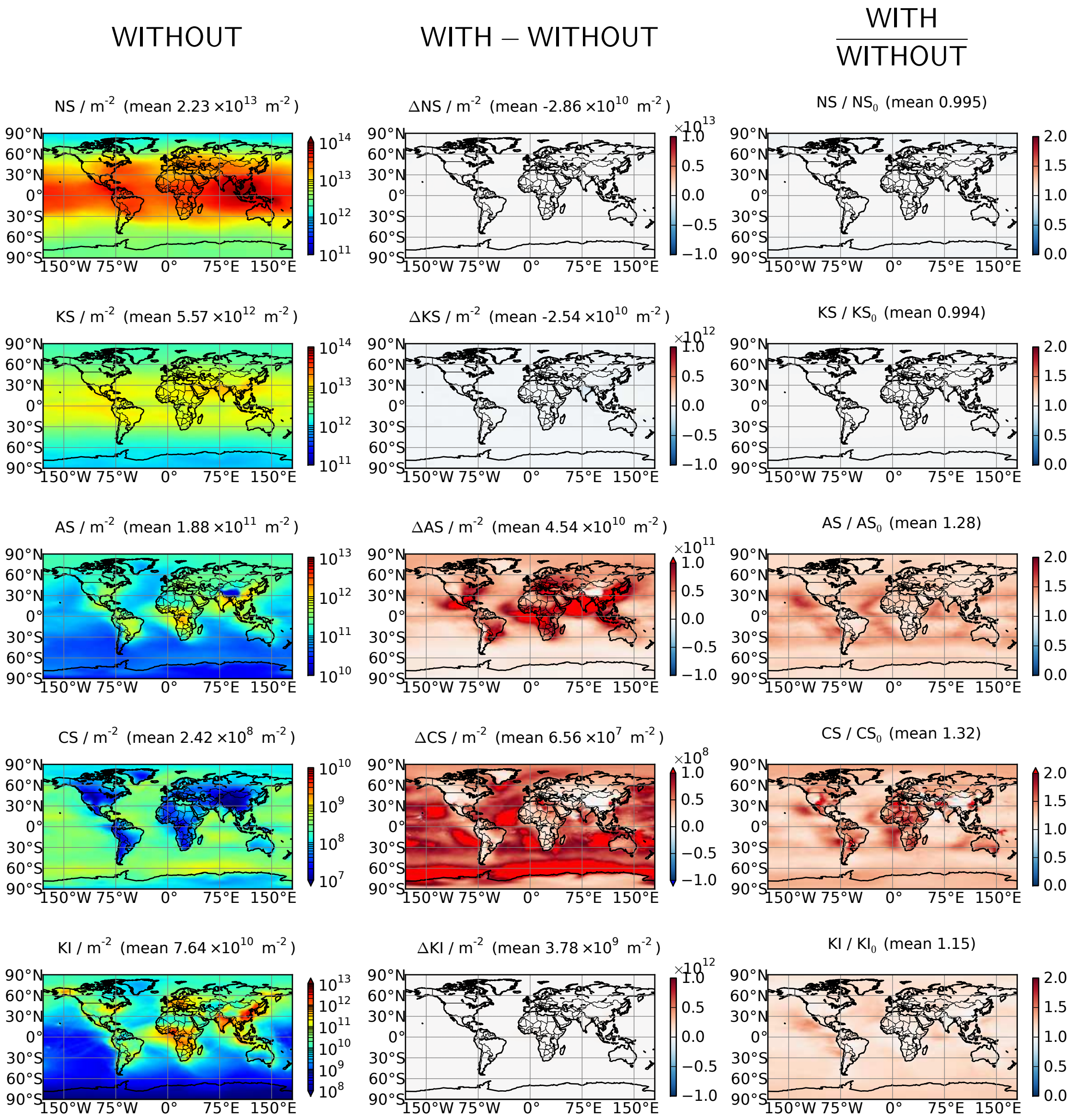

Figure 3.12: Annual mean 2009 number burden of each aerosol mode as simulated by HadGEM3–UKCA-2011 (including the in-plume convective scavenging of Section 3.4) without aerosol release by re-evaporation of precipitation (left), and the change when this is included for in-cloud nucleation scavenging by large-scale precipitation – expressed as an absolute difference (middle), and in relative form as (burden with)/(burden without) such that 1.0 means no difference (right). (NS=soluble nucleation mode; KS=soluble Aitken mode; AS=soluble accumulation mode; CS=soluble coarse mode; KI=insoluble Aitken mode. Mineral dust particles are not included in these modes, and are not shown because they are unchanged.)

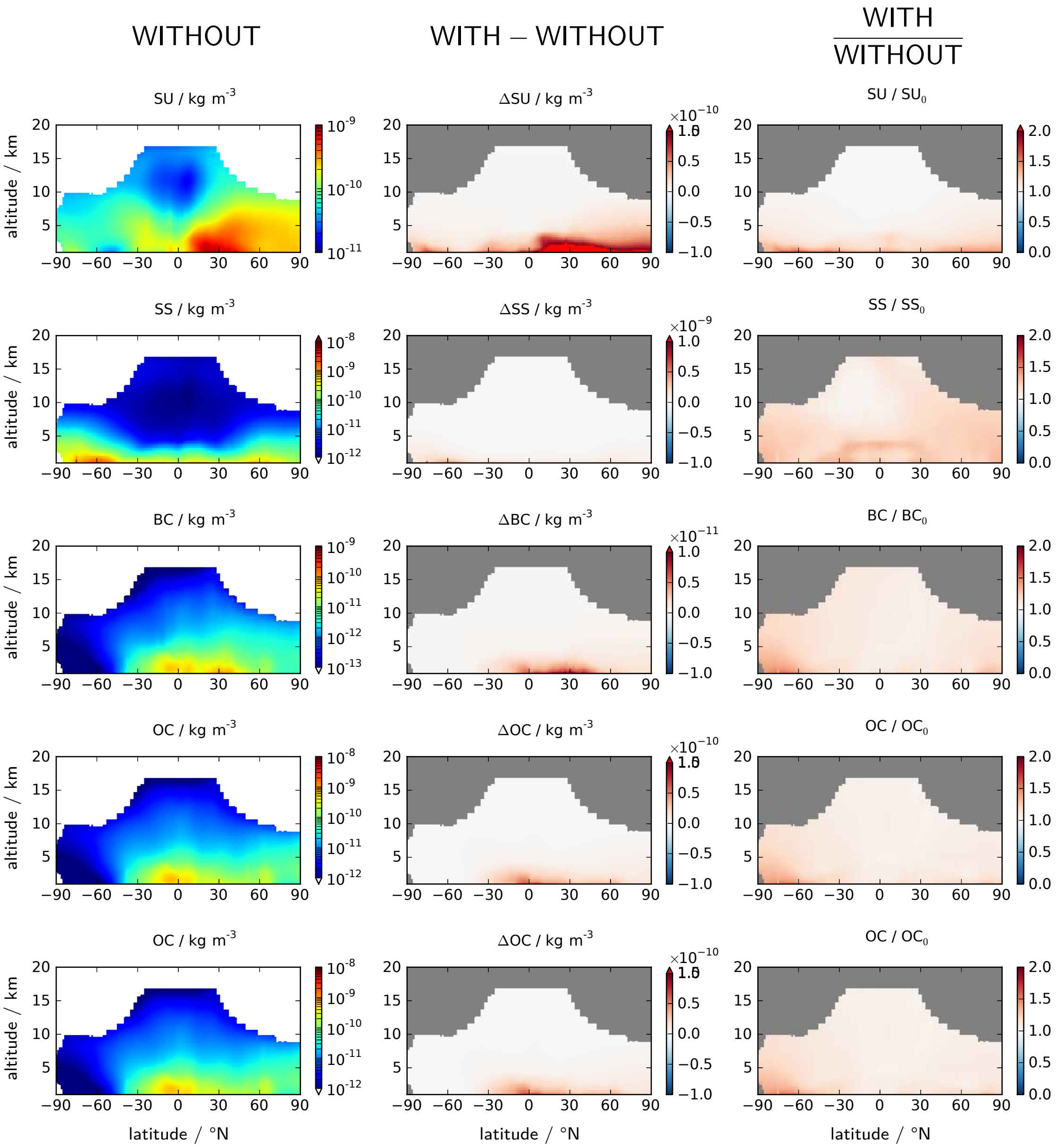

Figure 3.13: Annual and zonal mean 2009 mass concentration profile (up to the mean tropopause height) of each aerosol component simulated by HadGEM3–UKCA-2011 (including the in-plume convective scavenging of Section 3.4) without aerosol release by re-evaporation of precipitation (left), and the change when this is included for in-cloud nucleation scavenging by large-scale precipitation – expressed as an absolute difference (middle), and in relative form as (burden with)/(burden without) such that 1.0 means no difference (right). (SU=sulphate; SS=sea-salt; BC=black carbon; OC=organic carbon; mineral dust is omitted because it is unchanged.)

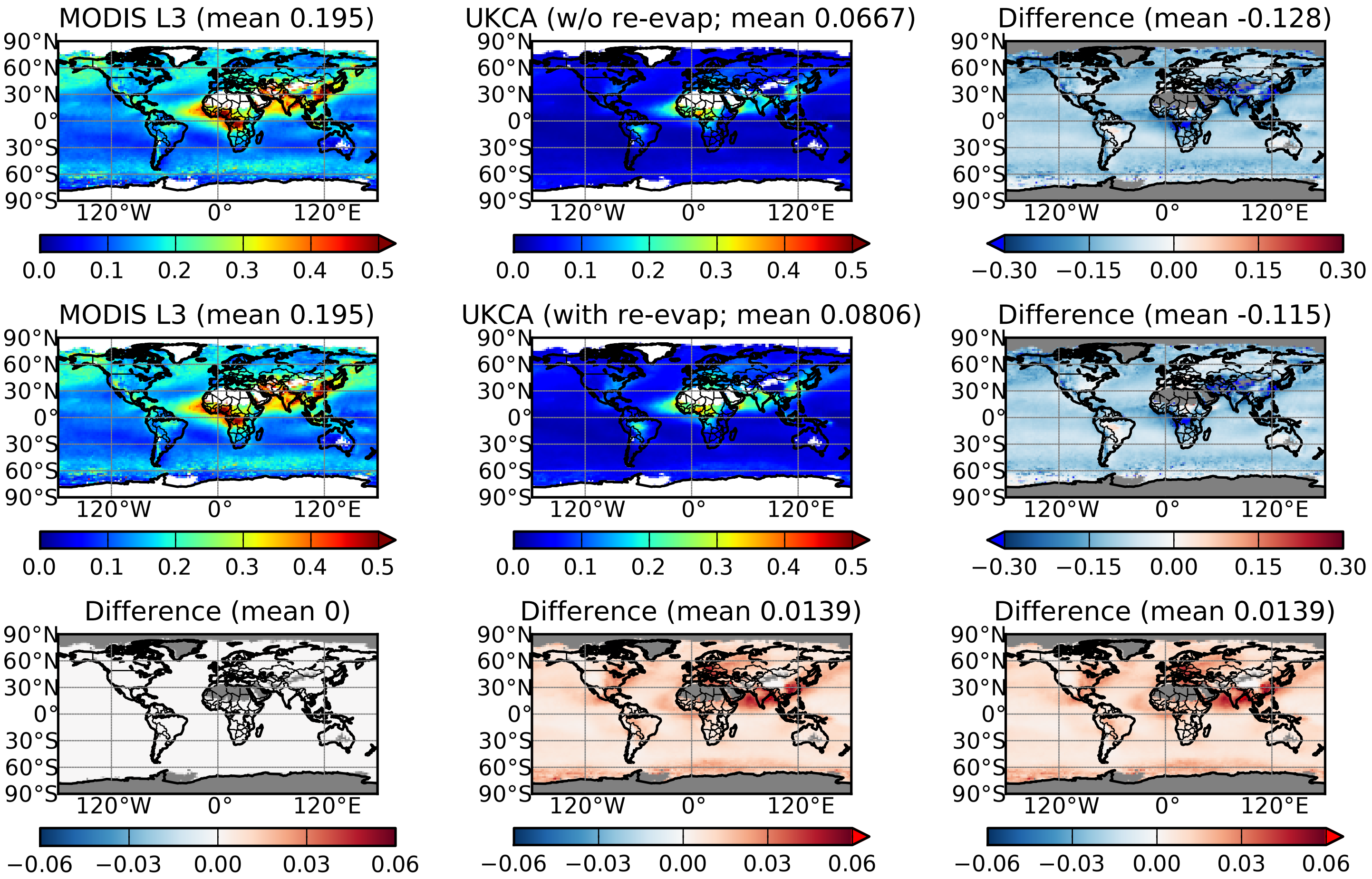

Figure 3.14: One-year mean aerosol optical depth from Terra–MODIS (left: level 3, collection 5 for the year 2009) and HadGEM3–UKCA-2011 (centre: including the in-plume convective scavenging of Section 3.4, nudged to ERA-40 for the same year, and collocated with the daily MODIS dataset), and the difference between them (right: model minus satellite). The top row is without aerosol release by re-evaporation of precipitation, the middle row is with this included as described in the text, and the bottom row shows the difference between these two cases (middle row minus top).

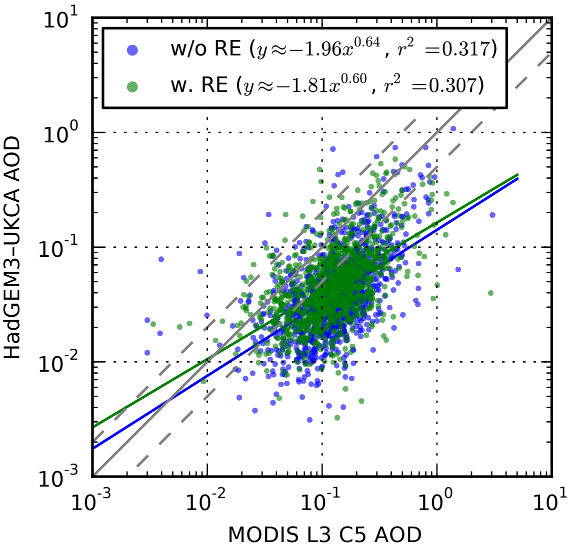

Figure 3.15: Scatter plot and linear regression of annual-mean AOD (left) and log-AOD (right) from HadGEM3–UKCA-2011 (including the in-plume convective scavenging of Section 3.4), with and without inclusion of aerosol release by re-evaporation of precipitation as described in the text, against that from Terra–MODIS (collection 5, level 3), over the model grid points, for the year 2009. The scatter plot is sub-sampled to show only 5000 randomly-selected points for each simulation; however the regression statistics use the full data set. The dashed lines represent a factor of two either side of the solid grey 1:1 line.

altitude in regions of persistent drizzle as noted above, and therefore a more detailed regional evaluation might be more informative.

3.6 Summary and conclusions

This chapter has looked at some of the shortcomings of the aerosol scavenging scheme in HadGEM3–UKCA, and investigated how it might be improved to more closely represent the physical processes involved.

An approach was presented that aims for maximum consistency with the microphysics of the large-scale precipitation scheme, tracking aerosol material through the various types of hydrometeor until it is either deposited at the surface or re-released as aerosol particles by evaporation of droplets or sublimation of ice particles. However, such an approach is computationally complex and requires detailed knowledge of the hydrometeor size distribution. In the one-moment bulk mass microphysics of the HadGEM3 large-scale precipitation scheme, these size distributions are all assumed rather than explicitly simulated. Although consistency with the size distributions assumed by the precipitation scheme can be achieved, as derived in detail in Appendix A, these are still arbitrary and may negate the aim of greater physical realism.

As an alternative, it was shown how improvements may be made within the existing scavenging framework through three main approaches. Firstly, the fixed rainout timescale was replaced with a first-order loss rate proportional to the rate at which cloud water is converted to rain in the large-scale precipitation scheme. This caused a decrease in global aerosol burdens and AOD, which resulted in a larger bias compared to MODIS: the simulated MODIS-collocated year-2000 global mean 550 nm AOD decreased from 0.128 to 0.118, compared to 0.159 for MODIS. However, the correlation (r^2) between the MODIS and model log(daily-mean AOD) fields increased from 0.294 to 0.309, suggesting that the process representation was better although compensating errors were unmasked – although the statistical significance of this result is difficult to assess due to spatial autocorrelation in the data.

Secondly, scavenging by convective precipitation was moved into the convection scheme itself, so that scavenging and transport were no longer operator-split. This dramatically increased the efficiency of convective scavenging in the model, reduced the amount of aerosol in the larger modes reaching the upper troposphere, and thereby enhanced the nucleation of new particles. Again, although the negative AOD bias compared to MODIS was increased (simulated year-2009 AOD decreased from 0.088 to 0.057, compared to 0.168 from MODIS), the correlation between MODIS and model log(daily-mean AOD) increased from 0.289 to 0.317. These effects will be evaluated further in Chapter 4, with particular emphasis on evaluating the changes to the vertical distribution which are poorly constrained by a column-integrated measurement such as AOD, and also on establishing statistical significance.

Thirdly, the large-scale scavenging scheme was extended to account for the aerosol contained in rain which evaporates before reaching the surface. By releasing this aerosol back to the atmosphere at the point of evaporation, rather than discarding it, the number of accumulation-mode particles was increased by almost a factor of two in regions of persistent stratocumulus – where the sensitivity of the indirect aerosol effects to changes in CCN are likely to be high – although the global-scale impact on burdens and AOD is quite small. Although the version of HadGEM3 used here does not include a detailed representation of the indirect effects, it would therefore be very interesting to study the impact of re-evaporation in a version which does (e.g. as used in West et al., 2013).

The approach considered at the start of the chapter, of following the precipitation microphysics in detail, may well be worth revisiting in the context of a two-moment (or even three-moment) size-resolved cloud and precipitation microphysics scheme, such as is currently under development for future versions of the Met. Office Unified Model, where it would no longer be necessary to use assumed size distributions.

Chapter 4

Constraining black carbon burdens and vertical profiles with observations

The work described in this chapter has been published as Kipling, Z., Stier, P., Schwarz, J. P., Perring, A. E., Spackman, J. R., Mann, G. W., Johnson, C. E., and Telford, P. J.: Constraints on aerosol processes in climate models from vertically-resolved aircraft observations of black carbon, Atmos. Chem. Phys., 13, 5969–5986, doi:10.5194/acp-13-5969-2013, 2013.

The text, figures, simulations and analysis presented here are the work of Kipling, under the supervision of Stier and Johnson. Schwarz, Perring and Spackman contributed the HIPPO SP2 dataset; Mann contributed the GLOMAP-mode aerosol scheme; Telford contributed the nudging code and the basis for the HadGEM3–UKCA flight-track sampling code.

As discussed in Chapter 1, aerosol particles in the atmosphere play an important role in the climate through direct, indirect and semi-direct effects. Black carbon (BC) aerosol can contribute to all of these classes of effect, although its absorption of short-wave radiation makes it of particular interest in the context of the direct and semi-direct effects (Stier et al., 2007; Ramanathan and Carmichael, 2008). The relative magnitudes of these effects, and thus the sign of the net (semi-)direct forcing due to BC, are thought to depend heavily on the vertical distribution of BC, and in particular its altitude relative to cloud layers (Johnson et al., 2004; Zarzycki and

Bond, 2010; Samset and Myhre, 2011; Samset et al., 2013). In addition, “aged” BC particles with a soluble coating can act as cloud condensation nuclei (Penner et al., 1996; Lohmann et al., 2000), and thus contribute to indirect effects; ageing may also reduce the lifetime of black carbon (by increasing susceptibility to wet deposition) and enhance its absorption of radiation (Ackerman and Toon, 1981; Stier et al., 2006; Schwarz et al., 2008).

Some progress has been made in analysing the relative positions of BC and cloud layers, and the resulting radiative effects, from satellite observations (Peters et al., 2011; Wilcox, 2012). However, neither passive satellite remote sensing nor ground-based observations can provide well-resolved vertical profiles of BC (or aerosol in general), and thus the evaluation in this chapter focuses on in-situ aircraft observations. Although such observations are limited in spatial and temporal coverage, they can provide data with much better vertical resolution than can be obtained from other sources, as well as more direct measurements of the quantities (e.g. concentrations, mixing ratios, composition and particle size distributions) represented in aerosol models. (While satellite-based LIDAR instruments such as CALIOP can provide vertically-resolved optical extinction profiles, and these are valuable in assessing the vertical distribution on a global basis, such optical measurements do not translate directly into the number and mass mixing ratios simulated by current models.)

Previous studies using aircraft observations to evaluate aerosol models on a global scale have generally compared monthly-mean model profiles with campaign-mean profiles from a collection of separate campaigns (which may differ in their methodology), each over a limited geographical area (e.g. Koch et al., 2009). Other studies have focused on more detailed evaluation on a regional scale using individual flight campaigns – e.g. Reddington et al. (2013), which also highlights the importance of uncertainties in the size distribution of BC as well as its total mass.

The large-scale flight campaign conducted by the High-performance Instrumented Airborne Platform for Environmental Research (HIAPER) Pole-to-Pole Observations (HIPPO) of Carbon Cycle and Greenhouse Gases Study (Wofsy et al., 2011) provides the opportunity to evaluate against consistently-collected data from a single campaign over a large area of the Pacific region. The data are described in more detail in Section 4.1. The BC data from the first phase of the HIPPO campaign are analysed in Schwarz et al. (2010), where the observed vertical profiles are used to evaluate the simulated BC profiles from the Aerosol Comparisons between Observations and Models (AeroCom; `http://aerocom.met.no/`) Phase I (Textor et al., 2006) models, comparing climatological monthly-mean model profiles against regional-mean profiles from HIPPO. The model diversity is large – one to two orders of magnitude over a wide altitude range, both in the Pacific regions studied in Schwarz et al. (2010) and the continental regions in Koch et al. (2009) – but both the mean and median of the model ensemble systematically overestimate the BC mass mixing ratio (MMR) compared to the observations.

This chapter presents a more detailed evaluation of the vertical distribution of BC in two particular models, HadGEM3–UKCA and ECHAM5–HAM2, against BC mass mixing ratio data derived from the first three phases of the HIPPO campaign. Rather than averaging the instantaneous observations on a regional basis and comparing to model climatology, nudging and interpolation techniques are used to sample the models in time and space along the track of the flight campaign, as described in Section 4.2.

This approach is applied to investigate and constrain the effects of convective scavenging (which has an important role in controlling vertical transport, as shown in Section 3.4) and biomass-burning emissions (which are the most temporally and spatially variable source of BC) on the vertical profile of BC in the models. To this end, a series of sensitivity tests are conducted, as described in Section 4.4, to assess how the agreement with the observations is affected by the choice of convective scavenging scheme and emissions inventory.

4.1 Observational data

There have been five phases of the HIPPO campaign completed (`http://hippo.ucar.edu/`); data from the first three (in January 2009, October/November 2009 and March/April 2010) were available in time for this analysis. Each phase consists of an approximate meridional transect over the Pacific, with detours into neighbouring continental regions – the flight tracks can be seen in Figure 4.1. Along each track, a series of fairly regular ascents and descents were made, providing vertically-resolved measurements, typically spanning 300 m above the surface to 8.5 km above sea level with some profiles extending to $\sim 14\,\mathrm{km}$. In total, 184 suitable vertical profiles are identified (the criteria used are discussed in Section 4.3.1).

A wide range of instruments were carried on these flights, but for the purposes of this analysis the most relevant data comes from a Single Particle Soot Photometer (SP2; Schwarz et al., 2006), which measures the mass of BC in individual aerosol particles. Particles were detected within a range of ~ 0.8 to 175 fg BC (~ 75 to 540 nm volume-equivalent diameter, assuming a void-free density of $1.8 \times 10^3\,\mathrm{kg\,m^{-3}}$).

Following Schwarz et al. (2010), the MMR of BC in the atmosphere is calculated by aggregating the observed particles over 1-minute intervals:

$$m_{\mathrm{BC}} = 1.1 \frac{F}{\rho_{\mathrm{air}}} \sum_{i=1}^{N} M_i, \tag{4.1}$$

where $(M_1, \ldots, M_N)$ are the masses of BC in each individual particle observed by the SP2 instrument, F is the volumetric flow rate at which the air is sampled ($4\,\mathrm{cm}^3\,\mathrm{s}^{-1}$, constant) and ρ_{air} is the density of the sampled air, derived from contemporaneous measurements of ambient pressure from the HIPPO flight data, and a fixed tem-

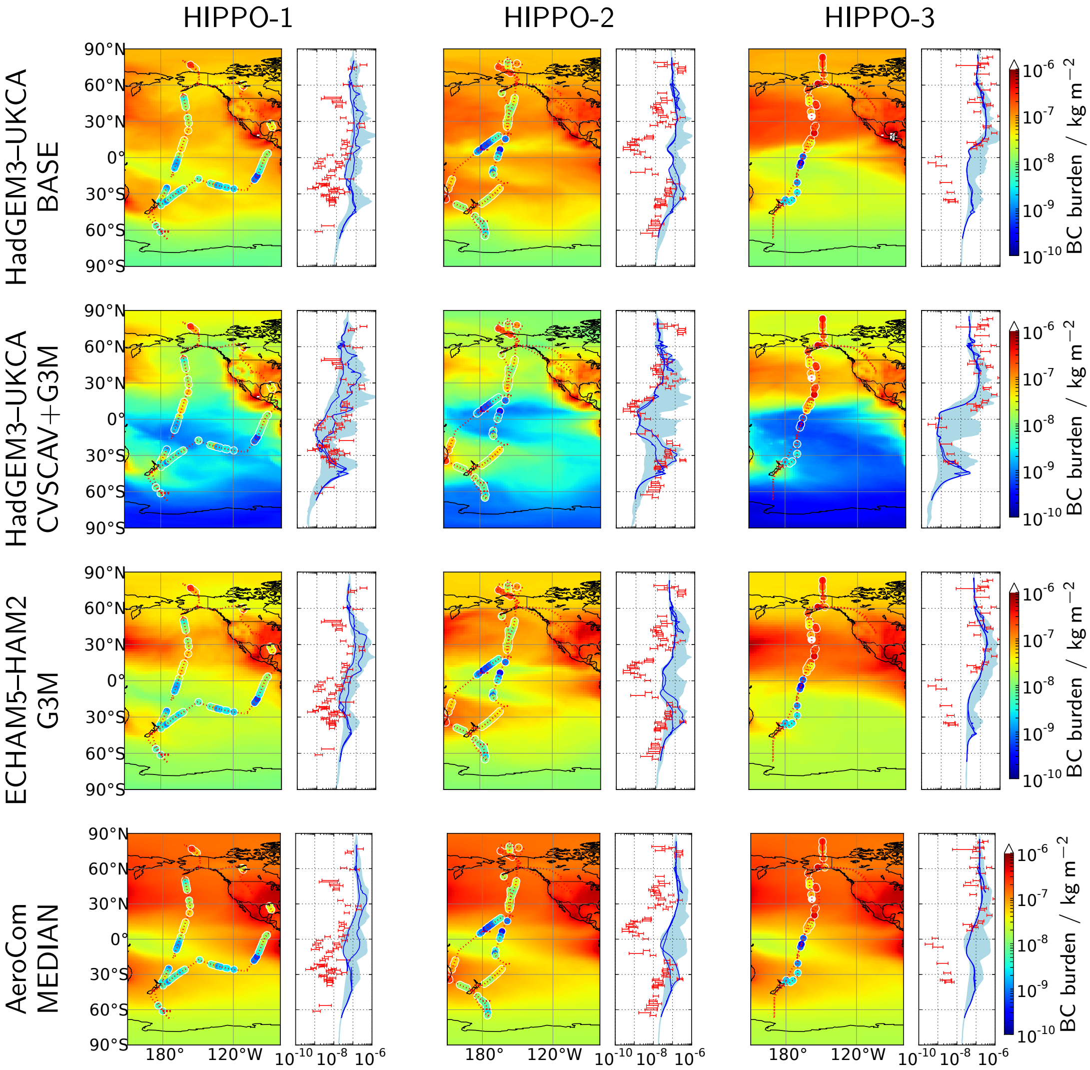

Figure 4.1: Flight tracks for the first three phases of the HIPPO campaign (January 2009, October/November 2009 and March/April 2010). The circles show the BC burden (in kg m^{-2}) estimated from the HIPPO SP2 observations over each vertical profile, while the background shading shows the monthly-mean BC burden from the HadGEM3–UKCA (BASE and CVSCAV+G3M) and ECHAM5–HAM2 (G3M) simulations. The bottom row shows the burdens from the AeroCom Phase I (Textor et al., 2006) median model (constructed from the ARQM, GISS, GOCART, GRANTOUR, KYU, LOA, MATCH, MPI_HAM, MOZGN, PNNL, UIO_CTM, UIO_GCM, ULAQ and UMI models). The side plots show the observed burdens (red bars, representing the range due to uncertainty in extrapolation of profiles to the surface and a 15 km lid, plus the 30% uncertainty in the mixing ratios used), the along-track model burden (blue line, two-valued due to the southbound and northbound legs) and the zonal range of the model burden between the map edges (shading).

perature of 290 K representing the cabin air temperature of the aircraft. These are an approximation of the actual sampling conditions, but the resulting error is small compared to that from other sources (J. P. Schwarz, pers. comm.) The factor of 1.1 inflates the mass by 10% to account for the portion of the aerosol size spectrum which the instrument does not detect, as per Schwarz et al. (2010). A “curtain” plot of BC MMR against latitude and altitude is then produced to show the distribution of BC over a vertical slice through the atmosphere (top row of Figure 4.2). An uncertainty of ±30% is attached to these MMR values, as the ±40% quoted in Schwarz et al. is now considered overly cautious (J. P. Schwarz, pers. comm.) In the cleanest regions (BC MMR less than $\sim 0.5\,\mathrm{ng\,kg^{-1}}$), where only a small number of particles were detected per minute, the sampling uncertainty of the observations is likely to contribute significantly to the scatter in the results (A. E. Perring, pers. comm.); however this is not considered further in the present study.

With the exception of HIPPO-2, which made a detour to Australia at about 30°S, there is generally more BC seen in the northern hemisphere than the southern hemisphere at all levels (which is consistent with the greater anthropogenic emissions in the north) – this contrast is particularly stark for HIPPO-3, which spent very little time near land. While some BC is seen in the lower and mid tropical troposphere ($\sim 10^{-11}\,\mathrm{kg\,kg^{-1}}$ in places), very little is seen at higher levels in the tropics in any of the phases (typically less than $10^{-12}\,\mathrm{kg\,kg^{-1}}$ above about 6 km); at higher latitudes, however, significant BC mass mixing ratios (above $10^{-11}\,\mathrm{kg\,kg^{-1}}$) frequently extend into the upper troposphere.

4.2 Models

Two aerosol–climate models are considered here: HadGEM3–UKCA-2011 and ECHAM5–HAM2. These are described in Section 1.6, and the major differences relevant to black carbon aerosol are summarised in Table 4.1.

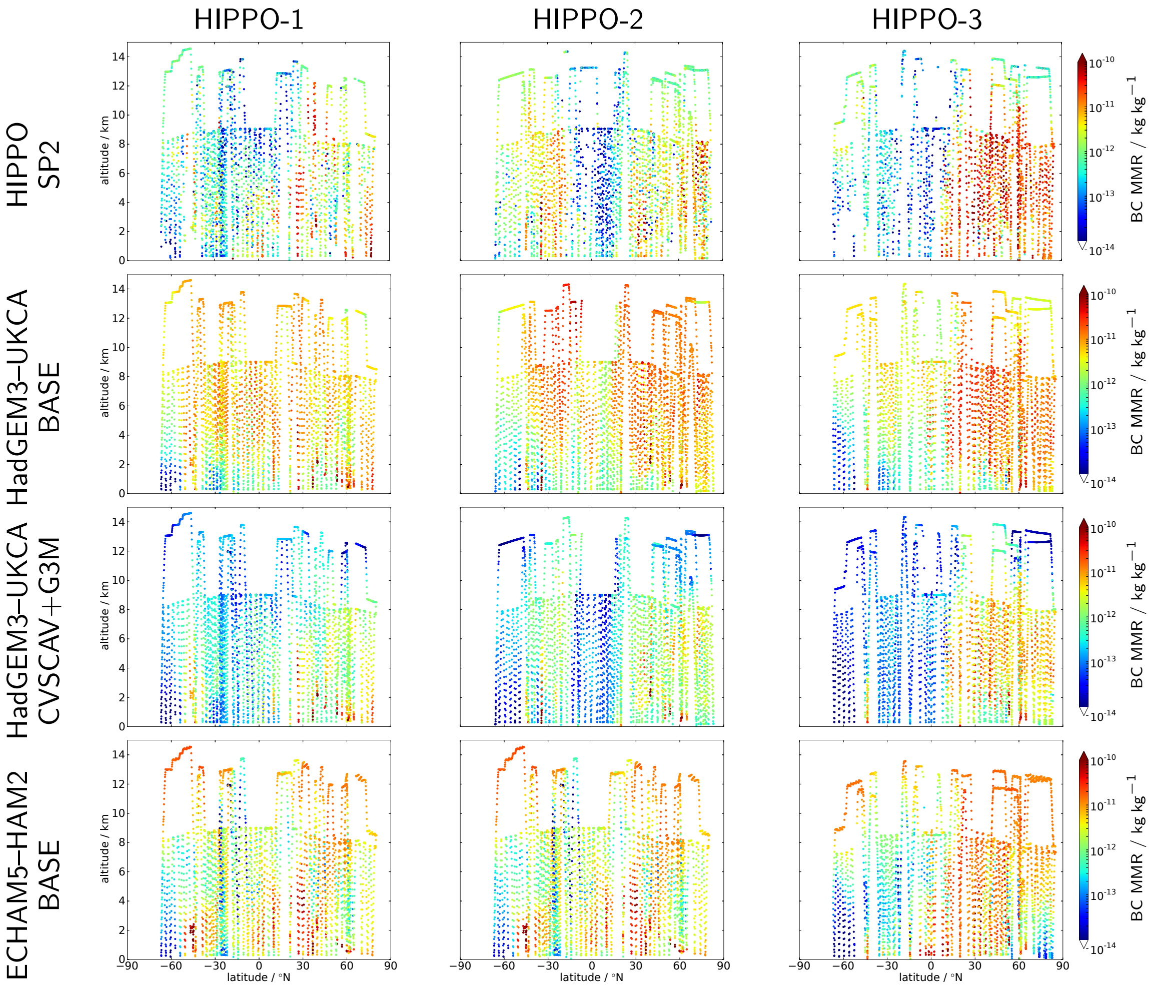

Figure 4.2: Mass mixing ratio (kg kg^{-1}) of BC in the atmosphere, from each phase of the HIPPO campaign, calculated by aggregating SP2 data over 1-minute intervals, and from nudged HadGEM3–UKCA (BASE and CVSCAV) and ECHAM5–HAM2 (BASE) simulations, sampled along the HIPPO flight track (also at 1-minute intervals)

Table 4.1: Differences relevant to black carbon between the aerosol schemes in HadGEM3–UKCA-2011 and ECHAM5–HAM2, in their BASE configurations

Process	HadGEM3–UKCA	ECHAM5–HAM2
Biofuel emission size	same as fossil fuel (60 nm diameter)	same as biomass-burning (150 nm diameter)
Fossil fuel and biofuel emissions	added to lowest level	applied as surface flux in vertical diffusion
Biomass-burning emission height	uniform in height over $\sim$ 50 m to 3 km	biome-dependent (Dentener et al., 2006)
Ageing insoluble to soluble	10 monolayers required	1 monolayer required
Dry deposition	Slinn (1982) Zhang et al. (2001) operator-split	Ganzeveld et al. (1998) as surface flux in vertical diffusion
Below-cloud scavenging	Slinn (1984)	Seinfeld and Pandis (1998)
In-cloud nucleation scavenging	100% of soluble accumulation and coarse modes Rain only Immediate removal	Prescribed fractions of all modes Rain and snow Replaced where precipitation evaporates
Convective scavenging	Operator-split, acting on grid-box means	In-plume, acting on tracer fluxes
Aerosol feedbacks on meteorology (direct/semi-direct/indirect effects)	Disabled	Enabled

For the sensitivity tests (described in more detail in Section 4.4), four HadGEM3–UKCA and three ECHAM5–HAM2 simulations were carried out covering the period of the first three phases of the HIPPO campaign, as shown in Table 4.2. All simulations were run from September 2008 through to the end of April 2010, allowing four months spin-up before the start of HIPPO-1. No re-tuning of the model was performed for any of the simulations.

4.2.1 Nudging

In order to capture the meteorological conditions at the time of the flight campaign, the technique of nudging (Jeuken et al., 1996) is used, where the large-scale dynamical variables are continuously relaxed towards fields from a reanalysis product – in this case ERA-Interim (Dee et al., 2011).

In the HadGEM3–UKCA implementation (Telford et al., 2008, 2013), the nudging is applied to the potential temperature and horizontal wind fields. The relaxation time constant is the "natural" one of 6 h (the time spacing of the reanalysis data); this choice is validated in Telford et al. (2008). The nudging is applied between levels 14 (~ 4 km) and 32 (~ 21 km) inclusive; levels 13 and 33 are nudged at half strength (i.e. with a 12 h time constant), and no nudging is performed on levels outside this range. Free-running simulations (without nudging) were also run for comparison.

In the ECHAM5–HAM2 implementation (Jeuken et al., 1996), temperature, vorticity, divergence and surface log-pressure are relaxed towards the 6-hourly reanalysis fields with time constants of 24 h, 6 h, 48 h and 24 h, respectively, on all model levels. The nudging is performed in spectral space, on all but the wavenumber-0 (global-mean) spectral component.

Although neither water vapour nor any cloud variables are nudged directly, Telford et al. (2008) show that large-scale cloud and precipitation patterns are reproduced well in a nudged model, while Russo et al. (2011) show that for convection a nudged

Table 4.2: Configurations and emissions used for model simulations of the HIPPO campaign. The inventory (GFED2 or GFED3.1) used for biomass-burning emissions is shown, along with the year for which these emissions are specified. Other emissions are taken from the AeroCom Hindcast inventory, or (for additional gas phase emissions in UKCA) RCP 8.5.

Model	Label	Description	Biomass-burning emissions
HadGEM3–UKCA	BASE	Basic configuration, with only diagnostic modifications for flight-track sampling.	GFED2 1997–2006 clim. (monthly)
	G3M	As BASE, but with GFED3.1 monthly biomass emissions.	GFED3.1 2008–2010 (monthly)
	CVSCAV	As BASE, but with in-plume convective scavenging scheme added, as described in the text.	GFED2 1997–2006 clim. (monthly)
	CVSCAV+G3M	Combining both in-plume convective scavenging (CVSCAV) and GFED3.1 emissions (G3M).	GFED3.1 2008–2010 (monthly)
ECHAM5–HAM2	BASE	Basic configuration, with only diagnostic modifications for flight-track sampling.	GFED2 1997–2006 clim. (monthly)
	G3M	As BASE, but with GFED3.1 monthly biomass emissions using modified vertical distribution.	GFED3.1 2008–2010 (monthly)
	G3H	As BASE, but with GFED3.1 3-hourly biomass emissions using modified vertical distribution.	GFED3.1 2008–2010 (3-hourly)

model performs as well as an offline chemical transport model (CTM) driven directly by meteorological fields from a reanalysis.

4.2.2 Flight-track sampling

Nudging allows simulations to be conducted under large-scale meteorological conditions which reflect those during the flight campaign. To sample from the resulting simulation in a manner consistent with the observations, an interpolating "flight-track sampling" diagnostics scheme is used. Following O'Connor et al. (2005), the instantaneous mass mixing ratio fields at each timestep are interpolated to the point in space and time of each observation along the flight track. The spatial interpolation is linear in log-pressure and both horizontal directions; temporally, each observation is matched to the following model timestep.

The implementation in HadGEM3–UKCA is based on that of Telford et al. (2013), extended to sample the tracers from the aerosol scheme as well as the gas-phase chemistry scheme; an equivalent sampling module has also been implemented in ECHAM5–HAM2.

4.3 Method

As mentioned earlier, to best compare the simulations with the aircraft measurements from the HIPPO campaign, the model output is sampled along the flight track. However, to give a general indication of how the models' BC distributions compare to the observations, regional maps of the simulated BC column burden are shown, with that derived from the SP2 measurements over-plotted along the flight track (Figure 4.1).

4.3.1 Burdens

From a modelling perspective, column-integrated mass burdens are a useful metric by which to measure the distribution of aerosol. However, it is difficult to obtain direct measurements of aerosol burden on large scales, as satellite-based instruments can only measure integrated optical properties (with passive instruments) or vertically-resolved backscatter (with active LIDAR). Burdens cannot be inferred from such measurements without additional knowledge of the chemical and microphysical properties of the aerosol particles. Ground-based sun-photometers and LIDAR are similarly limited, while ground-based in-situ measurements are limited to particles near the surface. The geographical and vertical coverage of the HIPPO campaign, however, provides a basis on which to evaluate model burdens directly.

The local BC column burden is estimated in the vicinity of each HIPPO ascent or descent profile. Suitable profiles are identified as periods of near-continuous ascent or descent covering at least the 0.5 km to 7.5 km altitude range. From each profile, the mean BC concentration (mass of BC per unit volume) in each 0.5 km altitude interval from 0 to 15 km is calculated. These are then integrated vertically to give an estimate of the column burden (shown on the maps in Figure 4.1 as coloured circles).

Because the HIPPO profiles do not extend all the way to the surface or the 15 km "lid", there is some uncertainty in how the profile should be extrapolated when calculating the burden. A lower estimate is calculated by assuming the BC concentration is zero outside the altitude range of the observations; for an upper estimate, the BC concentrations observed at the bottom and top of the profile are assumed to continue to the surface and 15 km respectively. (This does not give a true upper bound on the burden, since the concentrations outside the observed altitude range may be higher then those within, but provides an estimate of the extrapolation uncertainty.) Because Schwarz et al. (2010) attribute the largest part of the ±30% uncertainty in BC MMR to calibration (correlated) rather than random (uncorrelated) error, it is assumed that the full ±30% may apply to the derived burden estimates. These ranges (including both the extrapolation and measurement uncertainty) are shown as the red bars on the side-plots in Figure 4.1.

4.3.2 Point-by-point comparison

For a more detailed point-by-point comparison, the model fields are interpolated onto the HIPPO flight track as described in Section 4.2.2. Coupled with nudging to reproduce the observed synoptic conditions as described in Section 4.2.1 (notwithstanding the uncertainty in reanalysis fields in remote regions with sparse observations), this allows the model output to be sampled consistently with the observations rather than using a monthly mean or climatology. Once this sampling has been done, the model output can be evaluated pointwise against the actual HIPPO observations both visually and quantitatively. For a visual comparison the difference in MMR is simply plotted at each point along the flight track (see Figures 4.3 and 4.4, discussed in detail in Sections 4.5.1 and 4.5.2). A more quantitative analysis looks at the mean difference (bias) and correlation coefficient between the logarithms of the observed and simulated mass mixing ratios, over all the points along the flight track (see Figure 4.5, discussed in detail in Section 4.5.3). Logarithms are taken as the distribution of observed mixing ratios appears to be approximately log-normal; this results in a distribution which is more symmetric and closer to a normal distribution, making standard statistical techniques more meaningful. Without logarithms, the correlation coefficient is distorted by differences in the long upper tail of the distribution.

To estimate the uncertainty in the quantitative analysis, bootstrapping is used to construct 95% confidence intervals for the bias and correlation. Because both the observed and modelled data series show significant autocorrelation, a moving-block bootstrap (Kunsch, 1989) is used with block length 30 (i.e. resampling in approximately half-hour blocks). This provides an estimate of the uncertainty due to random sampling variability. To incorporate the uncertainty in the SP2-derived mixing ratios, the error bars on the bias are extended by ±30% (to accommodate the worst-case effect on the bias, of a systematic calibration error). For the correlation, random multiplicative Gaussian white noise with a standard deviation of 30% is applied to each bootstrap sample (to accommodate the worst-case effect on the correlation, of completely uncorrelated observation errors).

There is some additional uncertainty in the comparison, due to the limited size range of the SP2 measurements – the measurements are adjusted as described in Section 4.1 to account for this, but some uncertainty remains as in practice the fraction of BC which is within the detectable range will be variable. An alternative approach, of calculating the number of modelled particles which would contain a detectable amount of BC, is problematic because the models assume uniform composition, with BC mass spread over all particles in a given mode. This results in lower BC masses per particle, and many fewer detectable particles, than if the BC is confined to a subset of particles – which Reddington et al. (2013) show may indeed be the case, at least in the more polluted air over continental Europe.

4.4 Sensitivity tests

4.4.1 Biomass-burning emissions

One of the most variable and uncertain sources of BC is from biomass burning (responsible for approximately half the BC emissions by mass in the models, the remainder coming from fossil fuel and biofuel burning). The emissions used in the BASE configurations of both models are a monthly climatology derived from the AeroCom hindcast inventory, itself based on the Global Fire Emissions Database (GFED), version 2 (van der Werf et al., 2006). However, GFED version 3.1 is now available (van der Werf et al., 2010). Amongst various improvements to the emission estimates, there is a substantial reduction in total carbon emissions from biomass burning, which is reflected in the BC emissions. In addition, GFED3.1 provides daily fractional emission fields (at the same 0.5° resolution as the monthly data, but not resolved by chemical species) which can be applied to each month's data to estimate emissions at daily time resolution, and a diurnal profile for each month (also at 0.5° resolution, in 3-hour intervals), giving estimates at 3-hourly time resolution (Mu et al., 2011). The new dataset now covers the period to the end of 2010, sufficient for simulations during the first three phases of the HIPPO campaign and removing the need to extrapolate the emission dataset. Switching to GFED3.1 emissions for biomass burning gives the G3M (monthly emissions) and G3H (3-hourly emissions) configurations (the latter only implemented in ECHAM5–HAM2).

In HadGEM3–UKCA, both BASE and G3M configurations distribute the biomass-burning emissions uniformly in height over levels 2 to 12 ($\sim$ 50 m to 3 km). In ECHAM5–HAM2, the BASE configuration uses a biome-dependent vertical profile for the emissions, as in AeroCom Phase I (Dentener et al., 2006), while the G3M and G3H configurations divide the emissions equally between the model levels diagnosed to be within the boundary layer.

4.4.2 Convective scavenging

As discussed in Section 3.4, convection is of great importance for both the vertical transport and removal of aerosol. Schwarz et al. (2010) identify the treatment of this process as likely to be a major factor in the diversity of the AeroCom models and their high bias compared to the HIPPO-1 SP2 observations, particularly in the tropics.

The models used here take two different approaches to convective scavenging. In the operator-split approach, as used in the BASE configuration of HadGEM3–UKCA, convective scavenging removes aerosol from the grid-box mean field after the convection scheme (including convective tracer transport) has run. In the in-plume approach, as used in ECHAM5–HAM2, aerosol is removed directly from the tracer flux in the convective updraught, along with the removal of water by convective precipitation. Additional simulations with HadGEM3–UKCA have also been carried out using the in-plume scheme described in Section 3.4 (CVSCAV and CVSCAV+G3M configurations).

Although this chapter focuses on the impact of the coupling between convective transport and wet deposition, it is worth noting that the parameterisation of convective transport itself (in particular entrainment and detrainment) may have a significant impact on the vertical distribution of tracers, as demonstrated in Hoyle et al. (2011) and Croft et al. (2012).

4.5 Results

4.5.1 HadGEM3–UKCA

The BC MMR from HadGEM3–UKCA (in its BASE configuration), sampled at 1-minute intervals along the flight track for the first three phases of the HIPPO campaign, is shown in the second row of Figure 4.2. Although some features (e.g. the disparity between the hemispheres in the HIPPO-3 data) are well reproduced, the model does not appear to reproduce other large-scale features of the observations very well. Most noticeably, for all three phases, the model has a significant excess of BC in the upper troposphere, especially in the tropics.

Figure 4.3 shows the difference between the HadGEM3–UKCA simulations in each configuration and the actual observations from each phase of the HIPPO campaign.

It is clear from these difference plots that, at least for HIPPO-1 and HIPPO-2, the upper-tropospheric excess seen in the BASE configuration is largely removed when the in-plume convective scavenging scheme is switched on (i.e. in CVSCAV and CVSCAV+G3M), suggesting that the lack of realistic convective scavenging may

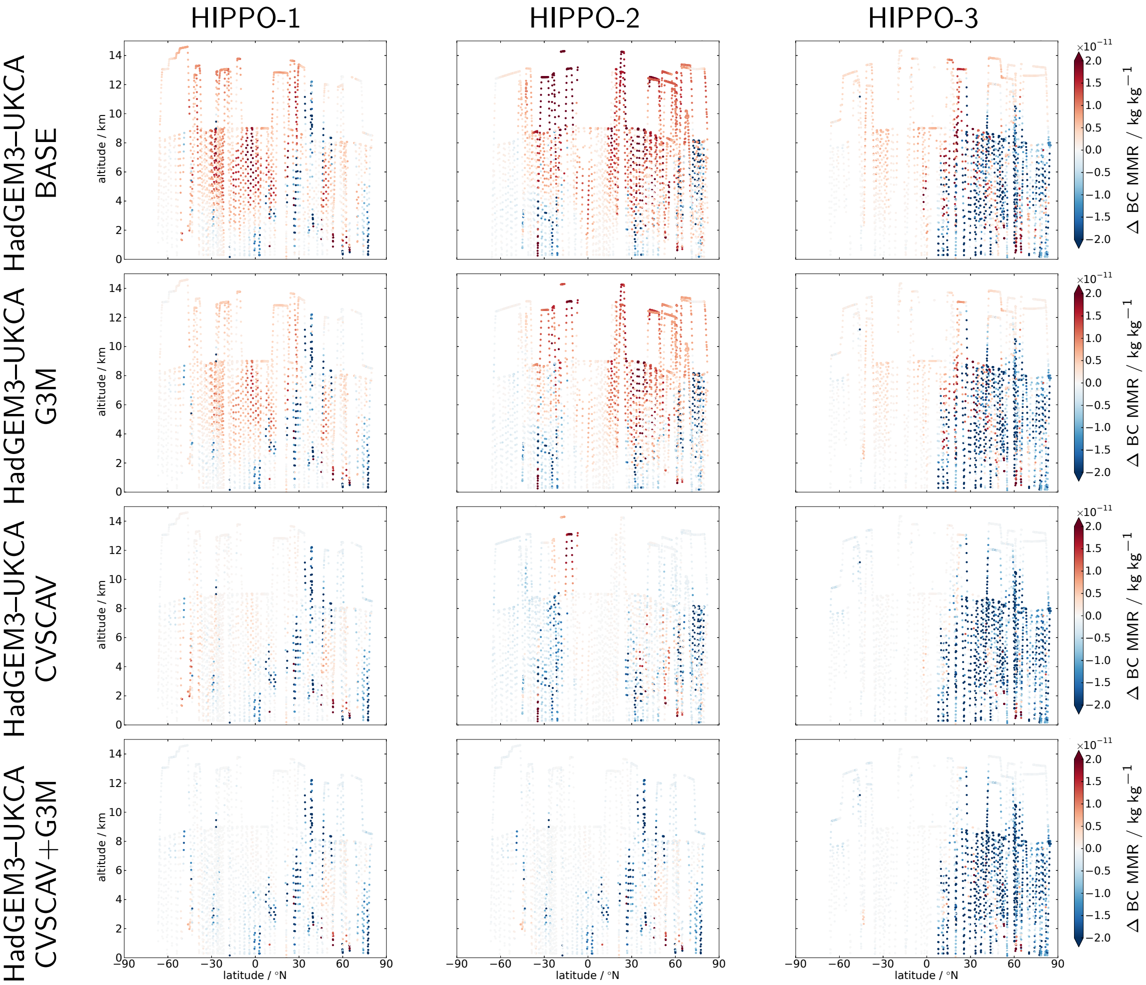

Figure 4.3: Difference of BC mass mixing ratio (kg kg^{-1}) simulated by HadGEM3–UKCA in each configuration (rows) from that observed during each phase of the HIPPO campaign (columns). The model is nudged and sampled along the HIPPO flight track at 1-minute intervals; observed mixing ratio is calculated from HIPPO SP2 data aggregated over 1-minute intervals.

have been responsible. This is supported by the fact that – without adjusting any other parameters in the model – the improvement is so strong, while introducing very little in the way of new visible errors which might be expected if the new scheme was compensating for errors in a different process (which would likely have a different structure). The third row of Figure 4.2 shows the BC mixing ratio from the CVSCAV+G3M simulation, which is visibly more realistic with respect to the observations. For HIPPO-3, the improvement is largely confined to the southern hemisphere; in the northern hemisphere both simulations produce too little aerosol at lower levels and too much aloft. This is despite the fact that HIPPO-3 observed more BC at upper levels in the northern hemisphere than the earlier phases.

The change in switching to GFED3.1 biomass-burning emissions (i.e. BASE to G3M) is less dramatic. While, for HIPPO-1 and HIPPO-2, the difference plot for the G3M simulation (second row of Figure 4.3) indicates less of a positive bias than for BASE, the upper-tropospheric excess remains clear. Applying the emissions change on top of the in-plume convective scavenging (i.e. going from CVSCAV to CVSCAV+G3M) removes what little excess remains in the middle and upper troposphere, but appears to leave an overall negative bias compared to the observations. For HIPPO-3, the differences from the choice of emissions are even less clear. Unlike for convective scavenging, it is difficult to be confident that the small improvements seen here are genuinely attributable to better emissions, rather than compensating for biases elsewhere in the model.

It thus appears that for HIPPO-1 and HIPPO-2 globally, and for HIPPO-3 in the southern hemisphere, the disagreement between the BASE model and observations is dominated by the lack of realistic convective scavenging, and is much improved when an in-plume approach is introduced. For HIPPO-3 in the northern hemisphere, however, it appears that the disagreement is dominated by other effects which have not yet been identified. This is consistent with HIPPO-3 occurring in northern-hemisphere spring, when convective precipitation in the northern mid-latitude Pacific is relatively weak.

The differences can also be seen in the burdens (top two rows of Figure 4.1). The BASE simulation over-predicts the BC burden at most of the profile locations, in many cases by an order of magnitude. CVSCAV+G3M performs much better, with the model burden frequently close to the range estimated from the HIPPO observations. For brevity, the separate plots for CVSCAV and G3M are omitted; however as before, most of the improvement is seen in the former and is particularly pronounced over the tropical warm pool region where strong convective scavenging is expected. The high burdens observed in the Arctic in HIPPO-1 were attributed to a localised biomass-burning plume (Schwarz et al., 2010) as they were dominated by two particular profiles which were close together. In HIPPO-2 and HIPPO-3, however, the high Arctic burdens are a more systematic feature of the profiles in this region (J. P. Schwarz, pers. comm.) This suggests that the model is underestimating the transport of BC to the Arctic – either due to errors in the transport itself, or because it is removed too rapidly (probably by large-scale wet scavenging, since this affects both BASE and CVSCAV simulations).

4.5.2 ECHAM5–HAM2

The BC MMR from ECHAM5–HAM2 (in its BASE configuration), sampled at 1-minute intervals along the flight track for the first three phases of the HIPPO campaign, is shown in the bottom row of Figure 4.2. These do not exhibit the large upper-troposphere excesses seen in the HadGEM3–UKCA BASE simulation, but there are some unexpectedly large mixing ratios at even higher altitudes (including into the lower stratosphere).

Figure 4.4 shows the difference between the ECHAM5–HAM2 simulations in each configuration and the actual observations from each phase of the HIPPO campaign.

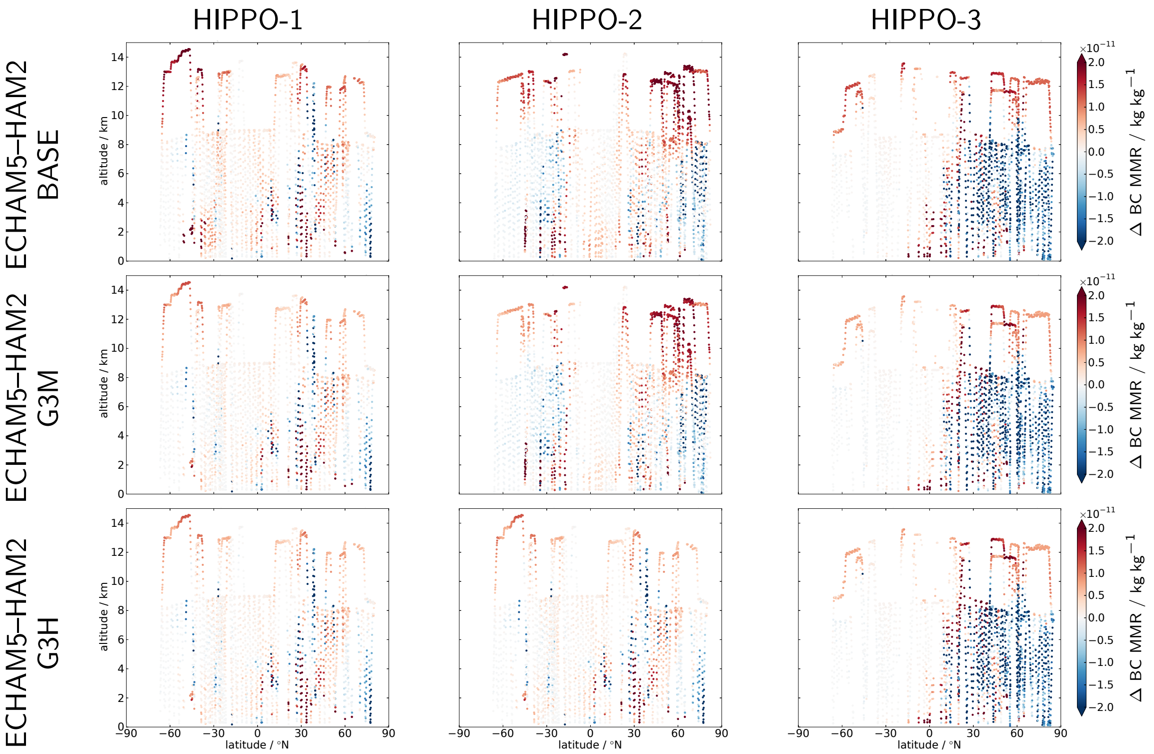

Figure 4.4: Difference of BC mass mixing ratio (kg kg^{-1}) simulated by ECHAM5–HAM2 in each configuration (rows) from that observed during each phase of the HIPPO campaign (columns). The model is nudged and sampled along the HIPPO flight track at 1-minute intervals; observed mixing ratio is calculated from HIPPO SP2 data aggregated over 1-minute intervals.

The lower-stratosphere anomalies are clear in all simulations, and for HIPPO-1 and HIPPO-2 the BASE configuration shows patches of (mostly positive) bias throughout the troposphere that are not immediately obvious from Figure 4.2.

Some of the strongest biases are reduced in the G3M simulation: in particular, at lower levels around the equator (for all three phases) and also in the southern mid-latitudes (for HIPPO-1). This suggests that part of the tropospheric error in the BASE configuration may be attributable to the choice and implementation of biomass-burning emissions; however as in HadGEM3–UKCA, the improvement is not decisive enough to exclude the possibility that this is simply compensating for other biases in the model. It is also possible that some of this difference is due to the different vertical profile of emissions between BASE and G3M. However, an additional simulation (not shown here) for HIPPO-1 with the same GFED2 emissions as BASE, but the boundary-layer-following vertical profile of G3M shows results very similar to BASE. This suggests that it is the updated inventory, rather than the change in vertical profile, which makes the difference. Similarly, using a boundary-layer-following emission profile in HadGEM3–UKCA (instead of the default fixed ~ 50 m to 3 km profile) makes little difference, indicating that the different emission profiles do not contribute significantly to the differences between the two models.

As in HadGEM3–UKCA (CVSCAV), HIPPO-3 looks rather different to the earlier phases. There appears to be little change between the ECHAM5–HAM2 BASE and G3M simulations, with the tropospheric error in both simulations dominated by negative anomalies throughout most of the northern hemisphere.

For all three phases, there is almost no visible difference between the G3M and G3H simulations. This indicates that, at least for simulations in remote regions such as those covered in the HIPPO campaign, monthly biomass-burning emissions are sufficient as any high-frequency variability at the source is smoothed out during transport. Higher-time-resolution emissions could provide more benefits for simulations closer to source regions, however.

The ECHAM5–HAM2 simulated burdens (third row of Figure 4.1) show a similar pattern of overestimating the observations as the HadGEM3–UKCA BASE simulation, despite ECHAM5–HAM2 already having an in-plume convective scavenging scheme. This analysis cannot determine what process is responsible for the high burden in ECHAM5–HAM2 – a more detailed study of the role of the different processes in this model would be required. It may still be some aspect of scavenging which is too weak, but equally the problem may be elsewhere. The AeroCom Phase I (Textor et al., 2006) median model, shown in the bottom row, shows a similar positive bias.

The presence of high BC burdens in the remote Pacific in these models, in a way that does not correspond with observations, suggests that the model BC

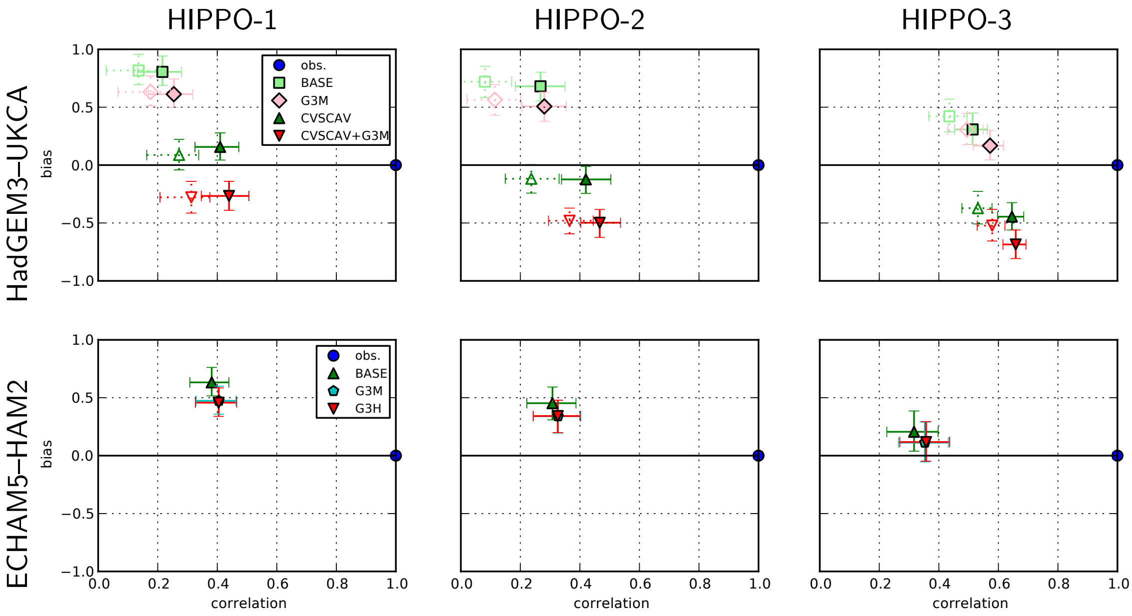

Figure 4.5: Bias–correlation plots of log(BC mass mixing ratio) between the HadGEM3–UKCA (top row) and ECHAM5–HAM2 (bottom row) simulations and each phase of the HIPPO campaign (columns). The error bars represent a 95% confidence interval based on a moving-block bootstrap and the ±30% error in the SP2-derived mixing ratios from HIPPO-1. The solid symbols represent nudged simulations, while the hollow symbols (for HadGEM3–UKCA) represent free-running simulations. The “obs.” point on the right-hand side indicates where a model which reproduces the observations perfectly would be located.

lifetime is too long. In HadGEM3–UKCA this appears to be a structural issue with convective scavenging; in ECHAM5–HAM2 and other models it may be due to different processes.

4.5.3 Quantitative evaluation

Figure 4.5 shows the bias and correlation coefficient of log(BC MMR) for each simulation against each phase of the HIPPO campaign, along with bootstrap uncertainty estimates as described in Section 4.3.

The improvement in both bias and correlation when switching to in-plume convective scavenging in HadGEM3–UKCA can clearly be seen when going from

BASE to CVSCAV, or from G3M to CVSCAV+G3M (with the exception of the negative bias against HIPPO-2 and HIPPO-3 in the CVSCAV+G3M simulation). The improvement in correlation should perhaps be regarded as more relevant, as the bias is likely to be more susceptible to model tuning/calibration. For all three phases, this increase in correlation (0.22 → 0.41, 0.27 → 0.42, 0.51 → 0.65 between BASE and CVSCAV for HIPPO-1, -2, -3 respectively) is statistically significant in the sense that the error bars of the nudged BASE and CVSCAV (or G3M and CVSCAV+G3M) simulations do not overlap. Carrying out the analysis separately for the points in the two hemispheres (not shown) indicates that the increase in correlation comes largely from the northern hemisphere.

For both models, a small improvement in correlation (although not in bias for HadGEM3–UKCA CVSCAV) is seen when going from BASE to G3M (or CVSCAV to CVSCAV+G3M), although the overlapping error bars indicate that this is not statistically significant. As with the visual analysis, there is almost no difference between the ECHAM5–HAM2 G3M and G3H simulations. It is probably the case that evaluation closer to source regions would be more powerful in distinguishing between emissions inventories and their time resolution.

The correlation and, in most cases, also the bias are much improved in the nudged HadGEM3–UKCA simulations (solid symbols) compared to their free-running counterparts (hollow symbols). The correlation increases for the BASE configuration are 0.14 → 0.22, 0.08 → 0.27, 0.44 → 0.51 between free-running and nudged simulations for HIPPO-1, -2, -3, respectively. In addition, the improvement in bias and correlation from changes to the model configuration is enhanced in the nudged simulations. This is particularly significant for HIPPO-1, where nudging eliminates the overlapping error bars on the correlation axis between BASE and CVSCAV. This allows the conclusion that the improvement in CVSCAV is statistically significant, which may not have been clear from the free-running simulations alone. (It should be noted in this context that the error bars on the free-running models are an underestimate – ensemble simulations would be needed to quantify the additional uncertainty from the simulated meteorology.) Thus, not only does nudging help to produce realistic simulations of aerosol during a given flight campaign, but it also makes it easier to evaluate the effect of changes to the aerosol scheme by damping errors due to differences in large-scale dynamics.

4.5.4 Comparison with profile curves

To compare the point-by-point analysis presented here with a more traditional approach, vertical profile curves have been constructed from the HIPPO-1 observations for four latitude bands using the (geometric) mean and standard deviation over all the profiles identified for the burden analysis (as described in Section 4.3.1) in each latitude band. Corresponding curves have also been constructed from the January 2009 monthly-mean output from the HadGEM3–UKCA simulations, by horizontally interpolating to the location of each profile identified in the observations.

The results are shown in Figure 4.6. Although the construction is similar to that in Schwarz et al. (2010), the curves are not identical due to the different profile-detection algorithm used. While some improvement from both CVSCAV and G3M can be seen in these curves, this is rather less clear than in the point-by-point analysis (Figure 4.3). In many cases, the differences are overshadowed either by the variability between profiles within a region (e.g. in the 60°N–80°S band, where all four model curves lie almost entirely within the spread of the observed profiles) or by overall regional biases (e.g. in the 20°S–20°N band, where all four model curves lie almost entirely outside the spread of the observed profiles). It is therefore difficult to ascribe statistical significance to the model improvements from this analysis, as was possible in Section 4.5.3 from Figure 4.5.

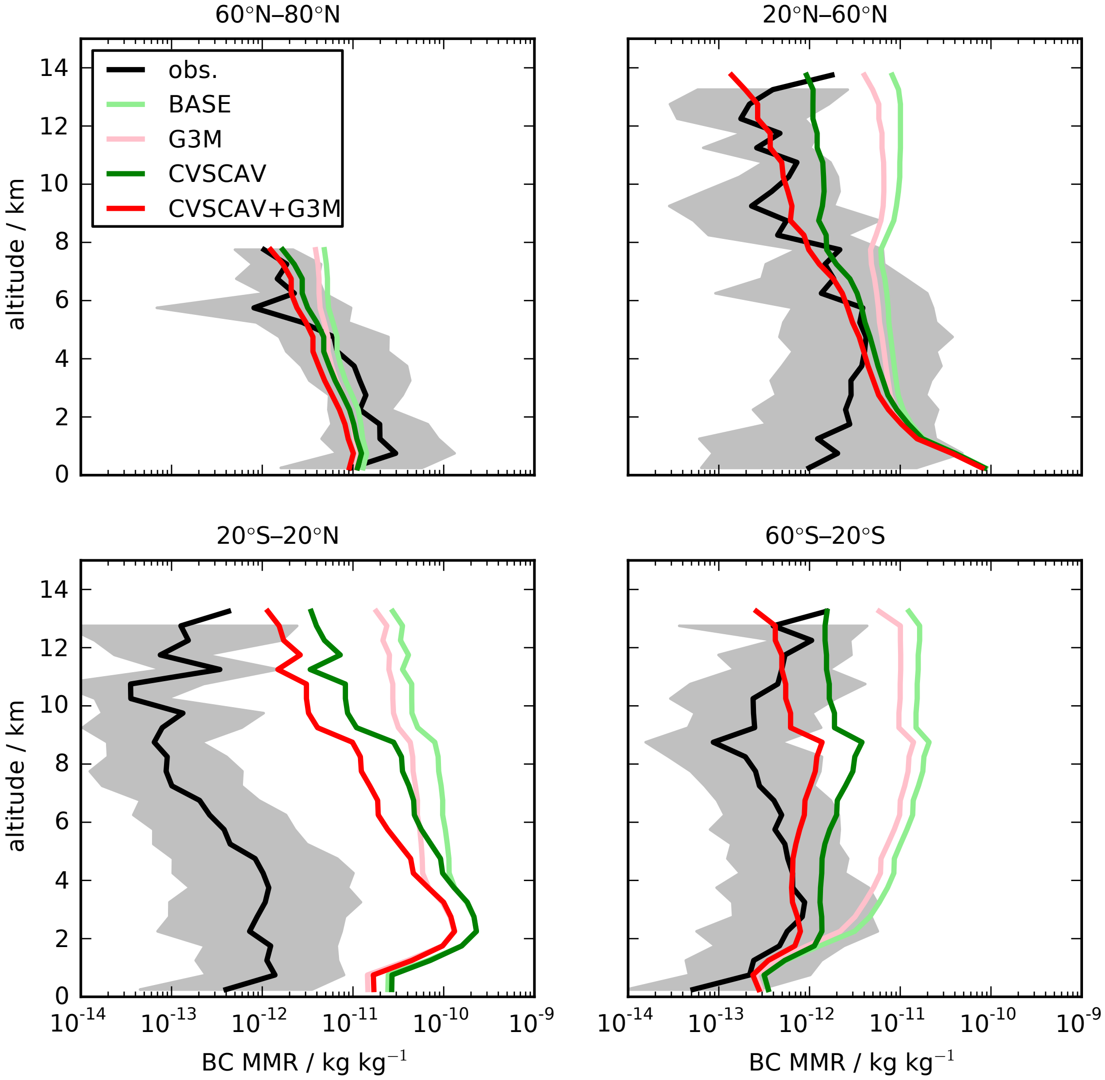

Figure 4.6: Vertical profile curves of BC mass mixing ratio for HIPPO-1 and horizontally-matched locations in the January 2009 monthly-mean output from the HadGEM3–UKCA simulations. The shaded region shows the (geometric) standard deviation of the observed MMR values over the profiles in each latitude band, plus the ±30% measurement error.

This demonstrates the usefulness of the point-by-point analysis presented here in allowing the evaluation of process-level changes to the model with rather more confidence than can be obtained from a more traditional approach.

4.6 Summary and conclusions

The vertical distribution of aerosol is not well constrained by observations on the global scale. Aiming to address this, methods were developed in this chapter for evaluating aerosol–climate models against large-scale aircraft campaigns, and applied to investigate the impact of convective scavenging and biomass-burning emissions on the vertical profile of black carbon.

By running two aerosol–climate models in nudged configurations and interpolating their output onto the track of a flight campaign, a detailed pointwise comparison was made between model output and in-situ aircraft observations. Using data from a campaign such as HIPPO, which has good vertical resolution over an extended geographical area, this gives a powerful tool for evaluating the vertical distribution of aerosol in the models. It was also shown how these measurements can be used to evaluate column-integrated burdens in the models, which are a more direct product of most models than the optical or radiative properties (e.g. aerosol optical depth) which can be evaluated via remote sensing.

This approach was applied to black carbon aerosol in the HadGEM3–UKCA and ECHAM5–HAM2 models, showing how each has different areas of disagreement with the HIPPO SP2 observations. Both models significantly over-predicted BC burden, by up to an order of magnitude in the more remote regions, suggesting that the BC lifetime in the models is too long.

In the case of HadGEM3–UKCA, the largest discrepancy (an excess of aerosol in the tropical upper troposphere) was eliminated by switching from the default operator-split convective scavenging scheme to one which scavenges directly from the convective plume. This change improved both the vertical distribution of BC and the simulated burdens against the HIPPO observations, yielding a statistically significant increase in the pointwise correlation coefficient for all three phases of the HIPPO campaign (0.22 → 0.41, 0.27 → 0.42, 0.51 → 0.65 for HIPPO-1, -2, -3, respectively).

ECHAM5–HAM2 also shows an overall positive bias, although the discrepancies have a less systematic structure than in HadGEM3–UKCA. One noteworthy feature, however, is the presence of unexpectedly high BC mass mixing ratios extending into the lower stratosphere in ECHAM5–HAM2. This is currently unexplained, but further work to establish its cause may help to identify structural or tuning errors in the model.

In both models, a somewhat smaller and not statistically significant improvement was seen when switching from GFED2-based biomass-burning emissions to GFED3.1; however, there was virtually no change in this region – which is remote from biomass-burning sources – when the time resolution of these emissions was increased from monthly to 3-hourly in ECHAM5–HAM2. It seems likely that a similar analysis with a wider range of flight campaigns, including the major biomass-burning regions, might better constrain the choice of such emissions.

For HadGEM3–UKCA, both the correlation between the BASE configuration and the observations, and the increase in correlation due to the new convective scavenging scheme, were enhanced when the simulations were nudged as opposed to free-running. In this way, nudging can enable statistically significant improvements in the model to be detected where they might not be in a free-running simulation; e.g. the above increase in the correlation of the nudged model against HIPPO-1 (from 0.22 to 0.41) was statistically significant, while the corresponding increase for the free-running model (from 0.14 to 0.27) was not.

In an analysis of this kind, there is always the potential for compensating errors in different parts of the model to obscure which processes are poorly represented.

This is particularly true in this case where a change was made in the biomass-burning emissions and compared to observations in remote regions; an analysis nearer the source regions might better distinguish emissions effects from other sources of bias. For convective scavenging in HadGEM3–UKCA, however, a very clear improvement was seen from a more physically-realistic implementation without adjusting any other model parameters, with very little new error introduced. It is thus reasonable to conclude that this is not simply compensating for other errors, but that it is the convective scavenging itself which must be accurately represented in the model to obtain a realistic vertical profile.

It is clear that vertically-resolved in-situ measurements of aerosol have an important role to play in evaluating the aerosol distributions simulated by aerosol–climate models, in conjunction with satellite remote sensing and ground-based observations, and that they can provide particular insight into the processes governing the vertical transport of aerosol in the atmosphere, as has been shown in this chapter for convective scavenging.

This chapter has considered the effect of two specific processes on the vertical distribution of aerosol; Chapter 5 will look at the sensitivity of the vertical profile to the full range of aerosol and transport processes.

Chapter 5

What controls the vertical profile of aerosol? Relationships between process sensitivity in HadGEM3–UKCA and inter-model variation from AeroCom Phase II

The work described in this chapter is in preparation for submission to the journal Atmospheric Chemistry and Physics *as* Kipling, Z., Stier, P., Johnson, C. E., Mann, G. W., Bellouin, N., Bauer, S. E., Bergman, T., Chin, M., Diehl, T., Ghan, S. J., Iversen, T., Kirkevåg, A., Kokkola, H., Liu, X., Luo, G., Myhre, G., van Noije, T., Pringle, K. J., von Salzen, K., Schulz, M., Seland, Ø., Takemura, T., Tsigaridis, K., and Zhang, K.: What controls the vertical distribution of aerosol? Relationships between process sensitivity in HadGEM3–UKCA and inter-model variation from AeroCom Phase II, in prep., 2013.

The text, figures, HadGEM3–UKCA simulations and analysis presented here are the work of Kipling, under the supervision of Stier and Johnson. The other authors contributed datasets from the various AeroCom models, as listed in Table 5.1; Mann also contributed the GLOMAP-mode aerosol scheme used in the HadGEM3–UKCA simulations.

As mentioned in Section 1.4 and Chapter 4, the relative magnitudes, and in some cases even the sign, of the different aerosol effects are strongly influenced by the vertical distribution of aerosol and especially its altitude relative to cloud layers. However, the observational constraints on vertical profiles are rather weak, and there is a large diversity in the profiles simulated by current aerosol–climate models (see e.g. Samset et al., 2013).

Aerosol–climate models vary considerably in their complexity, but typically include a range of emission, transport, deposition, microphysical and chemical processes that may affect both the horizontal and vertical distribution of aerosol. This chapter aims to identify in one particular model the processes which play a dominant role in controlling the vertical profile using a series of coarse sensitivity tests.

This chapter also investigates the extent to which variations in the strength of the processes thus identified can replicate the current inter-model diversity in aerosol vertical profiles, or whether further structural differences between models are required to explain this diversity.

5.1 AeroCom

The Aerosol Comparisons between Observations and Models (AeroCom; `http://aerocom.met.no/`) project is an international initiative for the intercomparison and evaluation of global aerosol–climate models and a wide range of observations.

Textor et al. (2006) investigated the vertical distribution of aerosol in the AeroCom Phase I models, amongst many other aspects of the aerosol life cycle. They show large variations in the profiles between the models, but these are not attributed to specific processes. Koffi et al. (2012) evaluate the vertical profiles in these models against CALIOP satellite LIDAR observations, showing that for all models the match to observations varies considerably by both region and season. Samset et al. (2013)

show that the inter-model diversity in the vertical profile of black carbon in particular causes a large diversity in its radiative forcing.

In this chapter, monthly-mean aerosol mass mixing ratio fields are used from the models which contributed to the Phase II present-day "control" experiment (Myhre et al., 2013), referred to as A2.CTRL. The models included here are those contributing to this experiment which (a) provided monthly 3D mass mixing ratio fields for at least four of sulphate (SO_4), sea-salt (SS), black carbon (BC), organic aerosol (OA) and mineral dust (DU); and (b) provided sufficient vertical-coordinate information to plot vertical profiles and calculate column mass integrals. Some of the models also include ammonium (NH_4) and nitrate (NO_3) aerosol components; however these components are not included in this study.

Based on these requirements, there are 18 suitable models which submitted results to the A2.CTRL experiment, which are summarised in Table 5.1 along with references giving further detail for each model. Six of these are chemical transport models (CTMs) driven by meteorological fields from a reanalysis dataset for the year 2006; the other twelve are general circulation models (GCMs) in which both the meteorology and composition are simulated. Nine of the GCMs submitted results from a nudged configuration (Jeuken et al., 1996; Telford et al., 2008). The three non-nudged (free-running) GCMs submitted a monthly climatology from a five-year run, while the CTMs and nudged GCMs submitted (at least) monthly output for the year 2006. A number of the models calculate oxidant fields (which control the production of secondary aerosol) online using a tropospheric gas-phase chemistry scheme, while the remainder rely on prescribed oxidant fields from a climatology.

The models use a mixture of modal/sectional and one-/two-moment aerosol schemes. The modal schemes represent the aerosol size distribution as a superposition of a small number of (usually log-normal) "modes", each with its own composition. The sectional schemes divide the size distribution into a (sometimes much) larger number of discrete "bins". In the two-moment schemes, there are separate tracers for

Table 5.1: Models from the AeroCom Phase II control experiment (A2.CTRL) included in this study. (SO_4=sulphate; SS=sea-salt; BC=black carbon; OA=organic aerosol; DU=mineral dust. Y=included; m=included in model but MMR field not available in AeroCom archive.)

Model	**Type**	**Reanalysis**	**Year**	**Resolution**	**Aerosol**	**Oxidants**	**Components**					**References**
				δlat×δlon×levels			SO_4	**SS**	**BC**	**OA**	**DU**	
CAM4–Oslo	GCM	free-running		1.9°×2.5°×26	tagged[a]	prescribed	Y	Y	Y	Y	Y	Kirkevåg et al. (2013)
CAM5.1	GCM	free-running		1.9°×2.5°×30	modal (2m)	mixed[b]	Y	Y	Y	Y	Y	Liu et al. (2012)
CanAM4–PAM	GCM	free-running		3.8°×3.7°×35	pcwise-lgnrmal (2m)	prescribed	Y	Y	Y	Y	Y	Peng et al. (2012)
ECHAM5–HAM	GCM	ERA-Interim	2006	1.9°×1.9°×31	modal (2m)	prescribed	Y	Y	Y	Y	Y	Stier et al. (2005) Zhang et al. (2012)
ECHAM5–SALSA	GCM	ERA-Interim	2006	1.9°×1.9°×31	sectional (2m)	prescribed	Y	Y	Y	Y	Y	Bergman et al. (2012)
EMAC	GCM	ERA-Interim	2006	2.8°×2.8°×19	modal (2m)	online	Y	Y	Y	Y	Y	Pringle et al. (2010)
GEOS–Chem	CTM	GEOS-5	2006	2.0°×2.5°×47	sectional (1m)	online	Y	Y	Y	Y	Y	Yu and Luo (2009)
GISS–MATRIX	GCM	NCEP	2006	2.0°×2.5°×40	modal (2m QMOM)	online	Y	Y	Y	Y	Y	Bauer et al. (2008)
GISS–modelE	GCM	NCEP	2006	2.0°×2.5°×40	modal (1m), except DU: sectional (1m)	online	Y	Y	Y	Y	Y	Bauer et al. (2007)
GLOMAP-bin	CTM	ERA-Interim	2006	2.8°×2.8°×31	sectional (2m)	prescribed	Y	Y	Y	Y	–	Spracklen et al. (2005)
GLOMAP-mode	CTM	ERA-Interim	2006	2.8°×2.8°×31	modal (2m)	prescribed	Y	Y	Y	Y	Y	Mann et al. (2010)
GOCART	CTM	GEOS-4	2006	2.0°×2.5°×30	modal (1m), except SS, DU: sectional (1m)	prescribed	Y	Y	Y	m	Y	Chin et al. (2000) Ginoux et al. (2001)
HadGEM2	GCM	ERA-Interim	2006	1.3°×1.9°×38	modal (1m), except DU: sectional (1m)	online	Y	Y	Y	Y	Y	Collins et al. (2008) Bellouin et al. (2007)
HadGEM3–UKCA	GCM	ERA-Interim	2006	1.3°×1.9°×63	modal (2m), except DU: sectional (1m)	online	Y	Y	Y	Y	Y	Hewitt et al. (2011) Mann et al. (2010, 2013)
INCA	GCM	ECMWF IFS	2006	1.9°×3.8°×19	modal (2m)	online	Y	Y	Y	Y	Y	`www-lsceinca.cea.fr`
OsloCTM2	CTM	ECMWF IFS	2006	2.8°×2.8°×60	modal (1m), except SS, DU: sectional (1m)	online	Y	Y	Y	Y	m	Myhre et al. (2007, 2009)
SPRINTARS	GCM	NCEP	2006	1.1°×1.1°×56	modal (2m)	prescribed	Y	Y	Y	Y	Y	Takemura et al. (2005)
TM5	CTM	ERA-Interim	2006	2.0°×3.0°×34	modal (2m)	online	Y	Y	Y	Y	Y	Aan de Brugh et al. (2011) van Noije et al. (in prep.)

[a] Mass concentrations of SO_4, SS, BC, OA, DU in four size classes are tagged according to production mechanism; based on 44 sectional size bins and log-normal distributions at the point of emission, look-up tables yield physical properties of the processed aerosols (Kirkevåg et al., 2013)

[b] H_2O_2 is diagnosed online; other oxidants are prescribed (S. J. Ghan, pers. comm.)

number and mass in each mode or bin, allowing the mean particle size to vary within set limits (although the width remains fixed); in the one-moment schemes there is a single tracer for each mode or bin and an assumed size distribution is used. Note that some of the models use distinct schemes for different aerosol components, including HadGEM3–UKCA (described in more detail in Section 1.6.1) which has a 6-bin 1-moment sectional scheme for mineral dust and a 5-mode 2-moment modal scheme for other aerosol; GISS–modelE, GOCART and HadGEM2 have similar mixed schemes. Three of the models use somewhat different approaches: CAM4–Oslo uses mass concentrations in several size classes tagged according to production mechanism, and look-up tables to determine the physical properties (Kirkevåg et al., 2013); CanAM4–PAM uses a piecewise log-normal representation; and GISS–MATRIX uses the quadrature method of moments (McGraw, 1997).

5.2 Method

5.2.1 HadGEM3–UKCA process sensitivity tests

The model processes which have the potential to affect the vertical distribution of aerosol broadly divide into four categories: emissions, transport, microphysics and chemistry, and deposition. While some model processes can be adjusted via continuous parameters, as in the approach taken by Lee et al. (2011) to assess parametric uncertainty in models, this is not true for all relevant processes. In order to cover the widest possible range of processes, albeit at the cost of a less quantitative assessment of sensitivity, a simple on/off approach is adopted here for most processes.

Emissions can affect the vertical distribution directly by the vertical range over which they are injected into the model – this is of particular importance for biomass-burning emissions, where plume heights are variable and not particularly well constrained. Limiting cases are considered, of injecting all such emissions at the surface (BB_SURF), or extending them uniformly in height to the tropopause (BB_TROP/z). The size distribution of emitted particles may also affect the development of the vertical profile, and consideration is given to increasing (EM_LARGE) or decreasing (EM_SMALL) the size of all primary particles by a factor of $\sqrt{10}$ (≈ 3.16, chosen to match the spacing of HadGEM3 dust bins) while keeping the total mass of emissions constant.

Vertical transport of aerosol in the model is due to large-scale vertical advection, boundary-layer turbulent mixing and convection. The effect of switching off each of these processes is considered (NO_VADV, NO_BLMIX and NO_CVTRANS, respectively).

Consideration is also given to the effect of switching off each of the microphysical processes: condensation (NO_COND), coagulation (NO_COAG) and nucleation of new particles (NO_NUCL), as well as the effect of adding boundary-layer nucleation (WITH_BLN) using the cluster-activation approach of Kulmala et al. (2006) – which is available in the model but not included in the standard configuration. Further configurations switch off the in-cloud production of sulphate by aqueous oxidation (NO_WETOX) and the "cloud processing" process which moves activated cloud condensation nuclei (CCN) from the soluble Aitken mode to the accumulation mode (NO_CLDPROC), and consider the limiting cases of instant ageing (AGE_INST) and no ageing (AGE_NEVER) of insoluble aerosol to the soluble modes.

Deposition processes can preferentially remove aerosol from certain ranges in the vertical, and the effect of switching off each of the following processes is considered: dry deposition and sedimentation (NO_DDEP), large-scale in-cloud/nucleation scavenging (NO_LS_RO), convective in-cloud/nucleation scavenging (NO_CV_RO) and below-cloud impaction scavenging (NO_WASHOUT). Although the total precipitation in the model is energetically constrained by evaporation at the surface, the division of precipitation between the large-scale and parameterised convective schemes is somewhat arbitrary and varies considerably between different resolutions and configurations of the Met. Office Unified Model (which cover global and regional climate modelling and also high-resolution weather forecasting); because of this, the effect of switching off all in-cloud/nucleation scavenging is considered (NO_RAINOUT). Finally, the inclusion of a re-evaporation process is considered, in which scavenged aerosol is returned to the atmosphere where rain evaporates before reaching the surface (WITH_REEVAP) – which is not included in the standard configuration, but implemented as in Section 3.5.

The full set of simulations for the sensitivity tests is summarised in Table 5.2. All simulations were run with nudged meteorology from September 2008 through to the end of December 2009, allowing four months spin-up before a full year, and include both the in-plume convective scavenging scheme described in Section 3.4 and the GFED3.1 biomass-burning emissions introduced in Chapter 4 (i.e. this chapter's BASE configuration is equivalent to CVSCAV+G3M from Chapter 4). No re-tuning of the model was performed for the different configurations. To analyse effects on direct radiative forcing, a second set of simulations were run using pre-industrial aerosol and precursor emissions based on year 1850 of Lamarque et al. (2010).

It should be noted that, for technical reasons, the model configuration used here differs from that used for the HadGEM3–UKCA A2.CTRL submission, which used a more recent snapshot of the UKCA code, and was run at N96L63 (same horizontal resolution and model top, but 63 vertical levels instead of 38).

5.2.2 Derivation of vertical profiles

Most of the AeroCom models use a hybrid sigma/pressure vertical coordinate, from which (given the fixed hybrid coefficients for each level and a surface pressure field) a global 3D pressure field can easily be calculated, while neither geometric nor geopotential height is readily available. The exceptions are the HadGEM models, which use a hybrid-height vertical coordinate, but for these a prognostic pressure

Table 5.2: Configurations of HadGEM3–UKCA-2011 used for process sensitivity test simulations

	Configuration	**Description**
	BASE	Standard N96L38 HadGEM3–UKCA-2011 aerosol configuration at UM 7.3, plus in-plume convective scavenging (as described in Section 3.4) and GFED3.1 biomass-burning emissions
Emissions	BB_SURF	All biomass-burning emissions injected in lowest level
	BB_TROP/z	Biomass-burning emissions injected uniformly in height up to tropopause
	EM_LARGE	All primary particle sizes increased by a factor of $\sqrt{10}$ (total mass unchanged)
	EM_SMALL	All primary particle sizes decreased by a factor of $\sqrt{10}$ (total mass unchanged)
Transport	NO_VADV	No large-scale vertical advection of aerosol
	NO_BLMIX	No boundary-layer mixing of aerosol
	NO_CVTRANS	No convective transport (and therefore also no convective in-cloud/nucleation scavenging) of aerosol
Microphysics/chemistry	NO_COND	No condensation from gas phase onto existing aerosol
	NO_COAG	No coagulation of aerosol particles
	NO_NUCL	No nucleation of new particles from the gas phase
	WITH_BLN	Boundary-layer nucleation switched on
	NO_WETOX	No production of aerosol via aqueous chemistry.
	AGE_INST	Insoluble particles aged to soluble modes instantly (i.e. 0 monolayers required)
	AGE_NEVER	Insoluble particles never age to soluble modes (i.e. ∞ monolayers required)
	NO_CLDPROC	No Aitken→accumulation mode transition due to aerosol activation
Deposition	NO_DDEP	No dry deposition or sedimentation of aerosol
	NO_LS_RO	No large-scale in-cloud/nucleation scavenging (rainout) of aerosol
	NO_CV_RO	No convective in-cloud/nucleation scavenging (rainout) of aerosol
	NO_RAINOUT	No in-cloud/nucleation scavenging (rainout) of aerosol
	NO_WASHOUT	No below-cloud impaction scavenging (washout) of aerosol
	WITH_REEVAP	Re-evaporation (release of scavenged aerosol due to evaporation of precipitation) switched on

field is readily available in the output. For simplicity across the full range of models, vertical profiles in pressure coordinates are therefore used for this analysis.

For all the models used here, monthly mass mixing ratio fields are available for each of the included aerosol components (either directly, or by summing over several tracers for different size bins or modes). For a global (or regional) mean vertical profile, the mean mixing ratio is taken (on model-level surfaces) and plotted against monthly-mean pressure (again averaged on model-level surfaces).

For the HadGEM3–UKCA sensitivity tests, size-resolved vertical number profiles are also calculated in the form of condensation nuclei (CN) greater than 3, 10, 14, 30, 50, 100, 300 and 500 nm dry diameter. These are calculated by integrating the relevant portion of the log-normal size distribution for each of the UKCA aerosol modes, and adding the number of mineral dust particles based on the separate one-moment sectional dust scheme. Where the CN size cut-off falls within a dust bin D, this is calculated assuming that the number distribution within the bin is log-uniform. (This is not entirely consistent with the dust scheme itself, which assumes that the volume distribution – rather than the number distribution – is log-uniform within each bin. Any error introduced, however, will only affect CN > 100 nm and above since the smallest dust bin starts at 63.5 nm.)

5.2.3 A vertical position metric

As a means of quantifying the vertical position of aerosol, such that it can be plotted on a map or as a zonal mean on a line graph, the vertical centre-of-mass of each aerosol component C in each column is calculated in pressure coordinates (i.e. the aerosol-mass-weighted mean pressure level):

$$\bar{p}_C = \left(\sum_k m_k^{(C)} M_k p_k \right) \bigg/ \left(\sum_k m_k^{(C)} M_k \right) , \tag{5.1}$$

where p_k is the mid-point pressure of model layer k, $m_k^{(C)}$ is the mass mixing ratio of aerosol component C in that layer, and M_k is the contribution of layer k to the column air mass. Where M_k is not provided in the model output, it is calculated assuming hydrostatic balance as:

$$M_k = \frac{1}{g}\left|p_{k+1/2} - p_{k-1/2}\right| , \tag{5.2}$$

where $p_{k\pm 1/2}$ are the pressures at the upper and lower boundaries of layer k, and g is the acceleration due to gravity (assumed constant, neglecting a small decrease with height over the troposphere).

Proceeding similarly for the CN number profiles in HadGEM3–UKCA, the vertical centre-of-number of CN with diameter larger than a in each column can be calculated (i.e. the CN-number-weighted mean pressure level):

$$\bar{p}_{CN>a} = \left(\sum_k n_k^{(>a)} M_k p_k\right) \Big/ \left(\sum_k n_k^{(>a)} M_k\right) , \tag{5.3}$$

where $n_k^{(>a)}$ is the number of CN larger than a per unit mass of air in layer k.

5.2.4 Impact on radiative forcing

To investigate the impact of the various processes considered in HadGEM3–UKCA on the direct aerosol effect, due to the change in vertical profile, the instantaneous direct radiative effect (DRE) is calculated at the tropopause due to aerosol for each of the configurations in Table 5.2 using both present-day and pre-industrial emissions. This is done using a double call of the radiation scheme in the model, as in Bellouin et al. (2013), with aerosol effects active only in a diagnostic call; the difference in radiative fluxes between the two calls gives the instantaneous DRE due to all aerosol. By further taking the difference between the present-day and pre-industrial DRE, the direct radiative forcing (DRF) due to present-day anthropogenic aerosol is obtained.

The interaction between UKCA aerosol and the radiation scheme in HadGEM3 is described in detail in Bellouin (2010).

Much of the change in forcing between different configurations, however, is likely to be due to changes in the total amount of aerosol in the atmosphere rather than its vertical distribution. In order to (at least partially) remove such effects, the global-mean radiative forcing is normalised by the global-mean anthropogenic aerosol optical depth (at 550 nm wavelength):

$$NRFA = \frac{\langle DRE_{\mathrm{PD}} - DRE_{\mathrm{PI}} \rangle}{\langle AOD_{\mathrm{PD}} - AOD_{\mathrm{PI}} \rangle}. \tag{5.4}$$

5.3 Results

5.3.1 Global-mean vertical mass profiles

The annual and global mean vertical profiles of each aerosol component are shown in Figure 5.1, from the AeroCom A2.CTRL models (left column) and the HadGEM3–UKCA process-sensitivity tests (right column). The spread of the latter generally covers the inter-model spread in the AeroCom models, suggesting that sufficiently-strong variations in the processes considered here can largely replicate the model diversity as far as global-mean profiles are concerned. The main feature which is not replicated is the “inverted S” shape exhibited by several of the AeroCom models for sulphate, black carbon and organic aerosol: specifically the ECHAM5–HAM, INCA and SPRINTARS models exhibit this shape for all three components; ECHAM–SALSA and GOCART do for sulphate, while GISS–modelE does for black carbon and organic aerosol. This is seen very weakly in some of the HadGEM3–UKCA simulations for sulphate, and for black carbon and organic aerosol only in BB_TROP/z; however no configuration of HadGEM3–UKCA shows such a strong shape as can be seen in e.g. ECHAM5–HAM.

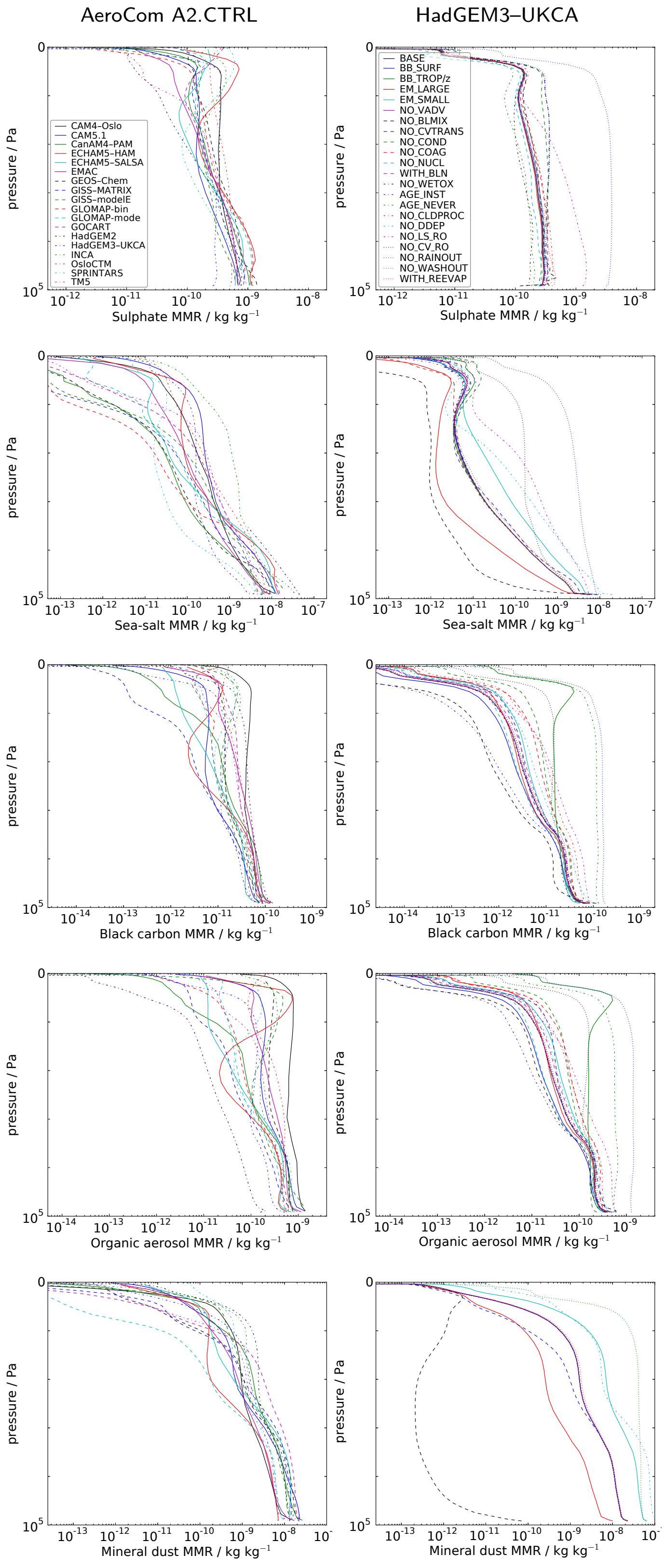

Figure 5.1: Annual and global mean vertical profiles of sulphate, sea-salt, black carbon, organic aerosol and mineral dust mass mixing ratio from the AeroCom Phase II models (left) and HadGEM3–UKCA sensitivity-test simulations (right).

5.3.2 Zonal-mean vertical position by mass

The zonal-mean vertical positions of each aerosol component (as represented by the mass-weighted mean pressure level) are shown in Figure 5.2, for the AeroCom A2.CTRL models (left column) and the HadGEM3–UKCA process-sensitivity tests (right column). The AeroCom models show a large inter-model spread for all components, and for sulphate, black carbon and organic aerosol the profiles vary between fairly flat (vertical position independent of latitude) and strongly "U-shaped" (aerosol located much higher in polar regions than tropics). Specifically, the CAM4–Oslo, EMAC, GEOS–Chem and HadGEM3–UKCA models show a fairly flat profile for all three components; in addition CanAM4–PAM and GISS–modelE do for sulphate, while GISS–MATRIX does for organic aerosol, and GOCART, HadGEM2 and TM5 do for both black carbon and organic aerosol. The remaining cases show a distinct "U" shape.

Unlike the other components, sea-salt is strongly asymmetric between the hemispheres (probably due to the difference in land fraction, and strong emissions driven by Southern Ocean winds). Mineral dust shows a "W" shape in several of the models (strongly in CAM4–Oslo, CAM5.1, GISS–modelE and TM5; weakly in EMAC, GEOS–Chem and GISS–MATRIX), with an additional peak in the tropics (probably due to dust transported aloft from desert regions e.g. in the Saharan outflow). In the remaining models, mineral dust shows a "U" shape as seen for other components.

The HadGEM3–UKCA simulations are all on the flat end of the spectrum seen in the AeroCom models, and generally cover a smaller vertical range. None of the configurations in the process-sensitivity test are able to reproduce the "U-shaped" curves seen in many of the AeroCom models, except for mineral dust and for sulphate in the NO_WETOX simulation. For all components, many of the simulations produce curves similar to BASE, with only a minority of processes significantly shifting the vertical position of the aerosol. The set of processes which have the strongest effects varies between the different aerosol components.

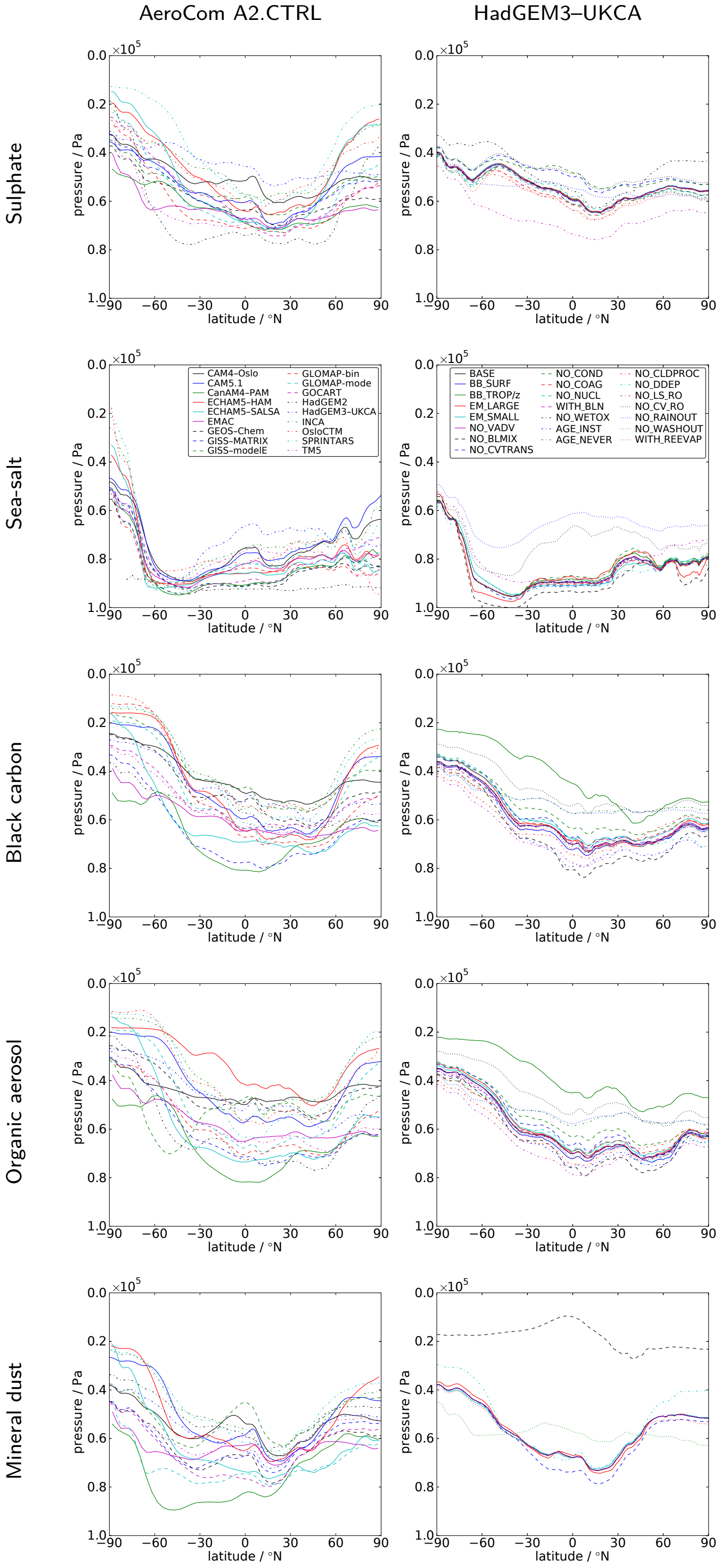

Figure 5.2: Annual and zonal mean mass-weighted mean pressure level (vertical centre of mass in pressure coordinates) of sulphate, sea-salt, black carbon, organic aerosol and mineral dust from the AeroCom Phase II models (left) and HadGEM3–UKCA sensitivity-test simulations (right).

For sulphate, large-scale rainout (in-cloud nucleation scavenging, the dominant removal process) has the largest effect – there is a strong downward shift at all latitudes in NO_LS_RO. There are also notable upward shifts from NO_CVTRANS, NO_CV_RO, NO_COND and (particularly at middle and high latitudes) NO_WETOX.

For sea-salt, convective rainout has the largest effect on the vertical distribution (even though dry deposition dominates removal) – there is a strong upward shift at all latitudes in NO_CV_RO. Large-scale rainout takes over at high latitudes, with NO_LS_RO causing a similar shift there. Boundary-layer mixing also appears important, with NO_BLMIX showing a downward shift except at latitudes with relatively little ocean (Antarctica and the northern mid-latitudes).

For black carbon and organic aerosol, the picture is a little more complex. BB_TROP/z shows a large upward shift, while BB_SURF shows only a small downward shift – this suggests that biomass-burning emissions are well-mixed by the boundary layer scheme and thus the emission profile only becomes important if it extends well into the free troposphere. This is borne out by the larger downward shift seen in NO_BLMIX. The effects of rainout and condensation are similar to those for sulphate, with a downward shift from NO_LS_RO and upward shifts from NO_CV_RO and NO_COND. Ageing also plays a big role, as primary BC/OA are emitted into the insoluble modes: AGE_INST (which will hasten removal) shows a downward shift, while AGE_NEVER shows an upward shift very similar to NO_RAINOUT (as expected since the aerosol never becomes soluble, and is thus not susceptible to in-cloud scavenging).

For mineral dust, boundary layer mixing dominates – in NO_BLMIX, aerosol emitted at the surface is never mixed upwards and is immediately removed by dry deposition in the same timestep due to the operator-splitting of emission and deposition in the model. (The high altitude shown in the plots is an artefact of the very small amount of dust still present from the starting state of the model – removal from the tropopause layer is very slow, while the rest of the troposphere has been cleaned of dust during the spin-up period.) Dry deposition and washout (below-cloud impaction scavenging) also play a significant role – NO_DDEP and NO_WASHOUT show an enhanced "U" shape (due to an upward shift at high latitudes) and a flattening of the curve (due to both a downward shift at high latitudes and an upward shift in the tropics) respectively.

5.3.3 Size-resolved CN profiles

The annual and global mean vertical number profiles of CN larger than 3, 10, 14, 30, 50, 100, 300 and 500 nm diameter from the HadGEM3–UKCA process-sensitivity tests are shown in Figure 5.3. There is a steady progression going from smaller to larger diameters: for most configurations, the global mean profiles go from peaking strongly in the tropopause to fairly well-mixed in the vertical, and then to peaking near the surface.

The zonal mean vertical position of CN larger than each of these diameters (as represented by the number-weighted mean pressure level) is shown in Figure 5.4. Again, the progression in size can be seen, with smaller diameters showing a humped shape with their highest average position in the tropics, while larger diameters show a "U" shape similar to that seen for component masses in many of the AeroCom models, with their highest position towards the poles. In the CN > 14 and 30 nm size range, the meridional profile of vertical position is almost flat.

For the smallest (and most numerous) particles which dominate CN > 3 nm, the strongest effects are seen from the microphysical processes. NO_NUCL reduces the number of particles at all levels (Figure 5.3), but especially (and by several orders of magnitude) in the tropopause layer where most nucleation occurs – thus producing a strong downward shift in mean position (Figure 5.4), which is strongest in the tropics, reversing the humped shape shown in BASE. NO_COND also produces a strong downward shift, but by a different route leaving the tropical "hump" intact –

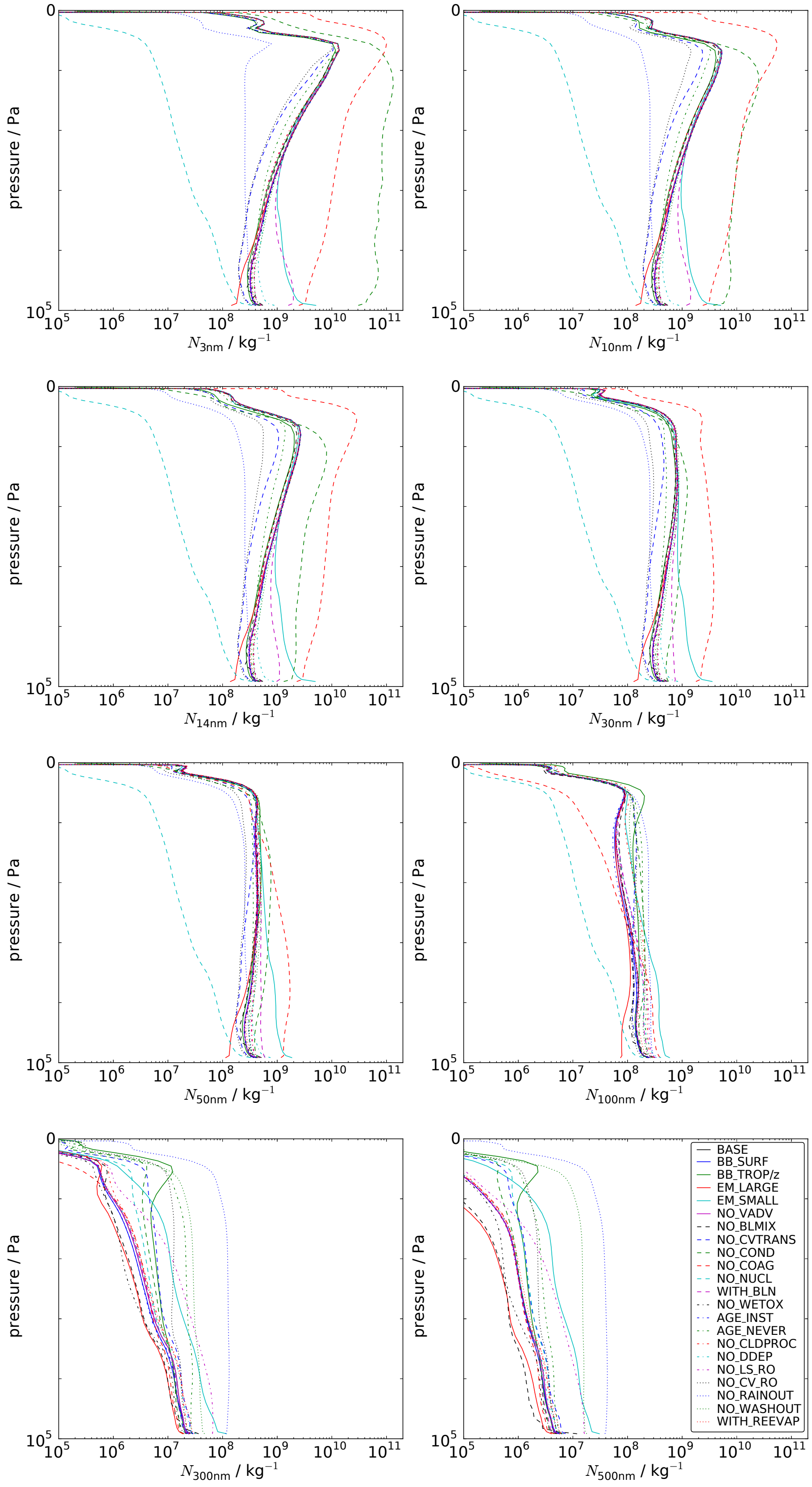

Figure 5.3: Annual and global mean vertical profiles of condensation nuclei (CN) above 3, 10, 14, 30, 50, 100, 300 and 500 nm dry diameter from the HadGEM3–UKCA sensitivity-test simulations

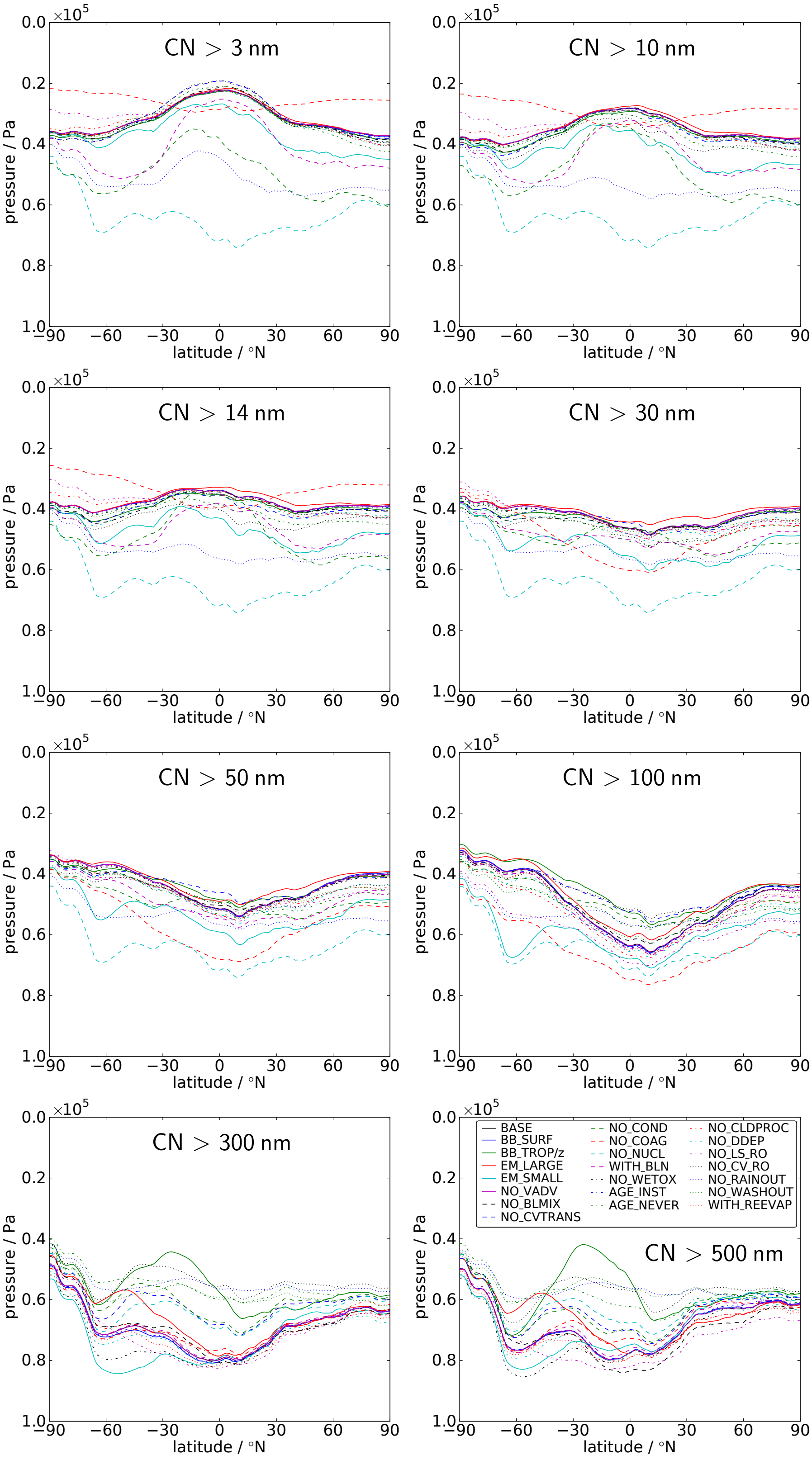

Figure 5.4: Annual and zonal mean number-weighted mean pressure level (vertical centre of number in pressure coordinates) of condensation nuclei (CN) above 3, 10, 14, 30, 50, 100, 300 and 500 nm dry diameter from the HadGEM3–UKCA sensitivity-test simulations

particle numbers increase at all levels, but especially in the lower troposphere where the condensation sink normally suppresses nucleation. NO_COAG results in a very high mean vertical position at all latitudes, although the global mean profile does not change shape much but the particle count increases by about an order of magnitude at all levels. WITH_BLN increases the particle number in the lower troposphere, causing a downward shift in mean position especially in the mid-latitudes. In addition to microphysical processes, NO_RAINOUT causes a downward shift even though CN > 3 nm is dominated by particles too small to be activated as CCN; the effect from NO_LS_RO or NO_CV_RO alone is rather small however. (Although there are no changes to the scavenging of gas-phase aerosol precursors in any of these simulations, the scavenging of larger particles will affect the condensation sink and consequently the nucleation rate.) A modest downward shift at all latitudes is also seen from EM_SMALL, which increases particle numbers in the lower troposphere where most emissions are injected.

Looking at only the larger particles (CN > 50 nm and CN > 100 nm) which may act as CCN if they have a soluble component, the picture is somewhat changed. Microphysics remain important, with NO_NUCL still reducing particle numbers at all levels and causing a downward shift, although less dramatically than at smaller sizes, while WITH_BLN no longer has much effect at all. NO_COND shows a much more modest increase in particle numbers than at smaller sizes, and acts to flatten the “U” shape of the meridional profile, mostly by an upward shift in the tropics. At these larger sizes, NO_COAG reduces the particle number especially at higher levels, leading to a downward shift at all latitudes. Wet deposition becomes much more important in this size range, with NO_LS_RO showing a downward shift at all latitudes, while NO_CV_RO shows an upward shift in the tropics; these combine in NO_RAINOUT to give a largely-flat meridional profile. There is also now a (weaker) flattening from NO_WASHOUT, and a small downward shift at all latitudes from NO_DDEP as particles collect in the lowest layer. Primary emission height and size distribution, and ageing, also become important, with BB_TROP/z showing an upward shift, EM_LARGE and EM_SMALL showing an upward and a downward shift respectively, and AGE_NEVER showing a flattening of the meridional profile.

At still larger sizes (for CN $>$ 300nm and CN $>$ 500nm), the picture changes again. The impact of wet deposition processes becomes even stronger, with NO_LS_RO, NO_CV_RO, NO_RAINOUT and NO_WASHOUT all dramatically increasing the total number of particles; NO_LS_RO concentrates the profile towards the surface, giving a downward shift at most latitudes, while the other processes show an upward shift making both the global vertical profile and meridional profile of vertical position more uniform. The impact of biomass-burning emission profiles becomes much stronger, with BB_TROP/z showing a pronounced peak in the global vertical profile around the tropopause and an upward shift concentrated in the 50°S–10°N latitude range. Primary particle size continues to be important, as do ageing and microphysics. Aqueous chemistry, boundary-layer mixing and re-evaporation also start to have an effect: NO_WETOX shows a downward shift in the southern hemisphere; NO_BLMIX shows a downward shift in the tropics and northern hemisphere for CN $>$ 500 nm (likely due to the increasing contribution of mineral dust to the particle count at larger sizes); and WITH_REEVAP shows a small downward shift at all latitudes.

A number of the processes make little difference to any of the number profiles: BB_SURF, AGE_INST, NO_VADV all look very similar to BASE.

5.3.4 Normalised direct radiative forcing

The AOD-normalised radiative forcing (NRFA) due to anthropogenic aerosol in each of the HadGEM3–UKCA configurations is shown in Figure 5.5, along with the absolute RF and anthropogenic change in AOD from which NRFA is calculated. Strong effects are seen in BB_TROP/z, NO_WETOX and NO_COND (where NRFA becomes much more strongly negative than in BASE – and in the case of NO_COND, the absolute RF also becomes stronger); also in NO_LS_RO and NO_RAINOUT (where NRFA becomes more weakly negative due to the very large increase in ΔAOD compared to the change in absolute RF); and finally in AGE_NEVER (where NRFA changes sign to become positive, because ΔAOD becomes negative although the absolute RF remains negative). A more modest weakening of NRFA is seen in NO_BLMIX, EM_LARGE and EM_SMALL (due to weaker absolute RF), and in NO_CVTRANS, WITH_REEVAP and NO_CV_RO (due to increased ΔAOD).

5.4 Discussion

Although the overall inter-model spread of the AeroCom A2.CTRL global-mean vertical profiles is well covered by the spread of profiles from the HadGEM3–UKCA process-sensitivity tests (Figure 5.1), the same is not true for the meridional variation in vertical position, where the spread from these simulations is typically narrower than that of the AeroCom models (Figure 5.2). In addition, none of the (fairly strongly perturbed) HadGEM3–UKCA simulations are able to reproduce either the strong “inverted S” shape seen in the global-mean vertical profile of several of the AeroCom models, or the “U” shape in the meridional profile of vertical position.

For sulphate, where nucleation and condensation provide a significant upper-troposphere source, a weak version of the “inverted S” shape is seen in most of the process-sensitivity test simulations, but none of the configurations enhance the shape seen in BASE to anything approaching the shape seen in e.g. ECHAM5–HAM2. For black carbon and organic aerosol, a similar shape is seen in BB_TROP/z (where biomass-burning emissions are extended all the way to the tropopause). It is very unlikely that any realistic model would actually inject such emissions as high as this, but it is possible that emissions at a lower level followed by convective transport with weak scavenging and a high detrainment level might cause a similar effect. Although the effect of switching off convective transport or scavenging in HadGEM3–UKCA

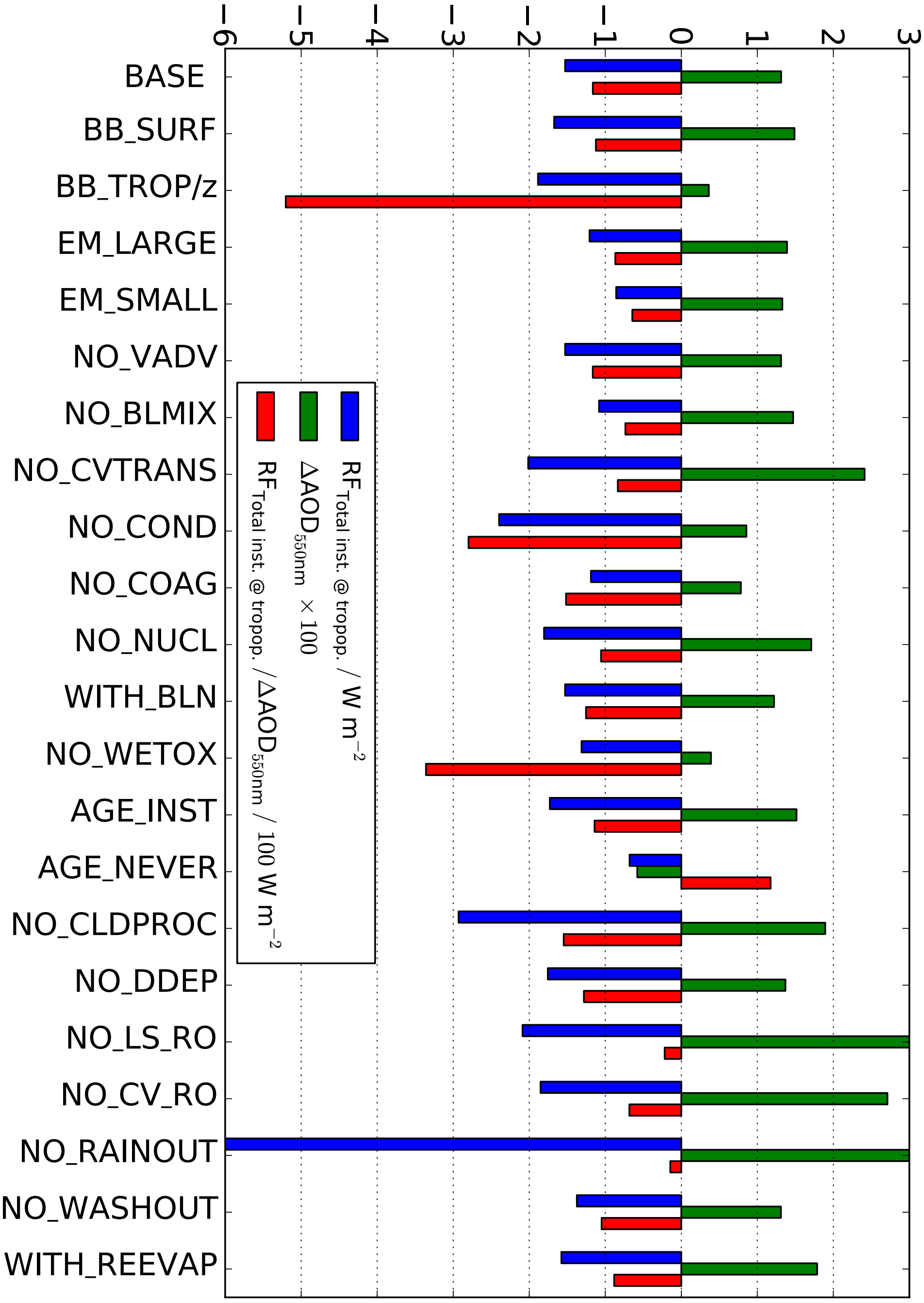

Figure 5.5: Annual and global mean direct radiative forcing (DRF), change in AOD, and AOD-normalised DRF, due to anthropogenic aerosol, for each of the HadGEM3–UKCA configurations. Note that, to fit on the same scale as the absolute DRF in W m^{-2}, the AOD has been multiplied by 100 and the AOD-normalised DRF correspondingly divided by 100.

is considered, the effect of changes to the convective parameterisation which might alter the vertical profile with which aerosol is detrained has not been tested – such an experiment might shed further light on the mechanism by which this profile shape is generated.

A “U” shape is seen in the meridional profile of vertical position for mineral dust in HadGEM3–UKCA (which is transported by a separate scheme), but not for any of the other aerosol components which are included in UKCA. The only exception is for sulphate in the NO_WETOX simulation, where (presumably due to the loss of a major free-troposphere source of sulphate) such a shape does develop. Unlike the other components, dust emissions are heavily concentrated at low latitudes, which would be expected to cause the dust burden in the tropics to be dominated by freshly-emitted dust near the surface.

The variation with particle size of the meridional profile of vertical position by number (Figure 5.4) suggests the possibility that this “U” shape (which is seen in the number profile of larger CN in HadGEM3, and inverted for smaller CN) might be related to the size distribution: shifting the balance from small nucleation- and Aitken-mode particles to larger accumulation-mode particles might produce more of a “U” shape in the mass profiles. However, no such effect is seen in NO_NUCL, where the lack of new-particle nucleation should produce such a shift in the size distribution.

For all aerosol components, only a minority of the processes show a significant effect on vertical position in HadGEM3–UKCA (although the specific processes which are important vary by component). Transport by large-scale vertical advection shows very little effect on the zonal-mean vertical position of any of the components by mass, or of CN at any size by number. This suggests that, at a typical global climate model resolution, vertical transport of aerosol is dominated by unresolved scales (i.e. convection and boundary-layer turbulence). There are further processes (nucleation, coagulation and emission size) which affect only the CN number profiles, while having very little effect on the component mass profiles.

From the changes in AOD and radiative forcing seen in Figure 5.5, it can be seen that, of the processes which affect the vertical profile of aerosol, the ones that have the greatest potential impact on direct radiative forcing are the extent of biomass-burning emissions into the free troposphere, production of sulphate by aqueous oxidation, ageing of insoluble particles, in-cloud scavenging and to a lesser extent the size distribution of primary emissions.

5.5 Summary and conclusions

This chapter has investigated the impact of a wide range of processes on aerosol vertical distribution in the HadGEM3–UKCA aerosol–climate model through a series of limiting-case process-based sensitivity tests. It was shown that the processes which have the greatest impact on the vertical distribution vary both between different aerosol components, and over the particle size spectrum.

In-cloud scavenging (both large-scale and convective) was shown to be important for all components except mineral dust (which never ages to become soluble in HadGEM3). Growth of particles by condensation from the gas phase was important for sulphate and carbonaceous aerosol, with growth by aqueous oxidation also important for sulphate. Ageing from insoluble to soluble (which controls the susceptibility to removal by in-cloud scavenging) was also important for carbonaceous aerosol. Boundary-layer mixing was of great importance for those components emitted purely at or near the surface (mineral dust and sea-salt). Dry deposition and below-cloud scavenging affected only the profile of mineral dust (which includes very large particles, and is not removed by in-cloud scavenging in this model).

In terms of particle size, microphysical processes (nucleation, condensation and coagulation) were shown to be the dominant processes in terms of the vertical profile of the smallest and most numerous particles (CN $> 3\,\mathrm{nm}$), while the size distribution and altitude of primary emissions, and removal processes, became progressively more important at larger sizes.

For the AOD-normalised direct radiative forcing, the strongest effects came mostly from processes which affect the vertical mass distribution: aqueous oxidation, ageing, in-cloud scavenging and the extent of biomass-burning emissions into the free troposphere; however there were smaller effects due to the size distribution of primary emissions, which had little effect on the vertical mass profile but did affect the CN number profiles (as well as being expected to change the optical properties of the aerosol).

From studying the process sensitivity of the vertical profiles in a single model, it cannot be determined whether the processes identified are universally the most important for controlling the vertical profile, or whether this varies amongst models. It would therefore be illuminating to conduct similar sensitivity tests with one or more other models, to establish the consistency (or otherwise) of the processes controlling the vertical profile.

In addition, the spread of vertical profiles from these HadGEM3–UKCA sensitivity-test simulations was compared with the inter-model diversity from the AeroCom Phase II control experiment. This showed that, although these processes could account for the overall spread in the global-mean AeroCom profiles, there were certain features which none of the HadGEM3–UKCA simulations could reproduce: specifically an “inverted S” shape in the global mass profiles (where the vertical mass distribution had a secondary peak in mixing ratio in the upper troposphere), and a “U” shape in the meridional profile of mass-weighted vertical position (where the centre-of-mass of aerosol was lower in the tropics than at higher latitudes).

This suggests that there are additional structural differences between the AeroCom models that are important for controlling the vertical distribution, beyond those captured by the processes considered here (e.g. in the parameterisation of convective transport). Identifying these structural differences may help to better understand the causes of the diversity between models, and thus to quantify and (with the help of observations) reduce the uncertainty in our modelling of aerosol vertical profiles and the resulting effects on Earth's climate.

Chapter 6

Summary and conclusions

Aerosol particles in the atmosphere play an important role in global and regional climate, both through direct effects on the radiative balance in the atmosphere and indirect effects via interaction with clouds and precipitation. There are both natural and anthropogenic sources of aerosol, and their effects represent some of the largest uncertainties in current estimates of human impact on climate.

Interactions between aerosol, cloud and precipitation are two-way: not only do aerosols affect the properties of clouds, including the development of precipitation, but clouds and precipitation play a role in the processing and removal of aerosol. Cloud droplets (and ice particles) take up aerosol particles either via activation as they form, or by subsequent impaction; the aerosol is then either removed from the atmosphere in precipitation, or returned to the atmosphere when droplets evaporate (or sublime). The former process (scavenging or wet deposition) represents a major sink of aerosol; the latter (cloud cycling) causes a shift toward larger aerosol particles of mixed composition, due to the coalescence of cloud droplets between formation and evaporation.

Being relatively short-lived in the atmosphere, aerosol particles are not well-mixed, and their climatic effects depend not only on the total mass of aerosol but also on its size distribution, mixing state and vertical profile. This thesis has attempted to address several aspects of this dependence, with a view to reducing the overall uncertainty in estimates of the direct and indirect effects of aerosol. The approach has been primarily model-based, but using satellite and in-situ aircraft observations to evaluate and constrain the model results.

6.1 Summary of work presented in previous chapters

The extent to which aerosol particles (and indeed water) are repeatedly cycled through cloud is not well constrained by direct observations. Chapter 2 aimed to quantify this in order to assess its potential role in controlling the size distribution and mixing state of aerosol. That was achieved using simulations with the HadGEM3–UKCA global aerosol–climate model, and the results compared with two previous studies (one based on a simple global budget argument, and the other using a different global model), to establish the consistency of estimates from different models.

A method was developed to diagnose the cycling rates of both water and aerosol through large-scale cloud in the model, based on the increments to cloud water and cloud fraction from the prognostic cloud scheme and the diagnostic split between in-cloud and interstitial aerosol assumed by the in-cloud nucleation scavenging scheme.

A one-year simulation with this model showed water cycling on average 0.96 times through large-scale cloud, and aerosol mass 0.17 times. These figures are lower than those of Hoose et al. (2008a) using ECHAM5–HAM (1.8 and 0.53) and Pruppacher and Jaenicke (1995) from a global budget argument (2.6 and 0.4). However, the figure for HadGEM3–UKCA was found to vary considerably between the different aerosol components, according to the dominant removal mechanism. Sulphate (mostly removed by wet deposition, and with significant in-cloud production) was cycled 2.7 times, while sea-salt (mostly removed by dry deposition) was only cycled 0.13 times, giving a range much larger than the spread of the three all-aerosol estimates.

Differences in the split between large-scale and convective cloud may also play a role, as the analysis of Pruppacher and Jaenicke suggests that including convective cloud dramatically increases the number of cycles.

Moving on to consider the influence of precipitating cloud on aerosol, Chapter 3 asked to what extent model representations of the effects of in-cloud scavenging on the global distribution and transport of aerosol can be improved through introducing greater physical realism. To this end, several shortcomings of the aerosol scavenging scheme in HadGEM3–UKCA were identified, and potential improvements proposed and evaluated.

A physically-detailed approach was proposed for scavenging by large-scale cloud and precipitation, aiming for maximum consistency with the microphysics of the large-scale precipitation scheme. This would track aerosol through cloud water, ice, rain and snow until it is either deposited at the surface or re-released upon evaporation or sublimation. However, the hydrometeor size distributions are all assumed in the bulk microphysics of HadGEM3. Although consistency with these assumed distributions can in theory be achieved (as derived in Appendix A), their use is likely to negate the aims of greater physical realism and reduced reliance on arbitrary parameters such that the complexity of this approach is unwarranted.

It was then shown how improvements could be made within the existing framework, by (i) replacing the fixed rainout timescale with a first-order loss rate proportional to the rate at which cloud water is converted to rain in the large-scale precipitation scheme, (ii) by moving convective scavenging into the convection scheme itself, so that these are no longer operator-split, and (iii) by accounting for the aerosol released when large-scale rain evaporates.

The first two both produced a decrease in global aerosol burdens and aerosol optical depth (AOD), as large-scale and convective scavenging respectively became more efficient at removing aerosol from the atmosphere; these decreases in AOD worsen the negative bias of this version of the model compared to MODIS. Changes in more recent versions of HadGEM3–UKCA, however, have led to a positive AOD bias which appears to be reduced by the in-plume convective scavenging scheme.

For the proportional-rate large-scale scheme, the simulated annual global mean MODIS-collocated 550 nm AOD decreased from 0.128 to 0.118 (compared to 0.159 from MODIS), but the correlation in log-AOD over the days and grid points improved (r^2 increased from 0.294 to 0.309) – suggesting that the process representation was an improvement, although compensating errors elsewhere were unmasked.

For the in-plume convective scavenging, the simulated year-2009 AOD decreased from 0.088 to 0.057 (compared to 0.168 from MODIS), while the correlation again increased from 0.289 to 0.317. In this case, the reduction in aerosol had a strong vertical profile with accumulation-mode aerosol (which represents most of the mass) drastically reduced in the middle and upper troposphere. Additionally, increased nucleation- and Aitken-mode aerosol was seen, which was likely due to the reduced condensation sink leading to enhanced nucleation of new sulphate particles.

In the case of aerosol release from evaporating precipitation, the effects on global aerosol burdens and AOD were modest, but increases of a factor of two in number and mass were seen in regions of clean marine stratocumulus where the model is known to underestimate the number of cloud condensation nuclei (CCN), and where the indirect effect is likely to be particularly sensitive to an increase in CCN.

The vertical distribution of aerosol is not well constrained by observations on the global scale, due to the limitations of remote sensing techniques and the limited spatial and temporal coverage of in-situ observations. Aiming to provide further constraints on the vertical profile and the processes controlling it, methods were developed in Chapter 4 for evaluating aerosol–climate models against observations from large-scale aircraft campaigns. These methods were applied to investigate the impact of convective scavenging and biomass-burning emissions on the vertical profile of black carbon in the HadGEM3–UKCA and ECHAM5–HAM2 models.

By running the models in nudged configurations and interpolating their output onto the flight track, a detailed pointwise comparison was made between the simulated mass of black carbon (BC) aerosol and in-situ aircraft observations from a Single-Particle Soot Photometer (SP2) flown during the HIPPO campaign. These measurements were also used to evaluate column-integrated BC burdens from the two models, which are a more direct output than the optical or radiative properties which can be evaluated via remote sensing.

Both models over-predicted BC burden compared to the HIPPO measurements, by up to an order of magnitude in remote regions, suggesting that the BC lifetime in the models is too long. In HadGEM3–UKCA, the largest discrepancy (an excess in the tropical upper troposphere) was eliminated by replacing the standard operator-split convective scavenging scheme with the in-plume scheme of Section 3.4. This improved the simulated column burdens, bringing them within the estimated error bounds of those derived from the HIPPO observations at many locations, and also the vertical distribution, giving a statistically significant increase in the pointwise correlation with all three phases of HIPPO included in the analysis (r increased from 0.22 to 0.41, 0.27 to 0.42, and 0.51 to 0.65 for HIPPO-1, -2, and -3, respectively).

In both models, a smaller and not statistically significant improvement was seen when changing from GFED2 to the newer GFED3.1 biomass-burning emissions inventory, and there was virtually no change in ECHAM5–HAM2 between using these emissions at monthly or 3-hourly time resolution.

It was also shown in HadGEM3–UKCA that the model–observation correlation was increased in nudged simulations compared to their free-running equivalents, and furthermore that the difference in correlation between configurations was enhanced. In particular, the improvement from in-plume convective scavenging could only be shown to be statistically significant when the simulations were nudged.

Having demonstrated the importance of convective scavenging for the vertical profile of black carbon, Chapter 5 broadened the focus to ask more generally what processes are responsible for controlling the vertical distribution of aerosol, and quantify their impact on the direct radiative effect. This was investigated using a series of limiting-case process-sensitivity tests in HadGEM3–UKCA, for a wide range of processes. This showed that the processes having the strongest impact on the vertical distribution vary both between different aerosol components, and over the particle size spectrum.

In-cloud scavenging was found to be important for all components except mineral dust (which does not interact with cloud at all in this model). Growth by condensation from the gas phase was important for sulphate and carbonaceous aerosol, with aqueous oxidation of dissolved SO_2 in cloud droplets also important for sulphate. The insoluble-to-soluble transition (ageing) and altitude of primary emissions were also important for carbonaceous aerosol. Boundary-layer mixing was very important for mineral dust and sea-salt, which are emitted purely at or near the surface. Dry deposition and below-cloud scavenging only had a significant effect on the vertical profile of mineral dust.

Microphysical processes dominated the vertical profile of the smallest particles, as represented by condensation nuclei larger than 3 nm diameter (CN $>$ 3 nm). At larger sizes, the size distribution and altitude of primary emissions, and removal processes, became progressively more important.

The strongest effects on the AOD-normalised direct radiative forcing due to anthropogenic aerosol came from the processes affecting the vertical mass distribution (aqueous oxidation, ageing, in-cloud scavenging and the extent of biomass-burning emissions into the free troposphere), although there were also smaller effects due the size distribution of primary emissions.

There is a substantial diversity in aerosol vertical profiles between current aerosol–climate models, and Chapter 5 also asked to what extent this diversity can be accounted for by the processes identified as controlling the vertical profile. To answer this, the spread of vertical profiles from the sensitivity-test simulations was compared with the inter-model diversity from the AeroCom Phase II models. Although the processes considered could account for the overall spread in the global-mean AeroCom profiles, there were two particular features common to multiple models which none of the HadGEM3–UKCA simulations could reproduce: an “inverted S” shape in the global mass profiles, and a “U” shape in the meridional profile of mass-weighted vertical position. This suggests that there are further structural differences between some of the models that influence the vertical distribution, beyond those studied in HadGEM3–UKCA in this chapter.

6.2 General conclusions and recommendations for further work

The work presented here highlights the importance of interactions with cloud and precipitation in controlling the global distribution of atmospheric aerosol.

The results from Chapter 2 suggest that sulphate and carbonaceous aerosol in the atmosphere have, on average, been cycled through non-precipitating large-scale cloud more than once. Although the number of cycles is less than the estimates of Pruppacher and Jaenicke (1995), this is consistent with the work of Hoose et al. (2008a) and Croft (2011, ch. 4). This suggests that the shift towards larger particle sizes and greater internal mixing from the coalescence of aerosol-containing cloud droplets is likely to play a significant role in controlling the size distribution and mixing state of aerosol on a global scale. It is therefore expected that a realistic parameterisation of this mechanism is important if models are to accurately simulate the size distribution and mixing state of aerosol able to act as CCN.

In a two-moment cloud scheme, where droplet number is a prognostic variable, the effect on aerosol can be modelled explicitly in the parameterisation of droplet coalescence. However, in a one-moment cloud scheme such as that in HadGEM3, where droplet number is a diagnostic function of liquid water content, this is not possible. While switching to a two-moment cloud scheme would bring many benefits, if this is not practical then consideration should be given to a parameterisation of in-cloud aerosol coalescence based only on bulk cloud variables. Such a scheme is likely to have limited accuracy, but an improvement on the existing “cloud processing” mechanism in UKCA (which simply shifts particles larger than 37.5 nm from the Aitken to the accumulation mode) should be possible. It is also recommended that cycling through convective cloud should be investigated further, and its effects parameterised if it is found to be important – as the work of Pruppacher and Jaenicke (1995) and Croft (2011, ch. 4) suggest is the case.

Precipitating cloud also has a strong influence on aerosol via scavenging and wet deposition. The work in Chapter 3 shows that increasing the physical realism with which scavenging is represented in HadGEM3–UKCA can lead to substantial changes in the global burden, geographical distribution and vertical profile of aerosol. In particular, when convective scavenging is tightly coupled with convective transport using an in-plume scheme, the amount of aerosol reaching the middle and upper troposphere is much reduced compared to when an operator-split scheme is used. This also leads to a reduction in column burdens globally, but especially in remote regions which suggests that this is a key process in controlling the long-range transport of aerosol. The work in Chapter 4 (and Kipling et al., 2013) demonstrates that, for black carbon at least, this reduced upward and long-range transport produces a better match to in-situ aircraft observations. It is therefore recommended that convective scavenging and transport should not be operator-split in models, and that further consideration should be given to accurately modelling its strength, given its strong role in controlling the global and vertical distribution of aerosol.

Although the microphysically-detailed large-scale scavenging scheme described in Section 3.2 was not implemented due to the likely limited benefit of such detail in the context of a one-moment bulk cloud scheme with assumed hydrometeor size distributions, the large role played by cloud cycling, scavenging and wet deposition in the life cycle of atmospheric aerosol suggests that consideration should be given to such a scheme in the context of a future two-moment cloud and precipitation scheme.

The inclusion of aerosol release by re-evaporation of falling precipitation has only a modest impact globally, as shown in Section 3.5, but leads to factor-of-two increases in accumulation-mode aerosol number in many regions of persistent marine stratocumulus. These are precisely the regions where the indirect aerosol effects are thought to be of particular importance. Further experiments investigating the impact of the re-evaporation scheme in a version of the model containing a representation of the first and second indirect effects (as used in West et al., 2013) are therefore recommended.

The model evaluation carried out in Chapter 4 also serves to demonstrate the powerful role that vertically-resolved in-situ aircraft observations can have in evaluating aerosol–climate models, especially when coupled with nudging and flight-track sampling in the model. Although the evaluation carried out here focused on the remote Pacific region, it is suggested that similar analyses using data from campaigns in other regions would be beneficial. In particular, obtaining similar observational constraints in near-source regions would complement this work well – and would be better suited to resolving questions related to emission processes.

The analysis presented in Chapter 5 confirms the importance of in-cloud scavenging (both large-scale and convective) as one of the processes having the strongest effect on the vertical distribution of aerosol, and identifies the other processes having large effects. These vary between the different aerosol components, but in general the vertical distribution of the larger particles (and thus the total mass) is mostly controlled by removal and secondary production processes, while that of the smaller particles is heavily influenced by the microphysical processes. This suggests that, while a bulk mass-based evaluation can constrain source and removal processes (as in Chapter 4), a size-resolved evaluation using similar techniques would have the potential to constrain aerosol microphysics as well.

Because the range of processes studied in Chapter 5 appears insufficient to reproduce broad features of the aerosol distribution appearing in several of the AeroCom models, it is recommended that further investigations be carried out to identify the structural factors in the models which are responsible for these features. It is also suggested that equivalent process-based sensitivity tests be conducted in additional models, to establish the extent to which the processes controlling the vertical distribution are consistent between models – which would give increased confidence that these are indeed the processes which determine the vertical profile of aerosol in the atmosphere.

Appendix A

Mathematical formulation of a microphysically-consistent scavenging scheme for HadGEM3–UKCA

This appendix presents a derivation of the continuous equations representing the microphysically-detailed large-scale scavenging scheme described in Section 3.4, and their discretisation to the model grid and timestep.

The microphysical transfer terms in Table 3.2 can be grouped into mass transfers between the different phases (these are all in mass of water per unit mass of air per unit time, i.e. $\mathrm{kg_{(water)}\,kg^{-1}_{(air)}\,s^{-1}}$):

$$T_{q_{\mathrm{cl}}\rightarrow q} = P_{\mathrm{LSETEV}} + P_{\mathrm{IDEP1}} \tag{A.1}$$

$$T_{q_{\mathrm{cl}}\rightarrow q_{\mathrm{R}}} = P_{\mathrm{RACW}} + P_{\mathrm{RAUT}} \tag{A.2}$$

$$T_{q_{\mathrm{R}}\rightarrow q} = P_{\mathrm{REVP}} \tag{A.3}$$

$$T_{q_{\mathrm{cl}}\rightarrow q_{\mathrm{cfc}}} = P_{\mathrm{IACW}} + P_{\mathrm{IPRM1}} + P_{\mathrm{IFRW}} \tag{A.4}$$

$$T_{q\rightarrow q_{\mathrm{cfc}}} = P_{\mathrm{IDEP1}} + P_{\mathrm{IDEP2}} + P_{\mathrm{IPRM2}} \tag{A.5}$$

$$T_{q_{\mathrm{cfc}}\rightarrow q_{\mathrm{R}}} = P_{\mathrm{IMLT}} \tag{A.6}$$

$$T_{q_{\mathrm{cfc}}\to q} = P_{\mathrm{ISUB}} + P_{\mathrm{IMLTEV}} \tag{A.7}$$

$$T_{q_{\mathrm{R}}\to q_{\mathrm{cfc}}} = P_{\mathrm{IACR}} \tag{A.8}$$

$$T_{q_{\mathrm{cl}}\to q_{\mathrm{cfa}}} = P_{\mathrm{SACW}} + P_{\mathrm{SDEP1}} \tag{A.9}$$

$$T_{q\to q_{\mathrm{cfa}}} = P_{\mathrm{SDEP2}} \tag{A.10}$$

$$T_{q_{\mathrm{cfa}}\to q_{\mathrm{R}}} = P_{\mathrm{SMLT}} \tag{A.11}$$

$$T_{q_{\mathrm{cfa}}\to q} = P_{\mathrm{SSUB}} + P_{\mathrm{SMLTEV}} \tag{A.12}$$

$$T_{q_{\mathrm{R}}\to q_{\mathrm{cfa}}} = P_{\mathrm{SACR}} \tag{A.13}$$

$$T_{q_{\mathrm{cfc}}\to q_{\mathrm{cfa}}} = P_{\mathrm{SAUT}} + P_{\mathrm{SACI}} \tag{A.14}$$

$$T_{q_{\mathrm{cfa}}\to q_{\mathrm{graup}}} = P_{\mathrm{GAUT}} + P_{\mathrm{GACS}} \tag{A.15}$$

$$T_{q_{\mathrm{cl}}\to q_{\mathrm{graup}}} = P_{\mathrm{GACW}} \tag{A.16}$$

$$T_{q_{\mathrm{graup}}\to q_{\mathrm{R}}} = P_{\mathrm{GMLT}}. \tag{A.17}$$

The total mass mixing ratio $m_{\mathrm{T}}^{(i)}$ of a chemical species i is split into a gaseous portion $m^{(i)}$ and portions taken up by each of the water phases ($m_{\mathrm{cl}}^{(i)}$, $m_{\mathrm{cfc}}^{(i)}$, $m_{\mathrm{cfa}}^{(i)}$, $m_{\mathrm{R}}^{(i)}$, $m_{\mathrm{graup}}^{(i)}$) so that

$$m_{\mathrm{T}}^{(i)} = m_{\mathrm{cl}}^{(i)} + m_{\mathrm{cfc}}^{(i)} + m_{\mathrm{cfa}}^{(i)} + m_{\mathrm{R}}^{(i)} + m_{\mathrm{graup}}^{(i)} + m^{(i)}. \tag{A.18}$$

For aerosol species, the “free” or interstitial aerosol $m^{(i)}$ is divided into modes $m_{M}^{(i)}$, as in the existing scheme, while the portion taken up by the water phases follows the size distribution assumed for droplets or ice particles. Thus the same equation applies, with

$$m^{(i)} = \sum_{M\in\mathcal{M}} m_{M}^{(i)}, \tag{A.19}$$

where $\mathcal{M}$ is the set of aerosol modes, i.e.

$$m_{\mathrm{T}}^{(i)} = m_{\mathrm{cl}}^{(i)} + m_{\mathrm{cfc}}^{(i)} + m_{\mathrm{cfa}}^{(i)} + m_{\mathrm{R}}^{(i)} + m_{\mathrm{graup}}^{(i)} + \sum_{M\in\mathcal{M}} m_M^{(i)}. \tag{A.20}$$

The evolution of water in each phase in the large-scale precipitation scheme is given by

$$\frac{\partial q_x}{\partial t} = \sum_{y\in\mathcal{P}} \left(T_{q_y\to q_x} - T_{q_x\to q_y} \right) + \frac{1}{\rho}\frac{\partial F_{q_x\downarrow}}{\partial z} \tag{A.21}$$

for each $x \in \mathcal{P}$, where $\mathcal{P}$ is the set of water phases and $F_{x\downarrow}$ the downward precipitation flux of water in that phase (an area flux, i.e. mass of water per unit horizontal area per unit time or $\mathrm{kg\,m^{-2}\,s^{-1}}$).

The corresponding evolution of chemical or aerosol species in that water is given by

$$\frac{\partial m_x^{(i)}}{\partial t} = S_{q_x}^{(i)} - R_{q_x}^{(i)} + \sum_{y\in\mathcal{P}'} \left(\frac{T_{q_y\to q_x} m_y^{(i)}}{q_y} - \frac{T_{q_x\to q_y} m_x^{(i)}}{q_x} \right) + \frac{1}{\rho}\frac{\partial}{\partial z}\left(\frac{F_{q_x\downarrow} m_x^{(i)}}{q_x} \right) \tag{A.22}$$

for each $x \in \mathcal{P}'$, where $\mathcal{P}'$ is the set of water phases excluding vapour, $S_{q_x}^{(i)}$ is take-up (scavenging) from the gaseous/interstitial mode(s), and $R_{q_x}^{(i)}$ is release to those modes.

Note that the $T_{q_x\to q_y} m_x^{(i)}/q_x$ terms are ill-defined where q_x approaches zero. However, where q_x is small, it is clear that the transfer of chemical/aerosol out of this phase must also be small. Thus to avoid division by zero, the terms are dropped altogether when q_x is below a threshold value.

For the evolution of chemical species in the gaseous state, or total interstitial aerosol across all modes,

$$\frac{\partial m^{(i)}}{\partial t} = \sum_{x\in\mathcal{P}'} \left(R_{q_x}^{(i)} - S_{q_x}^{(i)} \right). \tag{A.23}$$

For aerosol species, it is necessary to consider the size spectrum, $S^{(i)}_{nx}(r)$ or $R^{(i)}_{nx}(r)$, of the aerosol taken up or released:

$$\frac{\partial n^{(i)}(r)}{\partial t} = \sum_{x\in\mathcal{P}'} \left(R^{(i)}_{nx}(r) - S^{(i)}_{nx}(r) \right), \tag{A.24}$$

with the total number and mass rates given by:

$$S^{(i)}_{Nx} = \int_0^\infty S^{(i)}_{nx}(r)\,\mathrm{d}r \qquad S^{(i)}_{qx} = \frac{4}{3}\pi\rho^{(i)} \int_0^\infty r^3 S^{(i)}_{nx}(r)\,\mathrm{d}r \tag{A.25}$$

$$R^{(i)}_{Nx} = \int_0^\infty R^{(i)}_{nx}(r)\,\mathrm{d}r \qquad R^{(i)}_{qx} = \frac{4}{3}\pi\rho^{(i)} \int_0^\infty r^3 R^{(i)}_{nx}(r)\,\mathrm{d}r, \tag{A.26}$$

assuming spherical aerosol particles. Given that at present the model only has a one-moment bulk scheme for cloud and precipitation, this requires assumed size distributions for cloud water droplets, raindrops and ice particles. These are considered for each process in turn below, based on those used by the precipitation scheme itself (Wilkinson et al., 2009). It is likely that a future version of HadGEM will gain a multi-moment prognostic cloud and precipitation scheme; when this is used, the simulated hydrometeor size distribution should be used instead.

A.1 Processes releasing aerosol from water phases to free/interstitial modes

A.1.1 LSETEV: evaporation of settling droplets

The implementation of droplet settling in the large-scale precipitation scheme assumes a Khrgian–Mazin gamma distribution $\Gamma(3, \theta_{\mathrm{cl}})$ of droplet radii,

$$n_{\mathrm{cl}}(r) = \frac{N_{\mathrm{cl}}}{2\theta_{\mathrm{cl}}^3} r^2 \mathrm{e}^{-\frac{r}{\theta_{\mathrm{cl}}}}, \tag{A.27}$$

where $N_{\mathrm{cl}} = \int_0^\infty n_{\mathrm{cl}}(r)\,\mathrm{d}r$ is the total droplet number density (currently fixed values over land and sea, although it could be diagnosed via aerosol activation), and the parameter θ_{cl} is given by

$$\theta_{\mathrm{cl}} = \sqrt[3]{\frac{\rho q_{\mathrm{cl}}}{80\pi\rho_{\mathrm{w}}N_{\mathrm{cl}}}}, \tag{A.28}$$

so that $\rho q_{\mathrm{cl}} = \frac{4}{3}\pi\rho_{\mathrm{w}}\int_0^\infty r^3 n_{\mathrm{cl}}(r)\,\mathrm{d}r$ (Wilkinson et al., 2009, §6.2.1), where spherical droplets are assumed. The droplets are assumed to fall at a terminal speed of:

$$V_{\mathrm{cl}}(r) = \mathcal{K}_1 r^2, \tag{A.29}$$

where $\mathcal{K}_1$ is a function of temperature only (Wilkinson et al., 2009, §6.2.1).

The downward number flux of droplets with radius r is thus

$$\begin{aligned} F_{n_{\mathrm{cl}}\downarrow}(r) &= n_{\mathrm{cl}}(r)V_{\mathrm{cl}}(r) && \text{(A.30)}\\ &= \frac{\mathcal{K}_1 N_{\mathrm{cl}}}{2\theta_{\mathrm{cl}}^3} r^4 \mathrm{e}^{-\frac{r}{\theta_{\mathrm{cl}}}}, && \text{(A.31)} \end{aligned}$$

giving a total downward mass flux

$$\begin{aligned} F_{q_{\mathrm{cl}}\downarrow} &= \frac{4}{3}\pi\rho_{\mathrm{w}}\int_0^\infty r^3 F_{n_{\mathrm{cl}}\downarrow}(r)\,\mathrm{d}r && \text{(A.32)}\\ &= \frac{4}{3}\pi\rho_{\mathrm{w}}\int_0^\infty \frac{\mathcal{K}_1 N_{\mathrm{cl}}}{2\theta_{\mathrm{cl}}^3} r^7 \mathrm{e}^{-\frac{r}{\theta_{\mathrm{cl}}}}\,\mathrm{d}r && \text{(A.33)}\\ &= 42\mathcal{K}_1\theta_{\mathrm{cl}}^2\rho q_{\mathrm{cl}}. && \text{(A.34)} \end{aligned}$$

Assuming that the distribution of droplets falling into cloudy and clear air are identical, the number rate of evaporation for droplets of radius r is

$$\begin{aligned} T_{n_\mathrm{cl}\to q}(r)\big|_\mathrm{LSETEV} &= \frac{T_{q_\mathrm{cl}\to q}\big|_\mathrm{LSETEV}}{F_{q_\mathrm{cl}\downarrow}} F_{n_\mathrm{cl}\downarrow}(r) && \text{(A.35)}\\ &= \frac{T_{q_\mathrm{cl}\to q}\big|_\mathrm{LSETEV}}{F_{q_\mathrm{cl}\downarrow}} \frac{\mathcal{K}_1 N_\mathrm{cl}}{2\theta_\mathrm{cl}^3} r^4 \mathrm{e}^{-\frac{r}{\theta_\mathrm{cl}}} && \text{(A.36)}\\ &= \frac{N_\mathrm{cl}\; T_{q_\mathrm{cl}\to q}\big|_\mathrm{LSETEV}}{84\theta_\mathrm{cl}^5 \rho q_\mathrm{cl}} r^4 \mathrm{e}^{-\frac{r}{\theta_\mathrm{cl}}}, && \text{(A.37)} \end{aligned}$$

i.e. a $\Gamma(5, \theta_\mathrm{cl})$ distribution with a total number rate

$$T_{N_\mathrm{cl}\to q}\big|_\mathrm{LSETEV} = \frac{2N_\mathrm{cl}\; T_{q_\mathrm{cl}\to q}\big|_\mathrm{LSETEV}}{7\rho q_\mathrm{cl}}. \tag{A.38}$$

Assuming a uniform concentration of the aerosol species i in the cloud water (which, as noted earlier, may not be realistic for small droplets), a spherical droplet of radius r_cl leaves behind a spherical aerosol particle of dry radius

$$r^{(i)} = \phi_\mathrm{cl}^{(i)} r_\mathrm{cl}, \tag{A.39}$$

where

$$\phi_\mathrm{cl}^{(i)} = \sqrt[3]{\frac{\rho_\mathrm{w}}{\rho^{(i)}} \frac{m_\mathrm{cl}^{(i)}}{q_\mathrm{cl}}}, \tag{A.40}$$

so that the dry size distribution of released aerosol particles is given by

$$R_{n_\mathrm{cl}}^{(i)}\Big|_\mathrm{LSETEV} \left(r^{(i)}\right) \mathrm{d}r^{(i)} = T_{n_\mathrm{cl}\to q}\big|_\mathrm{LSETEV} \left(r_\mathrm{cl}\right) \mathrm{d}r_\mathrm{cl}, \tag{A.41}$$

which leads to a $\Gamma(5, \theta_{\mathrm{cl}}^{(i)})$ distribution:

$$R_{n_{\mathrm{cl}}}^{(i)}\Big|_{\mathrm{LSETEV}}\left(r^{(i)}\right) = \frac{T_{q_{\mathrm{cl}}\to q}\big|_{\mathrm{LSETEV}}}{F_{q_{\mathrm{cl}}\downarrow}} \frac{\mathcal{K}_1 N_{\mathrm{cl}} \theta_{\mathrm{cl}}^2}{2\left(\theta_{\mathrm{cl}}^{(i)}\right)^5} \left(r^{(i)}\right)^4 \mathrm{e}^{-\frac{r^{(i)}}{\theta_{\mathrm{cl}}^{(i)}}} \tag{A.42}$$

$$= \frac{N_{\mathrm{cl}}\, T_{q_{\mathrm{cl}}\to q}\big|_{\mathrm{LSETEV}}}{84\rho q_{\mathrm{cl}} \left(\theta_{\mathrm{cl}}^{(i)}\right)^5} \left(r^{(i)}\right)^4 \mathrm{e}^{-\frac{r^{(i)}}{\theta_{\mathrm{cl}}^{(i)}}}, \tag{A.43}$$

where

$$\theta_{\mathrm{cl}}^{(i)} = \theta_{\mathrm{cl}} \phi_{\mathrm{cl}}^{(i)} \tag{A.44}$$

$$= \sqrt[3]{\frac{\rho m_{\mathrm{cl}}^{(i)}}{80\pi N_{\mathrm{cl}} \rho^{(i)}}}. \tag{A.45}$$

This gives a total number rate

$$R_{N_{\mathrm{cl}}}^{(i)}\Big|_{\mathrm{LSETEV}} = T_{N_{\mathrm{cl}}\to q}\big|_{\mathrm{LSETEV}} \tag{A.46}$$

$$= \frac{2N_{\mathrm{cl}}\, T_{q_{\mathrm{cl}}\to q}\big|_{\mathrm{LSETEV}}}{7\rho q_{\mathrm{cl}}}, \tag{A.47}$$

and mass rate

$$R_{q_{\mathrm{cl}}}^{(i)}\Big|_{\mathrm{LSETEV}} = \frac{m_{\mathrm{cl}}^{(i)}}{q_{\mathrm{cl}}} T_{q_{\mathrm{cl}}\to q}\big|_{\mathrm{LSETEV}}. \tag{A.48}$$

A.1.2 REVP: evaporation of rain

The large-scale precipitation scheme assumes a Marshall-Palmer negative-exponential distribution $\mathrm{Exp}(\lambda_{\mathrm{R}}) \equiv \Gamma(1, \frac{1}{\lambda_{\mathrm{R}}})$ for raindrop diameters:[1]

$$n_{\mathrm{R}}(D) = n_{\mathrm{a,R}} \lambda_{\mathrm{R}}^{n_{\mathrm{b,R}}} \mathrm{e}^{-\lambda_{\mathrm{R}} D}, \tag{A.49}$$

---

[1] The precipitation scheme (Wilkinson et al., 2009) uses diameters for raindrops and ice particles, but radii for cloud droplets. Here radii are preferred, except where diameter-based formulations are inherited from the documentation, as in this case.

where $n_{\mathrm{a,R}}$ and $n_{\mathrm{b,R}}$ are fixed parameters (note that $n_{\mathrm{b,R}}$ is a non-integer exponent), and λ_{R} will be determined from the rainfall rate (Wilkinson et al., 2009, §4.1).

The raindrops are assumed to fall at a terminal speed of:

$$V_{\mathrm{R}}(D) = c_{\mathrm{R}} D^{d_{\mathrm{R}}} \left(\frac{\rho_0}{\rho}\right)^{\mathcal{G}_{\mathrm{R}}}, \tag{A.50}$$

where c_{R}, d_{R}, $\mathcal{G}_{\mathrm{R}}$ and ρ_0 are fixed parameters (Wilkinson et al., 2009, §4.4); note that the exponents are non-integer. In fact, break-up of large drops is thought to lead to a significant number of smaller drops travelling at super-terminal speed due to their finite relaxation time (Montero-Martínez et al., 2009); however the assumption of the precipitation scheme is followed here.

The downward number flux of raindrops with diameter D is thus

$$F_{n_{\mathrm{R}}\downarrow}(D) = n_{\mathrm{R}}(D) V_{\mathrm{R}}(D) \tag{A.51}$$

$$= n_{\mathrm{a,R}} c_{\mathrm{R}} \left(\frac{\rho_0}{\rho}\right)^{\mathcal{G}_{\mathrm{R}}} \lambda_{\mathrm{R}}^{n_{\mathrm{b,R}}} D^{d_{\mathrm{R}}} \mathrm{e}^{-\lambda_{\mathrm{R}} D}, \tag{A.52}$$

where the parameter λ_{R} is given by

$$\lambda_{\mathrm{R}} = \left(\frac{\pi c_{\mathrm{R}} \left(\frac{\rho_0}{\rho}\right)^{\mathcal{G}_{\mathrm{R}}} \rho_{\mathrm{w}} n_{\mathrm{a,R}}}{F_{q_{\mathrm{R}}\downarrow}}\right)^{\frac{1}{4+d_{\mathrm{R}}-n_{\mathrm{b,R}}}}, \tag{A.53}$$

so that $F_{q_{\mathrm{R}}\downarrow} = \frac{\pi}{6}\rho_{\mathrm{w}} \int_0^\infty D^3 n_{\mathrm{R}}(D) V_{\mathrm{R}}(D)\,\mathrm{d}D$ (spherical raindrops are assumed).

Under the first of the proposed assumptions for the size-dependent evaporation of raindrops in Section 3.2 (no droplets shrink, and a uniform proportion across the size spectrum are removed), the complete-evaporation number rate for raindrops of diameter D is given by

$$T_{n_\mathrm{R}\to q}(D)\big|_\mathrm{REVP} = \frac{T_{q_\mathrm{R}\to q}\big|_\mathrm{REVP}}{F_{q_\mathrm{R}\downarrow}} F_{n_\mathrm{R}\downarrow}(D) \tag{A.54}$$

$$= \frac{T_{q_\mathrm{R}\to q}\big|_\mathrm{REVP}}{F_{q_\mathrm{R}\downarrow}} n_\mathrm{a,R} c_\mathrm{R} \left(\frac{\rho_0}{\rho}\right)^{\mathcal{G}_\mathrm{R}} \lambda_\mathrm{R}^{n_\mathrm{b,R}} D^{d_\mathrm{R}} \mathrm{e}^{-\lambda_\mathrm{R} D}, \tag{A.55}$$

and thus follows a $\Gamma(d_\mathrm{R}+1, \frac{1}{\lambda_\mathrm{R}})$ distribution with a total number rate

$$T_{N_\mathrm{R}\to q}\big|_\mathrm{REVP} = \frac{\Gamma\left(d_\mathrm{R}+1\right) T_{q_\mathrm{R}\to q}\big|_\mathrm{REVP}}{F_{q_\mathrm{R}\downarrow}} n_\mathrm{a,R} c_\mathrm{R} \left(\frac{\rho_0}{\rho}\right)^{\mathcal{G}_\mathrm{R}} \lambda_\mathrm{R}^{n_\mathrm{b,R}-d_\mathrm{R}-1} \tag{A.56}$$

$$= \frac{\Gamma\left(d_\mathrm{R}+1\right) T_{q_\mathrm{R}\to q}\big|_\mathrm{REVP}}{\pi\rho_\mathrm{w}} \left(\frac{\pi c_\mathrm{R} \left(\frac{\rho_0}{\rho}\right)^{\mathcal{G}_\mathrm{R}} \rho_\mathrm{w} n_\mathrm{a,R}}{F_{q_\mathrm{R}\downarrow}}\right)^{\frac{3}{4+d_\mathrm{R}-n_\mathrm{b,R}}} . \tag{A.57}$$

Assuming a uniform concentration of the aerosol species i in the rain water (not necessarily realistic, as noted earlier, but probably more so than for cloud droplets since growth to raindrop size is dominated by coalescence), a spherical droplet of diameter D_R leaves behind a spherical aerosol particle of dry radius

$$r^{(i)} = \frac{1}{2}\phi_\mathrm{R}^{(i)} D_\mathrm{R}, \tag{A.58}$$

where

$$\phi_\mathrm{R}^{(i)} = \sqrt[3]{\frac{\rho_\mathrm{w}}{\rho^{(i)}} \frac{m_\mathrm{R}^{(i)}}{q_\mathrm{R}}}, \tag{A.59}$$

so that the dry size distribution of released aerosol particles is given by

$$R_{n_\mathrm{R}}^{(i)}\Big|_\mathrm{REVP} \left(r^{(i)}\right) \mathrm{d}r^{(i)} = T_{n_\mathrm{R}\to q}\big|_\mathrm{REVP} \left(D_\mathrm{R}\right) \mathrm{d}D_\mathrm{R}, \tag{A.60}$$

which leads to a $\Gamma(d_\mathrm{R}+1, \frac{1}{\lambda_\mathrm{R}^{(i)}})$ distribution:

$$\left.R_{n_\mathrm{R}}^{(i)}\right|_\mathrm{REVP}(r^{(i)}) = \frac{T_{q_\mathrm{R}\to q}|_\mathrm{REVP}}{F_{q_\mathrm{R}\downarrow}} n_{\mathrm{a,R}} c_\mathrm{R} \left(\frac{\rho_0}{\rho}\right)^{\mathcal{G}_\mathrm{R}} \left(\frac{2}{\phi_\mathrm{R}^{(i)}}\right)^{1+d_\mathrm{R}-n_{\mathrm{b,R}}} \times \left(\lambda_\mathrm{R}^{(i)}\right)^{n_{\mathrm{b,R}}} \left(r^{(i)}\right)^{d_\mathrm{R}} \mathrm{e}^{-\lambda_\mathrm{R}^{(i)} r^{(i)}}, \quad \text{(A.61)}$$

where

$$\lambda_\mathrm{R}^{(i)} = \frac{2\lambda_\mathrm{R}}{\phi_\mathrm{R}^{(i)}}. \quad \text{(A.62)}$$

This gives a total number rate

$$\left.R_{N_\mathrm{R}}^{(i)}\right|_\mathrm{REVP} = T_{N_\mathrm{R}\to q}|_\mathrm{REVP} \quad \text{(A.63)}$$

$$= \frac{\Gamma\left(d_\mathrm{R}+1\right) T_{q_\mathrm{R}\to q}|_\mathrm{REVP}}{\pi\rho_\mathrm{w}} \left(\frac{\pi c_\mathrm{R}\left(\frac{\rho_0}{\rho}\right)^{\mathcal{G}_\mathrm{R}} \rho_\mathrm{w} n_{\mathrm{a,R}}}{F_{q_\mathrm{R}\downarrow}}\right)^{\frac{3}{4+d_\mathrm{R}-n_{\mathrm{b,R}}}}, \quad \text{(A.64)}$$

and mass rate

$$\left.R_{q_\mathrm{R}}^{(i)}\right|_\mathrm{REVP} = \frac{m_\mathrm{R}^{(i)}}{q_\mathrm{R}} T_{q_\mathrm{R}\to q}|_\mathrm{REVP}. \quad \text{(A.65)}$$

A.1.3 IDEP1/SDEP1: Bergeron–Findeisen process

When liquid water is converted to ice via the Bergeron–Findeisen process, it is first evaporated before being deposited onto existing ice particles. As for droplet settling, the droplets are assumed to follow a Khrgian–Mazin gamma distribution $\Gamma(3, \theta_\mathrm{cl})$:

$$n_\mathrm{cl}(r) = \frac{N_\mathrm{cl}}{2\theta_\mathrm{cl}^3} r^2 \mathrm{e}^{-\frac{r}{\theta_\mathrm{cl}}}. \quad \text{(A.66)}$$

If uniform total evaporation across the size spectrum is again assumed, the number rate of evaporation for droplets of diameter D is

$$\begin{aligned} T_{n_\mathrm{cl}\to q}(r)|_\mathrm{IDEP1+SDEP1} &= \frac{n_\mathrm{cl}(r)}{q_\mathrm{cl}}\, T_{q_\mathrm{cl}\to q}|_\mathrm{IDEP1+SDEP1} && \text{(A.67)}\\ &= \frac{N_\mathrm{cl}\, T_{q_\mathrm{cl}\to q}|_\mathrm{IDEP1+SDEP1}}{2\theta_\mathrm{cl}^3 q_\mathrm{cl}} r^2 \mathrm{e}^{-\frac{r}{\theta_\mathrm{cl}}}, && \text{(A.68)} \end{aligned}$$

with a total number rate

$$T_{N_\mathrm{cl}\to q}|_\mathrm{IDEP1+SDEP1} = \frac{N_\mathrm{cl}\, T_{q_\mathrm{cl}\to q}|_\mathrm{IDEP1+SDEP1}}{q_\mathrm{cl}}, \tag{A.69}$$

so that the dry size distribution of released aerosol particles is given by

$$R^{(i)}_{n_\mathrm{cl}}\Big|_\mathrm{IDEP1+SDEP1}\left(r^{(i)}\right) \mathrm{d}r^{(i)} = T_{n_\mathrm{cl}\to q}|_\mathrm{IDEP1+SDEP1}\left(r_\mathrm{cl}\right) \mathrm{d}r_\mathrm{cl}, \tag{A.70}$$

which leads to a $\Gamma(3, \theta_\mathrm{cl}^{(i)})$ distribution:

$$R^{(i)}_{n_\mathrm{cl}}\Big|_\mathrm{IDEP1+SDEP1}\left(r^{(i)}\right) = \frac{N_\mathrm{cl}\, T_{q_\mathrm{cl}\to q}|_\mathrm{IDEP1+SDEP1}}{2q_\mathrm{cl}\left(\theta_\mathrm{cl}^{(i)}\right)^3} \left(r^{(i)}\right)^2 \mathrm{e}^{-\frac{r^{(i)}}{\theta_\mathrm{cl}^{(i)}}}, \tag{A.71}$$

with a total number rate

$$\begin{aligned} R^{(i)}_{N_\mathrm{cl}}\Big|_\mathrm{IDEP1+SDEP1} &= T_{N_\mathrm{cl}\to q}|_\mathrm{IDEP1+SDEP1} && \text{(A.72)}\\ &= \frac{N_\mathrm{cl}\, T_{q_\mathrm{cl}\to q}|_\mathrm{IDEP1+SDEP1}}{q_\mathrm{cl}}, && \text{(A.73)} \end{aligned}$$

and mass rate

$$R^{(i)}_{q_\mathrm{cl}}\Big|_\mathrm{IDEP1+SDEP1} = \frac{m_\mathrm{cl}^{(i)}}{q_\mathrm{cl}}\, T_{q_\mathrm{cl}\to q}|_\mathrm{IDEP1+SDEP1}\,. \tag{A.74}$$

A.1.4 ISUB/IMLTEV/SSUB/SMLTEV: sublimation or evaporation of melting ice

The treatment of ice particles is made more complex by the fact that they are not in general spherical. The mass-diameter relationship is assumed to take the form of a power law, with the mass of a particle in phase x given by

$$M_x(D) = a_x D^{b_x}, \tag{A.75}$$

where a_x and b_x are fixed parameters[2] (Wilkinson et al., 2009, §4.5). Particle diameters are assumed to follow a $\Gamma(\alpha_x + 1, \frac{1}{\lambda_x})$ distribution, with the number of particles of diameter D given by

$$n_x(D) = n_{a,x} \lambda_x^{n_{b,x}} D^{\alpha_x} \mathrm{e}^{-\lambda_x D}, \tag{A.76}$$

where $n_{a,x}$, $n_{b,x}$ and α_x are fixed parameters (Wilkinson et al., 2009, §4.1), and λ_x is given by

$$\lambda_x = \left(\frac{\Gamma\left(\alpha_x + b_x + 1\right) n_{a,x} a_x}{q_x} \right)^{\frac{1}{1+\alpha_x+b_x-n_{b,x}}}, \tag{A.77}$$

so that $q_x = \int_0^\infty a_x D^{b_x} n_x(D)\,\mathrm{d}D$. As for rain, the fall velocities are given by

$$V_x(D) = c_x D^{d_x} \left(\frac{\rho_0}{\rho} \right)^{\mathcal{G}_x}, \tag{A.78}$$

where c_x, d_x, $\mathcal{G}x$ and ρ_0 are fixed parameters.

---

[2] This is a generalisation of the relationship for spherical liquid water drops (which are assumed for liquid cloud and rain), where $a_{\mathrm{R}} = a_{\mathrm{cl}} = \frac{\pi}{6} \times 10^3\,\mathrm{kg\,m^{-3}}$ and $b_{\mathrm{R}} = b_{\mathrm{cl}} = 3$.

The downward number flux of ice particles with diameter D is thus

$$F_{n_x\downarrow}(D) = n_x(D)V_x(D) \tag{A.79}$$

$$= n_{a,x}c_x\left(\frac{\rho_0}{\rho}\right)^{\mathcal{G}_x}\lambda_x^{n_{b,x}}D^{\alpha_x+d_x}\mathrm{e}^{-\lambda_x D}. \tag{A.80}$$

Instead of determining λ_x from the ice water content as above, it could also be determined from the snowfall rate as

$$\lambda_x = \left(\frac{\Gamma\left(\alpha_x+b_x+d_x+1\right)n_{a,x}a_x c_x}{F_{q_x\downarrow}}\left(\frac{\rho_0}{\rho}\right)^{\mathcal{G}_x}\right)^{\frac{1}{1+\alpha_x+b_x+d_x-n_{b,x}}}, \tag{A.81}$$

so that $F_{q_x\downarrow} = \int_0^\infty a_x D^{b_x} n_x(D)V_x(D)\,\mathrm{d}D$.

Under the assumption that a uniform proportion of ice particles across the size spectrum sublimes (or melts and evaporates) completely, the number rate for particles of diameter D is given by

$$T_{n_x\to q}(D)|_P = \frac{T_{q_x\to q}|_P}{F_{q_x\downarrow}}F_{n_x\downarrow}(D) \tag{A.82}$$

$$= \frac{T_{q_x\to q}|_P}{F_{q_x\downarrow}}n_{a,x}c_x\left(\frac{\rho_0}{\rho}\right)^{\mathcal{G}_x}\lambda_x^{n_{b,x}}D^{\alpha_x+d_x}\mathrm{e}^{-\lambda_x D}, \tag{A.83}$$

where $P \in \{\mathrm{ISUB}, \mathrm{SSUB}, \mathrm{IMLTEV}, \mathrm{SMLTEV}\}$, and thus follows $\Gamma(\alpha_x + d_x + 1, \frac{1}{\lambda_x})$ distribution with a total number rate

$$T_{N_x\to q}|_P = \frac{\Gamma\left(\alpha_x+d_x+1\right)T_{q_x\to q}|_P}{\Gamma\left(\alpha_x+b_x+d_x+1\right)} \times\left(\frac{\Gamma\left(\alpha_x+b_x+d_x+1\right)n_{a,x}c_x}{F_{q_x\downarrow}}\left(\frac{\rho_0}{\rho}\right)^{\mathcal{G}_x}\right)^{\frac{b_x}{1+\alpha_x+b_x+d_x-n_{b,x}}}. \tag{A.84}$$

Assuming a uniform concentration of the aerosol species i in the ice, an ice particle of diameter D_x leaves behind a spherical aerosol particle of dry radius

$$r^{(i)} = \frac{1}{2}\phi_x^{(i)} D_{\mathrm{R}}^{\frac{b_x}{3}}, \tag{A.85}$$

where

$$\phi_x^{(i)} = \sqrt[3]{\frac{6 a_x m_x^{(i)}}{\pi \rho^{(i)} q_x}}, \tag{A.86}$$

so that the dry size distribution of released aerosol particles is given by

$$\left. R_{n_x}^{(i)} \right|_P \left(r^{(i)}\right) \mathrm{d}r^{(i)} = \left. T_{n_x \to q} \right|_P (D_x) \, \mathrm{d}D_x, \tag{A.87}$$

which leads to a generalised gamma distribution:

$$\begin{aligned} \left. R_{n_x}^{(i)} \right|_P \left(r^{(i)}\right) = \frac{3 \left. T_{q_x \to q} \right|_P n_{a,x} c_x}{F_{q_x \downarrow} b_x} \left(\frac{\rho_0}{\rho}\right)^{\mathcal{G}_{\mathrm{R}}} \left(\frac{2}{\phi_x^{(i)}}\right)^{\frac{3}{b_x}(1+\alpha_x+d_x)-n_{b,x}} & \left(\lambda_x^{(i)}\right)^{\frac{3 n_{b,x}}{b_x}} \\ \times \left(r^{(i)}\right)^{\frac{3}{b_x}(1+\alpha_x+d_x)-1} \mathrm{e}^{-\left(\lambda_x^{(i)} r^{(i)}\right)^{\frac{3}{b_x}}} &, \end{aligned} \tag{A.88}$$

with a total number rate

$$\left. R_{N_x}^{(i)} \right|_P = \left. T_{N_x \to q} \right|_P \tag{A.89}$$

$$\begin{aligned} = & \frac{\Gamma(\alpha_x + d_x + 1) \left. T_{q_x \to q} \right|_P}{\Gamma(\alpha_x + b_x + d_x + 1)} \\ & \times \left(\frac{\Gamma(\alpha_x + b_x + d_x + 1) \, n_{a,x} c_x}{F_{q_x \downarrow}} \left(\frac{\rho_0}{\rho}\right)^{\mathcal{G}_x} \right)^{\frac{b_x}{1+\alpha_x+b_x+d_x-n_{b,x}}}, \end{aligned} \tag{A.90}$$

and mass rate

$$\left. R_{q_x}^{(i)} \right|_P = \frac{m_x^{(i)}}{q_x} \left. T_{N_x \to q} \right|_P, \tag{A.91}$$

where

$$\lambda_x^{(i)} = \frac{2}{\phi_x^{(i)}} \lambda_x^{\frac{b_x}{3}}. \tag{A.92}$$

A.2 Processes taking up free/interstitial aerosol to water phases

A.2.1 Activation and heterogeneous nucleation

Because there is no prognostic treatment of the aerosol taken up by cloud water and ice, the cumulative take-up of aerosol due to activation of CCN to form liquid cloud droplets and heterogeneous nucleation of ice must be diagnosed at the start of each timestep.

In the scheme currently used in HadGEM3–UKCA, a fixed fraction (usually either zero or one) of the mass and number in each mode M is assumed to be activated within the cloudy fraction of each grid box. This is not physically realistic however, as (for liquid cloud at least) Köhler theory predicts that particles will activate above a critical radius depending on their composition and the local supersaturation; thus large particles are preferentially activated and a higher proportion of mass than number will be activated.[3] The Abdul-Razzak and Ghan (2000) activation scheme, which has been introduced into the model by West et al. (2013), diagnoses the critical radius $r_{\mathrm{crit},M}$ for each mode based on its composition and the estimated maximum local supersaturation.

---

[3] This is partially represented in the current scheme by transferring the large end of the (unscavenged) soluble Aitken mode, above a *fixed* critical radius $r_{\mathrm{crit}} = 35$ nm, into the (fully-scavenged) accumulation mode.

In either case, the number of aerosol particles taken up into liquid cloud water is

$$n_{\mathrm{cl}}^{(i)}(r) = \begin{cases} C_{\mathrm{l}} n_{\mathrm{T}}^{(i)}(r) & r > r_{\mathrm{crit}}^{(i)} \\ 0 & r \leq r_{\mathrm{crit}}^{(i)}, \end{cases} \tag{A.93}$$

where $n_{\mathrm{T}}^{(i)}(r)$ is the prognostic aerosol number, and thus the total aerosol mass taken up is

$$m_{\mathrm{cl}}^{(i)} = \frac{4\pi\rho^{(i)}}{3} \int_{r_{\mathrm{crit}}^{(i)}}^{\infty} r^3 n_{\mathrm{cl}}^{(i)}(r)\,\mathrm{d}r. \tag{A.94}$$

This deals with liquid cloud, but further consideration needs to be given to ice nucleation. Initially this will be treated using fixed scavenging ratios for each mode, however a diagnostic scheme akin to that for activation would be desirable. Additional effects in mixed-phase clouds will need to be considered: it may be that, for example, soluble particles can be scavenged into ice in mixed phase clouds but not in ice-only clouds – they may be activated in cloud droplets which then freeze, which cannot be "remembered" without prognostic in-cloud aerosol.

Once the scavenged aerosol has been calculated, the remaining (interstitial) aerosol number and mass are then

$$n^{(i)}(r) = n_{\mathrm{T}}^{(i)}(r) - \sum_{x \in \mathcal{P}'} n_x^{(i)}(r) \tag{A.95}$$

$$m^{(i)}(r) = m_{\mathrm{T}}^{(i)}(r) - \sum_{x \in \mathcal{P}'} m_x^{(i)}(r). \tag{A.96}$$

A.2.2 Impaction scavenging

The existing scheme for impaction scavenging by rain can be retained, but will be incorporated into the framework described here, calculating the $S_{n_{\mathrm{R}}}^{(i)}(r)$ term. In this way, aerosol taken up by impaction scavenging may be re-released at a lower level if the rain evaporates. Consideration should be given to extending this to cover impaction scavenging by liquid cloud droplets (which may lead to cloud processing of particles too small to activate even in non-precipitating clouds) and ice particles, giving the other $S_{n_x}^{(i)}(r)$ terms.

A.3 Implementation in modal aerosol scheme

The aerosol size spectrum is represented in the model by a superposition of log-normal modes, with fixed (geometric) standard deviation and variable mean (within ranges separated by an order of magnitude).

If it is assumed that the size spectrum $R_{n_x}^{(i)}(r)|_P$ of aerosol released by a given evaporation or sublimation process P is "narrow" compared to the order-of-magnitude separation between the log-normal modes, it is reasonable to simply transfer the total number $R_{N_x}^{(i)}|_P$ and mass $R_{q_x}^{(i)}|_P$ released into the mode M which contains the mean-volume radius

$$\bar{r}_P = \left(\frac{3\, R_{q_x}^{(i)}\Big|_P}{4\pi\rho^{(i)}\, R_{N_x}^{(i)}\Big|_P} \right)^{\frac{1}{3}} \tag{A.97}$$

of the released aerosol:

$$\left.\frac{\partial N_M^{(i)}}{\partial t}\right|_P = R_{N_x}^{(i)}\Big|_P \qquad \left.\frac{\partial m_M^{(i)}}{\partial t}\right|_P = R_{q_x}^{(i)}\Big|_P . \tag{A.98}$$

This avoids having to explicitly integrate over the whole size distribution. The standard deviation of a gamma-distributed variable, $X \sim \Gamma(k, \theta)$, is

$$\sqrt{\mathrm{Var}(X)} = \frac{\mathbb{E}(X)}{\sqrt{k}}, \tag{A.99}$$

and so, provided $k \gg 1$, this should be a reasonable assumption for modes separated by an order of magnitude.

Following this approach, the equations for modal aerosol become:

$$\begin{aligned}
\frac{\partial N_M^{(i)}}{\partial t} &= -\sum_{x \in \mathcal{P}} I_{n_x}^{(i)}(M) + \sum_{\substack{P \in \mathcal{E} \\ \bar{r}_P \in M}} R_{N_x}^{(i)}\Big|_P && (M \in \mathcal{M}) \qquad \text{(A.100)} \\
\frac{\partial m_M^{(i)}}{\partial t} &= -\sum_{x \in \mathcal{P}} I_{m_x}^{(i)}(M) + \sum_{\substack{P \in \mathcal{E} \\ \bar{r}_P \in M}} R_{q_x}^{(i)}\Big|_P && (M \in \mathcal{M}) \qquad \text{(A.101)} \\
\frac{\partial m_x^{(i)}}{\partial t} &= \sum_{M \in \mathcal{M}} I_{m_x}^{(i)}(M) - \sum_{P \in \mathcal{E}} R_{q_x}^{(i)}\Big|_P \\
&\qquad + \sum_{y \in \mathcal{P}'} \left(\frac{T_{q_y \to q_x} m_y^{(i)}}{q_y} - \frac{T_{q_x \to q_y} m_x^{(i)}}{q_x} \right) \\
&\qquad + \frac{1}{\rho} \frac{\partial}{\partial z} \left(\frac{F_{q_x \downarrow} m_x^{(i)}}{q_x} \right) && (x \in \mathcal{P}), \qquad \text{(A.102)}
\end{aligned}$$

where $\mathcal{E} = \{\mathrm{LSETEV}, \mathrm{REVP}, \mathrm{IDEP1}, \mathrm{SDEP1}, \mathrm{ISUB}, \mathrm{SSUB}, \mathrm{IMLTEV}, \mathrm{SMLTEV}\}$ is the set of evaporation/sublimation processes and $I_{n_x}^{(i)}(M)$ and $I_{m_x}^{(i)}(M)$ are the number and mass scavenged from mode M by impaction with water phase x, as diagnosed by the impaction scavenging scheme.

A nucleation scavenging (activation) term does not appear in the time-evolution equations, as it is diagnosed as an “instantaneous” process at the start of the timestep (see Section A.2.1). (A refined scheme might consider separately in these equations the activation which occurs during the timestep, as distinct from that assumed to have already occurred.)

For modal aerosol, the total activated number and mass in each mode can be calculated by integrating (A.93) and (A.94) over the log-normal distribution $n_M^{(i)}(r)$:

$$N_{M,\mathrm{cl}}^{(i)} = \int_{r_{\mathrm{crit},M}}^{\infty} n_M^{(i)}(r)\, \mathrm{d}r \qquad \text{(A.103)}$$

$$N_{M,\mathrm{cl}}^{(i)} = \frac{4\pi\rho_M^{(i)}}{3} \int_{r_{\mathrm{crit},M}^{(i)}}^{\infty} n_M^{(i)}(r)\, \mathrm{d}r, \qquad \text{(A.104)}$$

calculating these as in the existing mode-merging algorithm.

A.4 Discretisation

The large-scale precipitation scheme solves the transfer processes sequentially; for consistency the chemical/aerosol transfers for each process P should be calculated in the same sequence, using the values of q_x on input to the corresponding process in the precipitation scheme. These mid-timestep values, denoted $q_x|_P$, can be determined by re-applying the diagnosed transfer rates in the same sequence as the original calculations:[4]

$$q_x|_{P_{j+1}} = q_x|_{P_j} + \left.\frac{\partial q_x}{\partial t}\right|_{P_j} \Delta t \qquad (j \in \{0, 1, \ldots, J-1\}) \,. \tag{A.105}$$

(Note that this cannot be done correctly in an operator-split manner if iterated microphysics are in use, without additional diagnostics for the per-iteration transfer rates.)

The full discrete equation set for modal aerosol species is given below, based on the continuous versions derived in the preceding sections. In what follows, $\mathcal{T}_{X\to Y}$ and $\mathcal{F}_{X\downarrow}$ are the sets of processes contributing to the transfer $T_{X\to Y}$ or flux $F_{X\downarrow}$ respectively, $F_{q_x}{}^{\downarrow}$ is the downward area flux of q_x across the top boundary of the grid box (equal to $F_{q_x\downarrow}$ in the box above), and $m_x^{(i)\downarrow}$ and $q_x{}^{\downarrow}$ represent the values of $m_x^{(i)}$ and q_x in the box above.

---

[4] LSET[EV]/IFALL/SFALL/*RFALL*/*GFALL*, IFRW, IPRM, IDEP/ISUB, SDEP/SSUB, *SAUT*, *SACI*, IACW, SACW, *GAUT*, *GACW*, *GACS*, IACR, SACR, IMLTEV, SMLTEV, IMLT, SMLT, *GMLT*, REVP, RACW, RAUT; those in italics only operate if additional prognostics are enabled.

At the start of the timestep, in-cloud aerosol is split out diagnostically by the activation scheme (see Section A.2.1):

$$N_M^{(i)} = N_{M,\mathrm{T}}^{(i)} - \sum_{x \in \mathcal{P}'} N_{M,x}^{(i)} \tag{A.106}$$

$$m_M^{(i)} = m_{M,\mathrm{T}}^{(i)} - \sum_{x \in \mathcal{P}'} m_{M,x}^{(i)}. \tag{A.107}$$

The increments to mass and number in each mode from each microphysical process P in the large-scale precipitation scheme are

$$\Delta N_M^{(i)}\Big|_P = R_{N_x}^{(i)}\Big|_P \Delta t \qquad (M \in \mathcal{M}, P \in \mathcal{E}, \bar{r}_P \in M) \tag{A.108}$$

$$\Delta m_M^{(i)}\Big|_P = R_{q_x}^{(i)}\Big|_P \Delta t \qquad (M \in \mathcal{M}, P \in \mathcal{E}, \bar{r}_P \in M)\,, \tag{A.109}$$

and the increments to in-cloud aerosol mass are given by

$$\Delta m_x^{(i)}\Big|_P = \left\{ \begin{array}{ll} \left(\dfrac{F_{q_x}{}^{\downarrow} m_x^{(i)\downarrow}}{q_x{}^{\downarrow}} - \dfrac{F_{q_x \downarrow}\, m_x^{(i)}\Big|_P}{q_x\big|_P} \right) \dfrac{\Delta t}{\Delta z} & (P \in \mathcal{F}_{q_x \downarrow}) \\ - R_{q_x}^{(i)}\Big|_P \Delta t & (P \in \mathcal{T}_{q_x \to q}) \\ \dfrac{P_P\, m_y\big|_P}{q_y\big|_P} \Delta t & (P \in \mathcal{T}_{q_y \to q_x}, y \in \mathcal{P}') \\ - \dfrac{P_P\, m_x\big|_P}{q_x\big|_P} \Delta t & (P \in \mathcal{T}_{q_x \to q_y}, y \in \mathcal{P}') \end{array} \right\} \quad (x \in \mathcal{P}) \tag{A.110}$$

for falling/settling processes, evaporation/sublimation, and transfers into and out of the phase q_x respectively. (The expressions for R_X for the individual evaporation/sublimation processes are given at the end of this summary.)

The mid-timestep values of number and mass in each mode, and in-cloud mass, used for calculating these increments sequentially as per the precipitation scheme, are calculated as:

$$N_M^{(i)}\Big|_{P_{j+1}} = \begin{cases} N_M^{(i)}\Big|_{P_j} + \Delta N_M^{(i)}\Big|_{P_j} & (P_j \in \mathcal{E}, \bar{r}_{P_j} \in M) \\ N_M^{(i)}\Big|_{P_j} & \text{otherwise} \end{cases} \quad \begin{matrix} (M \in \mathcal{M}, \\ j \in \{0, 1, \ldots, J-1\}) \end{matrix} \tag{A.111}$$

$$m_M^{(i)}\Big|_{P_{j+1}} = \begin{cases} m_M^{(i)}\Big|_{P_j} + \Delta m_M^{(i)}\Big|_{P_j} & (P_j \in \mathcal{E}, \bar{r}_{P_j} \in M) \\ m_M^{(i)}\Big|_{P_j} & \text{otherwise} \end{cases} \quad \begin{matrix} (M \in \mathcal{M}, \\ j \in \{0, 1, \ldots, J-1\}) \end{matrix} \tag{A.112}$$

$$m_x^{(i)}\Big|_{P_{j+1}} = \begin{cases} m_x^{(i)}\Big|_{P_j} + \Delta m_x^{(i)}\Big|_{P_j} & (P_j \in \mathcal{T}^*_{q_x}) \\ m_x^{(i)}\Big|_{P_j} & \text{otherwise} \end{cases} \quad \begin{matrix} (x \in \mathcal{P}', \\ j \in \{0, 1, \ldots, J-1\}), \end{matrix} \tag{A.113}$$

where

$$\mathcal{T}^*_{q_x} = \left(\bigcup_{y \in \mathcal{P}'} \mathcal{T}_{q_y \to q_x} \right) \cup \left(\bigcup_{y \in \mathcal{P}} \mathcal{T}_{q_x \to q_y} \right) \tag{A.114}$$

is the set of all transfer processes affecting the amount of aerosol in phase q_x.

The total increments due to scavenging over the timestep are given by summing over both the contributions from precipitation microphysics and those from impaction scavenging (as noted before, activation is treated instantaneously at the start of the timestep, so does not appear here):

$$\Delta N_M^{(i)} = \sum_{x \in \mathcal{P}'} I_{n_x}^{(i)}(M) \Delta t + \sum_{\substack{P \in \mathcal{E} \\ \bar{r}_P \in M}} \Delta N_M^{(i)}\Big|_P \qquad (M \in \mathcal{M}) \tag{A.115}$$

$$\Delta m_M^{(i)} = \sum_{x \in \mathcal{P}'} I_{m_x}^{(i)}(M) \Delta t + \sum_{\substack{P \in \mathcal{E} \\ \bar{r}_P \in M}} \Delta m_M^{(i)}\Big|_P \qquad (M \in \mathcal{M}) \tag{A.116}$$

$$\Delta m_x^{(i)} = \sum_{M \in \mathcal{M}} I_{m_x}^{(i)}(M) \Delta t + \sum_{P \in \mathcal{T}^*_{q_x}} \Delta m_M^{(i)}\Big|_P \qquad (x \in \mathcal{P}). \tag{A.117}$$

Finally, the R_X terms for the number and mass of aerosol released by evaporation/sublimation processes are given below, as derived in Section A.1. For evaporation of settling cloud droplets,

$$R^{(i)}_{N_{\mathrm{cl}}}\Big|_{\mathrm{LSETEV}} = \frac{2\; N_{\mathrm{cl}}|_{\mathrm{LSETEV}}\, P_{\mathrm{LSETEV}}}{7\rho\; q_{\mathrm{cl}}|_{\mathrm{LSETEV}}} \tag{A.118}$$

$$R^{(i)}_{q_{\mathrm{cl}}}\Big|_{\mathrm{LSETEV}} = \frac{P_{\mathrm{LSETEV}}\; m^{(i)}_{\mathrm{cl}}\Big|_{\mathrm{LSETEV}}}{q_{\mathrm{cl}}|_{\mathrm{LSETEV}}}; \tag{A.119}$$

and for evaporation of rain,

$$R^{(i)}_{N_{\mathrm{R}}}\Big|_{\mathrm{REVP}} = \frac{\Gamma\left(d_{\mathrm{R}}+1\right) P_{\mathrm{REVP}}}{\pi\rho_{\mathrm{w}}} \left(\frac{\pi c_{\mathrm{R}} \left(\frac{\rho_0}{\rho}\right)^{\mathcal{G}_{\mathrm{R}}} \rho_{\mathrm{w}} n_{\mathrm{a,R}}}{F_{q_{\mathrm{R}}\downarrow}}\right)^{\frac{3}{4+d_{\mathrm{R}}-n_{\mathrm{b,R}}}} \tag{A.120}$$

$$R^{(i)}_{q_{\mathrm{R}}}\Big|_{\mathrm{REVP}} = \frac{m^{(i)}_{\mathrm{R}}}{q_{\mathrm{R}}} P_{\mathrm{REVP}}. \tag{A.121}$$

For the Bergeron–Findeisen process (deposition of evaporating droplets onto ice particles),

$$R^{(i)}_{N_{\mathrm{cl}}}\Big|_{P} = \frac{N_{\mathrm{cl}} P_P}{q_{\mathrm{cl}}} \qquad (P \in \{\mathrm{IDEP1}, \mathrm{SDEP1}\}) \tag{A.122}$$

$$R^{(i)}_{q_{\mathrm{cl}}}\Big|_{P} = \frac{m^{(i)}_{\mathrm{cl}}}{q_{\mathrm{cl}}} P_P \qquad (P \in \{\mathrm{IDEP1}, \mathrm{SDEP1}\})\,; \tag{A.123}$$

for sublimation of (or evaporation of melting) ice crystals,

$$R^{(i)}_{N_{\mathrm{cfc}}}\Big|_{P} = \frac{\Gamma\left(\alpha_{\mathrm{cfc}}+d_{\mathrm{cfc}}+1\right)\, T_{q_{\mathrm{cfc}}\to q}|_P}{\Gamma\left(\alpha_{\mathrm{cfc}}+b_{\mathrm{cfc}}+d_{\mathrm{cfc}}+1\right)} \times \left(\frac{\Gamma\left(\alpha_{\mathrm{cfc}}+b_{\mathrm{cfc}}+d_{\mathrm{cfc}}+1\right) n_{\mathrm{a,cfc}} c_{\mathrm{cfc}}}{F_{q_{\mathrm{cfc}}\downarrow}} \left(\frac{\rho_0}{\rho}\right)^{\mathcal{G}_{\mathrm{cfc}}}\right)^{\frac{b_{\mathrm{cfc}}}{1+\alpha_{\mathrm{cfc}}+b_{\mathrm{cfc}}+d_{\mathrm{cfc}}-n_{\mathrm{b,cfc}}}} \qquad (P \in \{\mathrm{ISUB}, \mathrm{IMLTEV}\}) \tag{A.124}$$

$$R^{(i)}_{q_{\mathrm{cfc}}}\Big|_{P} = \frac{m^{(i)}_{\mathrm{cfc}}}{q_{\mathrm{cfc}}}\, T_{N_{\mathrm{cfc}}\to q}|_P \qquad (P \in \{\mathrm{ISUB}, \mathrm{IMLTEV}\}); \tag{A.125}$$

and for sublimation of (or evaporation of melting) snow aggregates (as above for ice crystals, bar the different subscripts),

$$\begin{aligned}
\left. R^{(i)}_{N_{\mathrm{cfa}}} \right|_P &= \frac{\Gamma\left(\alpha_{\mathrm{cfa}} + d_{\mathrm{cfa}} + 1\right) \left. T_{q_{\mathrm{cfa}} \to q} \right|_P}{\Gamma\left(\alpha_{\mathrm{cfa}} + b_{\mathrm{cfa}} + d_{\mathrm{cfa}} + 1\right)} \\
&\quad \times \left(\frac{\Gamma\left(\alpha_{\mathrm{cfa}} + b_{\mathrm{cfa}} + d_{\mathrm{cfa}} + 1\right) n_{\mathrm{a,cfa}} c_{\mathrm{cfa}}}{F_{q_{\mathrm{cfa}}\downarrow}} \left(\frac{\rho_0}{\rho} \right)^{\mathcal{G}_{\mathrm{cfa}}} \right)^{\frac{b_{\mathrm{cfa}}}{1 + \alpha_{\mathrm{cfa}} + b_{\mathrm{cfa}} + d_{\mathrm{cfa}} - n_{\mathrm{b,cfa}}}} \\
&\qquad\qquad\qquad\qquad\qquad\qquad (P \in \{\mathrm{SSUB}, \mathrm{SMLTEV}\}) \qquad (\mathrm{A}.126)
\end{aligned}$$

$$\left. R^{(i)}_{q_{\mathrm{cfa}}} \right|_P = \frac{m^{(i)}_{\mathrm{cfa}}}{q_{\mathrm{cfa}}} \left. T_{N_{\mathrm{cfa}} \to q} \right|_P \qquad (P \in \{\mathrm{SSUB}, \mathrm{SMLTEV}\}). \qquad (\mathrm{A}.127)$$

Glossary

Terminology and names

accumulation mode aerosol particles between $\sim 100\,\mathrm{nm}$ and $\sim 1\,\mu\mathrm{m}$ dry diameter, accounting for the majority of the aerosol mass in the atmosphere

activation the process by which *cloud condensation nuclei* grow to become cloud drops in a supersaturated environment

AeroCom an international initiative for the intercomparison and evaluation of global aerosol–climate models and a wide range of observations

burden column-integrated mass (or number) of a component of the atmosphere (e.g. water, a trace gas, or a type of aerosol), expressed in mass (or number) per unit area of the globe

ageing the process by which insoluble or *hydrophobic* aerosols become partially soluble or *hygroscopic* through *coagulation* and condensation

Aitken mode aerosol particles between $\sim 10\,\mathrm{nm}$ and $\sim 100\,\mathrm{nm}$ dry diameter

albedo the fraction of incident radiation which is reflected from a surface

below-cloud scavenging *impaction scavenging* of aerosol particles by falling precipitation

black carbon strongly light-absorbing graphite-like material produced during combustion as a principal component of soot

CALIOP the Cloud–Aerosol Lidar with Orthogonal Polarization, an instrument on board the CALIPSO satellite

coagulation the merging of two aerosol particles to form a single larger particle

coalescence the merging of two cloud droplets to form a single larger droplet

coarse mode aerosol particles larger than ~ 1 µm dry diameter, primarily mineral dust and sea-salt

condensation nuclei aerosol particles identified by their ability to *nucleate* water droplets in supersaturated air

cloud condensation nuclei aerosol particles which can *nucleate* cloud droplets at the small supersaturations found in the atmosphere, in a process called *activation*

dry deposition the removal of aerosol particles as they settle out due to gravity and diffusion, eventually attaching to the surface

ECHAM the climate model developed at the Max Planck Institute for Meteorology

elemental carbon an alternative term for *black carbon*, often used when identified by its refractory properties (ability to withstand very high temperatures) rather than its light-absorbing properties

ERA-40, ERA-Interim atmospheric reanalysis products from the European Centre for Medium-range Weather Forecasts

GFED the Global Fire Emissions Database (van der Werf et al., 2006, 2010)

GLOMAP the GLObal Model of Aerosol Processes, which exists in sectional (GLOMAP-bin; Spracklen et al., 2005) and modal (GLOMAP-mode; Mann et al., 2010) versions, the latter of which forms the aerosol scheme in UKCA

HadGEM the Hadley Centre Global Environmental Model, developed at the UK Met. Office

HAM the *M7*-based modal aerosol scheme developed at the Max Planck Institute for Meteorology as an add-on to *ECHAM* (Stier et al., 2005)

HIPPO the HIAPER Pole-to-Pole Observations of Greenhouse Gases Study (Wofsy et al., 2011), a large-scale aircraft campaign over the Pacific conducted between 2009 and 2011

hydrophobic resistant to wetting by liquid water

hygroscopic able to grow by adsorbing or dissolving in liquid water

ice nuclei aerosol particles which can *nucleate* ice crystals at temperatures too warm for homogeneous freezing of liquid water or homogeneous *nucleation* of ice from water vapour

impaction scavenging *scavenging* of aerosol particles due to collision with hydrometeors

in-cloud scavenging *scavenging* of aerosol particles by cloud droplets or cloud ice particles

M7 the 7-mode aerosol scheme developed by Vignati (2004), on which parts of both *HAM* and *GLOMAP*-mode are based

MetUM the UK Met. Office Unified Model, an atmospheric GCM used for operational weather forecasting as well as forming the basis for *HadGEM*

MODIS the Moderate Resolution Imaging Spectroradiometer, an instrument on board the Aqua and Terra satellites

nucleation formation of a new aerosol particle or hydrometeor from the gas phase

nucleation mode aerosol particles smaller than $\sim 10\,\mathrm{nm}$ dry diameter, typically produced by *nucleation* from the gas phase

nucleation scavenging *in-cloud scavenging* of aerosol particles when they *activate* as *cloud condensation nuclei* or *ice nuclei*

nudging a technique for keeping the large-scale dynamics of a GCM close to a reanalysis product, by Newtonian relaxation of key fields to their counterparts in the reanalysis (Jeuken et al., 1996)

operator splitting an approach to numerical modelling of complex systems, where the equations describing multiple processes are discretised sequentially within each timestep rather than being solved simultaneously

organic aerosol see *particulate organic matter*

organic carbon the carbon content of *particulate organic matter*

particulate organic matter biological debris and *secondary aerosol* from chemical processing and condensation of organic gases of both natural and anthropogenic origin

PC2 the prognostic cloud scheme in HadGEM (Wilson et al., 2008)

primary aerosol aerosol directly emitted in particulate form at source

radiative forcing the change in net downward radiative flux at the tropopause after stratospheric temperatures have re-adjusted to equilibrium, but with the tropospheric state unchanged (Forster et al., 2007)

rainout see *in-cloud scavenging*

scavenging the process by which aerosol particles are taken up by hydrometeors, leading to *wet deposition*

secondary aerosol aerosol produced from atmospheric trace gases by *nucleation*, condensation and/or chemical reactions

SP2 the Single-Particle Soot Photometer, an instrument which measures the mass and mixing state of *black carbon* in individual aerosol particles by laser ablation and incandescence

UKCA the UK Chemistry and Aerosols sub-model, which couples to the atmosphere component of *HadGEM* (`http://www.ukca.ac.uk/`)

washout see *below-cloud scavenging*

wet deposition the removal of *scavenged* aerosol particles in precipitation at the surface

Abbreviations and acronyms

AS	Accumulation mode (Soluble)
AOD	Aerosol Optical Depth
BC	Black Carbon
CN	Condensation Nuclei
CCN	Cloud Condensation Nuclei
CS	Coarse mode (Soluble)
DRE	Direct Radiative Effect
DRF	Direct Radiative Forcing
EC	Elemental Carbon
IN	Ice Nuclei
KI	aitKen mode (Insoluble)
KS	aitKen mode (Soluble)
MMR	Mass Mixing Ratio
NRFA	Normalised Radiative Forcing with respect to Aerosol optical depth
NS	Nucleation mode (Soluble)
OA	Organic Aerosol
OC	Organic Carbon
PD	Present Day
PI	Pre-Industrial
POM	Particulate Organic Matter
RF	Radiative Forcing
SST	Sea Surface Temperature

Bibliography

Aan de Brugh, J. M. J., Schaap, M., Vignati, E., Dentener, F., Kahnert, M., Sofiev, M., Huijnen, V., and Krol, M. C.: The European aerosol budget in 2006, Atmos. Chem. Phys., 11, 1117–1139, doi:10.5194/acp-11-1117-2011, 2011.

Abdul-Razzak, H. and Ghan, S. J.: A parameterization of aerosol activation 2. Multiple aerosol types, J. Geophys. Res., 105, 6837–6844, 2000.

Ackerman, A. S., Toon, O. B., Stevens, D. E., Heymsfield, A. J., Ramanathan, V., and Welton, E. J.: Reduction of Tropical Cloudiness by Soot, Science, 288, 1042–1047, doi:10.1126/science.288.5468.1042, 2000.

Ackerman, T. P. and Toon, O. B.: Absorption of visible radiation in atmosphere containing mixtures of absorbing and nonabsorbing particles, Appl. Opt., 20, 3661–3667, doi:10.1364/AO.20.003661, 1981.

Albrecht, B. A.: Aerosols, Cloud Microphysics, and Fractional Cloudiness, Science, 245, 1227–1230, 1989.

Andreae, M. O., Hegg, D. A., and Baltensperger, U.: Sources and Nature of Atmospheric Aerosols, in: Levin and Cotton (2008), chap. 3, pp. 45–89, 2008.

Andres, R. J. and Kasgnoc, A. D.: A time-averaged inventory of subaerial volcanic sulfur emissions, J. Geophys. Res., 103, 25 251–25 261, doi:10.1029/98JD02091, 1998.

Bala, G., Caldeira, K., and Nemani, R.: Fast versus slow response in climate change: implications for the global hydrological cycle, Clim. Dyn., 35, 423–434, doi:10.1007/s00382-009-0583-y, 2010.

Bauer, S. E., Koch, D., Unger, N., Metzger, S. M., Shindell, D. T., and Streets, D. G.: Nitrate aerosols today and in 2030: a global simulation including aerosols and tropospheric ozone, Atmos. Chem. Phys., 7, 5043–5059, doi:10.5194/acp-7-5043-2007, 2007.

Bauer, S. E., Wright, D. L., Koch, D., Lewis, E. R., McGraw, R., Chang, L.-S., Schwartz, S. E., and Ruedy, R.: MATRIX (Multiconfiguration Aerosol TRacker of mIXing state): an aerosol microphysical module for global atmospheric models, Atmos. Chem. Phys., 8, 6003–6035, doi:10.5194/acp-8-6003-2008, 2008.

Beard, K. V. and Grover, S. N.: Numerical Collision Efficiencies for Small Raindrops Colliding with Micron Size Particles, J. Atmos. Sci., 31, 543–550, doi:10.1175/1520-0469(1974)031<0543:NCEFSR>2.0.CO;2, 1974.

Bellouin, N.: Interaction of UKCA aerosols with radiation: UKCA RADAER, Internal report, Met. Office, Exeter, UK, URL `http://www.ukca.ac.uk/wiki/images/d/dc/UKCA_RADAER.pdf`, 13pp., 2010.

Bellouin, N., Boucher, O., Haywood, J., Johnson, C., Jones, A., Rae, J., and Woodward, S.: Improved representation of aerosols for HadGEM2, Hadley Centre Technical Note 73, Met. Office, Exeter, UK, URL `http://www.metoffice.gov.uk/archive/science/climate-science/hctn73`, 43pp., 2007.

Bellouin, N., Mann, G. W., Woodhouse, M. T., Johnson, C., Carslaw, K. S., and Dalvi, M.: Impact of the modal aerosol scheme GLOMAP-mode on aerosol forcing in the Hadley Centre Global Environmental Model, Atmos. Chem. Phys., 13, 3027–3044, doi:10.5194/acp-13-3027-2013, 2013.

Bergman, T., Kerminen, V.-M., Korhonen, H., Lehtinen, K. J., Makkonen, R., Arola, A., Mielonen, T., Romakkaniemi, S., Kulmala, M., and Kokkola, H.: Evaluation of the sectional aerosol microphysics module SALSA implementation in ECHAM5-HAM aerosol-climate model, Geosci. Model Dev., 5, 845–868, doi:10.5194/gmd-5-845-2012, 2012.

Bond, T. C., Doherty, S. J., Fahey, D. W., Forster, P. M., Berntsen, T., DeAngelo, B. J., Flanner, M. G., Ghan, S., Kärcher, B., Koch, D., Kinne, S., Kondo, Y., Quinn, P. K., Sarofim, M. C., Schultz, M. G., Schulz, M., Venkataraman, C., Zhang, H., Zhang, S., Bellouin, N., Guttikunda, S. K., Hopke, P. K., Jacobson, M. Z., Kaiser, J. W., Klimont, Z., Lohmann, U., Schwarz, J. P., Shindell, D., Storelvmo, T., Warren, S. G., and Zender, C. S.: Bounding the role of black carbon in the climate system: A scientific assessment, J. Geophys. Res., 118, 5380–5552, doi:10.1002/jgrd.50171, 2013.

Borys, R. D., Lowenthal, D. H., Cohn, S. A., and Brown, W. O. J.: Mountaintop and radar measurements of anthropogenic aerosol effects on snow growth and snowfall rate, Geophys. Res. Lett., 30, 1538, doi:10.1029/2002GL016855, 2003.

Cantrell, W. and Heymsfield, A.: Production of Ice in Tropospheric Clouds: A Review, Bull. Amer. Meteorol. Soc., 86, 795–807, doi:10.1175/BAMS-86-6-795, 2005.

Carslaw, K. S., Boucher, O., Spracklen, D. V., Mann, G. W., Rae, J. G. L., Woodward, S., and Kulmala, M.: A review of natural aerosol interactions and feedbacks within the Earth system, Atmos. Chem. Phys., 10, 1701–1737, doi:10.5194/acp-10-1701-2010, 2010.

Chin, M., Rood, R. B., Lin, S.-J., Müller, J.-F., and Thompson, A. M.: Atmospheric sulfur cycle simulated in the global model GOCART: Model description and global properties, J. Geophys. Res., 105, 24 671–24 687, doi:10.1029/2000JD900384, 2000.

Collins, W. J., Bellouin, N., Doutriaux-Boucher, M., Gedney, N., Hinton, T., Jones, C. D., Liddicoat, S., Martin, G., O'Connor, F., Rae, J., Senior, C., Totterdell, I., Woodward, S., Reichler, T., and Kim, J.: Evaluation of the HadGEM2 model, Hadley Centre Technical Note 74, Met. Office, Exeter, UK, URL `http://www.metoffice.gov.uk/archive/science/climate-science/hctn74`, 47pp., 2008.

Croft, B.: Aerosol Wet Scavenging and Cloud Processing of Aerosols in a Global Climate Model, Ph.D. thesis, Department of Physics & Atmospheric Science, Dalhousie University, Halifax, Nova Scotia, Canada, URL `http://hdl.handle.net/10222/13241`, 212pp., 2011.

Croft, B., Lohmann, U., Martin, R. V., Stier, P., Wurzler, S., Feichter, J., Posselt, R., and Ferrachat, S.: Aerosol size-dependent below-cloud scavenging by rain and snow in the ECHAM5-HAM, Atmos. Chem. Phys., 9, 4653–4675, doi:10.5194/acp-9-4653-2009, 2009.

Croft, B., Lohmann, U., Martin, R. V., Stier, P., Wurzler, S., Feichter, J., Hoose, C., Heikkilä, U., van Donkelaar, A., and Ferrachat, S.: Influences of in-cloud aerosol scavenging parameterizations on aerosol concentrations and wet deposition in ECHAM5-HAM, Atmos. Chem. Phys., 10, 1511–1543, doi:10.5194/acp-10-1511-2010, 2010.

Croft, B., Pierce, J. R., Martin, R. V., Hoose, C., and Lohmann, U.: Uncertainty associated with convective wet removal of entrained aerosols in a global climate model, Atmos. Chem. Phys., 12, 10 725–10 748, doi:10.5194/acp-12-10725-2012, 2012.

Davies, T.: A new dynamical core of the Met Office's global and regional modelling of the atmosphere, Q. J. R. Meteorol. Soc., 131, 1759–1782, doi:10.1256/qj.04.101, 2005.

Dee, D. P., Uppala, S. M., Simmons, A. J., Berrisford, P., Poli, P., Kobayashi, S., Andrae, U., Balmaseda, M. A., Balsamo, G., Bauer, P., Bechtold, P., Beljaars, A. C. M., van de Berg, L., Bidlot, J., Bormann, N., Delsol, C., Dragani, R., Fuentes, M., Geer, A. J., Haimberger, L., Healy, S. B., Hersbach, H., Hólm, E. V., Isaksen, L., Kållberg, P., Köhler, M., Matricardi, M., McNally, A. P., Monge-Sanz, B. M., Morcrette, J.-J., Park, B.-K., Peubey, C., de Rosnay, P., Tavolato, C., Thépaut, J.-N., and Vitart, F.: The ERA-Interim reanalysis: configuration and performance of the data assimilation system, Q. J. R. Meteorol. Soc., 137, 553–597, doi:10.1002/qj.828, 2011.

DeMott, P. J., Prenni, A. J., Liu, X., Kreidenweis, S. M., Petters, M. D., Twohy, C. H., Richardson, M. S., Eidhammer, T., and Rogers, D. C.: Predicting global atmospheric ice nuclei distributions and their impacts on climate, Proc. Natl. Acad. Sci. U. S. A., 107, 11 217 –11 222, doi:10.1073/pnas.0910818107, 2010.

Denman, K. L., Brasseur, G., Chidthaisong, A., Ciais, P., Cox, P. M., Dickinson, R. E., Hauglustaine, D., Heinze, C., Holland, E., Jacob, D., Lohmann, U., Ramachandran, S., da Silva Dias, P. L., Wofsy, S. C., and Zhang, X.: Couplings Between Changes in the Climate System and Biogeochemistry, in: Solomon et al. (2007), chap. 7, pp. 499–587, 2007.

Dentener, F., Kinne, S., Bond, T., Boucher, O., Cofala, J., Generoso, S., Ginoux, P., Gong, S., Hoelzemann, J. J., Ito, A., Marelli, L., Penner, J. E., Putaud, J.-P., Textor, C., Schulz, M., van der Werf, G. R., and Wilson, J.: Emissions of primary aerosol and precursor gases in the years 2000 and 1750 prescribed data-sets for AeroCom, Atmos. Chem. Phys., 6, 4321–4344, doi:10.5194/acp-6-4321-2006, 2006.

Diehl, T., Heil, A., Chin, M., Pan, X., Streets, D., Schultz, M., and Kinne, S.: Anthropogenic, biomass burning, and volcanic emissions of black carbon, organic carbon, and SO2 from 1980 to 2010 for hindcast model experiments, Atmos. Chem. Phys. Discuss., 12, 24 895–24 954, doi:10.5194/acpd-12-24895-2012, 2012.

Easter, R. C. and Hales, J. M.: Interpretation of the OSCAR data for reactive gas scavenging, in: Pruppacher et al. (1983), pp. 649–662, 1983.

Fan, J., Zhang, R., Tao, W.-K., and Mohr, K. I.: Effects of aerosol optical properties on deep convective clouds and radiative forcing, J. Geophys. Res., 113, D08 209, doi:10.1029/2007JD009257, 2008.

Feingold, G., Jiang, H., and Harrington, J. Y.: On smoke suppression of clouds in Amazonia, Geophys. Res. Lett., 32, L02 804, doi:10.1029/2004GL021369, 2005.

Feng, J.: A size-resolved model for below-cloud scavenging of aerosols by snowfall, J. Geophys. Res., 114, D08 203, doi:10.1029/2008JD011012, 2009.

Forster, P., Ramaswamy, V., Artaxo, P., Berntsen, T., Betts, R., Fahey, D. W., Haywood, J., Lean, J., Lowe, D. C., Myhre, G., Nganga, J., Prinn, R., Raga, G., Schulz, M., and Dorland, R. V.: Changes in Atmospheric Constituents and in Radiative Forcing, in: Solomon et al. (2007), chap. 2, pp. 129–234, 2007.

Fountoukis, C. and Nenes, A.: Continued development of a cloud droplet formation parameterization for global climate models, J. Geophys. Res., 110, D11 212, doi:10.1029/2004JD005591, 2005.

Fuchs, N. A. and Sutugin, A. G.: Highly dispersed aerosols, in: Hidy and Brock (1971), pp. 1–60, 1971.

Ganzeveld, L., Lelieveld, J., and Roelofs, G.-J.: A dry deposition parameterization for sulfur oxides in a chemistry and general circulation model, J. Geophys. Res., 103, 5679–5694, doi:10.1029/97JD03077, 1998.

Ghan, S. J. and Easter, R. C.: Impact of cloud-borne aerosol representation on aerosol direct and indirect effects, Atmos. Chem. Phys., 6, 4163–4174, doi:10.5194/acp-6-4163-2006, 2006.

Ginoux, P., Chin, M., Tegen, I., Prospero, J. M., Holben, B., Dubovik, O., and Lin, S.-J.: Sources and distributions of dust aerosols simulated with the GOCART model, J. Geophys. Res., 106, 20 255–20 273, doi:10.1029/2000JD000053, 2001.

Gong, S. L.: A parameterization of sea-salt aerosol source function for sub- and super-micron particles, Global Biogeochem. Cycles, 17, 1097, doi:10.1029/2003GB002079, 2003.

Gregory, D. and Rowntree, P. R.: A Mass Flux Convection Scheme with Representation of Cloud Ensemble Characteristics and Stability-Dependent Closure, Mon. Weather Rev., 118, 1483–1506, doi:10.1175/1520-0493(1990)118<1483:AMFCSW>2.0.CO;2, 1990.

Grover, S. N. and Pruppacher, H. R.: The Effect of Vertical Turbulent Fluctuations in the Atmosphere on the Collection of Aerosol Particles by Cloud Drops, Journal of the Atmospheric Sciences, 42, 2305–2318, doi:10.1175/1520-0469(1985)042<2305:TEOVTF>2.0.CO;2, 1985.

Hansen, J., Sato, M., and Ruedy, R.: Radiative forcing and climate response, J. Geophys. Res., 102, 6831–6864, doi:10.1029/96JD03436, 1997.

Haywood, J., Donner, L., Jones, A., and Golaz, J.-C.: Global indirect radiative forcing caused by aerosols: IPCC (2007) and beyond, in: Heintzenberg and Charlson (2009), chap. 19, pp. 451–467, 2009.

Heintzenberg, J. and Charlson, R. J., eds.: Clouds in the Perturbed Climate System: Their Relationship to Energy Balance, Atmospheric Dynamics, and Precipitation, MIT Press, Cambridge, MA, 576pp., 2009.

Hewitt, H. T., Copsey, D., Culverwell, I. D., Harris, C. M., Hill, R. S. R., Keen, A. B., McLaren, A. J., and Hunke, E. C.: Design and implementation of the infrastructure of HadGEM3: the next-generation Met Office climate modelling system, Geosci. Model Dev., 4, 223–253, doi:10.5194/gmd-4-223-2011, 2011.

Hidy, G. M. and Brock, J. R., eds.: Topics in current aerosol research, vol. 2 of *International reviews in aerosol physics and chemistry*, Pergamon Press, New York, 157pp., 1971.

Hill, A. A. and Dobbie, S.: The impact of aerosols on non-precipitating marine stratocumulus. II: The semi-direct effect, Q. J. R. Meteorol. Soc., 134, 1155–1165, doi:10.1002/qj.277, 2008.

Hoffmann, T., Odum, J. R., Bowman, F., Collins, D., Klockow, D., Flagan, R. C., and Seinfeld, J. H.: Formation of Organic Aerosols from the Oxidation of Biogenic Hydrocarbons, J. Atmos. Chem., 26, 189–222, doi:10.1023/A:1005734301837, 1997.

Hoose, C., Lohmann, U., Bennartz, R., Croft, B., and Lesins, G.: Global simulations of aerosol processing in clouds, Atmos. Chem. Phys., 8, 6939–6963, doi:10.5194/acp-8-6939-2008, 2008a.

Hoose, C., Lohmann, U., Stier, P., Verheggen, B., and Weingartner, E.: Aerosol processing in mixed-phase clouds in ECHAM5-HAM: Model description and comparison to observations, J. Geophys. Res., 113, D07 210, doi:10.1029/2007JD009251, 2008b.

Hoyle, C. R., Marécal, V., Russo, M. R., Allen, G., Arteta, J., Chemel, C., Chipperfield, M. P., D'Amato, F., Dessens, O., Feng, W., Hamilton, J. F., Harris, N. R. P., Hosking, J. S., Lewis, A. C., Morgenstern, O., Peter, T., Pyle, J. A., Reddmann, T., Richards, N. A. D., Telford, P. J., Tian, W., Viciani, S., Volz-Thomas, A., Wild, O., Yang, X., and Zeng, G.: Representation of tropical deep convection in atmospheric models – Part 2: Tracer transport, Atmos. Chem. Phys., 11, 8103–8131, doi:10.5194/acp-11-8103-2011, 2011.

Jeuken, A. B. M., Siegmund, P. C., Heijboer, L. C., Feichter, J., and Bengtsson, L.: On the potential of assimilating meteorological analyses in a global climate model for the purpose of model validation, J. Geophys. Res., 101, 16 939–16 950, doi:10.1029/96JD01218, 1996.

Jimenez, J. L., Canagaratna, M. R., Donahue, N. M., Prevot, A. S. H., Zhang, Q., Kroll, J. H., DeCarlo, P. F., Allan, J. D., Coe, H., Ng, N. L., Aiken, A. C., Docherty, K. S., Ulbrich, I. M., Grieshop, A. P., Robinson, A. L., Duplissy, J., Smith, J. D., Wilson, K. R., Lanz, V. A., Hueglin, C., Sun, Y. L., Tian, J., Laaksonen, A., Raatikainen, T., Rautiainen, J., Vaattovaara, P., Ehn, M., M. Kulmala, Tomlinson, J. M., Collins, D. R., Cubison, M. J., Dunlea, E. J., Huffman, J. A., Onasch, T. B., Alfarra, M. R., Williams, P. I., Bower, K., Kondo, Y., Schneider, J., Drewnick, F., Borrmann, S., Weimer, S., Demerjian, K., Salcedo, D., Cottrell, L., Griffin, R., Takami, A., Miyoshi, T., Hatakeyama, S., Shimono, A., Sun, J. Y., Zhang, Y. M., Dzepina, K., Kimmel, J. R., Sueper, D., Jayne, J. T., Herndon, S. C., Trimborn, A. M., Williams, L. R., Wood, E. C., Middlebrook, A. M., Kolb, C. E., Baltensperger, U., and Worsnop, D. R.: Evolution of Organic Aerosols in the Atmosphere, Science, 326, 1525–1529, doi:10.1126/science.1180353, 2009.

Johnson, B. T., Shine, K. P., and Forster, P. M.: The semi-direct aerosol effect: Impact of absorbing aerosols on marine stratocumulus, Q. J. R. Meteorol. Soc., 130, 1407–1422, doi:10.1256/qj.03.61, 2004.

Jones, A. and Roberts, D. L.: An interactive DMS emissions scheme for the unified model, Hadley Centre Technical Note 47, Met. Office, Exeter, UK, URL `http://www.metoffice.gov.uk/archive/hadley-centre-technical-note-47`, 14pp., 2004.

Kettle, A. J., Andreae, M. O., Amouroux, D., Andreae, T. W., Bates, T. S., Berresheim, H., Bingemer, H., Boniforti, R., Curran, M. A. J., DiTullio, G. R., Helas, G., Jones, G. B., Keller, M. D., Kiene, R. P., Leck, C., Levasseur, M., Malin, G., Maspero, M., Matrai, P., McTaggart, A. R., Mihalopoulos, N., Nguyen, B. C., Novo, A., Putaud, J. P., Rapsomanikis, S., Roberts, G., Schebeske, G., Sharma, S., Simó, R., Staubes, R., Turner, S., and Uher, G.: A global database of sea surface dimethylsulfide (DMS) measurements and a procedure to predict sea surface DMS as a function of latitude, longitude, and month, Global Biogeochem. Cycles, 13, 399–444, doi:10.1029/1999GB900004, 1999.

Khain, A., Rosenfeld, D., and Pokrovsky, A.: Aerosol impact on the dynamics and microphysics of deep convective clouds, Q. J. R. Meteorol. Soc., 131, 2639–2663, doi:10.1256/qj.04.62, 2005.

Khain, A. P. and Pinsky, M. B.: Turbulence effects on the collision kernel. II: Increase of the swept volume of colliding drops, Q. J. R. Meteorol. Soc., 123, 1543–1560, doi:10.1002/qj.49712354205, 1997.

Khain, A. P., Rosenfeld, D., and Pokrovsky, A.: Simulating convective clouds with sustained supercooled liquid water down to -37.5°C using a spectral microphysics model, Geophys. Res. Lett., 28, 3887–3890, doi:10.1029/2000GL012662, 2001.

Khairoutdinov, M. and Kogan, Y.: A New Cloud Physics Parameterization in a Large-Eddy Simulation Model of Marine Stratocumulus, Mon. Weather Rev., 128, 229–243, doi:10.1175/1520-0493(2000)128<0229:ANCPPI>2.0.CO;2, 2000.

Kipling, Z., Stier, P., Schwarz, J. P., Perring, A. E., Spackman, J. R., Mann, G. W., Johnson, C. E., and Telford, P. J.: Constraints on aerosol processes in climate models from vertically-resolved aircraft observations of black carbon, Atmos. Chem. Phys., 13, 5969–5986, doi:10.5194/acp-13-5969-2013, 2013.

Kirkevåg, A., Iversen, T., Seland, Ø., Hoose, C., Kristjánsson, J. E., Struthers, H., Ekman, A. M. L., Ghan, S., Griesfeller, J., Nilsson, E. D., and Schulz, M.: Aerosol–climate interactions in the Norwegian Earth System Model – NorESM1-M, Geosci. Model Dev., 6, 207–244, doi:10.5194/gmd-6-207-2013, 2013.

Koch, D. and Del Genio, A. D.: Black carbon semi-direct effects on cloud cover: review and synthesis, Atmos. Chem. Phys., 10, 7685–7696, doi:10.5194/acp-10-7685-2010, 2010.

Koch, D., Schulz, M., Kinne, S., McNaughton, C., Spackman, J. R., Balkanski, Y., Bauer, S., Berntsen, T., Bond, T. C., Boucher, O., Chin, M., Clarke, A., De Luca, N., Dentener, F., Diehl, T., Dubovik, O., Easter, R., Fahey, D. W., Feichter, J., Fillmore, D., Freitag, S., Ghan, S., Ginoux, P., Gong, S., Horowitz, L., Iversen, T., Kirkevåg, A., Klimont, Z., Kondo, Y., Krol, M., Liu, X., Miller, R., Montanaro, V., Moteki, N., Myhre, G., Penner, J. E., Perlwitz, J., Pitari, G., Reddy, S., Sahu, L., Sakamoto, H., Schuster, G., Schwarz, J. P., Seland, Ø., Stier, P., Takegawa, N., Takemura, T., Textor, C., van Aardenne, J. A., and Zhao, Y.: Evaluation of black carbon estimations in global aerosol models, Atmos. Chem. Phys., 9, 9001–9026, doi:10.5194/acp-9-9001-2009, 2009.

Koffi, B., Schulz, M., Bréon, F.-M., Griesfeller, J., Winker, D., Balkanski, Y., Bauer, S., Berntsen, T., Chin, M., Collins, W. D., Dentener, F., Diehl, T., Easter, R., Ghan, S., Ginoux, P., Gong, S., Horowitz, L. W., Iversen, T., Kirkevåg, A., Koch, D., Krol, M., Myhre, G., Stier, P., and Takemura, T.: Application of the CALIOP layer product to evaluate the vertical distribution of aerosols estimated by global models: AeroCom phase I results, J. Geophys. Res., 117, D10 201, doi:10.1029/2011JD016858, 2012.

Korhonen, P., Kulmala, M., Laaksonen, A., Viisanen, Y., McGraw, R., and Seinfeld, J. H.: Ternary nucleation of H2SO4, NH3, and H2O in the atmosphere, J. Geophys. Res., 104, 26 349–26 353, doi:10.1029/1999JD900784, 1999.

Kulmala, M., Laaksonen, A., and Pirjola, L.: Parameterizations for sulfuric acid/water nucleation rates, J. Geophys. Res., 103, 8301–8307, doi:10.1029/97JD03718, 1998.

Kulmala, M., Lehtinen, K. E. J., and Laaksonen, A.: Cluster activation theory as an explanation of the linear dependence between formation rate of 3nm particles and sulphuric acid concentration, Atmos. Chem. Phys., 6, 787–793, doi:10.5194/acp-6-787-2006, 2006.

Kunsch, H. R.: The Jackknife and the Bootstrap for General Stationary Observations, Ann. Statist., 17, 1217–1241, doi:10.2307/2241719, 1989.

Lamarque, J.-F., Bond, T. C., Eyring, V., Granier, C., Heil, A., Klimont, Z., Lee, D., Liousse, C., Mieville, A., Owen, B., Schultz, M. G., Shindell, D., Smith, S. J., Stehfest, E., Van Aardenne, J., Cooper, O. R., Kainuma, M., Mahowald, N., McConnell, J. R., Naik, V., Riahi, K., and van Vuuren, D. P.: Historical (1850–2000) gridded anthropogenic and biomass burning emissions of reactive gases and aerosols: methodology and application, Atmos. Chem. Phys., 10, 7017–7039, doi:10.5194/acp-10-7017-2010, 2010.

Lee, L. A., Carslaw, K. S., Pringle, K. J., Mann, G. W., and Spracklen, D. V.: Emulation of a complex global aerosol model to quantify sensitivity to uncertain parameters, Atmos. Chem. Phys., 11, 12 253–12 273, doi:10.5194/acp-11-12253-2011, 2011.

Levin, Z. and Brenguier, J.-L.: Effects of Pollution and Biomass Burning on Clouds and Precipitation: Observational Studies, in: Levin and Cotton (2008), chap. 6, pp. 205–241, 2008.

Levin, Z. and Cotton, W. R., eds.: Aerosol Pollution Impact on Precipitation: A Scientific Review, Springer, Dordrecht, 386pp., 2008.

Lin, S.-J. and Rood, R. B.: Multidimensional Flux-Form Semi-Lagrangian Transport Schemes, Mon. Weather Rev., 124, 2046–2070, doi:10.1175/1520-0493(1996)124<2046:MFFSLT>2.0.CO;2, 1996.

Liu, X., Easter, R. C., Ghan, S. J., Zaveri, R., Rasch, P., Shi, X., Lamarque, J.-F., Gettelman, A., Morrison, H., Vitt, F., Conley, A., Park, S., Neale, R., Hannay, C., Ekman, A. M. L., Hess, P., Mahowald, N., Collins, W., Iacono, M. J., Bretherton, C. S., Flanner, M. G., and Mitchell, D.: Toward a minimal representation of aerosols in climate models: description and evaluation in the Community Atmosphere Model CAM5, Geosci. Model Dev., 5, 709–739, doi:10.5194/gmd-5-709-2012, 2012.

Lohmann, U.: A glaciation indirect aerosol effect caused by soot aerosols, Geophys. Res. Lett., 29, 1052, doi:10.1029/2001GL014357, 2002.

Lohmann, U. and Feichter, J.: Global indirect aerosol effects: a review, Atmos. Chem. Phys., 5, 715–737, doi:10.5194/acp-5-715-2005, 2005.

Lohmann, U. and Hoose, C.: Sensitivity studies of different aerosol indirect effects in mixed-phase clouds, Atmos. Chem. Phys., 9, 8917–8934, doi:10.5194/acp-9-8917-2009, 2009.

Lohmann, U., Feichter, J., Penner, J., and Leaitch, R.: Indirect effect of sulfate and carbonaceous aerosols: A mechanistic treatment, J. Geophys. Res., 105, 12 193–12 206, doi:10.1029/1999JD901199, 2000.

Lohmann, U., Stier, P., Hoose, C., Ferrachat, S., Kloster, S., Roeckner, E., and Zhang, J.: Cloud microphysics and aerosol indirect effects in the global climate model ECHAM5-HAM, Atmos. Chem. Phys., 7, 3425–3446, doi:10.5194/acp-7-3425-2007, 2007.

Lohmann, U., Rotstayn, L., Storelvmo, T., Jones, A., Menon, S., Quaas, J., Ekman, A. M. L., Koch, D., and Ruedy, R.: Total aerosol effect: radiative forcing or radiative flux perturbation?, Atmos. Chem. Phys., 10, 3235–3246, doi:10.5194/acp-10-3235-2010, 2010.

Mann, G. W., Carslaw, K. S., Spracklen, D. V., Ridley, D. A., Manktelow, P. T., Chipperfield, M. P., Pickering, S. J., and Johnson, C. E.: Description and evaluation of GLOMAP-mode: a modal global aerosol microphysics model for the UKCA composition-climate model, Geosci. Model Dev., 3, 519–551, doi:10.5194/gmd-3-519-2010, 2010.

Mann, G. W., Johnson, C. E., Bellouin, N., Dalvi, M., Abraham, L., Carslaw, K. S., Boucher, O., Stier, P., Rae, J., Spracklen, D. V., Telford, P., Pyle, J. A., O'Connor, F., Carver, G., Pringle, K. J., and Woodhouse, M. T.: Evaluation of the new UKCA climate–composition model. Part 3: Tropospheric aerosol properties, in prep., 2013.

Marticorena, B. and Bergametti, G.: Modeling the atmospheric dust cycle: 1. Design of a soil-derived dust emission scheme, J. Geophys. Res., 100, 16 415–16 430, doi:10.1029/95JD00690, 1995.

McGraw, R.: Description of Aerosol Dynamics by the Quadrature Method of Moments, Aerosol Sci. Technol., 27, 255–265, doi:10.1080/02786829708965471, 1997.

Montero-Martínez, G., Kostinski, A. B., Shaw, R. A., and García-García, F.: Do all raindrops fall at terminal speed?, Geophys. Res. Lett., 36, L11 818, doi:10.1029/2008GL037111, 2009.

Morcrette, C. J. and Petch, J. C.: Analysis of prognostic cloud scheme increments in a climate model, Q. J. R. Meteorol. Soc., 136, 2061–2073, doi:10.1002/qj.720, 2010.

Mu, M., Randerson, J. T., van der Werf, G. R., Giglio, L., Kasibhatla, P., Morton, D., Collatz, G. J., DeFries, R. S., Hyer, E. J., Prins, E. M., Griffith, D. W. T., Wunch, D., Toon, G. C., Sherlock, V., and Wennberg, P. O.: Daily and 3-hourly variability in global fire emissions and consequences for atmospheric model predictions of carbon monoxide, J. Geophys. Res., 116, D24 303, doi:10.1029/2011JD016245, 2011.

Myhre, G., Bellouin, N., Berglen, T. F., Berntsen, T. K., Boucher, O., Grini, A., Isaksen, I. S. A., Johnsrud, M., Mishchenko, M. I., Stordal, F., and Tanré, D.: Comparison of the radiative properties and direct radiative effect of aerosols from a global aerosol model and remote sensing data over ocean, Tellus B, 59, 115–129, doi:10.1111/j.1600-0889.2006.00226.x, 2007.

Myhre, G., Berglen, T. F., Johnsrud, M., Hoyle, C. R., Berntsen, T. K., Christopher, S. A., Fahey, D. W., Isaksen, I. S. A., Jones, T. A., Kahn, R. A., Loeb, N., Quinn, P., Remer, L., Schwarz, J. P., and Yttri, K. E.: Modelled radiative forcing of the direct aerosol effect with multi-observation evaluation, Atmos. Chem. Phys., 9, 1365–1392, doi:10.5194/acp-9-1365-2009, 2009.

Myhre, G., Samset, B. H., Schulz, M., Balkanski, Y., Bauer, S., Berntsen, T. K., Bian, H., Bellouin, N., Chin, M., Diehl, T., Easter, R. C., Feichter, J., Ghan, S. J., Hauglustaine, D., Iversen, T., Kinne, S., Kirkevåg, A., Lamarque, J.-F., Lin, G., Liu, X., Lund, M. T., Luo, G., Ma, X., van Noije, T., Penner, J. E., Rasch, P. J., Ruiz, A., Seland, Ø., Skeie, R. B., Stier, P., Takemura, T., Tsigaridis, K., Wang, P., Wang, Z., Xu, L., Yu, H., Yu, F., Yoon, J.-H., Zhang, K., Zhang, H., and

Zhou, C.: Radiative forcing of the direct aerosol effect from AeroCom Phase II simulations, Atmos. Chem. Phys., 13, 1853–1877, doi:10.5194/acp-13-1853-2013, 2013.

Nenes, A. and Seinfeld, J. H.: Parameterization of cloud droplet formation in global climate models, J. Geophys. Res., 108, 4415, doi:10.1029/2002JD002911, 2003.

Neu, J. L. and Prather, M. J.: Toward a more physical representation of precipitation scavenging in global chemistry models: cloud overlap and ice physics and their impact on tropospheric ozone, Atmos. Chem. Phys., 12, 3289–3310, doi:10.5194/acp-12-3289-2012, 2012.

Nordeng, T. E.: Extended versions of the convective parameterization scheme at ECMWF and their impact on the mean and transient activity of the model in the tropics, Technical Memorandum 206, European Centre for Medium-Range Weather Forecasts, Reading, UK, URL `http://www.ecmwf.int/publications/library/ecpublications/_pdf/tm/001-300/tm206.pdf`, 42 pp., 1994.

O'Connor, F. M., Carver, G. D., Savage, N. H., Pyle, J. A., Methven, J., Arnold, S. R., Dewey, K., and Kent, J.: Comparison and visualisation of high-resolution transport modelling with aircraft measurements, Atmos. Sci. Lett., 6, 164–170, doi:10.1002/asl.111, 2005.

O'Connor, F. M., Johnson, C. E., Morgenstern, O., Abraham, N. L., Braesicke, P., Dalvi, M., Folberth, G. A., Sanderson, M. G., Telford, P. J., Young, P. J., Zeng, G., Collins, W. J., and Pyle, J. A.: Evaluation of the new UKCA climate-composition model – Part 2: The Troposphere, Geosci. Model Dev. Discuss., 6, 1743–1857, doi:10.5194/gmdd-6-1743-2013, 2013.

Ovchinnikov, M. and Easter, R. C.: Modeling aerosol growth by aqueous chemistry in a nonprecipitating stratiform cloud, J. Geophys. Res., 115, D14 210, doi:10.1029/2009JD012816, 2010.

Peng, Y., von Salzen, K., and Li, J.: Simulation of mineral dust aerosol with Piecewise Log-normal Approximation (PLA) in CanAM4-PAM, Atmos. Chem. Phys., 12, 6891–6914, doi:10.5194/acp-12-6891-2012, 2012.

Penner, J. E., Chuang, C. C., and Liousse, C.: The Contribution of Carbonaceous Aerosols to Climate Change, in: Nucleation and Atmospheric Aerosols 1996: Proceedings of the 14th International Conference on Nucleation and Atmospheric Aerosols, pp. 759–769, Elsevier Sci., New York, 994pp., 1996.

Peters, K., Quaas, J., and Bellouin, N.: Effects of absorbing aerosols in cloudy skies: a satellite study over the Atlantic Ocean, Atmos. Chem. Phys., 11, 1393–1404, doi:10.5194/acp-11-1393-2011, 2011.

Pinsky, M. B. and Khain, A. P.: Turbulence effects on the collision kernel. I: Formation of velocity deviations of drops falling within a turbulent three-dimensional flow, Q. J. R. Meteorol. Soc., 123, 1517–1542, doi:10.1002/qj.49712354204, 1997.

Pringle, K. J., Tost, H., Metzger, S., Steil, B., Giannadaki, D., Nenes, A., Fountoukis, C., Stier, P., Vignati, E., and Lelieveld, J.: Description and evaluation of GMXe: a new aerosol submodel for global simulations (v1), Geosci. Model Dev., 3, 391–412, doi:10.5194/gmd-3-391-2010, 2010.

Pruppacher, H. R. and Jaenicke, R.: The processing of water vapor and aerosols by atmospheric clouds, a global estimate, Atmos. Res., 38, 283–295, doi:10.1016/0169-8095(94)00098-X, 1995.

Pruppacher, H. R. and Klett, J. D.: Microphysics of Clouds and Precipitation, Atmospheric and Oceanographic Sciences Library, Springer, Dordrecht, 976pp., 1996.

Pruppacher, H. R., Semonin, R. G., and Slinn, W. G. N., eds.: Precipitation Scavenging, Dry Deposition, and Resuspension, Elsevier, New York, 748pp., 1983.

Ramanathan, V. and Carmichael, G.: Global and regional climate changes due to black carbon, Nature Geosci., 1, 221–227, doi:10.1038/ngeo156, 2008.

Randerson, D., ed.: Atmospheric Science and Power Production, US Department of Energy, Springfield, VA, 850pp., 1984.

Reddington, C. L., McMeeking, G., Mann, G. W., Coe, H., Frontoso, M. G., Liu, D., Flynn, M., Spracklen, D. V., and Carslaw, K. S.: The mass and number size distributions of black carbon aerosol over Europe, Atmos. Chem. Phys., 13, 4917–4939, doi:10.5194/acp-13-4917-2013, 2013.

Riahi, K., Rao, S., Krey, V., Cho, C., Chirkov, V., Fischer, G., Kindermann, G., Nakicenovic, N., and Rafaj, P.: RCP 8.5—A scenario of comparatively high greenhouse gas emissions, Climatic Change, 109, 33–57, doi:10.1007/s10584-011-0149-y, 2011.

Roeckner, E., Baeuml, G., Bonventura, L., Brokopf, R., Esch, M., Giorgetta, M., Hagemann, S., Kirchner, I., Kornblueh, L., Manzini, E., Rhodin, A., Schlese, U., Schulzweida, U., and Tompkins, A.: The atmospheric general circulation model ECHAM5. Part I: Model description, Report 349, Max Planck Institute for Meteorology, Hamburg, Germany, URL `http://www.mpimet.mpg.de/fileadmin/publikationen/Reports/max_scirep_349.pdf`, 2003.

Rogers, R. R. and Yau, M. K.: A Short Course in Cloud Physics, vol. 113 of *International Series in Natural Philosophy*, Pergamon Press, Oxford, 3rd edn., 1989.

Rosenfeld, D. and Woodley, W. L.: Deep convective clouds with sustained supercooled liquid water down to –37.5°C, Nature, 405, 440–442, doi:10.1038/35013030, 2000.

Ruijgrok, W., Davidson, C. I., and Nicholson, K. W.: Dry deposition of particles, Tellus B, 47, 587–601, doi:10.1034/j.1600-0889.47.issue5.6.x, 1995.

Russo, M. R., Marécal, V., Hoyle, C. R., Arteta, J., Chemel, C., Chipperfield, M. P., Dessens, O., Feng, W., Hosking, J. S., Telford, P. J., Wild, O., Yang, X., and Pyle, J. A.: Representation of tropical deep convection in atmospheric models – Part 1: Meteorology and comparison with satellite observations, Atmos. Chem. Phys., 11, 2765–2786, doi:10.5194/acp-11-2765-2011, 2011.

Samset, B. H. and Myhre, G.: Vertical dependence of black carbon, sulphate and biomass burning aerosol radiative forcing, Geophys. Res. Lett., 38, L24 802, doi:10.1029/2011GL049697, 2011.

Samset, B. H., Myhre, G., Schulz, M., Balkanski, Y., Bauer, S., Berntsen, T. K., Bian, H., Bellouin, N., Diehl, T., Easter, R. C., Ghan, S. J., Iversen, T., Kinne, S., Kirkevåg, A., Lamarque, J.-F., Lin, G., Liu, X., Penner, J. E., Seland, Ø., Skeie, R. B., Stier, P., Takemura, T., Tsigaridis, K., and Zhang, K.: Black carbon vertical profiles strongly affect its radiative forcing uncertainty, Atmos. Chem. Phys., 13, 2423–2434, doi:10.5194/acp-13-2423-2013, 2013.

Schulz, M., Textor, C., Kinne, S., Balkanski, Y., Bauer, S., Berntsen, T., Berglen, T., Boucher, O., Dentener, F., Guibert, S., Isaksen, I. S. A., Iversen, T., Koch, D., Kirkevåg, A., Liu, X., Montanaro, V., Myhre, G., Penner, J. E., Pitari, G., Reddy, S., Seland, Ø., Stier, P., and Takemura, T.: Radiative forcing by aerosols as derived from the AeroCom present-day and pre-industrial simulations, Atmos. Chem. Phys., 6, 5225–5246, doi:10.5194/acp-6-5225-2006, 2006.

Schwarz, J. P., Gao, R. S., Fahey, D. W., Thomson, D. S., Watts, L. A., Wilson, J. C., Reeves, J. M., Darbeheshti, M., Baumgardner, D. G., Kok, G. L., Chung, S. H., Schulz, M., Hendricks, J., Lauer, A., Kärcher, B., Slowik, J. G., Rosenlof, K. H., Thompson, T. L., Langford, A. O., Loewenstein, M., and Aikin, K. C.: Single-particle measurements of midlatitude black carbon and light-scattering aerosols from the boundary layer to the lower stratosphere, J. Geophys. Res., 111, D16 207, doi:10.1029/2006JD007076, 2006.

Schwarz, J. P., Spackman, J. R., Fahey, D. W., Gao, R. S., Lohmann, U., Stier, P., Watts, L. A., Thomson, D. S., Lack, D. A., Pfister, L., Mahoney, M. J., Baumgardner, D., Wilson, J. C., and Reeves, J. M.: Coatings and their enhancement of black carbon light absorption in the tropical atmosphere, J. Geophys. Res., 113, D03 203, doi:10.1029/2007JD009042, 2008.

Schwarz, J. P., Spackman, J. R., Gao, R. S., Watts, L. A., Stier, P., Schulz, M., Davis, S. M., Wofsy, S. C., and Fahey, D. W.: Global-scale black carbon profiles observed in the remote atmosphere and compared to models, Geophys. Res. Lett., 37, L18 812, doi:10.1029/2010GL044372, 2010.

Seinfeld, J. H. and Pandis, S. N.: Atmospheric Chemistry and Physics: From Air Pollution to Climate Change, Wiley-Interscience, New York, 1360pp., 1998.

Seinfeld, J. H. and Pandis, S. N.: Atmospheric Chemistry and Physics: From Air Pollution to Climate Change, Wiley-Interscience, Hoboken, NJ, 2nd edn., 1232pp., 2006.

Sekhon, R. S. and Srivastava, R. C.: Doppler Radar Observations of Drop-Size Distributions in a Thunderstorm, J. Atmos. Sci., 28, 983–994, doi:10.1175/1520-0469(1971)028<0983:DROODS>2.0.CO;2, 1971.

Slinn, W. G. N.: Predictions for particle deposition to vegetative canopies, Atmos. Environ., 16, 1785–1794, doi:10.1016/0004-6981(82)90271-2, 1982.

Slinn, W. G. N.: Precipitation Scavenging, in: Randerson (1984), pp. 466–532, 1984.

Smith, R. N. B.: A scheme for predicting layer clouds and their water content in a general circulation model, Q. J. R. Meteorol. Soc., 116, 435–460, doi:10.1002/qj.49711649210, 1990.

Solomon, S., Qin, D., Manning, M., Chen, Z., Marquis, M., Averyt, K. B., Tignor, M., and Miller, H. L., eds.: Climate Change 2007: The Physical Science Basis. Contribution of Working Group I to the Fourth Assessment Report of the Intergovernmental Panel on Climate Change, Cambridge University Press, 1009pp., 2007.

Spiro, P. A., Jacob, D. J., and Logan, J. A.: Global inventory of sulfur emissions with 1°×1° resolution, J. Geophys. Res., 97, 6023–6036, doi:10.1029/91JD03139, 1992.

Spracklen, D. V., Pringle, K. J., Carslaw, K. S., Chipperfield, M. P., and Mann, G. W.: A global off-line model of size-resolved aerosol microphysics: II. Identification of key uncertainties, Atmos. Chem. Phys., 5, 3233–3250, doi:10.5194/acp-5-3233-2005, 2005.

Stevens, B. and Feingold, G.: Untangling aerosol effects on clouds and precipitation in a buffered system, Nature, 461, 607–613, doi:10.1038/nature08281, 2009.

Stier, P., Feichter, J., Kinne, S., Kloster, S., Vignati, E., Wilson, J., Ganzeveld, L., Tegen, I., Werner, M., Balkanski, Y., Schulz, M., Boucher, O., Minikin, A., and Petzold, A.: The aerosol-climate model ECHAM5-HAM, Atmos. Chem. Phys., 5, 1125–1156, doi:10.5194/acp-5-1125-2005, 2005.

Stier, P., Seinfeld, J. H., Kinne, S., Feichter, J., and Boucher, O.: Impact of nonabsorbing anthropogenic aerosols on clear-sky atmospheric absorption, J. Geophys. Res., 111, D18 201, doi:10.1029/2006JD007147, 2006.

Stier, P., Seinfeld, J. H., Kinne, S., and Boucher, O.: Aerosol absorption and radiative forcing, Atmos. Chem. Phys., 7, 5237–5261, doi:10.5194/acp-7-5237-2007, 2007.

Sundqvist, H., Berge, E., and Kristjánsson, J. E.: Condensation and Cloud Parameterization Studies with a Mesoscale Numerical Weather Prediction Model, Mon. Weather Rev., 117, 1641–1657, doi:10.1175/1520-0493(1989)117<1641:CACPSW>2.0.CO;2, 1989.

Takemura, T., Nozawa, T., Emori, S., Nakajima, T. Y., and Nakajima, T.: Simulation of climate response to aerosol direct and indirect effects with aerosol transport-radiation model, J. Geophys. Res., 110, D02 202, doi:10.1029/2004JD005029, 2005.

Telford, P. J., Braesicke, P., Morgenstern, O., and Pyle, J. A.: Technical Note: Description and assessment of a nudged version of the new dynamics Unified Model, Atmos. Chem. Phys., 8, 1701–1712, doi:10.5194/acp-8-1701-2008, 2008.

Telford, P. J., Abraham, N. L., Archibald, A. T., Braesicke, P., Dalvi, M., Morgenstern, O., O'Connor, F. M., Richards, N. A. D., and Pyle, J. A.: Implementation of the Fast-JX Photolysis scheme (v6.4) into the UKCA component of the MetUM chemistry-climate model (v7.3), Geosci. Model Dev., 6, 161–177, doi:10.5194/gmd-6-161-2013, 2013.

Textor, C., Schulz, M., Guibert, S., Kinne, S., Balkanski, Y., Bauer, S., Berntsen, T., Berglen, T., Boucher, O., Chin, M., Dentener, F., Diehl, T., Easter, R., Feichter, H., Fillmore, D., Ghan, S., Ginoux, P., Gong, S., Grini, A., Hendricks, J., Horowitz, L., Huang, P., Isaksen, I., Iversen, I., Kloster, S., Koch, D., Kirkevåg, A., Kristjansson, J. E., Krol, M., Lauer, A., Lamarque, J. F., Liu, X., Montanaro, V., Myhre, G., Penner, J., Pitari, G., Reddy, S., Seland, Ø., Stier, P., Takemura, T., and Tie, X.: Analysis and quantification of the diversities of aerosol life cycles within AeroCom, Atmos. Chem. Phys., 6, 1777–1813, doi:10.5194/acp-6-1777-2006, 2006.

Tiedtke, M.: A Comprehensive Mass Flux Scheme for Cumulus Parameterization in Large-Scale Models, Mon. Weather Rev., 117, 1779–1800, doi:10.1175/1520-0493(1989)117<1779:ACMFSF>2.0.CO;2, 1989.

Tompkins, A. M.: A Prognostic Parameterization for the Subgrid-Scale Variability of Water Vapor and Clouds in Large-Scale Models and Its Use to Diagnose Cloud Cover, J. Atmos. Sci., 59, 1917–1942, doi:10.1175/1520-0469(2002)059<1917:APPFTS>2.0.CO;2, 2002.

Tripoli, G. J. and Cotton, W. R.: A Numerical Investigation of Several Factors Contributing to the Observed Variable Intensity of Deep Convection over South Florida, J. Appl. Meteorol., 19, 1037–1063, doi:10.1175/1520-0450(1980)019<1037:ANIOSF>2.0.CO;2, 1980.

Twomey, S.: The Influence of Pollution on the Shortwave Albedo of Clouds, Journal of the Atmospheric Sciences, 34, 1149–1152, doi:10.1175/1520-0469(1977)034<1149:TIOPOT>2.0.CO;2, 1977.

Tzivion, S., Feingold, G., and Levin, Z.: The Evolution of Raindrop Spectra. Part II: Collisional Collection/Breakup and Evaporation in a Rainshaft, Journal of the Atmospheric Sciences, 46, 3312–3328, doi:10.1175/1520-0469(1989)046<3312:TEORSP>2.0.CO;2, 1989.

van der Werf, G. R., Randerson, J. T., Giglio, L., Collatz, G. J., Kasibhatla, P. S., and Arellano Jr., A. F.: Interannual variability in global biomass burning emissions from 1997 to 2004, Atmos. Chem. Phys., 6, 3423–3441, doi:10.5194/acp-6-3423-2006, 2006.

van der Werf, G. R., Randerson, J. T., Giglio, L., Collatz, G. J., Mu, M., Kasibhatla, P. S., Morton, D. C., DeFries, R. S., Jin, Y., and van Leeuwen, T. T.: Global fire emissions and the contribution of deforestation, savanna, forest, agricultural, and peat fires (1997–2009), Atmos. Chem. Phys., 10, 11 707–11 735, doi:10.5194/acp-10-11707-2010, 2010.

Vignati, E.: M7: An efficient size-resolved aerosol microphysics module for large-scale aerosol transport models, J. Geophys. Res., 109, 1–17, doi:10.1029/2003JD004485, 2004.

Walters, D. N., Williams, K. D., Boutle, I. A., Bushell, A. C., Edwards, J. M., Field, P. R., Lock, A. P., Morcrette, C. J., Stratton, R. A., Wilkinson, J. M., Willett, M. R., Bellouin, N., Bodas-Salcedo, A., Brooks, M. E., Copsey, D., Earnshaw, P. D., Hardiman, S. C., Harris, C. M., Levine, R. C., MacLachlan, C., Manners, J. C., Martin, G. M., Milton, S. F., Palmer, M. D., Roberts, M. J., Rodríguez, J. M., Tennant, W. J., and Vidale, P. L.: The Met Office Unified Model Global Atmosphere 4.0 and JULES Global Land 4.0 configurations, Geosci. Model Dev. Discuss., 6, 2813–2881, doi:10.5194/gmdd-6-2813-2013, 2013.

Wang, P. K.: Ice Microdynamics, vol. 45 of *Advances in Geophysics*, Academic Press, San Diego, CA, 290pp., 2002.

Wang, X.: Uncertainty assessment of current size-resolved parameterizations for below-cloud particle scavenging by rain, Atmos. Chem. Phys., 10, 5685–5705, doi:10.5194/acp-10-5685-2010, 2010.

West, R. E. L., Stier, P., Jones, A., Johnson, C. E., Mann, G. W., Bellouin, N., and Kipling, Z.: The importance of vertical velocity variability for estimates of the indirect aerosol effects, Atmos. Chem. Phys. Discuss., 13, 27 053–27 113, doi:10.5194/acpd-13-27053-2013, 2013.

Wilcox, E. M.: Direct and semi-direct radiative forcing of smoke aerosols over clouds, Atmos. Chem. Phys., 12, 139–149, doi:10.5194/acp-12-139-2012, 2012.

Wilkinson, J., Wilson, D., and Forbes, R.: The Large-Scale Precipitation Parametrization Scheme, Unified Model Documentation Paper 26, Met. Office, Exeter, UK, Unified Model Version 7.3, 2009.

Wilson, D. R. and Ballard, S. P.: A microphysically based precipitation scheme for the UK Meteorological Office Unified Model, Q. J. R. Meteorol. Soc., 125, 1607–1636, doi:10.1002/qj.49712555707, 1999.

Wilson, D. R., Bushell, A. C., Kerr-Munslow, A. M., Price, J. D., and Morcrette, C. J.: PC2: A prognostic cloud fraction and condensation scheme. I: Scheme description, Q. J. R. Meteorol. Soc., 134, 2093–2107, doi:10.1002/qj.333, 2008.

Wofsy, S. C., the HIPPO Science Team, and Cooperating Modellers and Satellite Teams: HIAPER Pole-to-Pole Observations (HIPPO): fine-grained, global-scale measurements of climatically important atmospheric gases and aerosols, Phil. Trans. R. Soc. A, 369, 2073 –2086, doi:10.1098/rsta.2010.0313, 2011.

Woodward, S.: Modeling the atmospheric life cycle and radiative impact of mineral dust in the Hadley Centre climate model, J. Geophys. Res., 106, 18 155–18 166, doi:10.1029/2000JD900795, 2001.

Yu, F. and Luo, G.: Simulation of particle size distribution with a global aerosol model: contribution of nucleation to aerosol and CCN number concentrations, Atmos. Chem. Phys., 9, 7691–7710, doi:10.5194/acp-9-7691-2009, 2009.

Yu, F. and Turco, R. P.: Ultrafine aerosol formation via ion-mediated nucleation, Geophys. Res. Lett., 27, 883–886, doi:10.1029/1999GL011151, 2000.

Zarzycki, C. M. and Bond, T. C.: How much can the vertical distribution of black carbon affect its global direct radiative forcing?, Geophys. Res. Lett., 37, L20 807, doi:10.1029/2010GL044555, 2010.

Zhang, K., O'Donnell, D., Kazil, J., Stier, P., Kinne, S., Lohmann, U., Ferrachat, S., Croft, B., Quaas, J., Wan, H., Rast, S., and Feichter, J.: The global aerosol-climate model ECHAM-HAM, version 2: sensitivity to improvements in process representations, Atmos. Chem. Phys., 12, 8911–8949, doi:10.5194/acp-12-8911-2012, 2012.

Zhang, L., Gong, S., Padro, J., and Barrie, L.: A size-segregated particle dry deposition scheme for an atmospheric aerosol module, Atmos. Environ., 35, 549–560, doi:10.1016/S1352-2310(00)00326-5, 2001.